Mitochondrial dynamics as a hub in the control of muscle inflammation

Andrea Irazoqui Guimon

Mitochondrial dynamics as a hub in the control of muscle inflammation

Andrea Irazoqui Guimon

Barcelona, 2021

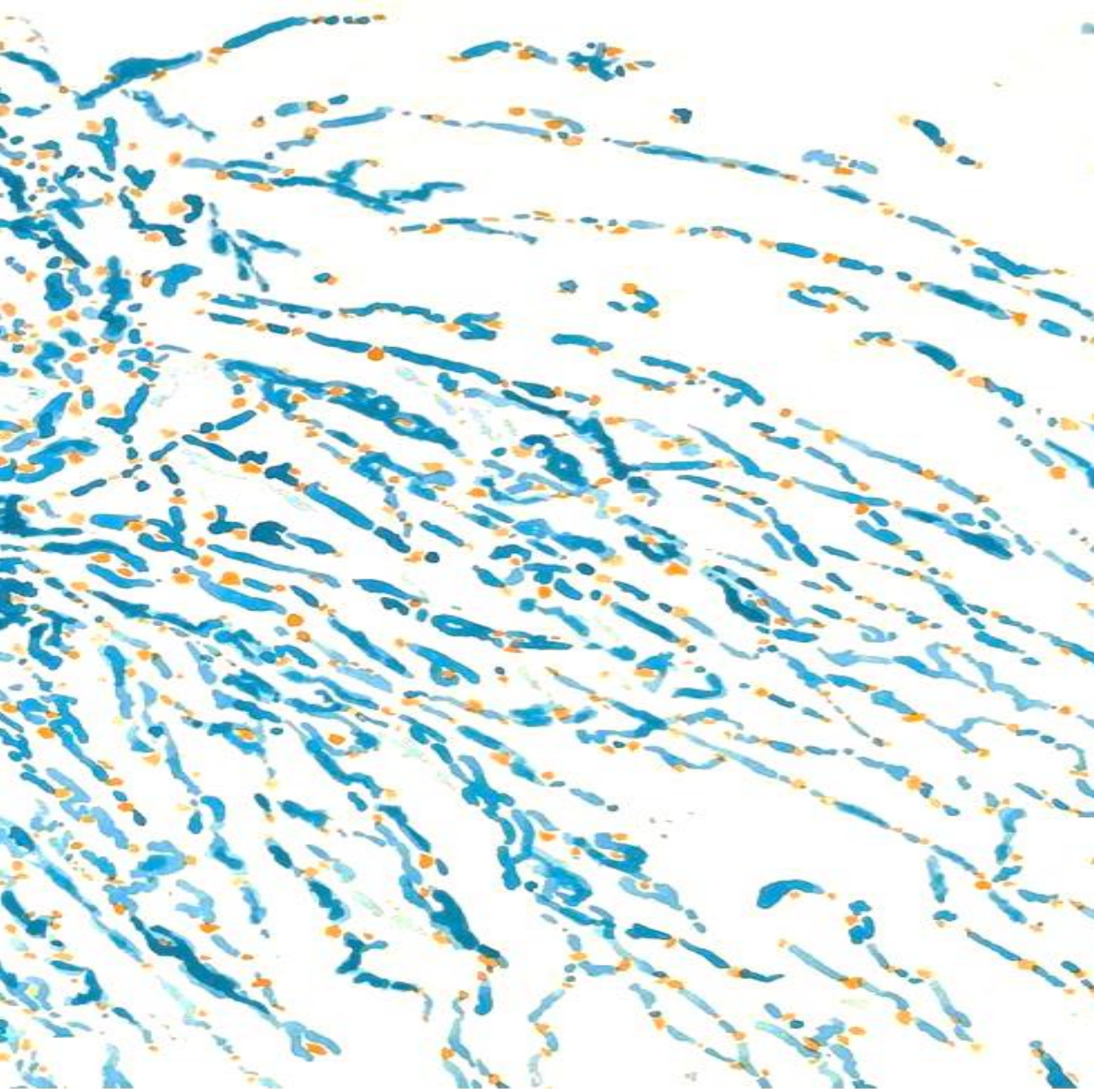

UNIVERSIDAD DE BARCELONA

FACULTAD DE BIOLOGÍA

DEPARTAMENTO DE BIOQUÍMICA Y BIOMEDICINA MOLECULAR

Mitochondrial dynamics as a hub in the control of muscle inflammation

La dinámica mitocondrial como eje en el control de la inflamación muscular

Andrea Irazoqui Guimon

Barcelona, 2021

FACULTAD DE BIOLOGÍA

DEPARTAMENTO DE BIOQUÍMICA Y BIOMEDICINA MOLECULAR

INSTITUTE FOR RESEARCH IN BIOMEDICINE (IRB BARCELONA)

PROGRAMA DE DOCTORADO EN BIOMEDICINA

Mitochondrial dynamics as a hub in the control of muscle inflammation

La dinámica mitocondrial como eje en el control de la inflamación muscular

Memoria presentada por Andrea Irazoqui Guimon para optar al grado de doctora por la Universidad de Barcelona.

Andrea Irazoqui Guimon
Doctoranda

Dr. Antonio Zorzano Olarte
Director y tutor

Dra. Anna Maria Gumà Garcia
Directora

Barcelona, 2021

“Life did not take over the world by combat,
but by networking.”

Lynn Margulis

Abstract

Some forms of mitochondrial dysfunction induce sterile inflammation through mitochondrial DNA (mtDNA) recognition by intracellular DNA sensors. However, our understanding of the processes operating this activation is partial. Here we have analyzed the participation of mitochondrial dynamics in the control of inflammatory responses. We document that mitochondrial fragmentation causes NFκB-dependent inflammation, whereas mitochondrial elongation activates both NFκB and type I interferon (IFN) inflammatory responses in muscle cells. This differential response is a consequence of activation of the DNA sensors TLR9 or cGAS. Surprisingly, we also document that Mfn1 deficiency-induced inflammation is associated with an enhanced encounter of mitochondria with early endosomes, which requires the participation of the early endosomal protein Rab5C. Mfn1 ablation in mouse skeletal muscles promoted NFκB activation, muscle atrophy, reduced physical performance and enhanced IL6 response to exercise, which were improved or rescued upon chronic anti-inflammatory treatment.

Taken together, our data demonstrate that mitochondrial dynamics is key in mitigating different inflammatory responses through mtDNA mislocation. We also demonstrate that muscle inflammation caused by mitochondrial fragmentation precedes the development of muscle atrophy and impaired physical performance. Therefore, we propose that inflammatory muscle disorders characterized by triggering of DNA sensors can be underpinned by therapeutic strategies promoting balanced mitochondrial dynamics.

Contents

Figure contents

Tables

Resumen en castellano

ABBREVIATIONS

A

Acta1: Skeletal alpha actin 1
AD: Autosomal dominant inheritance
ADOA: Autosomal dominant optic atrophy
ADPEO: Autosomal dominant progressive external ophthalmoplegia
AIM2: Absent in melanoma 2
ANOVA: Analysis of variance
AR: Autosomal recessive inheritance
Arp: Actin related protein
Asc: Apoptosis-associated speck-like protein containing a CARD
ATP: Adenosine triphosphate
AVM: Autophagic vacuolar myopathy

B

BAT: Brown adipose tissue
BCL2L13: BCL2-like 13
BNIP3: BCL2/adenovirus E1B 19kDa protein-interacting protein 3
BNIP3: BCL2/adenovirus E1B 19kDa protein-interacting protein 3 like
bp: base pairs
BSA: Bovine serum albumin

C

CARP2: Caspase 8/10 associated RING protein 2
CCCP: Carbonyl cyanide m-chlorophenyl hydrazone
Cd68: Cluster of differentiation 68
cDNA: Complementary DNA
cGAS: Cyclic-GAMP synthase
CJs: Cristae junctions
CK: Creatine kinase
Ckm: Muscle creatine kinase gene
CMA: Chaperon-mediated autophagy
CMTDIB: Charcot-Marie-Tooth dominant intermediate type B
CMTDIE: Charcot-Marie-Tooth dominant intermediate type E
CMT2A: Charcot-Marie-Tooth type 2A
CMT2K: Charcot-Marie-Tooth type 2K
CNM: Centronuclear myopathy
Cox2: Cyclooxygenase 2
CSA: Cross-sectional area
Cytb: Cytochrome b

D
DAMP: Damage-associated molecular pattern
DMD: Duchenne's muscular dystrophy
DMSO: Dimethyl sulfoxide
DMT1: Divalent metal transporter
DNA: Deoxyribonucleic acid
DNA2: DNA helicase/nuclease 2
DNM2: Dynamin 2
DRP1: Dynamin-related protein 1
DTT: Dithiothreitol

E
EC: Endothelial cells
ECAR: Extracellular acidification rate
EDTA: Ethylenediaminetetraacetic acid
EEA1: Early endosome antigen 1
ELISA: Enzyme-linked immune-sorbent assay
ER: Endoplasmic reticulum
Esr1: Estrogen receptor 1 (alpha)
ETC: Electron transport chain

F
FBS: Fetal bovine serum
FGF21: Fibroblast growth factor 21
Fis1: Mitochondrial fission 1 protein
FUNDC1: FUN14-domain containing protein 1

G
Gastro: Gastrocnemius
Gapdh: Glyceraldehyde-3-phophate dehydrogenase
GDAP1: *Glaglioside induced differentiation associated protein 1*
GSEA: Gene set enrichment analysis
GTP: Guanosine triphosphate

H
HeLa cells: Henrietta Lacks cells
HEPES: Hydroxyethyl piperazineethanesulfonic acid
HFD: High-fat diet
Hla-A: Human leukocyte antigen A
Hmgb1: High mobility group box 1

HRS: Hepatocyte growth factor-regulated tyrosin kinase substrate
HSA: Human skeletal actin

I
IBM: Inner boundary membranes
IF: Immunofluorescence
Ifit1: Interferon induced protein with tetratricopeptide repeats 1
IFN: Interferon
Ifnb: Interferon beta
IKKβ: Inhibitor of nuclear factor kappa B
Il1b: Interleukin 1 beta
IL6: Interleukin 6
IMM: Inner mitochondrial membrane
IMS: Intermembrane space
IP: Intraperitoneal
IP-MS: Immunoprecipitation-mass spectrometry
INF2: Inverted formin 2
IRF3: Interferon regulatory factor 3
Irf7: Interferon regulatory factor 7
ISGs: Interferon-stimulated genes
Isg15: Interferon-stimulated gene 15

K
KD: Knock-down
KO: Knock-out

L
LAMP1: Lysosomal-associated membrane protein 1
LC3: Light chain 3
LIR: LC3-interacting region
LoxP: Locus of X(cross)-over in P1
LPS: Lipopolysaccharide

M
MAVS: Mitochondrial antiviral protein
MDV: Mitochondria-derived vesicles
MEF: Mouse embryonic fibroblast
MELAS: Mitochondrial encephalopathy, lactic acidosis, and stroke-like episodes
MEMSA: Myoclonic epilepsy, myopathy and sensory ataxia
Mff: Mitochondrial fission factor
Mfn1: Mitofusin1

Mfn2: Mitofusin 2
Mfns: Mitofusins (1 and 2)
MGME1: *Mitochondrial genome maintenance exonuclease 1*
MHC: Myosin heavy chain
MHC Class I: Major histocompatibility complex class I
MHo: Maternal homoplasmic inheritance
MHe: Maternal heteroplasmic inheritance
MID49/51: Mitochondrial dynamics proteins 49kDa and 51 kDa
MIEF2: Mitochondrial elongation factor 2
MLASA3: Myopathy, lactic acidosis and sideroblastic anemia 3
MOI: Multiplicity of infection
mPTP: Mitochondrial permeability transition pore
mRNA: Messenger RNA
MSTO1: Misato 1, Mitochondrial Distribution And Morphology Regulator 1
mtDNA: Mitochondrial DNA
MTDR: Mitotracker Deep Red
MVBs: Multivesicular bodies
Myd88: Myeloid differentiation primary response protein 88

N
NADH: Nicotinamide-adenine dinucleotide
nDNA: Nuclear DNA
Nd4: NADH-ubiquinone oxidoreductase chain 4
NFκB: Nuclear factor kappa-light-chain-enhancer of activated B cells
NIX: NIP3-like protein 3 (or BNIP3L)
NLR: NOD-like receptors
NLRC4: NLR Family CARD domain containing 4
Nlrp3: NLR Family pyrin domain containing 3

O
O/N: Overnight
OCR: Oxygen consumption rate
OMA1: Zinc metalloendopeptidase
OMM: Outer mitochondrial membrane
OPA1: Optic atrophy 1
OPTN: Optineurin
OXPHOS: Oxidative phosphorylation

P
PAMP: Pathogen-associated molecular pattern

PBS: Phosphate buffered saline
PCR: Polymerase chain reaction
PEI: Polyethylenimine
PGC-1: Peroxisome proliferator-activated receptor gamma co-activator 1
POLG: DNA polymerase gamma
POMC neurons: Proopiomelanocortin neurons
PPAR-γ: Peroxisome proliferator-activated receptor gamma
PRR: Pattern recognition receptors

Q
qPCR: Quantitative PCR
Quadri: Quadriceps

R
Rage: Receptor for advanced glycation end products
RER: Respiratory exchange ratio
RNA: Ribonucleic acid
ROS: Reactive oxygen species
rpm: Revolutions per minute
RT: Room temperature

S
S100a9: S100 calcium binding protein A 9
SAVI: STING-associated vasculopathy with onset in infancy
Scr: Scramble
SdhA: Succinate dehydrogenase complex flavoprotein subunit A
SDS: Sodium dodecyl sulfate
shRNA: Short-hairpin RNA
siRNA: Short-interference RNA
sIBM: Sporadic inclusion body myositis
SkM: Skeletal muscle
SLC25A33: Solute carrier family 25 member 33
SLE*:* Systemic lupus erythematous
SPF: Specific pathogen free
Stat1: Signal transducer and activator of transcription 1
STAT3: Signal transducer and activator of transcription 3
STING: Stimulator of interferon genes

T
TBK1: TANK-binding kinase 1

TCA: Tricarboxylic acid
TEM: Transmission electron microscopy
TFAM: Mitochondrial transcription factor A
TIA1: T-cell intracellular antigen gene 1
TLR9: Toll-like receptor 9
TOM20: Translocase of the outer mitochondrial membrane 20
TNFα: Tumor necrosis factor α
TRAF6: TNF receptor associated factor 6
TWNK: Twinkle

U
UCP: Uncoupling protein
UPR: Unfolded protein response
Usp18: Ubiquitin specific peptidase 18

V
VDAC: Voltage-dependent anion channel
Vps15:Vacuolar protein sorting 15

W
WAT: White adipose tissue
WB: Western blot
WDM: Welander distal myopathy

Y
YME1L: Mitochondrial i-AAA protease
YY1: YingYang1

ΔΨm: Mitochondrial membrane potential

INTRODUCTION

2.1 Mitochondria: origins, function, structure and regulation

Mitochondria arouse around 1.5 billion years ago and evolved from endosymbiotic bacteria. This theory was proposed by Ivan Wallin[1], who experimentally worked on observations previously made by Andreas Schimper and Konstantin Mereschkovsky in the late 19th and early 20th centuries, respectively. Although this theory went unnoticed at that time, it was rescued and eventually supported in the well-known *On The Origin Of Mitosing Cells*, published by Lynn Margulis in 1967[2]. The theory, referred to as the endosymbiotic theory or symbiogenesis, holds that eukaryotic cells are the result of an engulfment of α-proteobacterium by other single-living proto-eukaryotes.

As a result of a successful symbiotic relationship, mitochondria and plastids, such as chloroplasts, share some features which allow the discrimination between former endosymbionts and organelles within eukaryotes: i) they are covered by double membranes; ii) these membranes contain transport proteins called porins, also found in bacterial cell membranes; iii) they contain and maintain their own genome; iv) genes initially encoded by the former endosymbiont genome are present in the nuclear genome of eukaryotic cells; and v) mitochondrial and plastid ribosomes are more similar to bacterial ribosomes (70S) rather than eukaryotic ribosomes. Despite some of the bacterial features that mammalian mitochondria have retained, recent genomic analyses estimate that only a small proportion of mammalian mitochondria derive from the original endosymbiont[3], suggesting the highly adaptive capacity these organelles have developed throughout evolution.

Mitochondria perform an entire plethora of functions. Besides their major role in producing adenosine triphosphate (ATP), mainly through oxidative phosphorylation, they are also involved in calcium storage and signalling, programmed cell death, iron metabolism and homeostasis, macromolecules

production, reactive oxygen species (ROS) production, and sensing and modulation of immune responses[3–6].

The structure of mitochondria is essential for proper function and homeostasis. Mitochondria are double-membraned organelles that present four structural compartments: the outer mitochondrial membrane (OMM), the intermembrane space (IMS), the inner mitochondrial membrane (IMM) and the matrix.

The OMM encloses the organelle and, despite its high permeability to small molecules and ions, it prevents the exit of harmful mitochondrial products to the intracellular media, such as ROS, immunogenic molecules or death signals[7]. It contains porins and translocases in order to allow cargo import and export. Indeed, the voltage-dependent anion channel (VDAC) is the primary transporter responsible for the exchange of metabolites, ions and nucleotides[8]. Besides, the OMM is able to stablish physical contact with membranous structures such as the endoplasmic reticulum (ER), lipid droplets, melanosomes, peroxisomes, lysosomes or Golgi apparatus, therefore allowing organelle-mitochondria communication[9].

The IMS, also known as the perimitochondrial space, encompasses the space between the outer and the inner membrane. Given the fact that the OMM is permeable to small molecules, the composition of the IMS is similar to that of the cytosol. Although the IMS is the temporary location for many small and large molecules that enter or exit mitochondria, it is also the resting location of other molecules, such as cytochrome c[10]. The release of cytochrome c from the IMS to the cytosol induces apoptosis, thus inferring the role of the IMS in regulating metabolic functions.

The IMS is separated from the matrix by the IMM, which forms tubular invaginations called cristae. According to the latest model for the organization of

the IMM, known as the cristae junction (CJ) model and proposed by Daems and Wisse in 1966[11], CJs separate cristae and inner boundary membranes (IBM), generating a 20-50nm diameter space that allows both structures to perform separate functions[12]. Unlike the OMM, the IMM is highly impermeable to all molecules, which, along with the activity of protein complexes involved in the electron transport chain (ETC), allows the establishment of a proton gradient across the IMM, generating a membrane potential (ΔΨm). The cristae morphology and the restricted permeability are two key features of the mitochondrial architecture that permit oxidative phosphorylation in mitochondria[13]. Oxidative phosphorylation encompasses the enzymatic reactions by which nutrient oxidation engages ATP production. During these reactions, electrons are transferred from electron donors to acceptors in the so called ETC, which allows transport of protons across the IMM. As a result, a potential energy is generated in the form of proton gradient, which is used for the generation of ATP by ATP synthases. Besides protein complexes involved in oxidative phosphorylation, the IMM also contains proteins involved in bioenergetics, cell death, mitochondrial dynamics and protein transport.

Lastly, the matrix is the space enclosed by the IMM where essential metabolic processes, such as the tricarboxylic acid (TCA) cycle, take place. Other processes include β-oxidation of fatty acids, urea cycle, heme group synthesis, transamination and protein synthesis. The matrix also contains the mitochondrial genome (mtDNA), as well as its replication, transcription and translation machinery, the biology of which will be explained in chapter 2.6.

Mitochondrial content is tightly regulated by mitochondrial biogenesis and degradation in order to accurately respond to the environmental demands. In fact, mitochondrial biogenesis is defined as the growth and division of pre-existing mitochondria not only in number, but also in size and mass. It is

influenced by environmental stimuli, such as caloric restriction, oxidative stress, exercise, cell division, low temperature or differentiation[14]. PGC-1α, a member of the peroxisome proliferator-activated receptor gamma (PPAR-γ) family of transcription co-activators, is the master regulator of mitochondrial biogenesis. It is known to co-activate the transcription factors responsible for the induction of expression of mitochondrial proteins, codified in genes located both at the nuclear and mitochondrial genome[14]. PGC-1α is also involved in the suppression of oxidative stress and induction of mitochondrial uncoupling proteins (UCPs)[15]. Mitochondrial degradation, the opposite process to mitochondrial biogenesis, is also essential in order to respond to environmental stimuli or eliminate defective mitochondria. Details related to this topic will be explained in chapter 2.3.

2.2 Mitochondrial dynamics

Mitochondrial dynamics is the process referred to changes in morphology and movement that mitochondria undergo in order to respond to environmental stimuli. It refers to the dynamic balance between fusion and fission events in the mitochondrial network[16]. The dynamic transition from fused to fragmented mitochondria and vice versa is governed by large GTPases that form the core machinery of mitochondrial dynamics (Figure 1).

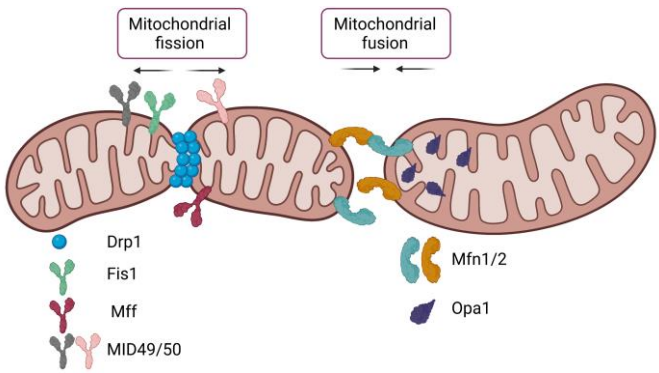

Figure 1: Schematic representation of mitochondrial dynamics and the proteins involved.

2.2.1 Mitochondrial fusion

Mitochondrial fusion is a two-step process by which two mitochondria come together to form a unit of the mitochondrial network. First, the fusion of the OMM takes place due to the interaction between mitofusins 1 and 2 (Mfn1/2). Given that these GTPases share 80% of their sequence, they are homologues in mammals, and therefore, their interaction can occur in an homo- or heterodimeric manner[17]. This oligomerization is dependent on GTP hydrolysis and mediated by a heptad repeat region in the C-terminus of both mitofusins[18].

Although the major role of these proteins is to promote mitochondrial fusion, recent studies have unravelled emerging functions for mitofusins: they play a role in autophagy[19,20], apoptosis[21,22], cell cycle progression[23,24], senescence[25,26], and antiviral signalling responses[27,28]. However, Mfn2 has been associated to a more extended set of processes such as brown adipose tissue (BAT) thermogenesis, phospholipid transfer between mitochondria and the ER, mitochondria-ER tethering, ER stress and the unfolded protein response (UPR) and early spermatogenesis development[29–34]. In fact, downregulation of mitofusins or disruption of their GTPase activity induces mitochondrial fragmentation[35]. Besides, while animals with heterozygous ablation of either mitofusins present full viability, homozygous mutants are embryonically lethal, suggesting an essential role for mitochondrial fusion during embryonic development[36].

A number of *in vivo* studies in which mitofusins were downregulated, especially Mfn2, has shown their impact in metabolism (Figure 2): Liver-Mfn1 deficiency induces an enhanced respiratory capacity and protects mice from high-fat diet (HFD)-induced insulin resistance[37]. However, Mfn1 loss-of-function in proopiomelanocortin (POMC) neurons, which are essential for nutrient availability sensing, alters central glucose sensing and impairs pancreatic insulin

secretion[38]. Mfn1 ablation in the heart confers protection against ROS-induced mitochondrial dysfunction[39]. Regarding the impact of Mfn2 in metabolism, its ablation in skeletal muscle shows an enhanced age-induced mitochondrial dysfunction, glucose intolerance, muscle atrophy and increased sarcopenia, leading to accelerated muscle aging[19]. Liver-Mfn2 ablation promotes glucose intolerance, enhanced hepatic gluconeogenesis and impaired insulin signalling[40]. Downregulation of Mfn2 in POMC neurons induces leptin resistance, hyperphagia, reduced energy expenditure and obesity[31]. Mfn2-deficient BAT presents impaired respiratory capacity and blunted response to adrenergic stimuli[29], while Mfn2-deficient white adipose tissue (WAT) displays hyperphagia, increased adiposity and impaired glucose metabolism[41]. It has also been demonstrated that ablation of Mfn2 in macrophages compromises the ROS-induced response to bacterial infection[42].

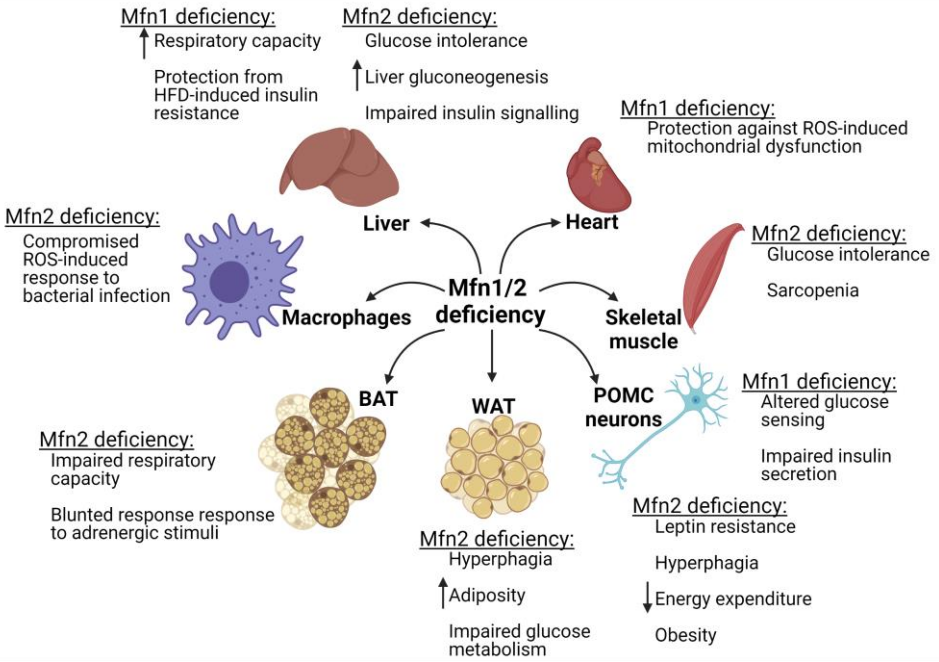

Figure 2: Revision of the metabolic effects of the deficiency of Mfn1 or Mfn2 in *in vivo* studies.

Besides, in humans, heterozygous mutations of *MFN2* result in motor and sensory neuropathy Charcot-Marie-Tooth (CMT) type 2A (CMT2A, OMIM #609260, #617087) and CMT type 6 (CMT6, OMIM #601152)[43] (Table 1).

The fusion of the OMM is followed by the fusion of the IMM which completely depends on optic atrophy 1 (Opa1). Opa1 locates at the IMM and the IMS, which subjects it to a number of post-translational modifications, resulting in the formation of eight isoforms in humans and four in mice[44,45]. In mice, Opa1 isoforms are discriminated by their molecular weight and they are produced by the proteolytic cleavage of the precursor Opa1 (long isoform, L-Opa1), which contains two cleavage sites, S1 and S2[46]. Two IMM proteases are responsible for Opa1 processing: on one hand, i-AAA protease (I, IMS oriented) Yme1L constitutively cleaves S2 site, and on the other hand, m-AAA (m, matrix oriented) metalloprotease Oma1 cleaves at S1. The activity of these enzymes establishes the appropriate molarity of long and short Opa1 isoforms in order to respond to the cellular demands[47].

Besides its essential role in mitochondrial fusion, Opa1 is key in maintaining cristae morphology, given homotypic trans-Opa1 interaction-mediated membrane tethering[48]. Cristae morphology maintenance, in turn, affects three aspects: i) mitochondrial respiration by promoting stability, and therefore function of the respiratory chain complexes located in the IMM, ii) regulation of pro-apoptotic-dependent cytochrome c release, and iii) stabilization of mtDNA[45,49].

Owing to its diverse functional nature, loss-of-function of Opa1 causes fragmentation of the mitochondrial network, mtDNA depletion, impaired resistance to apoptosis, imbalances in the redox state, disruption of mitochondrial respiration and nuclear factor κB (NF-κB) dependent inflammation[50,51]. In mice, Opa1 deficiency in skeletal muscle attenuates age-

induced weight gain and glucose intolerance, and it induces muscle loss and atrophy, muscle inflammation and systemic aging, resulting in premature death[51–53]. Interestingly, downregulation of Yme1L in the nervous system of mice also leads to retinal inflammation, blindness and locomotor impairment[54,55]. In humans, missense mutations in *OPA1* result in autosomal dominant optic atrophy (ADOA, OMIM #165500)[56,57], and in around 20% of ADOA cases, *OPA1* mutations lead to a multi-systemic disorder known as ADOA plus syndrome (ADOA+, OMIM #125250) (Table 1).

2.2.2. Mitochondrial fission

Mitochondrial fission is the process by which mitochondria divide into two separate units of the mitochondrial network. Dynamin-related protein 1 (Drp1) is the master regulator of mitochondrial fission and it mainly resides in the cytosol. It is recruited onto mitochondria at ER marked sites[58] and it interacts with its receptors in the OMM, which include mitochondrial fission factor (Mff), Mitochondrial fission 1 protein (Fis1), and mitochondrial dynamics proteins 49 kDa and 51 kDa (MID49 and MID51)[59]. Once Drp1 is recruited to the OMM forming dotted structures, it constricts the mitochondrial tubules in order to mediate membrane division.

Mitochondrial fission is necessary to ensure mitochondrial genome survival by distributing mtDNA copies to isolated mitochondrial fragments. It also prevents the accumulation of noxious mitochondrial products and allows their dilution throughout the mitochondrial population. Indeed, mitochondrial fission is considered to work as quality control system to suppress oxidative damage and thus, ensure cell survival[60].

Some associations between mutations in fission proteins and human genetic disorders have been described: i) a missense mutation in DRP1 was reported to cause premature death in a new born infant due to multiple developmental disorders, including optic atrophy, microcephaly, abnormal brain development and metabolic alterations[61], ii) a homozygous nonsense mutation in *MIEF2*, the gene encoding for MID49, has also been described to cause mitochondrial myopathy in a 15-year-old male[62], and iii) MFF loss-of-function has been associated to encephalopathy, optic atrophy and neuropathy[63] (Table 1).

Protein mutated	Human disease	OMIM	References
MFN2	CMT2A CMT6	#609260, #617087 #601152	[43]
OPA1	ADOA ADOA+	#165500 #125250	[56,57]
DRP1	Premature death in a newborn	Single report	[61]
MID49	Mitochondrial myopathy	Single report	[62]
MFF	Encephalopathy, optic atrophy and neuropathy	-	[63]

Table 1: Summary of mitochondrial dynamics proteins associated to human disease.

While ablation of each mitochondrial fission protein induces mitochondrial elongation, their downregulation results in different phenotypes. In mice, Drp1 loss-of-function promotes accumulation of damaged mitochondria, defective autophagy and increased apoptosis[64]; and inducible skeletal muscle-specific Drp1 ablation promotes body weight loss, muscle wasting and weakness due to enhanced protein degradation[65] as well as muscle denervation[66]. Moreover, Mff downregulation increases calcium uptake without alterations in mitochondrial

function[67]. Fis1 ablation promotes accumulation of both dysfunctional lysosomes and mitochondria, a reduction in peroxisomes, respiratory chain deficiency and inflammation[68,69]. Nevertheless, the mechanism of action of Fis1 is controversial given a recent study demonstrating its inhibitory activity on mitochondrial fusion protein, therefore, promoting fission by blocking fusion rather than by promoting fission itself[70]. Lastly, loss of MID49 and MID50 drives mitochondrial autophagy via Mfn2 and Fis1 degradation and sensitizes cells to cell death but it prevents cristae remodelling during intrinsic apoptosis[71,72].

2.3 Mitochondrial autophagy or mitophagy

A healthy mitochondrial network is characterized by an adequate balance between mitochondrial biogenesis and turnover. In fact, mitochondrial degradation is essential for cell survival as it is involved in the removal of obsolete or damaged mitochondria that could be harmful for the cell. Two degradation processes are responsible for mitochondrial turnover: vacuolar/lysosomal (autophagic) degradation and proteasomal degradation. While the latter is necessary to maintain mitochondrial proteostasis, autophagic degradation seems to be the main degradation pathway for mitochondria.

The autophagic degradation (autophagy or autophagocytosis) is the mechanism by which cellular components are orderly degraded and recycled. Three forms of autophagy pathways are described depending on their degradation target: macroautophagy, microautophagy and chaperon-mediated autophagy (CMA)[73]. In macroautophapgy (hereafter autophagy), cytosolic components are targeted to vesicles, known as autophagosomes, that fuse to lysosomes, forming autophagolysosomes (or autolysosomes). The hydrolases present in the lysosomes degrade the cargos and their components are recycled (Figure 3). The

autophagic process is essential in order to respond to certain stimuli, such as starvation, infection, programmed cell death or differentiation.

Mitophagy is the selective degradation of mitochondria via autophagy and it is essential to maintain cell health. It is also required to adjust the mitochondrial mass in order to adapt to the metabolic needs of the cell[74]. Two mechanistic models for mitophagy have been described in mammals: the Pink1-dependent pathways and the receptor-mediated pathways (Figure 3).

The former are based on the activity of the serine/threonine kinase Pink1, which contains a mitochondria-targeting sequence and requires mitochondrial membrane depolarization. Depolarized mitochondria recruit and stabilize Pink1 to their OMM where it forms large complexes with outer membrane translocases. This allows the translocation of Parkin, a E3 ubiquitin ligase, to mitochondria where it interacts with Pink1 and ubiquitinates OMM proteins[75], including VDAC and Mfn1/2[76,77]. Mitochondrial ubiquitination serves as a signal for autophagy mediators, such as p62, optineurin (OPTN) or NBR1, that target ubiquitinated mitochondrial proteins and promote the engulfment of mitochondria by autophagosomes. This process depends on direct binding between autophagy mediators and the autophagy light chain 3 (LC3) through their LC3-interaction region (LIR) motif[78]. Nevertheless, it seems that mitochondrial ubiquitination could also act as a signal for proteasomal degradation of the OMM and the IMS components[79]. In such cases, exposed IMM receptors like prohibitin 2 (PHB2) and cardiolipin can directly interact with LC3 and drive engulfment of the remaining mitochondrial components by autophagosomes[80,81]. In addition to Parkin, other E3 ubiquitin ligases, such as SMURF1 or Gp78[82,83], act as mitophagy regulators, which are included in the set of Pink1-dependent, Parkin-independent mitophagy mechanisms.

The receptor-mediated mitophagy pathways require OMM mitophagy receptors that directly interact with LC3. Such receptors include FUN14-domain containing protein 1 (FUNDC1), BCL2/adenovirus E1B 19kDa protein-interacting protein 3 (BNIP3), NIP3-like protein 3 (NIX or BNIP3L), BCL2-like 13 (BCL2L13 or BCL-rambo) and FKBP8 (also known as FKBP38). Indeed, FUNDC1, NIX and BNIP3 interact with LC3 and promote degradation of damaged mitochondria upon ΔΨm depolarization, mitochondrial permeability transition pore (mPTP) opening or hypoxia[84–86]. Furthermore, NIX is particularly essential in reticulocytes as it is the main mitophagy driver during their maturation[87]. FKBP8 is an OMM protein that has different roles in anti-apoptotic signalling and mTOR regulation. It mediates LIR-dependent recruitment of LC3 to damaged mitochondria, which promotes mitophagy[88]. Moreover, FKBP8 translocates from mitochondria to ER during Pink1-Parkin dependent mitopaghy, therefore escaping from degradation, which establishes a crosstalk between both pathways[89]. Lastly, BCL2L13 is a member of the BCL2 family that plays a central role in regulating apoptosis and it binds to LC3 upon ΔΨm depolarization in a Parkin-independent manner[90].

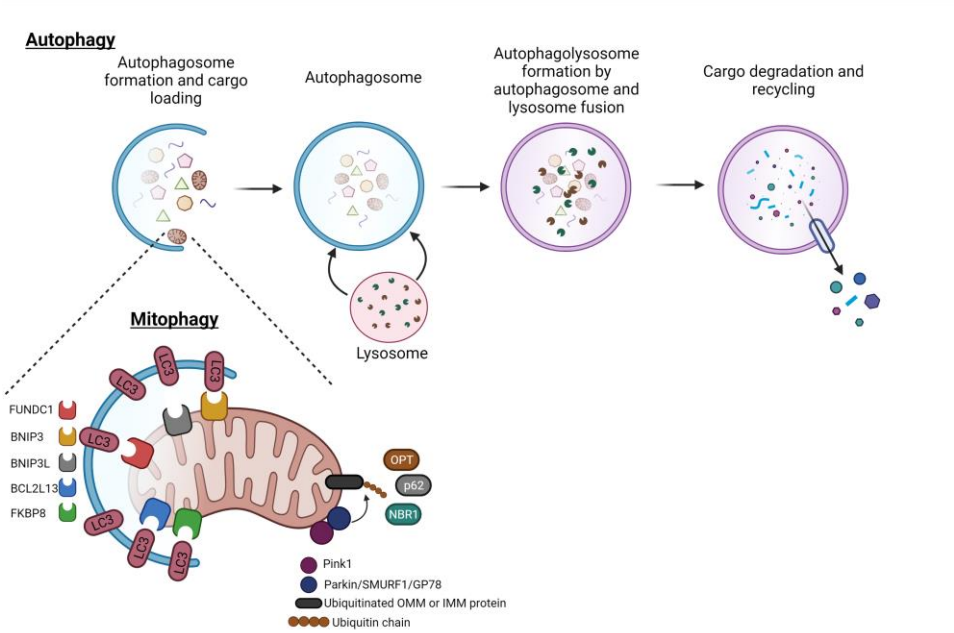

Figure 3: Schematic representation of the autophagic and mitophagic processes.

Mitochondrial turnover and biogenesis need to be in perfect tune in order to maintain mitochondrial and cellular homeostasis, in which mitochondrial dynamics is also a key player. Hence, mitophagy and mitochondrial fusion/fission events are tightly interconnected, contributing to the proper function of the mitochondrial quality system. In this regard, it is known that mitochondrial fission precedes mitophagy due to two facts: first, mitochondrial fission is an asymmetric process in which one of the resulting mitochondria exhibits increased ΔΨm and high probability of subsequent fusion, while the other one presents depolarized ΔΨm and reduced probability to undergo fusion. The fate of the latter relies on its ability to recover membrane polarization and health[91]. If functionality is not recovered, the mitophagy machinery would drive its degradation and recycling.

Second, fragmented mitochondria are more susceptible to undergo mitophagy owing to their smaller size compared to fused mitochondria. For this, dysfunctional mitochondria may induce degradation of the fusion machinery and/or enhancement of the fission machinery to prevent the incorporation of damaged mitochondria into the healthy mitochondrial network[92]. In fact, several studies in mice have demonstrated that impaired mitochondrial dynamics lead to disrupted autophagy. On one hand, downregulation of Mfn2 in the skeletal muscle blocks autophagy and mitophagy and induces BNIP3-dependent mitophagy via ROS production, which acts as an adaptive mitophagy pathway[19]. On the other hand, Opa1 loss-of-function in muscle cells shows disrupted mitophagy characterized by normal induction and followed by defective resolution[51]. Moreover, Drp1 deficiency in cardiomyocytes blocks autophagy by reducing autophagosome formation[64].

However, autophagy and mitophagy can also modulate mitochondrial dynamism. In fact, it has been demonstrated that Drp1 Ser 637 phosphorylation, which retains Drp1 in the cytosol, is enhanced during starvation-induced autophagy, thus, promoting mitochondrial elongation[93]. Besides, it has been described that mitophagy proteins such as Pink1, BCL2L13, FUNDC1 and BNIP3 are associated to mitochondrial fragmentation through different mechanisms. First, downregulation of Pink1 or FUNDC1 promotes mitochondrial fragmentation possibly due to an accumulation of damaged mitochondria unable to undergo mitophagy[84,94]. Interestingly, it has been recently described that BCL2L13 plays a key role in thermogenesis of beige adipocytes, which are white adipocytes that acquire characteristic features of brown adipocytes, by regulating mitochondrial dynamics. Indeed, BCL2L13 downregulation reduces the expression levels of mitochondrial fusion proteins, resulting in inhibition of the browning program of WAT preadipocytes[95]. Lastly, BNIP3 has been described

to directly bind to Opa1, inhibiting its function and therefore, blocking mitochondrial fusion[96].

Thus, the crosstalk between mitophagy and mitochondrial dynamics, either by the effect of mitochondrial dynamics in mitophagy or vice versa, is essential for the adaptations of mitochondria to the cellular needs and for the maintenance of mitochondrial fitness, and hence, health.

2.4 Mitochondrial dysfunction in the skeletal muscle

The skeletal muscle is one of the three muscle types that comprise the muscular system, along with the cardiac and the smooth muscle. The main feature of muscles is their ability to contract either in a voluntary or involuntary manner. Due to this, the skeletal muscle is responsible for skeletal movements such as locomotion and posture maintenance, thus, skeletal muscles locate throughout the body, covering up to 42% and 36% of body mass of humans, in men and women, respectively[97]. Each skeletal muscle is compartmentalized in muscle fascicles, which are in turn compartmentalized in muscle fibers, being muscle fibers the cellular unit of the organ. Muscle fibers are composed by myofibrils, which are in turn composed by sarcomeres, the functional unit of the muscle as they provide muscle contraction.

According to the sliding filament theory, proposed by Hugh Huxley and Jean Hanson in 1953, upon stimulation by an action potential, the thick filaments of muscle fibers (myosin) slide past the thin filaments (actin) promoting muscle contraction, while the length of both filaments remains relatively constant[98]. This mechanical process requires large amounts of calcium ions and ATP. The former are released from the ER upon stimulation and uncover the actin binding sites, allowing the interaction between the myosin heads and the actin filaments. The

latter binds to the cross bridges between myosin heads and actin filaments, and its conversion to adenosine diphosphate (ADP) powers the swivelling of the myosin head along the actin filament[99].

Owing the extensive use of calcium ions and ATP during muscle contraction, sarcomeres are covered by large ER structures, also known as sarcoplasmic reticulum, responsible for the storage, release and retrieval of calcium ions. Sarcomeres are also surrounded by an extended mitochondrial network categorized in two subpopulations depending on their location, *i.e.* subsarcolemmal (under the cell membrane) or interfibrillar (in between myofibrils) mitochondria. This distribution of mitochondria allows provision of ATP within all the structure of the muscle fibers. In fact, skeletal muscle dispose of four ATP sources during contraction: free ATP, phosphocreatine activity, glycolysis and cellular respiration. Thus, the presence of functional and healthy mitochondria in the skeletal muscle is essential for its function[100].

Skeletal muscle diseases, hereafter referred to as muscular dystrophies or myopathies, result in weakening of the musculoskeletal system. Although most of these disorders are monogenic, such as the Duchenne's muscular dystrophy (DMD), the cause of some of them arises from mitochondrial dysfunction, therefore, being categorized as mitochondrial myopathies. This group of disorders is characterized by mitochondrial alterations in the skeletal muscle and the surrounding tissues, although they are often accompanied by other symptoms generating syndromic conditions, such as the case of MELAS or Mitochondrial encephalopathy, lactic acidosis, and stroke-like episodes.

Mitochondrial myopathies are usually genetic disorders caused by mutations either in nuclear-encoded or mtDNA-encoded genes that codify for mitochondrial proteins (Table 2)[17]. This double genetic control of mitochondrial function results in different inheritance patterns of mitochondrial diseases.

In fact, since all mitophagy and mitochondrial dynamics proteins are nuclear encoded, the inheritance of mutations in their genes is mendelian. For instance, as mentioned in chapter 2.2, point mutations in *OPA1* are responsible for the development of ADOA plus syndrome[57], mutations in *MFN2* cause CMT2A and CMT6[43], both conditions characterized by muscle atrophy. Also, mutations in other genes involved in mitochondrial dynamics, such as Inverted formin 2, Glanglioside induced differentiation associated protein 1 and Dynamin 2 (*INF2, GDAP1* and *DNM2*, respectively) have been associated with other types of CMT[101–103], and in the case of mutations in *DNM2*, they are also the cause of dominant centronuclear myopathy (CNM)[104]. Recessive mutations in Misato 1, *MSTO1*, which cause alterations in mitochondrial dynamics, result in myopathy and ataxia[105]. Furthermore, mutations in *TIA1*, T-cell intracellular antigen gene 1, cause Welander distal myopathy (WDM), which is characterized by mitochondrial dysfunction since *TIA1* is also involved in mitochondrial dynamics[106].

Mutations in nuclear genes encoding for proteins involved in either mtDNA polymerization such as γ-polymerase, γ-polymerase 2 and twinkle (*POLG, POLG2* and *TWNK,* respectively), or mitochondrial nucleases such as mitochondrial genome maintenance exonuclease 1 and DNA helicase/nuclease 2 (*MGME1* and *DNA2*, respectively), among others[107] have also been associated with myopathies.

An extensive search in OMIM, ClinVar and Mitomap yielded in 60 genes causing mitochondrial myopathies, among which 29 were nuclear-encoded and 31 are mitochondrial genes[108] (Figure 4). Some of the latter include genes codifying for OXPHOS subunits such as Cytochrome B, NADH:Ubiquinone Oxidoreductase Core Subunit 5, Cytochrome c oxidase subunit 2 and ATP synthase membrane subunit 6 (*MTCYB, MTND5, MTCO2* and *MTATP6*, respectively). Mutations in

these genes are associated to exercise intolerance and muscle weakness, MELAS, mitochondrial myopathy and MLASA3 (myopathy, lactic acidosis and sideroblastic anemia 3), respectively[109–113].

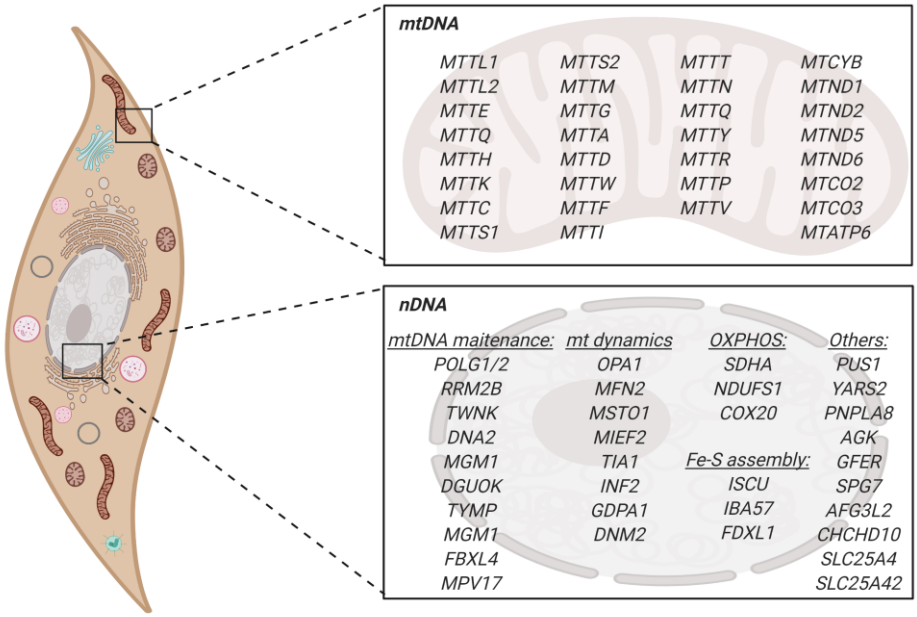

Figure 4: Revision of genes associated with myopathies. Adapted from Ahmed *et al.* 2018; El-Hattab, Craigen, and Scaglia 2017; and Taylor and Turnbull 2007[107,108,113]**.**

Encoding genome	Gene	Inheritance	Disease	OMIM	Reference
nDNA	*OPA1*	AD	ADOA ADOA+	165500 125250	[57]
	MFN2	AD/AR	CMT2A CMT6	609260, 617087 601152	[43]
	MSTO1	AD/AR	Myopathy and ataxia	617675	[105]
	TIA1	AD	WDM	604454	[106]
	INF2	AD	CMTDIE	614455	[101]
	GDPA1	AD/AR	CMT2K	607831	[102]
	DNM2	AD	CNM CMTDIB	160510 606482	[104] [103]
	POLG1 *POLG2*	AR AD	MEMSA Myopathy	 50009	[107]
	TWNK	AD	ADPEO	157640	[107]
	MGME1	AR	Myopathy	50009	[107]
	DNA2	AD	Myopathy	50009	[107]
mtDNA	*MTCYB*	Sporadic heteroplasmic	Exercise intolerance	516020	[109]
	MTCO2	MHe/Ho	Myopathy	50009	[114]
	MTND5	MHe	MELAS	540000	[110]
	MTATP6	MHe/Ho	MLASA3	500011	[112]

Table 2: Summary of the genes causing mitochondrial myopathy. More genes can be consulted in Ahmed *et al.* 2018; El-Hattab, Craigen, and Scaglia 2017; and Taylor and Turnbull 2007[107,108,113].

Although there are no reported cases describing associations between mutations in mitophagy proteins and myopathies in humans, there are studies in mice that suggest a relationship between disrupted mitophagy and muscle mass loss and atrophy. As mentioned in chapter 2.2, Opa1 or Mfn2 deficiency-induced

impairment of autophagy and mitophagy leads to muscle damage and atrophy[19,51]. Besides, muscle deficiency of the vacuolar protein sortin 15 (Vps15), involved in autophagosome formation, recapitulates the features of autophagic vacuolar myopathy (AVM)[115].

The basis underlying this evidence is the fact that deficient autophagy and mitophagy allows accumulation of damaged mitochondria, which affects muscle homeostasis and its maintenance, therefore resulting in chronic muscle damage and atrophy. Hence, taking into consideration these studies, targeting mitophagy to ameliorate the phenotype of muscle disorders has been suggested. For instance, resveratrol, a naturally synthesized phenol in plants, is able to induce the clearance of ROS and damaged mitochondria via mitophagy in *in vivo* models of DMD, which results in the amelioration of the phenotype[116]. Furthermore, treatment with the mitophagy inductor urolithin A, a metabolite ubiquitously found in human diet due to its presence in edible plants, improves exercise performance both in young rats and in different mouse models for age-related decline of muscle function[117]. These evidence demonstrate the feasibility of the design of mitophagy-targeting therapies to improve sarcopenia and/or muscle atrophy.

Mitochondrial dysfunction and disruption of autophagy and mitophagy can be a devastating combination in muscular dystrophies. In fact, another group of myopathies characterized by inflammation of the muscle and the surrounding tissues known as myositis or inflammatory myopathies, present this combination as hallmarks of the disease, along with chronic inflammation.

Sporadic inclusion body myositis (sIBM), the most common inflammatory myopathy in the elderly, is characterized at the cellular level by disrupted autophagy, mitochondrial dysfunction and accumulation of amyloidogenic proteins in the muscle[118]. The mitochondrial dysfunction present in sIBM

encompasses the following features: presence of mtDNA deletions, as well as a decrease in mtDNA content, decreased respiratory complex IV activity and decreased expression of Opa1[119]. The cause of myositis is unknown, however, it is widely accepted that the mitochondrial dysfunction in inflammatory myopathies is induced by the inflammatory response against the muscle. Nevertheless, since there are increasing evidences suggesting that primary alterations in mitochondrial homeostasis or mitophagy can induce muscle inflammation[51,54,68,120,121], whether the muscle inflammation in mitochondrial myositis is a primary or a secondary effect in the development of the disease is questioned.

Thus, this is becoming a controversial field that requires further research given the fact that accurately describing the primary cause of these disorders allows the design of therapeutic approaches that target the root of the disease.

2.5 Mitochondria and inflammation

Inflammation is a protective response of tissues to harmful stimuli that aims at the elimination of the original insult and allows tissue repair. The five classical signs of inflammation include heat, pain, redness, swelling and loss of function (from the Latin *calor*, *dolor*, *rubor*, *tumor* and *function laesa*) and it is considered an innate immune response[122]. Since too little inflammation can result in the destruction of the affected tissue by the insult and too much inflammation leads to chronic tissue damage, both the trigger and the resolution of inflammatory pathways are essential for a successful overcoming of the damage.

The immune cells are responsible for the engagement between the induction of inflammation and its resolution, therefore, the modulation of their metabolism, i. e. their mitochondrial activity, is key in driving the cognate immune response.

In fact, upon pro-inflammatory cytokine detection or antigen presentation, immune cells undergo metabolic rewiring from oxidative phosphorylation to aerobic glycolysis in order to promote macrophage activation or T-cell maturation[123]. Nevertheless, a pro-inflammatory environment can also induce mitochondrial dysfunction in non-immune cells by affecting their TCA cycle and the oxidative phosphorylation. Indeed, *in vitro* and *in vivo* studies demonstrate that cytokines such as tumour necrosis factor α (TNFα) and interleukin 1α (IL1α) reduce levels of pyruvate dehydrogenase (PDH), an enzyme of the TCA cycle, and reduce glucose oxidation by acting on cytochrome c oxidase[124–127].

Pro-inflammatory cytokines can also alter mitochondrial dynamics resulting in mitochondrial damage: IL1β has been described to promote mitochondrial fragmentation via Drp1 in astrocytes but not in 3T3-L1 adipocytes[128,129], TNFα promotes mitochondrial fission by increasing Fis1 levels and reducing Opa1 levels in 3T3-L1 adipocytes[129,130], and IL6 overexpression in an animal model of cachexia reduces Mfn1/2 levels in the skeletal muscle[131].

Although inflammation has a clear effect on mitochondria, either by promoting mitochondrial dysfunction in non-immune cells or by allowing modulation of metabolism in immune cells in order to drive adequate immune responses against the original insult, mitochondria themselves play a key role in the trigger of sterile intracellular inflammatory responses[6].

On one hand, mitochondria serve as platforms in the recruitment of complexes that forward signals to the nucleus in response to infections, with the aim of triggering inflammatory signaling pathways that, in turn, promote adequate immune responses. Indeed, upon retroviral infection, the mitochondrial antiviral protein (MAVS) is activated and recruited onto the surface of mitochondria promoting the activation of the kinases TBK1 or TRAF6, which allow downstream signaling pathways resulting in either the type I interferon (IFN) response or the

NFκB-dependent cytokine release, respectively[132]. Besides, the formation of inflammasomes, platforms for inflammatory caspase activation, takes place in the mitochondria-ER contact sites[133]. Inflammasomes contain pattern recognition receptors (PRR) that bind and recognize either damage- or pathogen-associated molecular patterns (DAMPs and PAMPs, respectively) that trigger inflammasome-mediated inflammatory signals. Inflammasome PRRs are either NOD-like receptors (NLR) or HIN200 proteins and there are five subtypes of inflammasomes: NLRP1, NLRP3, NLRP6 and NLRC4 inflammasomes (NLR inflammasomes), and the AIM2 inflammasome (HIN200-containing inflammasome). Upon pattern recognition, these inflammasomes recruit bipartite adaptor apoptosis-associated speck-like protein (ASC), which is essential for inflammasome assembly and activation[134]. This allows the recruitment of inflammatory caspases, such as caspase 1, which cleave pro-IL1β and pro-IL18 allowing their mature forms to be secreted to the extracellular media[135]. Interestingly, two studies have reported that, on one hand, the IMM phospholipid cardiolipin, and on the other hand, MAVS, can bind NLRP3 and enhance inflammasome formation and activation, establishing a physical interaction between mitochondria and inflammasome assembly[136,137].

Mitochondria also serve as a source of DAMPs (mtDAMPs) that initiate sterile inflammatory responses, which include mtDNA, ATP, cardiolipin, succinate, the mitochondrial transcription factor A (TFAM) and N-formyl peptides[138]. For instance, ATP is secreted under stress conditions, such as bacterial or mechanical insults in epithelial cells. High extracellular ATP levels are sensed by leukocytes, which initiate immune responses involving neutrophils, monocytes, macrophages and T lymphocytes[139]. Moreover, extracellular TFAM is described to induce an inflammatory response, as well as to enhance the immunogenicity of mtDNA[140]. Extracellular succinate is also recognized by immune cells and favors differentiation of T cells by stabilization of hypoxia-inducible factor 1α

(HIF1α)[141]. Furthermore, bacterial translation is characterized by the addition of a formyl group to the protein synthesis-starting methionine, a feature that is conserved in mitochondrial translation. N formyl-peptides serve as chemo-attractants that activate host phagocytes in bacteria whereas mitochondrial N-formyl peptides are only secreted by necrotic cells, which attract polymorphonuclear cells, such as neutrophils, that allow clearance of damaged cells[142]. Besides, cardiolipin is exposed to the extracellular media during cellular necrosis, which is recognized by T cells and triggers immune responses[143]. Lastly, owing to its resemblance to bacterial genome, mtDNA is considered a mtDAMP in extra-mitochondrial locations due to its ability to trigger different inflammatory pathways. However, the immunogenic nature of mtDNA will be further explained in chapter 2.6. As a summary, when either extracellular or intracellular stimuli induce mitochondrial dysfunction, mtDAMPs may be misplaced, activating inflammatory responses[6]. These scenarios are, in fact, of particular interest in the case of inflammatory diseases, such as myositis.

2.6 Mitochondrial DNA: its immunogenicity and inflammation

The mitochondrial genome is a small, double-stranded circular DNA molecule that encodes for 37 genes: one strand, known as the heavy chain, encodes for 12 subunits of the OXPHOS system, 2 ribosomal subunits (12S and 16S) and 14 tRNAs; while the other strand, known as the light chain, encodes for one OXPHOS subunit and 8 tRNAs. The remaining ~1500 mitochondrial genes are nuclear-encoded and their products are imported into the organelle. The number of mtDNA copies per cell ranges from hundreds to thousands and it is regulated both in physiological and in stress-induced conditions[144]. In fact, mtDNA is packaged in DNA-protein structures known as nucleoids, which are given by the packaging function of TFAM. Nucleoids provide mtDNA with a certain degree of

protection against oxidative and other non-bulky base damages[144]. The number of mtDNA molecules that compose a nucleoid has been a controversial topic. Different approaches based on quantification of number of nucleoids within a cell and mtDNA copy number ranged the number of mitochondrial genomes from 2 to 10 mtDNA molecules per nucleoid in human cell lines, however, next-generation imaging approaches have narrowed the average to 1.4 mitochondrial genomes per nucleoid, therefore suggesting that a single nucleoid is likely to be composed by one or two mtDNA molecules[145,146].

Given its ancestry as bacterial genome, mtDNA displays two characteristic features which confer mtDNA with immunogenicity: on one hand, it harbours remnants of bacterial DNA sequences, and on the other hand, its methylation profile is different to that of the nDNA, making it appear more "foreign" than "self" DNA. Moreover, although mitochondria dispose of mtDNA repair mechanisms, such as base-excision repair pathways, mtDNA is subjected to persistent oxidative damage, which can be immunostimulatory. Besides, many unique immunogenic nucleic acid species are generated during mtDNA transcription and replication, such as uncapped mRNAs, dsRNAs and RNA-DNA hybrids[147]. Therefore, mtDNA presents a number of signatures that are potentially recognized by DNA/RNA-sensing PRRs, which owes its nature as a mtDAMP (Table 3).

DNA sensing PRR	Stimulatory features	Signalling pathway	Immune response	References
TLR9	Hypomethylated mtDNA Oxidized mtDNA mtDNA-protein complex	MYD88-NFκB axis MYD88-IRF3 axis	Cytokine release Type I IFN response	[148,149]
cGAS	mtDNA (100-500bp) Oxidized mtDNA mtDNA-mtRNA hybrid mtDNA-protein complex	STING-IRF3 axis STING-NFκB axis	Type I IFN response Cytokine release	[150–152]
NLRP3	Oxidized mtDNA	ASC-caspase 1 axis	IL1β and IL18 release	[153]
NLRC4	mtDNA Oxidized mtDNA	Caspase 1	IL1β release	[154]
AIM2	mtDNA	ASC-caspase 1 axis	IL1β and IL18 release Piroptosis	[155]

Table 3: mtDNA as a DAMP for DNA-sensing PRRs. Adapted from West and Shadel, 2017.[147]

2.6.1 Mechanisms of mtDNA escape or mislocation

Mitochondrial membrane integrity is key in order to maintain mtDNA within mitochondria and to prevent the trigger of sterile inflammatory responses. When membrane integrity is compromised, nucleoids or mtDNA fragments might be able to escape from mitochondria and drive a plethora of inflammatory responses (Figure 5)[156]. For instance, activation of the mitochondrial permeability transition pore (mPTP) results in mtDNA escape under oxidative stress conditions. Transient opening of the mPTP allows homeostasis of solutes such as ions, small molecules, metabolites and proteins of the matrix. In contrast,

long-lasting opening of the mPTP induced by oxidative stress promotes irreversible loss of the ΔΨm, inhibition of ATP synthesis, cytochrome c release, mitochondrial swelling and cell death [157]. Under these conditions, mtDNA fragments smaller than 700bp codifying for OXPHOS complexes such as, *MTCO1, MTND3*, and *MTCYB* can also be released through the mPTP[158].

Disrupted mitochondrial clearance by mitophagy can cause damaged mtDNA to accumulate and release from mitochondria. Several studies have demonstrated that mitophagy impairment can result in the release of mtDNA to the cytosol or plasma, which activates diverse inflammatory responses. These studies include downregulation of auto/mitophagy proteins such as LC3, FUNDC1, Pink1 and Parkin, in physio- or pathophysiological processes such as heart failure, sepsis, hepatocarcinogenesis and exercise-induced systemic inflammation[120,159–161].

Furthermore, Bax/Bak-mediated apoptosis has also been described to allow mtDNA mislocation in the extracellular media. Indeed, cellular stress conditions can result in the OMM permeabilization mediated by the formation of Bax/Bak pores, resulting in the well-established intrinsic mitochondrial pathway of apoptosis[162]. In vitro experiments in different studies have shown that mtDNA can escape through the Bax/Bak pores and be released to the extracellular media during apoptosis, which can trigger different inflammatory pathways[163–165].

Lastly, mitochondrial dynamics is also related to the extramitochondrial localization of mtDNA. In fact, mitochondrial fragmentation, either by downregulation of Opa1 or by overexpression of Drp1, is associated with NFκB dependent inflammation, initiated by toll-like receptor 9 (TLR9)-mediated mtDNA recognition[51,166]. Downregulation of the Opa1 protease Yme1L is also associated to mtDNA leakage to the cytosol through VDAC pores resulting in inflammation[54]. In contrast, TFAM depletion-mediated mitochondrial hyperfusion induces release of mtDNA fragments to the cytosol, possibly through

VDAC transport[121,167,168]. These evidence suggest that hyperfused mitochondria are not degraded by mitophagy and accumulate aberrant mtDNA that leaks to the cytosol, whereas fragmented mitochondria are more likely to undergo mitophagy, despite the fact that mitophagy tends to be disrupted in these conditions, therefore allowing accumulation of mtDNA fragments in compartments where mtDNA engages TLR9 recognition. Thus, conditions that alter mitochondrial dynamics can cause mtDNA instability, leading to immune response activation by diverse intracellular inflammatory pathways.

2.6.2 Recognition of mtDNA by intracellular DNA sensors

Several nucleic acid sensors are located in different subcellular organelles in order to drive rapid primary inflammatory responses upon bacterial or viral infection. However, these sensors are not able to distinguish between foreign or self-nucleic acids, therefore, triggering sterile inflammatory responses upon mtDNA recognition by DNA sensors. Such sensors include TLR9, inflammasomes and cyclic GMP-AMP (cGAMP) synthase (cGAS), which induce different inflammatory responses (Figure 5) (Table 3).

2.6.2.1 mtDNA and TLR9

TLR9 is localized in the ER in resting cells and requires shuttling to the endosomal compartment to undergo its function. TLR9 traffics from the ER to the plasma membrane through the Golgi apparatus. Then, it is endocytosed and internalized in the endosomal compartment[169].

TLR9 recognizes unmethylated CpG motifs in short dsDNA sequences. Since mtDNA is hypomethylated, it is considered a TLR9 agonist. Although a particular oxidative status of mtDNA or its binding to proteins are not requirements for

TLR9 activation, it has been reported that both oxidized mtDNA and mtDNA-protein complexes can activate TLR9[148,149]. mtDNA recognition by TLR9 promotes a conformational change in TLR9 structure that allows the recruitment of the myeloid differentiation primary response protein 88 (MYD88), resulting in the activation of inflammatory kinases, such as TRAF6 and TBK1. These kinases activate the inflammatory mediators NFκB and interferon-response factor 3 (IRF3), which result in the release of cytokines or the induction type I IFN response, respectively (Table 3).

Some studies suggest that the specific endosomal compartment where TLR9 recognizes mtDNA determines the nature of the induced inflammatory response, *i.e.* either NFκB or IFN dependent responses. Indeed, it has been proposed that TLR9 activation in late endosomes drives NFκB dependent cytokine release, whereas TLR9 activation in early endosomes or lysosomes results in type I IFN response[170,171].

Nevertheless, the mechanisms by which mtDNA interacts with TLR9 in such compartments remain as major unanswered questions. Inhibition or disruption of auto/mitophagy seems the most feasible mechanism, as well as endocytosis of extracellular mtDNA sequences[172], although mitochondria-derived vesicles (MDVs) could also have a role. In fact, it has been demonstrated that MDVs mediate trafficking of mitochondrial components, including mtDNA, to endosomes in order to allow antigen presentation, where mtDNA could engage TLR9[173]. Besides, MDV-mediated trafficking could also be a mechanism by which mtDNA fragments are released to the cytosol and/or the extracellular media. Other mechanisms could involve the contribution of the newly-described adaptive mitophagy pathway mediated by $Rab5^{+}$ endosomes, characterized by mitochondrial engulfment by these vesicles via Parkin and Bnip3[174].

Lastly, a number of chronic inflammatory disorders are associated with TLR9 activation, including systemic lupus erythematous (SLE), non-alcoholic steatohepatitis, rheumatoid arthritis and psoriasis[169]. Interestingly, upregulated levels of TLRs, including TLR9, have been observed in skeletal muscle biopsies of patients with inflammatory myopathies. Furthermore, Opa1 knockout in skeletal muscle of mice results in mtDNA and TLR9-mediated muscle inflammation, providing an in vivo model for mitochondrial inflammatory myopathies[51,175].

2.6.2.2 mtDNA and cGAS

cGAS is a cytosolic dsDNA-sensor that synthetises cyclic GMP-AMP (cGAMP), a second messenger, which binds to and activates the stimulator of interferon genes (STING) located in the ER[176]. Activated STING induces the activity of TRAF6 and TBK1, which in turn promote the activation of NFκB or IRF3, respectively, thus leading to either the NFκB-dependent cytokine release or the type I IFN response[177] (Figure 5). Nevertheless, a recent study reported a non-canonical activation of STING, in which upon nuclear DNA damage, the DNA sensor IFI16 mediates the formation and activation of a STING-p53-TRAF6 complex, which leads to the activation of NF-κB[178]. Other studies have demonstrated that STING can translocate from the ER to mitochondria, where it interacts with MAVS and facilitates the trigger of its downstream signals[179]. These evidence suggest that while cGAS is not a requirement for STING activity, STING is essential in mediating cGAS-dependent inflammatory responses.

cGAS activity is DNA length dependent. In this regard, it has been shown that although low DNA concentrations can be sufficient for cGAS activation, it requires DNA fragments with a raging length between 100 and 500bp, which are considered long fragments[176]. Oxidized mtDNA, mtDNA-protein complexes and

mtDNA-mtRNA hybrids have also been reported to activate cGAS in the cytosol[150–152] (Table 3).

The mechanisms by which mtDNA nucleoids or fragments reach the cytosol are summarized earlier in this chapter, which include long-lasting mPTP opening, Bax/Bak pores, VDAC pores, mitophagy impairment and alterations in mitochondrial dynamics.

Abnormal cGAS-STING pathway activity is emerging as the initiation and pathogenesis of autoimmune and autoinflammatory diseases, including SLE, ataxia or STING-associated vasculopathy with onset in infancy (SAVI)[180]. Despite there are no reported cases associating activation of this pathway with inflammatory myopathies, a study using global Pink1 or Parkin knockout mice demonstrated that exercise-induced inflammation was exacerbated due to the leak of mtDNA to the plasma and the trigger of the cGAS-STING pathway in the knockout mice. The authors suggested that mitochondrial damage in these mice cannot be restored due to disruption of mitophagy, which results in mtDNA escape from the skeletal muscle, the most affected tissue by acute exercise, and activation of the pathway[120].

2.6.2.3 mtDNA and inflammasomes

As described in chapter 2.5, inflammasomes are cytosolic multiprotein complexes that drive inflammatory caspase activation, resulting in IL1β and IL18 secretion to the intra- and extracellular media. Inflammasomes require two sequential signals in order to fully undergo their activity: first, NFκB signalling pathway activation is required. In fact, the inflammasome components and inactive forms of cytokines are NFκB target genes, therefore, NFκB activation promotes upregulation of their protein levels. This signal, also known as priming signal, prepares the cells for a possible activation of inflammasomes. Second, the

DAMP or PAMP that recognizes the PRR of the inflammasomes triggers the oligomerization and activation of the super-complexes (Figure 5).

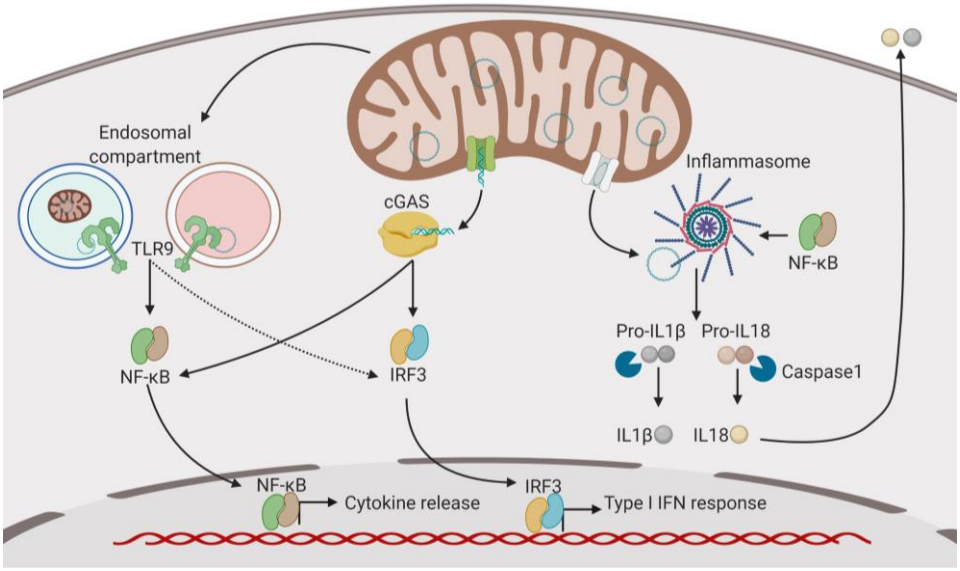

Figure 5: Activation of inflammatory pathways mediated by mtDNA and intracellular DNA sensor interaction. Location of mtDNA in the endosomal compartment allows its encounter with TLR9. Cytosolic mtDNA can be recognized by cGAS. Both TLR9 and cGAS can trigger the NFκB-dependent cytokine release and the type I IFN response. Cytosolic oxidized mtDNA can also be recognized by the inflammasomes and promote IL1β and IL18 release upon NFκB priming signal.

Several DAMP and PAMPs are recognized by inflammasomes, including ROS, bacterial or viral infection, ATP, potassium efflux, cathepsins, DNA, microbiota components or bacterial dipeptides[181]. Among all types of inflammasomes, NLRP3, NLRC4 and AIM2 inflammasomes are the ones that recognize mtDNA and trigger caspase-mediated cytokine release[153–155,182] (Table 3).

NLRP3 is the most studied type of inflammasome, however, since its mechanisms of activity are so diverse, there is controversy on whether it has affinity for a high number of DAMPs and PAMPs, or a single unknown molecular mechanism converges all its triggers. Cytosolic oxidized mtDNA activates NLRP3, and therefore, mitochondrial dysfunction leading to ROS overproduction and mtDNA

leakage is a potential inductor of NLRP3 inflammasome. Besides, the NLRP3 inflammasome cross-talks with a number of processes, such as mtDNA synthesis, mitophagy, and cGAS-STING or NFκB-dependent inflammatory pathways. First, it has been demonstrated that TLR-dependent MYD88 downstream elements supply deoxyribonucleotides for mtDNA synthesis, which promotes mtDNA accumulation, usually in an oxidative environment, allowing its oxidation and leakage into the cytosol. This, along with the NFκB dependent priming signal, allows NLRP3 activation, hence, engaging mtDNA synthesis with NLRP3 inflammasome response[183].

Apart from contributing to the priming signal, NFκB also plays a role in negatively regulating NLRP3 function. Indeed, the autophagosome adaptor p62, which can promote the degradation of dysfunctional mitochondria via mitophagy, is an NFκB target gene. Since mitochondria are essential for the NLRP3 inflammasome, first due to their nature as platforms for inflammasome oligomerization and, second, owing to their oxidized mtDNA production, NFκB-induced mitophagy via upregulation of p62 serves as a negative feedback mechanism on NLRP3 activity[184].

Lastly, it has been reported that bacterial or viral infection of human myeloid cells triggers the cGAS-STING pathway, which induces a cell death program that promotes potassium efflux leading to NLRP3 inflammasome. Although the authors did not reveal whether NFκB was active in these conditions, they demonstrated that STING traffics to lysosomes, where it triggers membrane permeabilization resulting in NLRP3 activating lysosomal cell death[185].

Despite it has been classically addressed only in macrophages, several studies report NLRP3 inflammasome activation in non-immune tissues, including heart and liver[160,186]. Furthermore, its activity has been associated to several inflammatory disorders, including Alzheimer's disease, atherosclerosis,

inflammatory bowel disease, non-alcoholic steatohepatitis, multiple sclerosis, myocardial infarction and type I diabetes, among others[187]. Nevertheless, its implication in triggering and/or driving muscle inflammation in inflammatory myopathies has not been reported yet.

2.7 Integrating mitochondrial dysfunction, inflammation and myopathies

Although preserving mitochondrial homeostasis is widely considered as essential in order to prevent muscle dysfunction and inflammation, few evidence have demonstrated the molecular mechanisms that link mitochondrial dysfunction with inflammation and, eventually, with muscle disorders. The skeletal muscle Opa1 knockout model[51] opened the way into a new research field that aims at not only the amelioration of muscle function in mitochondrial inflammatory myopathies, but also at increasing the knowledge on mechanisms allowing healthy muscle aging. The evidences proved by the Pink1 or Parkin global knockout models[120], as well as the Fis1 skeletal muscle-specific knockout model[68], also support the hypothesis that mitochondrial dysfunction can play as a priming signal that induces muscle inflammation and dysfunction. Interestingly, other cell type or tissue models for mitochondrial dysfunction or mitophagy disruption support this hypothesis, including the YME1L knockout in the nervous system, FUNDC1 downregulation or Drp1 overexpression in hepatocytes, and TFAM loss-of-function in kidney tubule cells or MEFs[54,55,121,160,166,167]. These studies encompass a global model in which primary mitochondrial dysfunctions result in sterile inflammatory responses. Hence, assessing and proving the model in the skeletal muscle can provide deep understanding on the molecular mechanisms underlying idiopathic (with unknown cause) inflammatory

myopathies, and therefore, providing insights on the design of accurate therapeutic approaches targeting the root of the disease.

OBJECTIVES

Previous data gathered by Dr. Aida Rodríguez-Nuevo in the group reported the impact of Opa1 deficiency in muscle inflammation, characterized by the involvement of mtDNA and TLR9[51]. Indeed, Opa1 plays several roles in mitochondrial function: besides its implication in mitochondrial fusion, it is also a fundamental asset in mtDNA stability and cristae formation. Moreover, recent evidence suggesting that downregulation of other mitochondrial proteins results in mtDNA-mediated sterile inflammation support the fact that mitochondrial dysfunction can cause inflammation in non-immune cells[54,120,121,160]. Furthermore, the physiological contribution of the activation of muscle sterile inflammation in the development of muscle atrophy remains unclear.

All the antecedents mentioned opened the question of whether primary alterations in mitochondrial dynamics have an impact in the control of inflammatory processes. This hypothesis motivated to pursue the present study with the aim of obtaining further insights on the involvement of mitochondrial dynamics in mitigating sterile inflammation and its contribution to muscle homeostasis. Thus, to address this overall aim, the following objectives and their respective approaches were proposed:

OBJECTIVE I: To describe what imbalances in mitochondrial dynamics induce inflammation and to assess the common mechanistic features involved.

- With the use of acute and stable knock-down muscle cell lines for different mitochondrial dynamics proteins, we aim at identifying associations between imbalanced mitochondrial dynamics and the activation of sterile inflammatory responses, as well as characterizing the main players in the mechanisms underlying.

OBJECTIVE II: To further characterize the molecular mechanisms connecting Mfn1 deficiency-induced mitochondrial fragmentation and intracellular inflammation.

- Given the antecedents on the link between Opa1 deficiency and muscle inflammation, and considering that Mfn2 plays other functions beyond mitochondrial fusion[188], we chose to further explore the molecular systems operating the inflammatory responses upon Mfn1 deficiency-induced mitochondrial fragmentation in muscle cells.

OBJECTIVE III: To investigate the impact of Mfn1 ablation in the development of muscle inflammation and atrophy, as well as evaluation of the physical performance.

- The effects of mitochondrial fragmentation in the development of muscle atrophy have been reported[19,51]. However, the role of Mfn1 in this association remains unexplored. To study the impact of muscle Mfn1 depletion *in vivo* and to corroborate the findings obtained in Objective I and II related to Mfn1 deficiency, we generated an inducible skeletal muscle-specific Mfn1 knockout mouse model and characterized metabolic and muscle health parameters.

RESULTS

Study I: Common mechanistic features linking imbalances in mitochondrial dynamics and sterile inflammation

Recent evidence link mitochondrial dysfunction with the induction of sterile inflammatory responses in non-immune cells. In fact, total ablation of the mitophagic protein Pink1 in mice subjected to exercise results in cGAS-mediated inflammation due to mtDNA leakage[120]. The same observations were described in hepatocytes upon downregulation of the mitophagic protein FUNDC1[160] and in mouse embryonic fibroblasts (MEFs) deficient for TFAM[121]. These studies confirm the importance of maintaining mitochondrial homeostasis to prevent sterile inflammation. Furthermore, it has been previously described by members of our lab that skeletal muscle downregulation of the mitochondrial protein Opa1, involved in mitochondrial fusion and in cristae formation, promotes NFκB-driven inflammation[51], as well as the downregulation of Yme1L in retinas of mice[54]. These evidence suggest the implication of balanced mitochondrial fusion and fission in mitigating sterile inflammation. However, direct links between impaired mitochondrial dynamics and the induction of inflammatory responses, as well as the mechanisms underlying, remain unexplored. Thus, we aimed at identifying what proteins involved in mitochondrial dynamics play a role in preventing the activation of intracellular inflammatory pathways in skeletal muscle cells, or myoblasts, and the common mechanistic features leading to such effects.

4.1.1 Effects of acute downregulation of mitochondrial proteins on the induction of inflammation

In order to assess what alterations in mitochondrial dynamics trigger sterile inflammation, we performed acute downregulation of several mitochondrial dynamics proteins in cultured myoblasts by siRNA transfection and quantified

the expression levels of NFκB target genes and type I IFN response genes. Considering the data relating Opa1 or Yme1L downregulation in activating NFκB target gene expression, we used the downregulation of these two proteins as a positive control of the experiment. As observed, downregulation of the fusion proteins Mfn1 and Mfn2, but not the Opa1 protease Oma1, lead to an induction in the expression levels of NFκB target genes – and not type I IFN response genes - compared to myoblasts transfected with a negative control siRNA. Interestingly, downregulation of Yme1L resulted in the induction genes involved in both pathways (Figure 6).

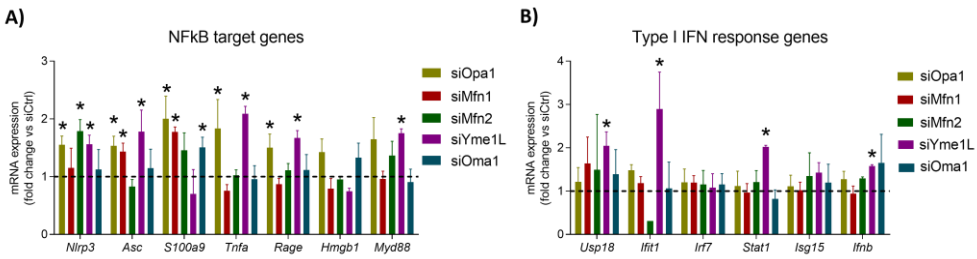

Figure 6: Inflammatory profile of acute downregulation of mitochondrial fusion proteins. A) NFκB target gene expression. B) Type I IFN gene expression. (n=4-6) Data represent mean ± SEM.

Regarding the acute downregulation of mitochondrial fission proteins, which include Drp1, Mff and Fis1, the stimulation of genes involved in both pathways was observed, especially upon Drp1 or Fis1 downregulation (Figure 7A-B).

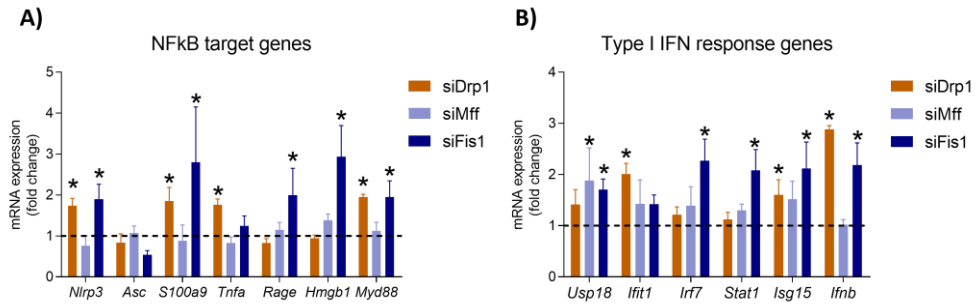

Figure 7: Inflammatory profile of acute downregulation of mitochondrial fission proteins. A) NFκB target gene expression. B) Type I IFN gene expression. (n=4-6) Data represent mean ± SEM.

These data indicate that, regardless of the cause of the imbalance in mitochondrial dynamics, altered fusion and fission events induce the expression of inflammatory genes. Considering this observation, we generated stable knock-down (KD) myoblasts for several mitochondrial dynamics proteins, including Mfn1, Mfn2, Yme1L, Fis1 and Drp1. This was achieved by lentiviral infection of cognate shRNAs, as described in *section 7.2.2.4*. Scramble myoblasts (Scr) were generated in parallel as negative controls. Of note, Yme1L was included in the study given the novelty of the effects on the induction of type I IFN response genes upon its deficiency in myoblasts. To validate the generation of the stable KD myoblast lines, quantification of the mRNA and protein levels of the targeted proteins was performed in each cell line (Figure 8A-D).

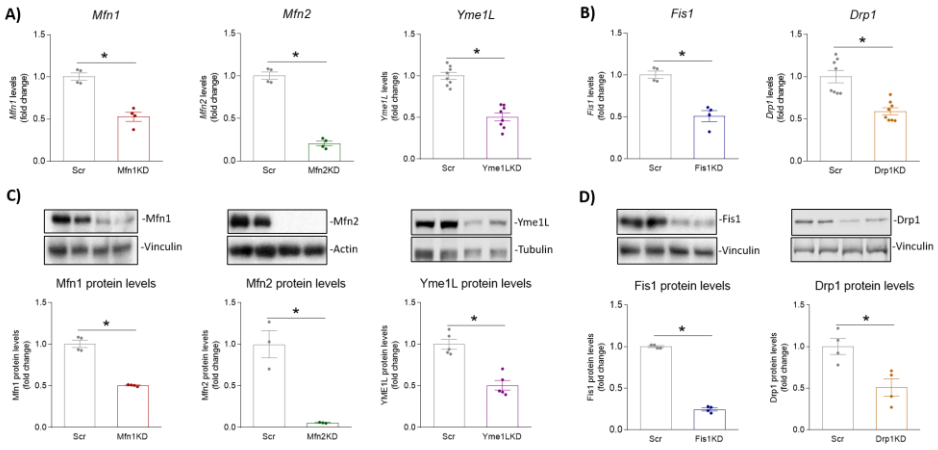

Figure 8: Validation of the stable KD myoblasts. A-B) mRNA and C-D) protein levels of the targeted genes in each stable KD cell line. (n=3-5) Data represent mean ± SEM. *p<0.05 vs. Scr.

As a further validation of the models, the resulting mitochondrial network morphology was assessed by immunofluorescence assays targeting the outer mitochondrial membrane protein TOM20 and quantifying the branch length of mitochondria within the networks (Figure 9A-C). As expected, downregulation of fusion proteins resulted in mitochondrial fragmentation characterized by a

reduction in the branch length of mitochondria, whereas fission protein deficiency promoted mitochondrial elongation characterized by increased branch length. In the case of Yme1L downregulation, mitochondrial fragmentation is caused by a decreased processing of the Opa1 isoforms, which results in reduced mitochondrial fusion.

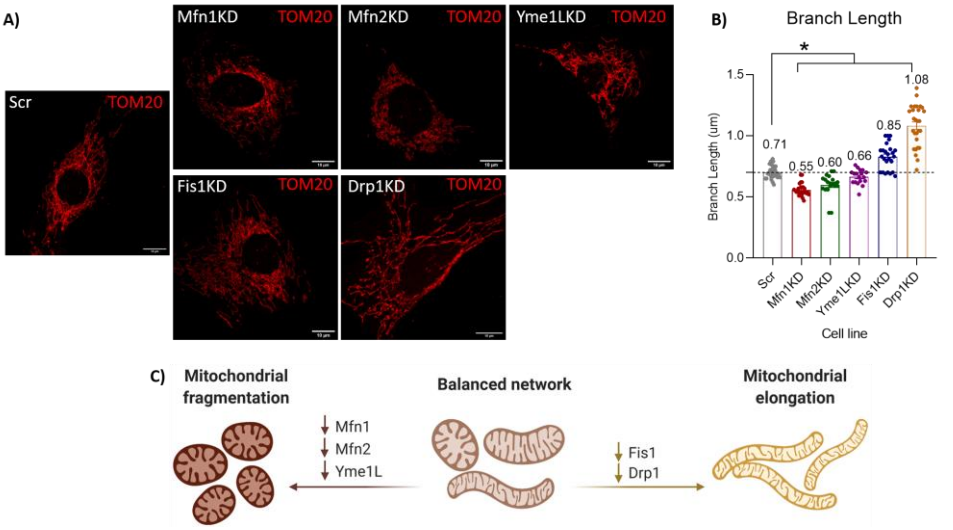

Figure 9: Validation of the mitochondrial morphology in stable KD myoblasts. A) Representative images of TOM20 immunostaining in each cell line. B) Quantification of the mean branch length of the mitochondrial network per cell line. C) Schematic representation of the mitochondrial morphology outcome upon downregulation of mitochondrial dynamics proteins. (n=20) Data represent mean ± SEM. *p<0.05 vs. Scr.

4.1.2 Characterization of the triggers of inflammation upon imbalanced mitochondrial dynamics

Upon validation of the stable KD muscle cell models, the assessment of the inflammatory profile was performed by quantification of the expression levels of NFκB target genes and type I IFN response genes. Confirming the results observed in the acute setting, downregulation of the mitochondrial fusion proteins Mfn1, Mfn2 and Yme1L resulted in NFκB-mediated inflammation, and

only for the latter the type I IFN response was induced. Strikingly, induced *Ifnb* expression was observed upon Mfn2 deficiency (Figure 10A-B).

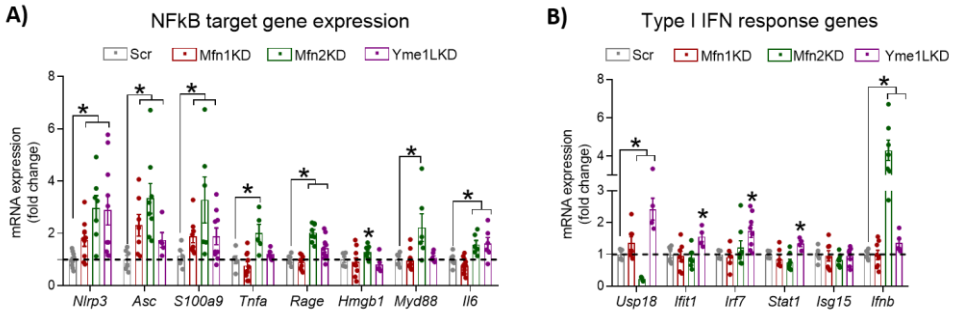

Figure 10: Inflammatory profile of Mfn1KD, Mfn2KD and Yme1LKD myoblasts. A) NFκB target gene expression. B) Type I IFN gene expression. (n=7) Data represent mean ± SEM. *p<0.05 vs. Scr.

In contrast, and as observed in the acute setting, Fis1 and Drp1 deficiencies in myoblasts resulted in the activation of both pathways (Figure 11A-B).

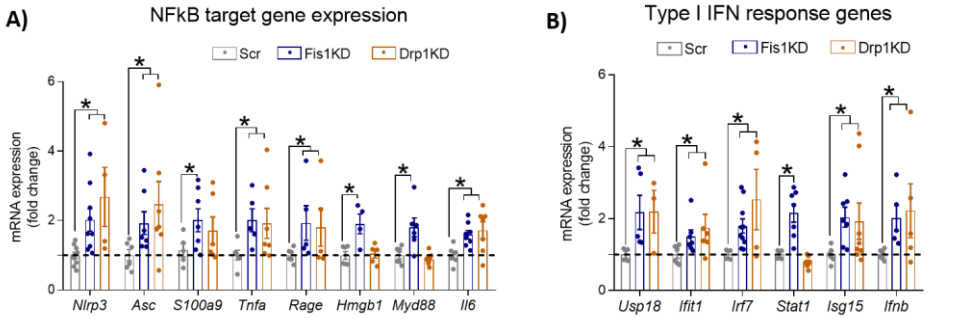

Figure 11: Inflammatory profile of Fis1KD and Drp1KD myoblasts. A) NFκB target gene expression. B) Type I IFN gene expression. (n=5-7) Data represent mean ± SEM. *p<0.05 vs. Scr.

These data indicate that mitochondrial fragmentation and elongation induce distinct inflammatory profiles, suggesting common mechanistic events coupling reduced mitochondrial fusion and fission to inflammation. Nevertheless, mitochondrial fragmentation induced by downregulation of Yme1L did not follow this line, most likely due to its vast variety of mitochondrial substrates

apart from Opa1, which could be contributing to a different mechanism resulting in inflammation.

Members of our lab previously described that inflammation upon Opa1 deficiency in myoblasts was induced due to mtDNA location in late endosomes. This location allows mtDNA recognition by TLR9, engaging NFκB-dependent inflammatory response[51]. Thus, we hypothesized that location of mtDNA in these cell lines could also be playing a major role in the trigger of inflammatory responses. To address this, we performed subcellular fractionation and subsequent qPCR to quantify mtDNA abundance in cytosolic fractions. As expected, Mfn1 and Mfn2 deficiencies did not exhibit increased presence of mtDNA sequences in cytosolic fractions, consistent with the absence of activation of the type I IFN response in these cell lines. Interestingly, Yme1L downregulation, as well as Fis1 and Drp1 downregulation, resulted in enhanced abundance of mtDNA in cytosolic fractions (Figure 12), which could be associated to cGAS activation and its resulting inflammatory outcome.

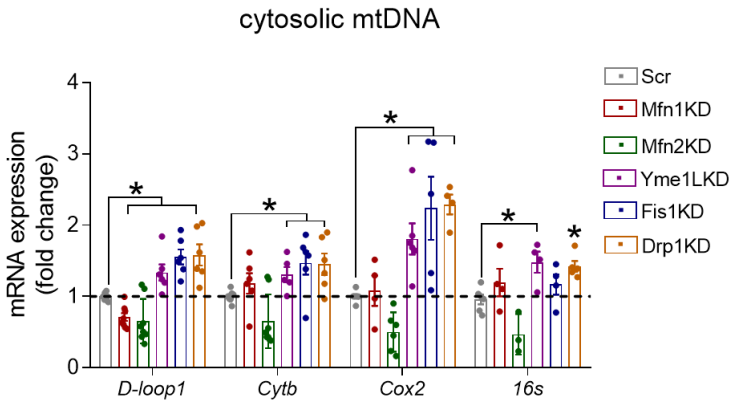

Figure 12: Cytosolic mtDNA abundance. Expression of mtDNA-encoded genes relative to nuclear-encoded genes (*bActin*) in cytosolic fractions of stable KD cell lines (n=5-6). Data are represented as mean ± SE. *p vs. Scr <0.05.

Fluctuations of mtDNA in the cytosol were independent of the total mtDNA content in all cell lines, except for Yme1LKD or Drp1KD myoblasts, which showed increased mtDNA content compared to control cells (Figure 13).

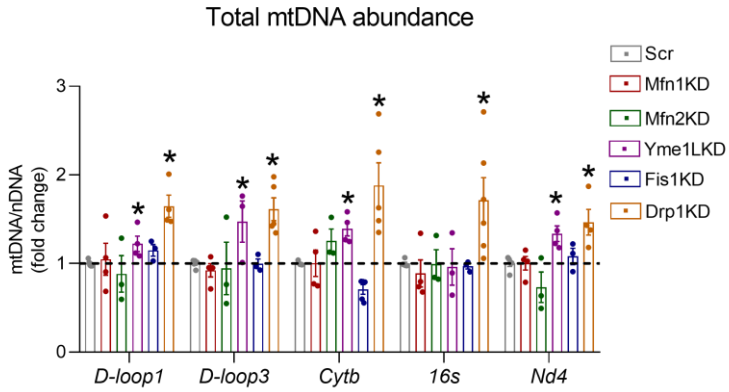

Figure 13: Total mtDNA abundance. Expression of mtDNA-encoded genes relative to nuclear-encoded genes (*bActin*) in total DNA extracts of stable KD cell lines (n=5-6). Data are represented as mean ± SE. *p vs. Scr <0.05.

In order to rule out other metabolic alterations and to further validate the implication of mtDNA mislocation in the activation of intracellular inflammatory responses upon imbalances in mitochondrial dynamics, several mitochondrial parameters and their parallelism with the inflammatory profile were assessed. First, given the association of reduced mitochondrial membrane potential (Δψm) to mitochondrial dysfunction, we evaluated this parameter in our KD myoblasts. Quantification of the Δψm relative to the mitochondrial mass showed that all cell lines presented decreased Δψm, with the exception of Drp1KD myoblasts, which exhibited increased Δψm (Figure 14).

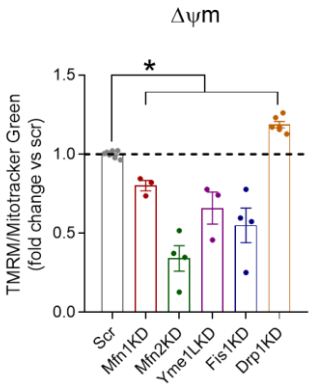

Figure 14: Δψm. TMRM signal relative to the mitochondrial mass per assay (n=3-5). Data are represented as mean ± SE. *p vs. Scr <0.05.

Next, mitochondrial ROS (mtROS) have been extensively considered as mtDAMPs[138], therefore we assessed their production upon imbalanced mitochondrial dynamics. Quantification of mtROS (superoxide) relative to the mitochondrial mass showed that, whereas Mfn1, Yme1L and Drp1 deficiencies lead to increased mtROS, Mfn2-deficient myoblasts showed a reduction. Fis1KD myoblasts, however, exhibited unchanged mtROS levels (Figure 15).

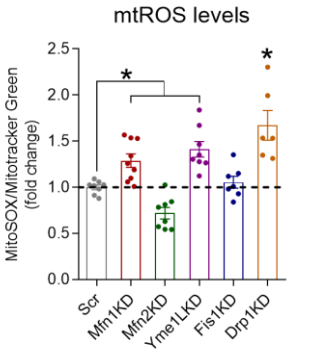

Figure 15: mitochondrial superoxide production. MitoSOX signal relative to the mitochondrial mass per assay (n=6-9). Data are represented as mean ± SE. *p vs. Scr <0.05.

Considering the implication of impaired mitophagy in the trigger of inflammatory responses due to cytosolic leakage of mtDNA[120,160], we assessed the mitophagic flux by calculating the ratio of the mitochondrial mass in the presence and absence of the lysosomal fusion inhibitor bafilomycin A1 ($\frac{Mitochondrial\ mass^{+baf}}{Mitochondrial\ mass^{-baf}}$). This assay showed that none of the muscle cell lines

presented significant impairment of this process besides Mfn1KD and Fis1KD myoblasts, which exhibited a remarkable increase in the mitophagic flux (Figure 16A-B). Nevertheless, the data related to Mfn2KD and Drp1KD cells contradicts the observations made in several studies that report that Mfn2 and Drp1 deficiencies impair autophagy and mitophagy[19,65,66]. Therefore, further approaches should be tackled in order to assess rigorously the mitophagic flux in these cell lines.

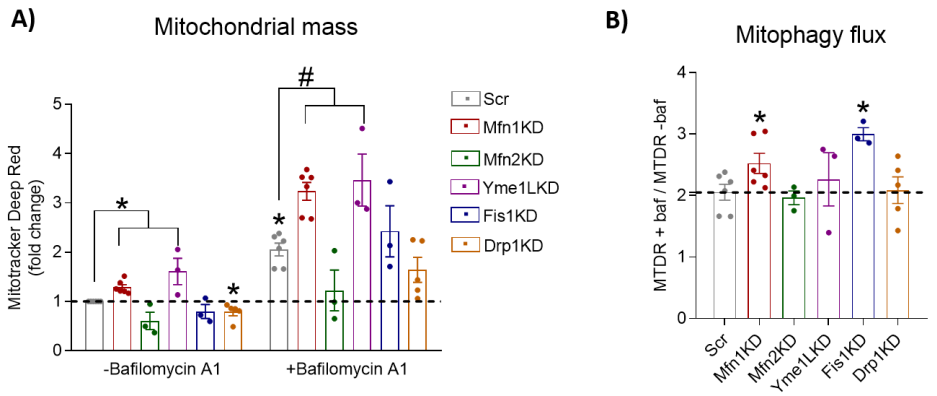

Figure 16: Mitophagic flux assessment. A) Quantification of the mitochondrial mass per cell line in the presence or absence of bafilomycin A1. B) Mitophagic flux calculation represented by the ratio of the mitochondrial mass with vs. without bafilomycin A1. (n=3-6) Data are represented as mean ± SE. *p vs. Scr <0.05; #p vs. Scr+Baf <0.05.

Last, impaired oxidative phosphorylation capacity has also been associated to activation of inflammatory responses[189], therefore we assessed the mitochondrial respiration in our myoblast lines. Quantification of the oxygen consumption rate suggested that Mfn1-deficient and Fis1-deficient cells showed improved mitochondrial respiration, whereas Yme1LKD myoblasts presented a remarkable decrease. As for Mfn2KD and Drp1KD cells, no significant changes were observed, with the exception of reduced maximal respiration in Drp1KD cells (Figure 17A-B).

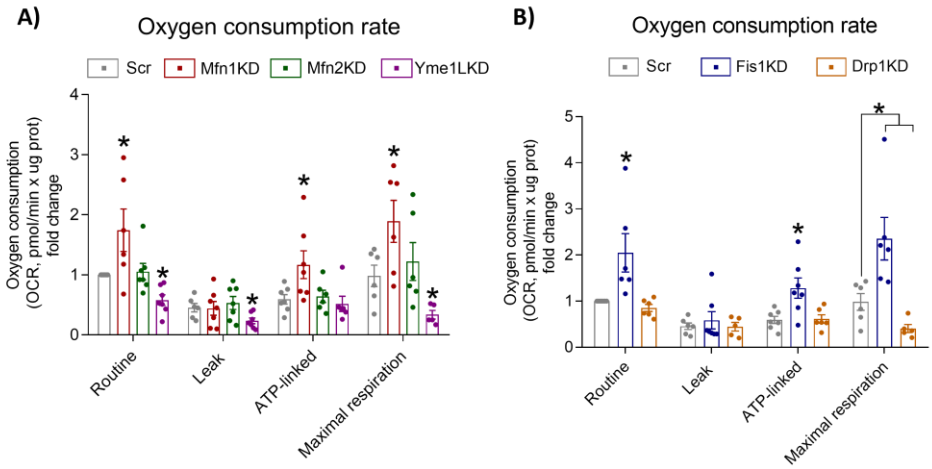

Figure 17: Oxygen consumption rates. A) Oxygen consumption rate in cell lines with mitochondrial fragmented networks. B) Oxygen consumption rate in cell lines with mitochondrial elongated networks. (n=6-7) Data are expressed as mean ± SE. *p vs. Scr <0.05.

Taken together, none of the data related to the metabolic phenotyping presented any parallelism with the inflammatory profile observed upon fragmentation or elongation of the mitochondrial network (Table 3), thus, supporting the hypothesis that mtDNA mislocation is key in driving inflammation in these contexts.

Cell line	Total mtDNA	Δψm	mtROS	Mitophagic flux	Oxygen consumption
Mfn1KD	=	↓	↑	↑	↑
Mfn2KD	=	↓	↓	=	=
Yme1LKD	↑	↓	↑	=	↓
Fis1KD	=	↓	=	↑	↑
Drp1KD	↑	↑	↑	=	= (except max O_2 consumption ↓)

Table 4: Summary of the metabolic phenotyping of all cell lines.

4.1.3 Involvement of mtDNA recognition by intracellular DNA sensors in inflammation upon imbalanced mitochondrial dynamics

In order to further analyze the implication of mtDNA mislocation in triggering inflammatory responses upon imbalanced mitochondrial dynamics, we assessed the co-distribution of mtDNA (green) together with the endosomal or cytosolic DNA sensors (red), TLR9 and cGAS, respectively, by super-resolution confocal microscopy. Visualization of the staining of mtDNA was achieved by dsDNA staining and subtraction of the signal from the nuclei.

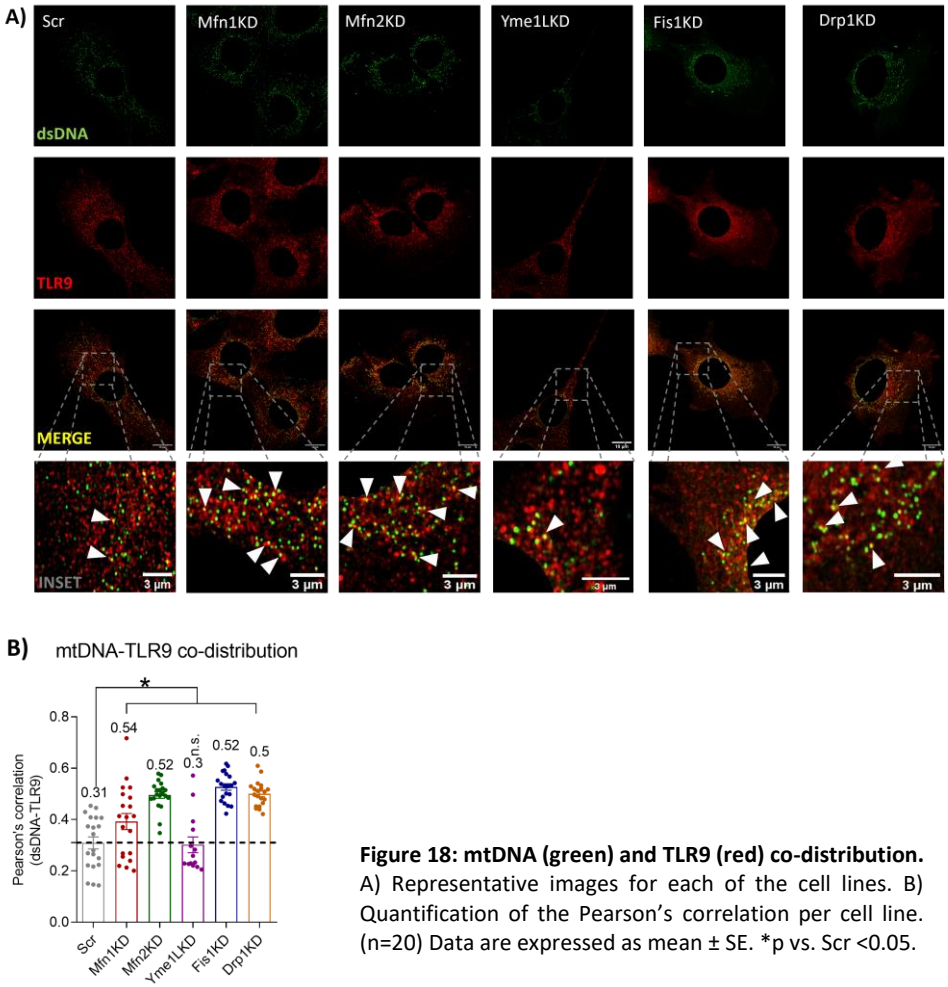

Figure 18: mtDNA (green) and TLR9 (red) co-distribution. A) Representative images for each of the cell lines. B) Quantification of the Pearson's correlation per cell line. (n=20) Data are expressed as mean ± SE. *p vs. Scr <0.05.

Interestingly, mtDNA and TLR9 co-distribution was increased in all cell lines, except for Yme1LKD myoblasts (Figure 18A-B). In contrast, co-distribution of mtDNA and cGAS was only increased in myoblasts with elongated mitochondrial network (*i.e.*, Drp1 and Fis1-deficient cells) or downregulated Yme1L (Figure 19).

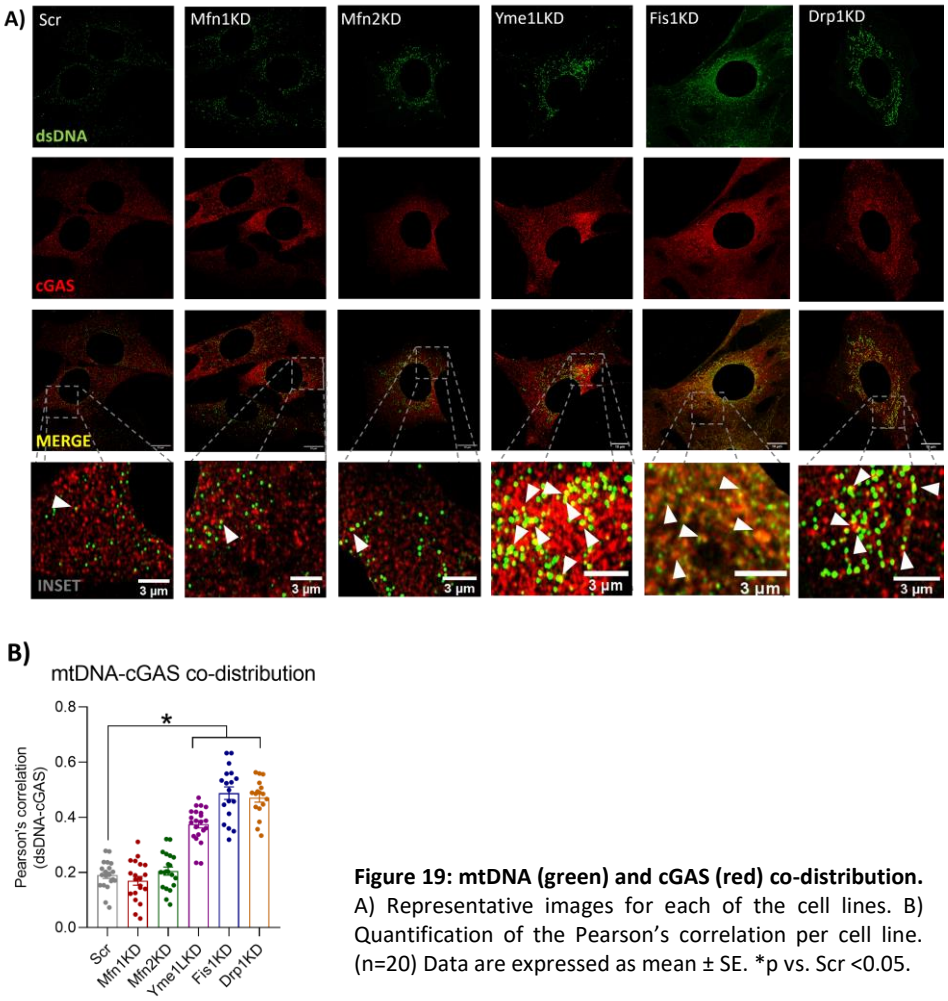

Figure 19: mtDNA (green) and cGAS (red) co-distribution. A) Representative images for each of the cell lines. B) Quantification of the Pearson's correlation per cell line. (n=20) Data are expressed as mean ± SE. *p vs. Scr <0.05.

In fact, unchanged co-distribution between mtDNA and cGAS in Mfn1KD and Mfn2KD cells reassured the fact that mtDNA does not leak to the cytosol upon downregulation of these mitochondrial fusion proteins and, hence, the type I IFN response is not induced. In contrast, increased co-distribution of mtDNA and

cGAS in Yme1LKD, Fis1KD or Drp1KD cells goes in line with the increased cytosolic mtDNA abundance detected in these cells, along with the activation of both the type I IFN response and the NFκB-mediated inflammation.

To elucidate the contribution of mtDNA-DNA sensor engagement to the activation of inflammation, we treated all muscle cell lines with either the antagonist of TLR9, namely ODN2088[190], or the specific inhibitor of cGAS, Ru.521[191], according to the mtDNA-DNA sensor co-distribution profile they exhibited. First, inhibition of TLR9 in Mfn1 and Mfn2-deficient cells normalized the expression levels of NFκB target genes, as well as *Ifnb* in Mfn2KD cells (Figures 20A-B).

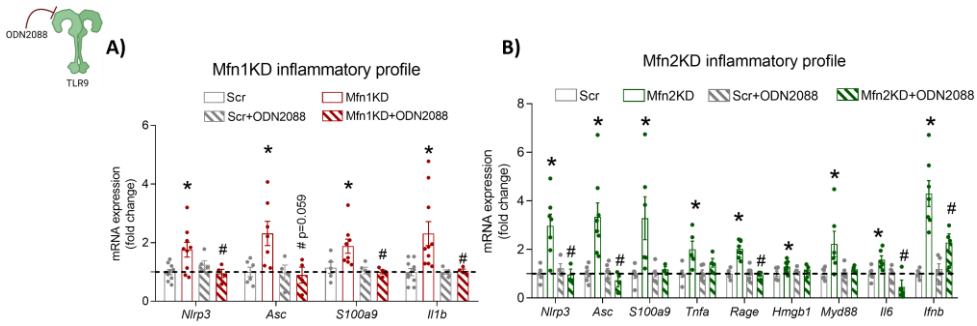

Figure 20: Inflammatory profile in Mfn1KD and Mfn2KD myoblasts upon ODN2088 treatment. A) Inflammatory profile rescue in Mfn1KD myoblasts. B) Inflammatory profile rescue in Mfn2KD myoblasts. (n=6-8) Data are expressed as mean ± SE. *p vs. Scr <0.05; #p vs. KD <0.05.

Furthermore, in the case of Mfn1KD myoblasts, this experiment was further validated by acute downregulation of *Tlr9* and assessment of NFκB target gene expression (Figure 21A-B). As expected, TLR9 deficiency in Mfn1KD myoblasts also normalized the NFκB-mediated inflammation compared to Mfn1KD cells transfected with a control siRNA. These data suggest that, recapitulating the Opa1KD scenario, mitochondrial fragmentation induced by downregulation of Mfn1 or Mfn2 promotes a TLR9-mediated NFκB-dependent inflammation.

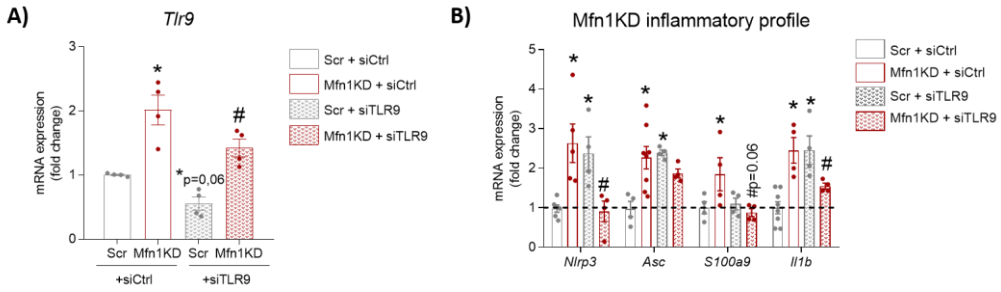

Figure 21: Inflammatory profile rescue in Mfn1KD cells upon *Tlr9* downregulation. A) Validation of *Tlr9* downregulation using siRNA delivery in control and Mfn1KD myoblasts. B) Inflammatory profile of Mfn1KD cells upon *Tlr9* downregulation. (n=4-5) Data are expressed as mean ± SE. *p vs. Scr+siCtrl <0.05; #p vs. KD+siCtrl <0.05

In keeping with the increased co-distribution of mtDNA only with cGAS, Yme1LKD cells rescued the expression levels of both NFκB target genes and type I IFN response genes upon Ru.521 treatment (Figure 22), which suggests that the inflammation triggered by Yme1L deficiency in myoblasts is cGAS-mediated.

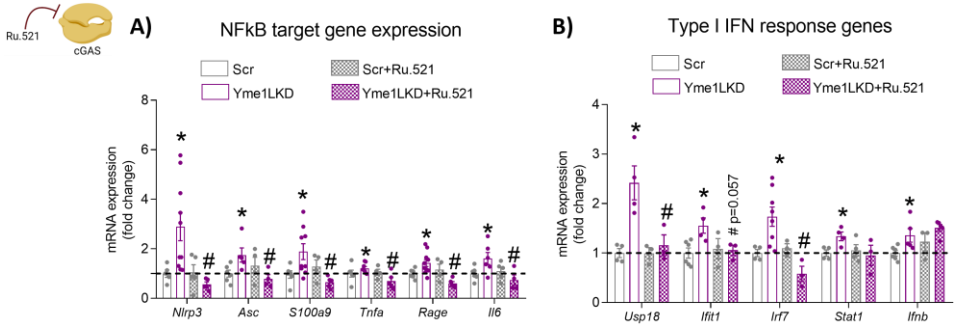

Figure 22: Inflammatory profile rescue in Yme1LKD myoblasts upon Ru.521 treatment. A) NFκB target gene expression. B) Type I IFN gene expression. (n=4-8) Data are expressed as mean ± SE. *p vs. Scr <0.05; #p vs. KD <0.05.

As for Fis1KD or Drp1KD myoblasts, ODN2088 or Ru.521 treatments blocked to different extent the expression of inflammatory genes. Upon Drp1 downregulation, both treatments exerted a mild effect in repressing NFκB target

genes or type I IFN response genes (Figure 23). However, similarly to the effects of TLR9 inhibition upon Fis1 deficiency, these effects were not accompanied by statistical significance (Figure 24A-B). In fact, Fis1KD myoblasts fully normalized the expression of NFκB target genes and type I IFN response genes upon cGAS inhibition (Figure 24C-D), suggesting a major implication of cGAS in the activation of inflammatory responses upon mitochondrial elongation.

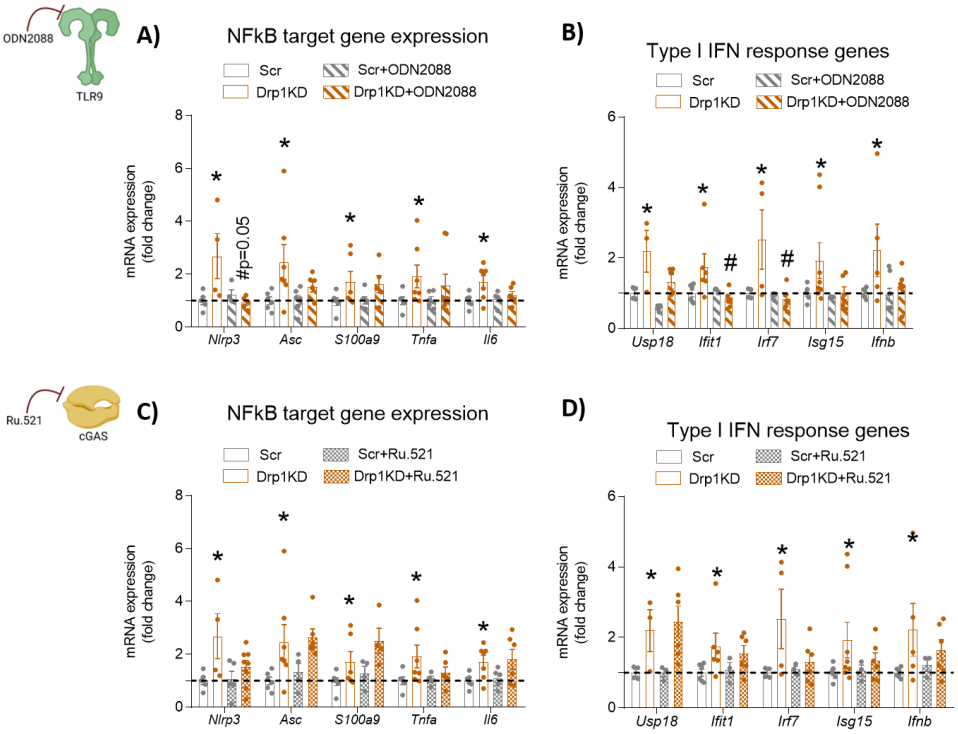

Figure 23: Inflammatory profile rescue in Drp1KD cells upon ODN2088 or Ru.521 treatment. A) Effects of ODN2088 treatment on A) NFκB target genes or B) type I IFN response genes. C) Effects of Ru.521 treatment on A) NFκB target genes or D) type I IFN response genes. (n=4-5) Data are expressed as mean ± SE. *p vs. Scr <0.05; #p vs. KD <0.05.

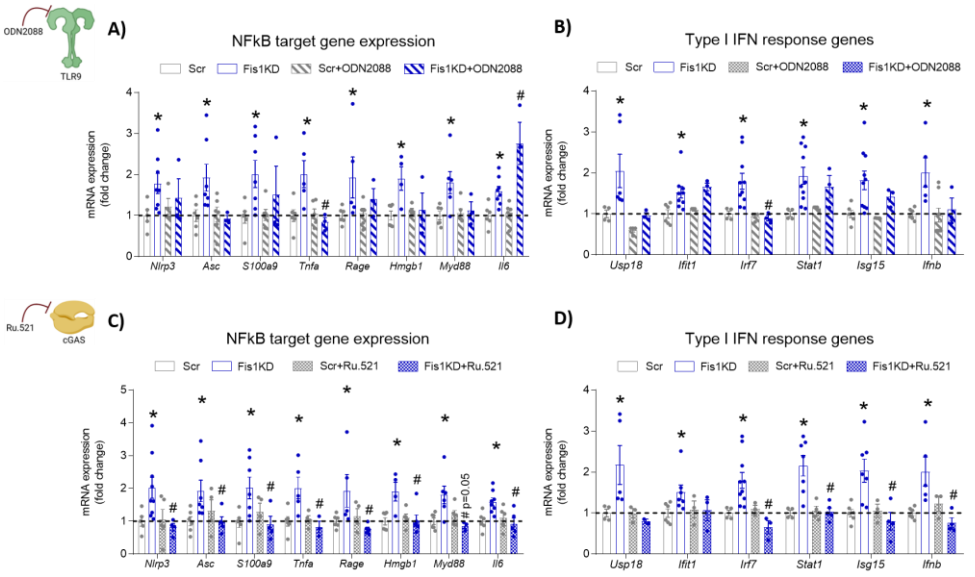

Figure 24: Inflammatory profile rescue in Fis1KD cells upon ODN2088 or Ru.521 treatment. A) Effects of ODN2088 treatment on A) NFκB target genes or B) type I IFN response genes. C) Effects of Ru.521 treatment on A) NFκB target genes or D) type I IFN response genes. (n=4-9) Data are expressed as mean ± SE. *p vs. Scr <0.05; #p vs. KD <0.05.

All in all, the following observations were made by assessing mtDNA and DNA sensor co-distributions and by blocking TLR9 or cGAS activities upon alterations in mitochondrial dynamics in myoblasts (Table 4): i) mitochondrial fragmentation induced by Mfn1 or Mfn2 downregulation causes TLR9-mediated NFκB-dependent inflammation, and ii) Yme1L deficiency promotes mtDNA leakage and cGAS activation, iii) mitochondrial elongation associates to engagement of mtDNA with both TLR9 and cGAS, although the contribution of the latter upon cytosolic mtDNA leakage appears to be more significant.

Cell line	Inflammatory profile		mtDNA-DNA sensor codistribution		Inhibitor effects	
	NFκB	Type I IFN	TLR9	cGAS	ODN2088	Ru.521
Mfn1KD	↑	=	↑	=	↓	-
Mfn2KD	↑	= (except for *Ifnb*)	↑	=	↑	-
Yme1LKD	↑	↑	=	↑	-	↓
Fis1KD	↑	↑	↑	↑	≈↓	↓
Drp1KD	↑	↑	↑	↑	≈↓	≈↓

Table 5: Summary of the results obtained in the inflammatory phenotyping of all stable KD cell lines.

At this point, Sprenger *et al.* 2021 published the molecular mechanisms linking Yme1L downregulation to mtDNA leakage and cGAS activation[55]. According to this study, Yme1L deficiency in MEFs promotes the accumulation of the pyrimidine transporter SLC25A33, one of the substrates of Yme1L. Increase of SLC25A33 upon Yme1L downregulation promotes an enhanced nucleotide entry to mitochondria, which results in increased mtDNA synthesis. In order to maintain homeostasis, mtDNA sequences are released through VDAC pores – and not Bax-Bak pores- to the cytosol, where cGAS recognizes them and triggers both the NFκB-dependent and the type I IFN responses. To validate this pathway in our Yme1LKD muscle cell model and to assess the implication of this mechanism upon mitochondrial elongation, we quantified protein levels of both Yme1L and SLC25A33 in Yme1L, Fis1 and Drp1-deficient myoblasts. In keeping with the work from Sprenger *et al*. 2021, Yme1LKD myoblasts exhibited increased SLC25A33 protein amount (Figure 25), as well as increased total mtDNA abundance (Figure 13).

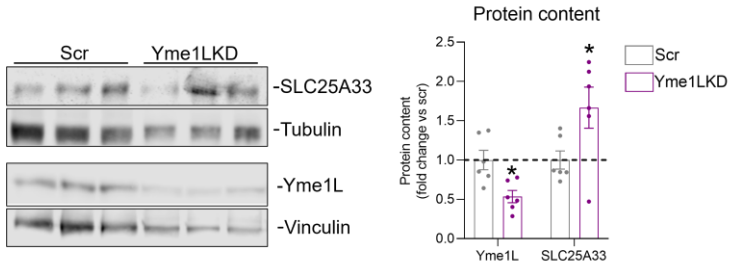

Figure 25: Yme1L and SLC25A33 protein levels in Yme1LKD myoblasts. (n=6) Data are expressed as mean ± SE. *p vs. Scr <0.05.

Interestingly, although no significant changes in Yme1L protein levels were observed upon neither Fis1 nor Drp1 deficiency, a significant increase of SLC25A33 was observed in Fis1KD cells (Figure 26), suggesting that increased pyrimidine import could be the cause of mtDNA exit to the cytosol in these cells, but not in Drp1KD myoblasts.

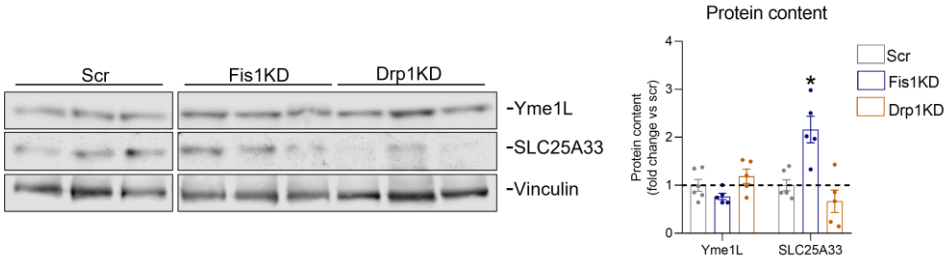

Figure 26: Yme1L and SLC25A33 protein levels in Fis1KD and Drp1KD myoblasts. (n=5) Data are expressed as mean ± SE. *p vs. Scr <0.05.

These data contradict the fact that Fis1KD cells present unchanged total mtDNA abundance, whereas Drp1KD cells exhibit increased mtDNA content, similarly to Yme1LKD myoblasts (Figure 13). In conclusion, despite our data indicate that the mechanisms promoting mtDNA leakage in Fis1 and Drp1-deficient myoblasts differ, in the context of mitochondrial elongation in myoblasts, mtDNA leakage

to the cytosol appears both as a common outcome and as a key driver of inflammation.

Taken together, our data demonstrate that imbalanced mitochondrial dynamics associate to the activation of different intracellular inflammatory pathways, and mislocation of mtDNA appears as a hub in the induction of sterile inflammation (Figure 27). On one hand, mitochondrial fragmentation mediated by downregulated Mfn1 and Mfn2 results in TLR9 activation and NFκB-driven inflammation, which goes in line with the downregulation of Opa1[51]. In the case of mitochondrial fragmentation induced by reduced Yme1L, mtDNA leakage and cGAS activation are the drivers of inflammation. The molecular mechanisms coupling Yme1L downregulation and cGAS activation have recently been described by Sprenger *et al.* 2021, which validated our results in Yme1LKD myoblasts. On the other hand, myoblasts with elongated mitochondrial networks show a more complex scenario: both TLR9 and cGAS contribute to different extends to the trigger of inflammation in Fis1KD or Drp1KD myoblasts, however, mtDNA leakage – probably by distinct mechanisms in each cell line – appears as a key factor.

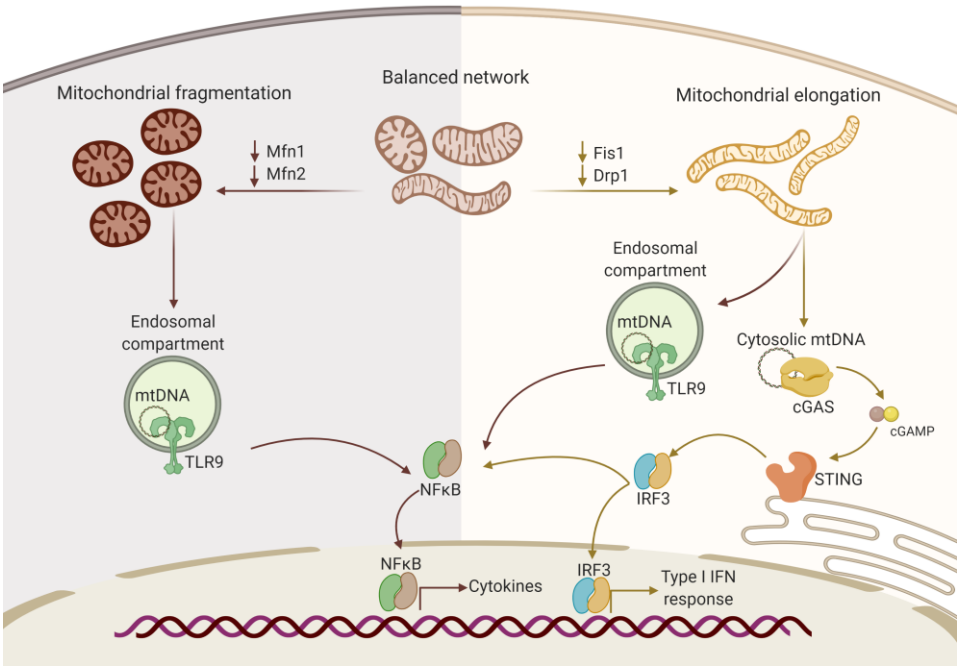

Figure 27: Schematic representation of the results obtained in this study. Mitochondrial fragmentation induced by Mfn1 and Mfn2 deficiency promote TLR9-mediated recognition of mtDNA, leading to NFκB-dependent cytokine release. Mitochondrial elongation induced by Fis1 and Drp1 downregulation promotes mtDNA leakage to the cytosol and subsequent cGAS activation. Increased mtDNA-TLR9 co-distribution is also observed upon Fis1KD and Drp1KD, therefore, TLR9 and cGAS activation drive the induction of NFκB-dependent inflammatory response, as well as the type I IFN response.

Study II: Identification of the molecular pathways driving inflammation in Mfn1-deficient myoblasts

Based on our initial data and because Mfn1 and Mfn2 deficiencies trigger a simple inflammatory response characterized by activation of NFκB– and not the type I IFN response – in a TLR9-dependent manner, we focused on describing the molecular mechanisms involved. Given that some of the cellular functions of Mfn2 are beyond mitochondrial fusion[188], we decided to further explore Mfn1-deficient myoblasts to elucidate the molecular mechanisms underlying.

4.2.1 Characterization of the endosomal location of mtDNA-TLR9 encounter in Mfn1KD myoblasts.

TLR9 localizes in the endosomal compartment in order to detect the presence of foreign DNA and to engage inflammation. Considering that the mechanisms mediating mtDNA arrival to the endosomal compartment upon Mfn1 deficiency are diverse, we first characterized the type of endosome in which mtDNA is more likely to be recognized by TLR9 in this context. For this, we performed a battery of co-distribution studies between mtDNA (green) and several endosomal markers, including Rab5 or EEA1 for early endosomes (red), Rab7 for late endosomes and lysosomes (red), HRS for intermediate species (red) and LAMP1 for late endosomes, lysosomes and autophagolysosomes (blue) (Figure 28A). Strikingly, increased co-distribution between mtDNA and early endosomal markers, *i.e*. Rab5 and EEA1, was found in Mfn1-deficient myoblasts (Figure 28B), suggesting that the likelihood of mtDNA encountering TLR9 is higher in early endosomes than in any other type of endosomal vesicle.

A)

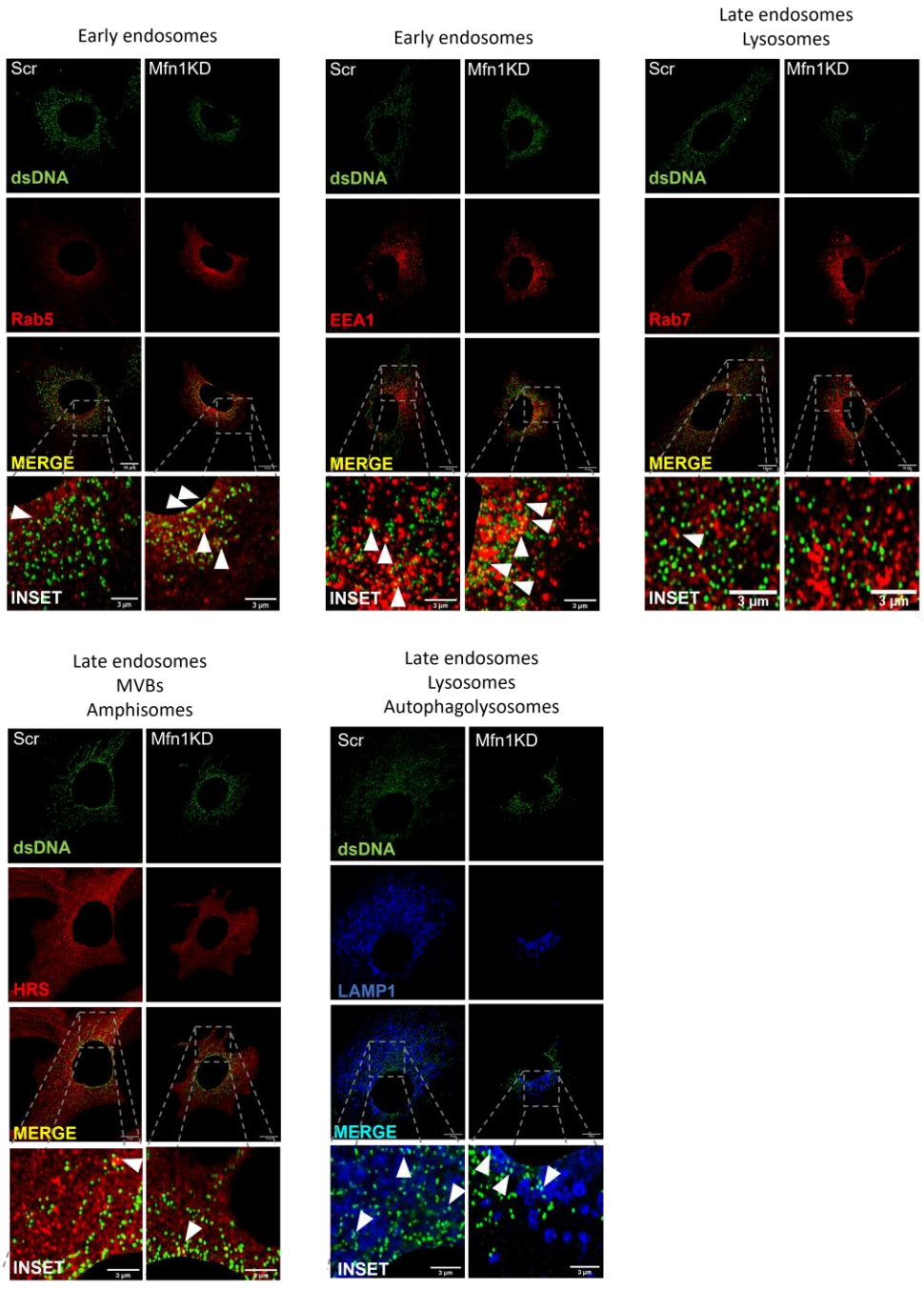
Early endosomes
Scr
Mfn1KD
dsDNA
Rab5
MERGE
INSET
Early endosomes
Scr
Mfn1KD
dsDNA
EEA1
MERGE
INSET
Late endosomes
Lysosomes
Scr
Mfn1KD
dsDNA
Rab7
MERGE
INSET
3 µm
3 µm
Late endosomes
MVBs
Amphisomes
Scr
Mfn1KD
dsDNA
HRS
MERGE
INSET
Late endosomes
Lysosomes
Autophagolysosomes
Scr
Mfn1KD
dsDNA
LAMP1
MERGE
INSET

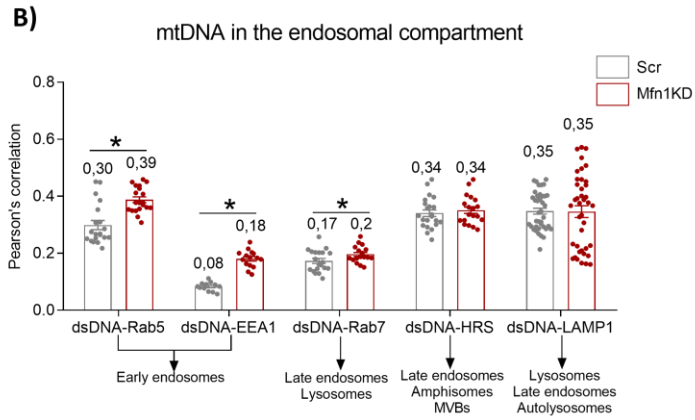

Figure 28: Co-distribution assessment between mtDNA and the endosomal compartment upon Mfn1 deficiency. A) Battery of immunofluorescences between mtDNA and different endosomal markers. B) Quantification of the Pearsons's correlation between mtDNA and each endosomal marker in control and Mfn1KD myoblasts**.** (n=20) Data represent mean ± SE. *p vs. Scr <0.05.

Based on these data, we hypothesized the molecular mechanisms promoting mtDNA localization in early endosomes: i) exocytosis and endocytosis of mtDNA[172], ii) mtDNA trafficking by MDVs.[173], iii) engulfment of mitochondria by early endosomes[174], iv) early endosome-mitochondria contacts and mtDNA transfer[192], or v) inclusion of $Rab5^{+}$ vesicles in mitochondria[193]. To narrow down the possible mechanisms implicated, we performed triple stainings of mtDNA (green), mitochondria (blue, using Mitotracker Deep Red or MTDR) and Rab5 or TLR9 (red), since the presence or absence of mitochondria in mtDNA-TLR9 or mtDNA-Rab5 contacts would implicate one mechanism or another. Subsequent 3D reconstruction of the images obtained with super-resolution microscopy showed that mtDNA-TLR9 and mtDNA-Rab5 contacts occur in the presence of mitochondria (Figure 29A-B).

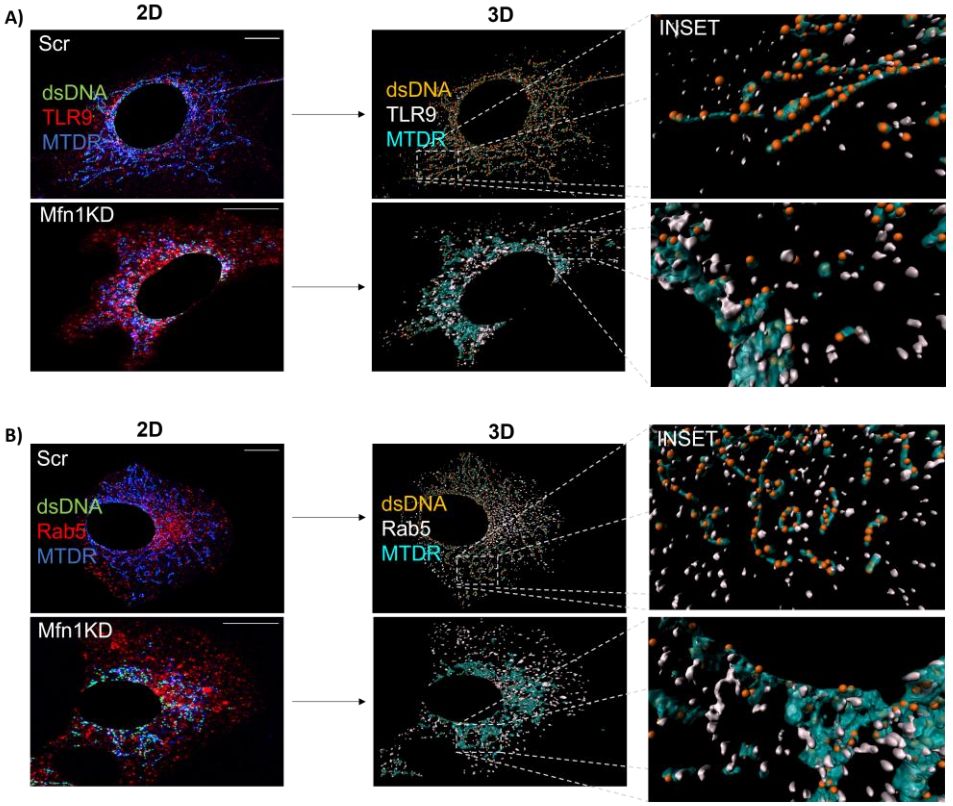

Figure 29: 3D reconstructions of triple immunostainings of control and Mfn1KD myoblasts. A) dsDNA-TLR9-mitochondria staining. B) dsDNA-Rab5-mitochondria staining.

In keeping with these data, quantification of the co-distribution between mitochondria and Rab5 or TLR9 in these triple stainings was increased in Mfn1KD myoblasts (Figure 30). These results suggest that exocytosis and endocytosis of mtDNA, as well as mtDNA trafficking by MDVs, are not feasible mechanisms for the trigger of TLR9-induced NFκB-mediated inflammation upon Mfn1 deficiency. This is due to the fact that these mechanisms would not require the presence of mitochondria in mtDNA-Rab5 or mtDNA-TLR9 contacts. Hence, we decided to further explore the relationship between early endosomes and mitochondria in the context of Mfn1 downregulation.

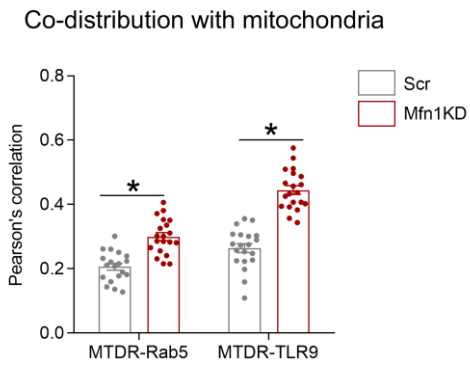

Figure 30: Quantification of the Pearson's correlation between mitochondria (MTDR) and Rab5 or TLR9. Quantification of the Pearsons's correlation between MTDR and Rab5 or TLR9. (n=20) Data represent mean ± SE. *p vs. Scr <0.05.

4.2.2 Nature of the relationship between early endosomes and mitochondria in Mfn1KD myoblasts

Early endosomes and mitochondria have been described to interact by engulfment of mitochondria by early endosomes[174], early endosome-mitochondria contacts[192], or inclusion of Rab5$^+$ vesicles in mitochondria[193]. In order to unravel whether either of these mechanisms could be contributing to the recognition of mtDNA by TLR9 upon Mfn1 deficiency, we performed immunogold assays by transmission electron microscopy, tagging mitochondria with SdhA (12nm) and early endosomes with Rab5 (18nm) in both control and Mfn1KD myoblasts. These assays showed that mitochondria and early endosomes appear to be more prone to establish physical contacts in Mfn1-deficient myoblasts (Figure 31A). Considering that juxtaposition between mitochondria and other membranous organelles, such as the ER, has been ranged from ≈10nm to ≈50nm[194], we quantified the distance between Rab5$^+$ endosomes and mitochondria in the immunogold images and the percentage of distances <30nm in each cell line. This analysis showed that the mean distance between Rab5$^+$ endosomes and mitochondria was of 150nm in control cells and

63nm in Mfn1KD cells (Figure 31B), among which 2,2% of the contacts present a distance <30nm in control cells and 46,5% in Mfn1KD cells (Figure 31C).

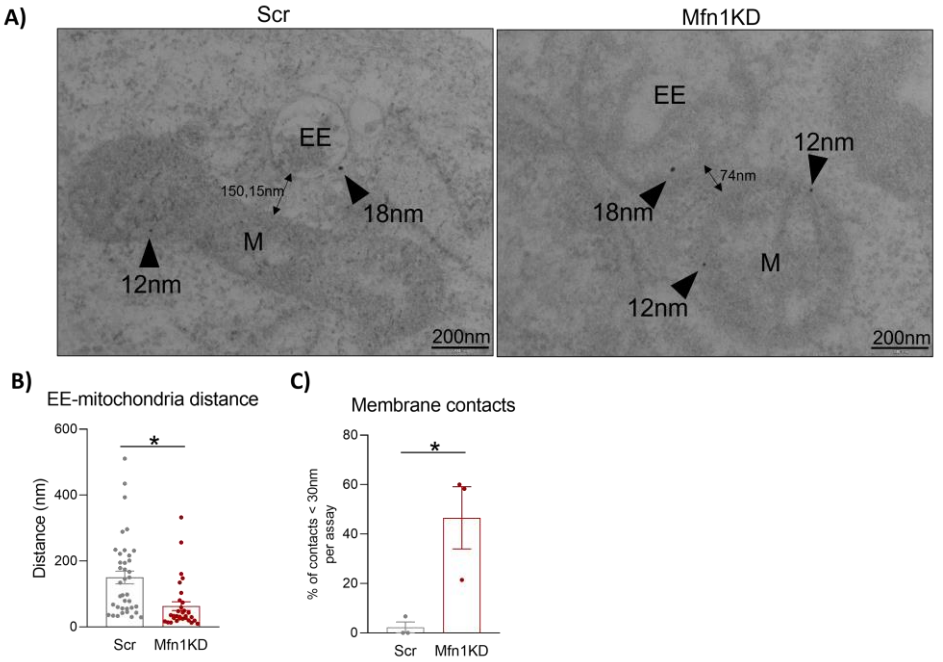

Figure 31: Visualization of the interaction between early endosomes and mitochondria. A) Immunogold assays of control and Mfn1KD myoblasts staining Rab5 (18nm) and Sdha (12nm) to mark early endosomes and mitochondria, respectively. B) Quantification of the distance between the marked organelles and C) percentage of distances <30nm per assay (n=31-38). Data represent mean ± SEM. *p<0.05 vs. Scr.

These results indicate that instead of incorporation of mitochondria in early endosomes, or vice versa, fragmented mitochondria and early endosomes stablish close contacts, possibly allowing the transfer of mtDNA to the lumen of early endosomes, where its recognition by TLR9 is promoted.

Mitochondria-endosome contacts and their protein interactors have been described to be involved in several cellular processes, including iron uptake and transfer to mitochondria[192], melanogenesis[195] or fusion of lysosomes to autophagosomes[196]. In fact, in these processes Mfn2 is the mitochondrial linker

to the endosomal compartment, thus, we hypothesized that upon Mfn1 deficiency, Mfn2 could be mediating the physical interaction between mitochondria and early endosomes. However, the identity of the early endosomal linker in this interaction remained undiscovered. Immunoprecipitation of endogenous Mfn2 followed by mass spectrometry analyses (IP-MS) in HeLa cells performed by Isabel Gordaliza-Alaguero suggested a potential list of Mfn2 interactors located in the endosomal compartment. Among the endosomal partners of Mfn2 obtained by IP-MS, Rab5C was the only early endosomal marker. In fact, Rab5C is a member of the Rab5 family and it resides in early endosomes[197]. Interestingly, we observed that protein levels of both Mfn2 and Rab5C were increased upon Mfn1 deficiency in myoblasts (Figure 32).

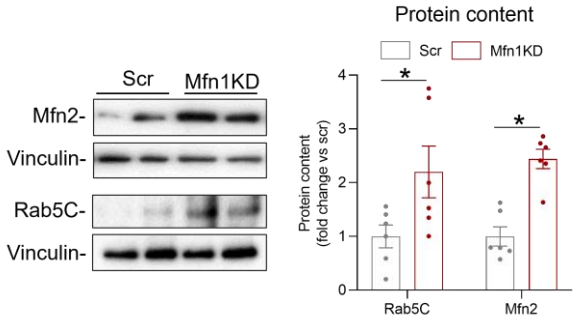

Figure 32: Protein abundance of Mfn2 and Rab5C upon Mfn1 deficiency. Representative immunoblot (n=6). Data represent mean ± SEM. *p<0.05 vs. Scr.

Thus, we decided to evaluate their interaction by immunoprecipitation assays. In keeping with the IP-MS data in HeLa cells, FLAG-RAB5C overexpression followed by FLAG immunoprecipitation in both control and Mfn1-deficient muscle cells revealed that Mfn2 and Rab5C interact, and that pulldown was strengthened upon Mfn1 deficiency (Figure 33). These results suggested an enhanced interaction between Mfn2 and Rab5C upon Mfn1 deficiency, which could be favoring the physical approximation of mitochondria and early endosomes in this context.

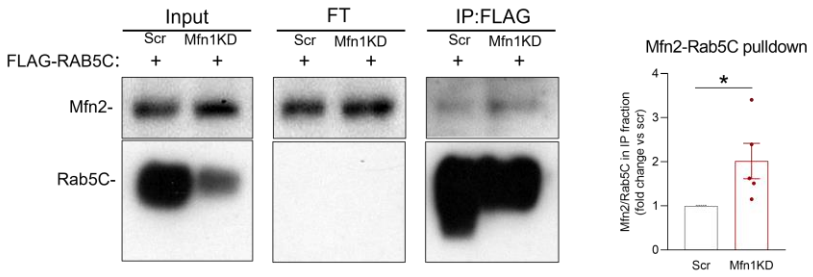

Figure 33: Immunoprecipitation of Mfn2 with Rab5C in FLAG-Rab5C expressing control and Mfn1KD myoblasts. Representative immunoblot and quantification of Mfn2 relative to Rab5C in the IP fraction per assay (n=5). Data represent mean ± SEM. *p<0.05 vs. Scr + FLAG-RAB5C

4.2.3 Biological impact of mitochondria-early endosomal contacts in Mfn1KD myoblasts

In order to assess the biological effect of this interaction, we performed functional assays and measured the activation of the NFκB-mediated inflammatory pathway. For that, we performed acute downregulation of Rab5C (Figure 34A-B) or Mfn2 (Figure 34C-D) in control and Mfn1-deficient myoblasts mediated by siRNA transfection.

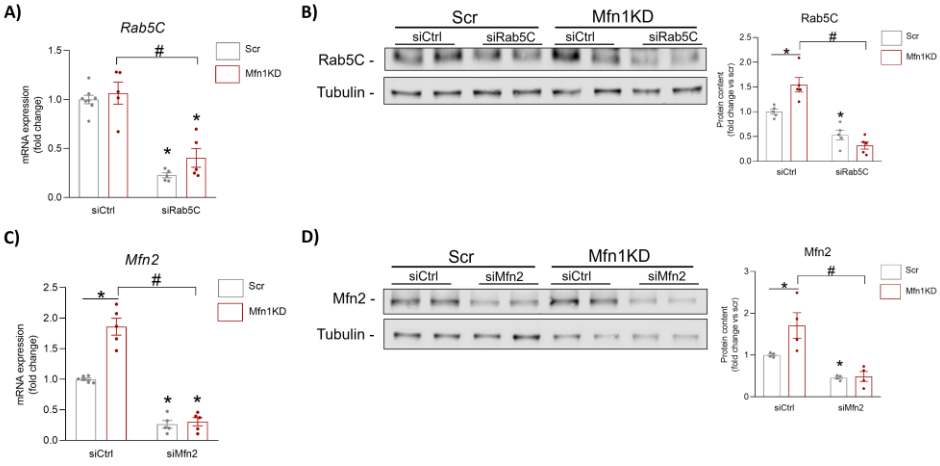

Figure 34: Validation of the acute downregulation of Rab5C or Mfn2. A) *Rab5C* mRNA and B) protein levels in control and Mfn1KD myoblasts upon delivery of a control siRNA or the *Rab5C*-targeting siRNA. C) *Mfn2* mRNA and D) protein levels in control and Mfn1KD myoblasts upon delivery of a control siRNA or the *Mfn2*-targeting siRNA. (n=4-6) Data represent mean ± SEM. *p<0.05 vs. Scr + siCtrl; #p<0.05 vs. KD + siCtrl.

Strikingly, attenuation of the interaction between Mfn2-Rab5C by downregulating any of them reduced the expression levels of NFκB target genes compared to Mfn1KD myoblasts transfected with a control siRNA (Figure 35A-B).

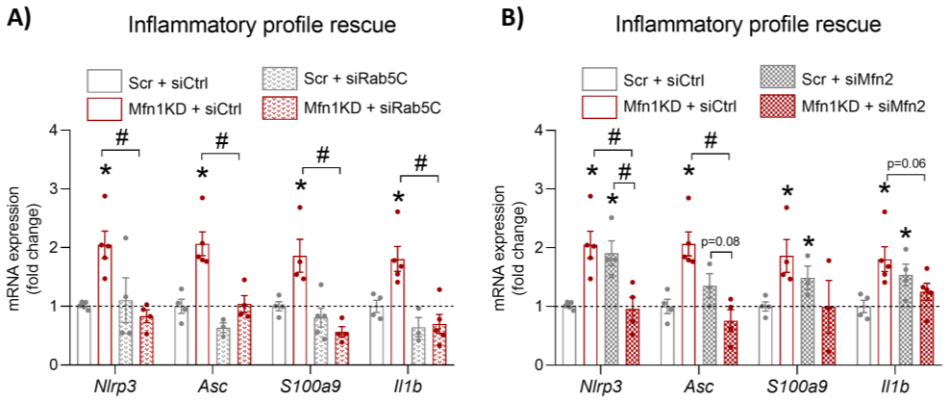

Figure 35: NFκB target gene expression. Inflammatory profile upon acute downregulation of A) *Rab5C* or B) *Mfn2* in control and Mfn1KD myoblasts. (n=4-6) Data represent mean ± SEM. *p<0.05 vs. Scr + siCtrl; #p<0.05 vs. KD + siCtrl.

In order to elucidate the role of the interaction of Mfn2 and Rab5C in allowing mtDNA-TLR9 engagement, we performed co-distribution assays between mtDNA (green) and TLR9 or EEA1 (red) upon Rab5C acute downregulation in control and Mfn1KD myoblasts. This analysis showed that the increased co-distribution between mtDNA and either TLR9 or EEA1 in Mfn1KD myoblasts transfected with a control siRNA was also normalized upon Rab5C deficiency (Figure 36). Thus, our data indicate that the interaction between Mfn2 and Rab5C is essential in promoting the engagement of mtDNA and TLR9, and therefore, the NFκB-mediated inflammation in Mfn1KD cells, since its abolishment completely rescues the phenotype.

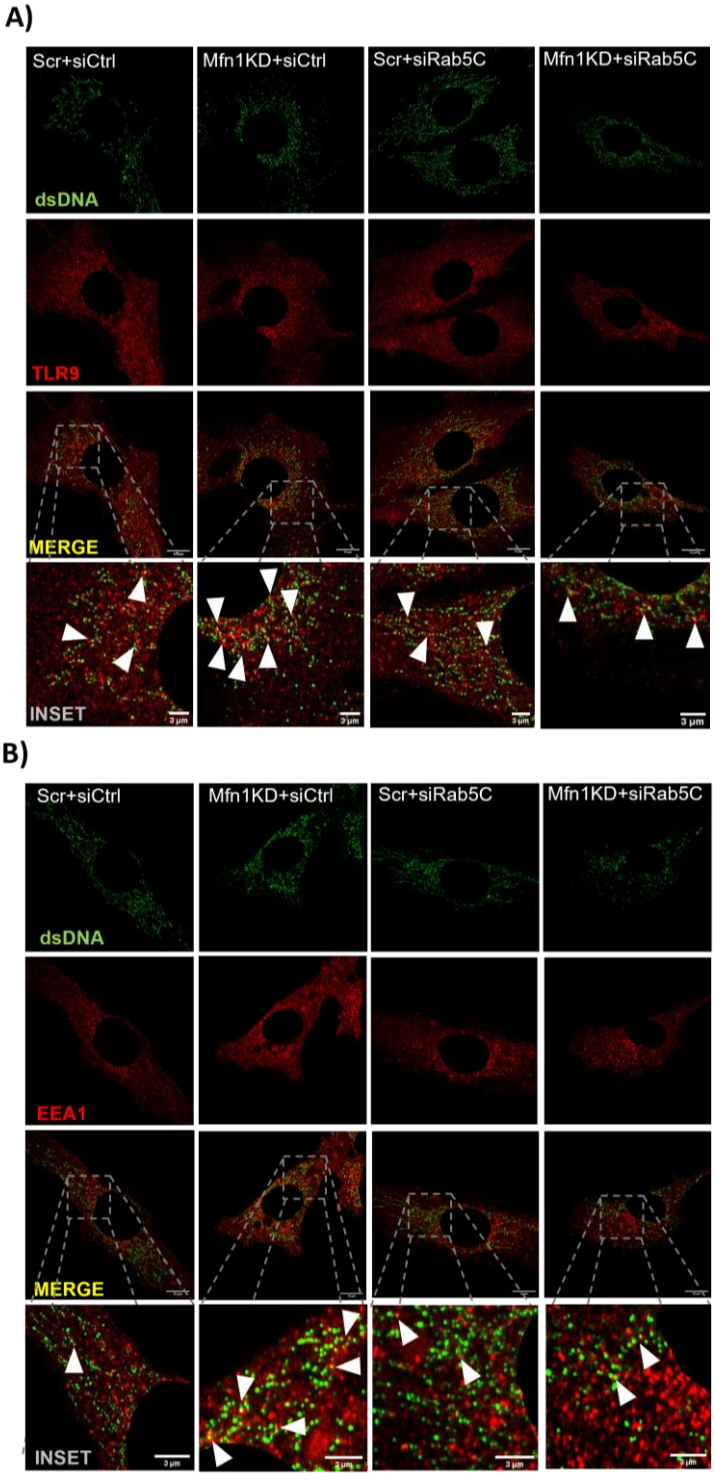
A)
Scr+siCtrl
Mfn1KD+siCtrl
Scr+siRab5C
Mfn1KD+siRab5C
dsDNA
TLR9
MERGE
INSET
B)
Scr+siCtrl
Mfn1KD+siCtrl
Scr+siRab5C
Mfn1KD+siRab5C
dsDNA
EEA1
MERGE
INSET

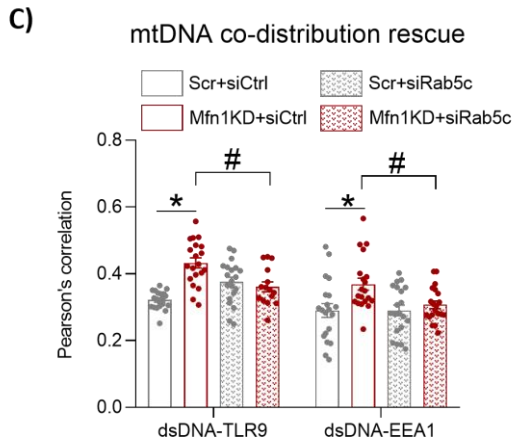

Figure 36: Effects of Rab5C acute downregulation on the co-distribution between mtDNA and TLR9 or EEA1. Immunofluorescence of mtDNA with A) TLR9 or B) EEA1. C) Quantification of the Pearson's correlation. (n=20) Data represent mean ± SEM. *p<0.05 vs. Scr + siCtrl; #p<0.05 vs. KD + siCtrl.

So far, we have observed that Mfn1 deficiency favors close contacts between early endosomes and mitochondria, which are promoted by the interaction between Mfn2 and Rab5C. In these conditions, we hypothesized that mtDNA sequences are transferred from mitochondria to early endosomes through pores, similar to processes described in the transfer of iron among the same organelles[192]. In fact, Das *et al.* 2016 characterized the duration and motility of the contacts between early endosomes and mitochondria in the events of iron transfer, and proposed VDAC pores as docking complexes allowing iron transfer between these organelles[192]. Bearing also in mind the implication of VDAC pores – and not Bax-Bak pores - in the exit of mtDNA from mitochondria to the cytosol in Yme1LKD myoblasts[55,167], we assessed whether this mechanism could also be implicated in the transfer of mtDNA in mitochondria-early endosome contacts upon Mfn1KD deficiency. Nonetheless, inhibition of oligomerization of VDAC pores by treating Mfn1KD myoblasts with VBIT-4[198] showed no conclusive effects

in the expression levels of NFκB target genes compared to DMSO-treated Mfn1KD myoblasts (Figure 37), suggesting that other pore-forming proteins or other mechanisms could be involved in this process.

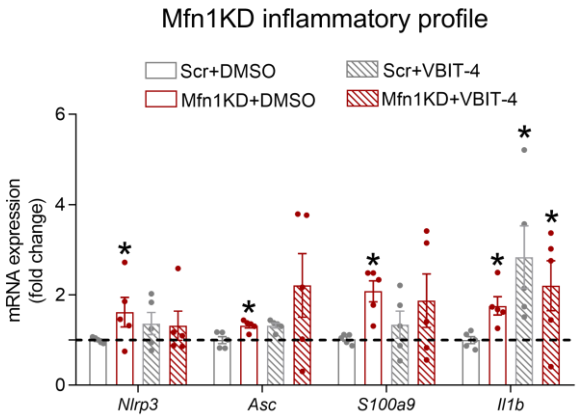

Figure 37: Inflammatory profile of Mfn1KD myoblast upon VBIT-4 treatment. (n=5) Data represent mean ± SEM. *p<0.05 vs. Scr+DMSO.

All in all, we have described that mitochondrial fragmentation induced by Mfn1 downregulation in myoblasts promotes TLR9-mediated NFκB-dependent inflammation, due to the establishment of mitochondria-early endosome contacts. These contacts are promoted by the newly described interaction between Mfn2 and Rab5C, which has proven to be key in mediating the recognition of mtDNA by TLR9 in Mfn1KD myoblasts (Figure 38).

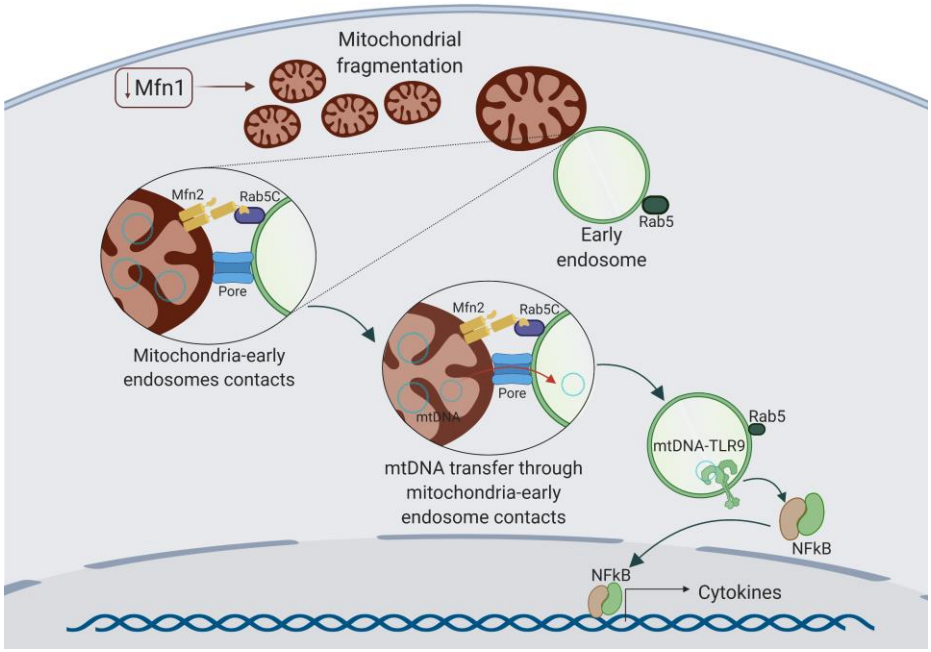

Figure 38: Working model of the molecular mechanisms linking Mfn1 downregulation and NFκB inflammation in myoblasts. Fragmented mitochondria in Mfn1-deficient myoblasts form close contacts with early endosomes, which are mediated by the newly described interaction between Mfn2 and Rab5C. Through putative pores, mtDNA is shuttled from mitochondria to the lumen of early endosomes, resulting in its recognition by TLR9 and subsequent NFκB activation.

Study III: Skeletal muscle health and performance upon Mfn1 ablation

The role of mitochondrial dynamics in maintaining muscle health has been widely described. In fact, *in vivo* models ablated from Opa1[51,53], Mfn2[19], Fis1[70] or Drp1[65,66], as well as double ablation of Mfn1 and Mfn2[199], in the skeletal muscles develop muscle health complications, including muscle atrophy[19,51,65,66], impaired mitophagy[19,70], systemic inflammation[51,53] or muscle denervation[66]. However, the impact of Mfn1 ablation in skeletal muscles remains unexplored.

To address this, we generated a conditional *Mfn1* knockout (KO) mouse model, crossing transgenic mice expressing a tamoxifen-inducible Cre-recombinase under the promoter of human skeletal actin (HSA), with mice containing floxed

sequences in exon 4 of *Mfn1* gene. As a result, the tamoxifen-inducible skeletal muscle-specific Mfn1KO (SkM-Mfn1KO) mice and the Cre-negative littermates (LoxP) were generated. To induce Cre expression, mice were fed with tamoxifen-enriched diet for 2 weeks at 12 weeks of age, after which chow diet was used for 2 weeks to allow proper tamoxifen washout. This method to induce Cre expression proved to be efficient in the ablation of Mfn1 exclusively in skeletal muscles (Figure 39A-C), which persisted even 12 months since induction (Figure 40).

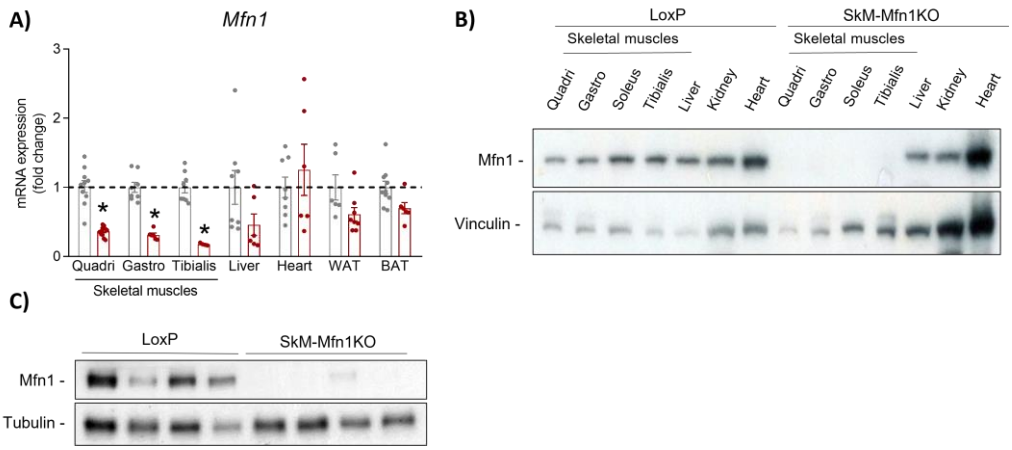

Figure 39: Validation of *Mfn1* expression in the *in vivo* model. LoxP and SkM-Mfn1KO mice 2 weeks after tamoxifen treatment. A) *Mfn1* mRNA levels in in different tissues. B) Mfn1 protein levels in different tissues. C) Mfn1 protein levels in quadriceps muscles. (n=4-8) Data represent mean ± SEM. *p<0.05 vs. LoxP.

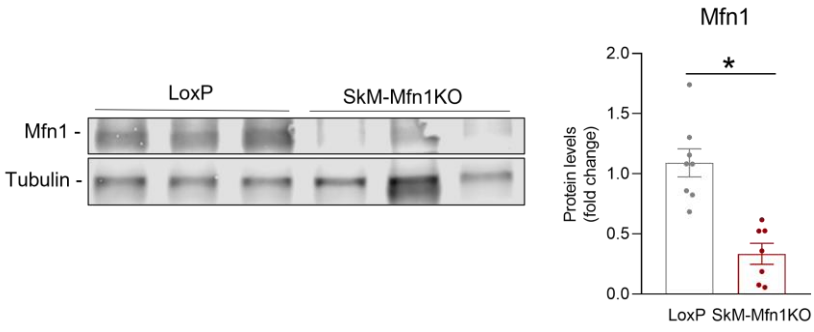

Figure 40: Mfn1 protein levels in quadriceps muscles. LoxP and SkM-Mfn1KO mice 12 months after tamoxifen treatment. (n=7-9) Data represent mean ± SEM. *p<0.05 vs. LoxP.

4.3.1 Metabolic and muscle health characterization of SkM-Mfn1KO mice

It has been widely described that altered mitochondrial dynamics in different tissues result in a number of metabolic outcomes[200]. In regard to the characterization of tissue-specific ablation of Mfn1, few studies have reported the use of Mfn1KO animals, which include Kulkarni *et al.* 2016, Papanicolaou *et al.* 2011 and Ramírez *et al.* 2017, using Mfn1KO models in liver[37], heart[39] and proopiomelanocortin (POMC) neurons[38], respectively. Alike these studies, evaluation of the mitochondrial morphology in skeletal muscles using transmission electron microscopy validated the presence of fragmented mitochondria in SkM-Mfn1KO mice compared to LoxP (Figure 41).

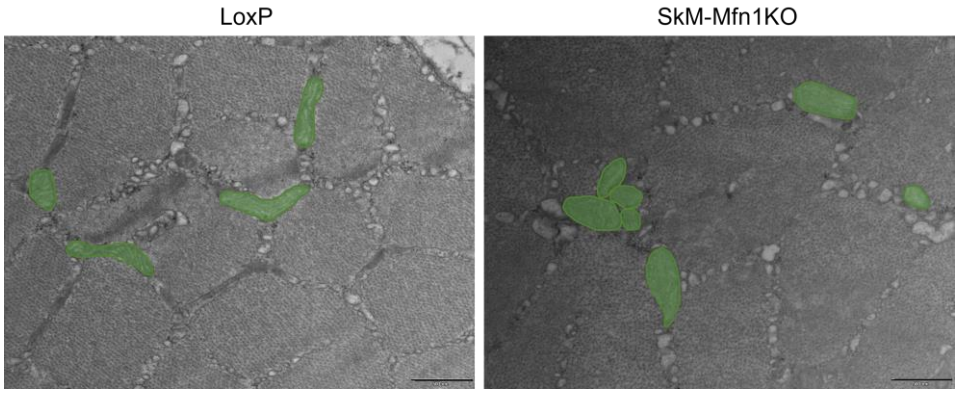

Figure 41: Evaluation of the mitochondrial morphology by TEM. Transversal sections of quadriceps muscles from LoxP and SkM-Mfn1KO mice 4 weeks after tamoxifen treatment. Mitochondria are highlighted in green. (n=3 mice per group and sex, 20 images per mouse).

Regarding the metabolic outcomes of Mfn1 ablation in the skeletal muscle, we performed an extensive metabolic phenotyping in these mice. First, similar to the liver-specific Mfn1KO model (L-Mfn1KO), SkM-Mfn1KO mice – both male and female – exhibited unchanged body weight (Figure 42A) and food intake (Figure 42B), as well as fat and lean mass (Figure 42C), after 2 months of inducing Mfn1 depletion.

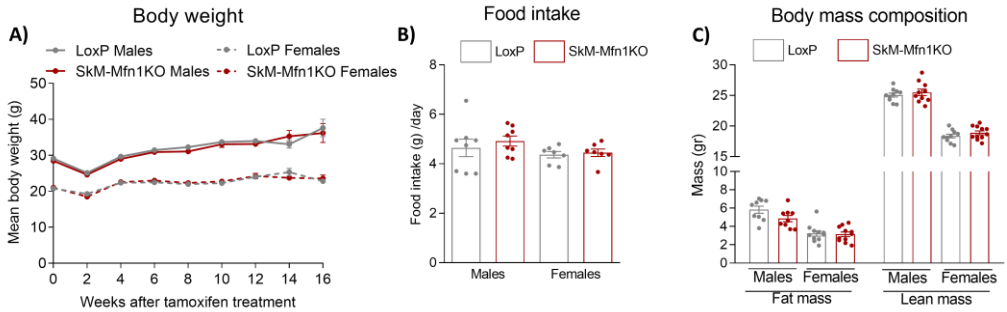

Figure 42: Body weight and mass, and food intake evaluation. A) Body weight monitorization since the initiation of the tamoxifen treatment. B) Food intake and C) body mass composition assessments 5 weeks after tamoxifen treatment. (n=8-20) Data represent mean ± SEM. *p<0.05 vs. LoxP.

Next, we evaluated the glucose metabolism in these mice. Whereas male SkM-Mfn1KO showed improved glucose tolerance while basal insulin levels and insulin tolerance remained unaltered compared to their LoxP littermates (Figure 43A-C), glucose and insulin tolerance tests revealed no changes in female SkM-Mfn1KO mice (Figure 44A-B).

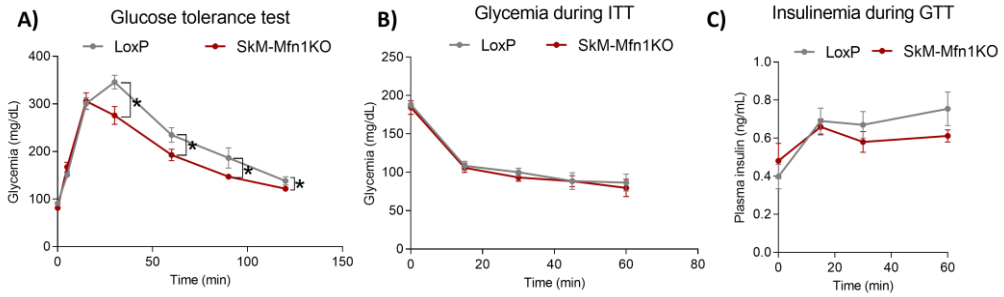

Figure 43: Assessment of the glucose metabolism in male mice. A) Glucose and B) insulin tolerance tests. C) Plasma insulin levels during glucose tolerance test (GTT) in male mice. Studies were performed 4 weeks after tamoxifen treatment. (n=6-11) Data represent mean ± SEM. *p<0.05 vs. LoxP.

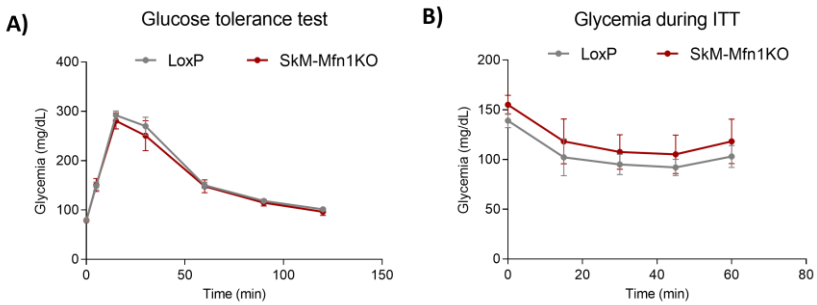

Figure 44: Assessment of the glucose metabolism in female mice. A) Glucose and B) insulin tolerance tests. Studies were performed 4 weeks after tamoxifen treatment. (n=4-5) Data represent mean ± SEM. *p<0.05 vs. LoxP.

Furthermore, *in vivo* indirect calorimetry analyses showed that total energy expenditure in both males and females remained unchanged between genotypes (Figure 45A-B). Strikingly, we observed a remarkable increase in the energy expenditure in females compared to males, regardless of their genotype (Figure 45C).

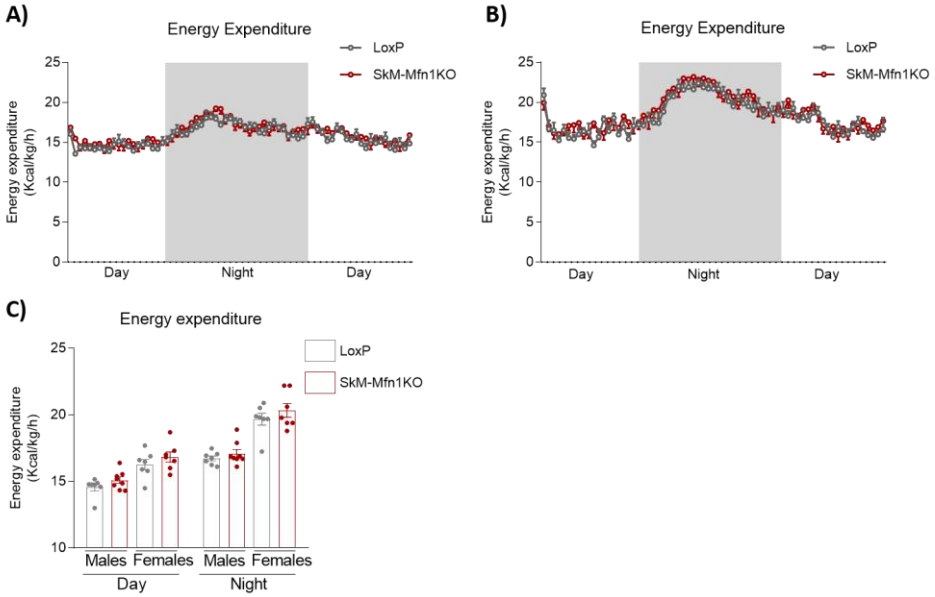

Figure 45: Energy expenditure assessment. Energy expenditure in A) males and B) females during the day. C) Mean energy expenditure. Study performed 6 weeks after tamoxifen treatment. (n=7-8) Data represent mean ± SEM.

These studies also allow evaluation of the substrate utilization. Detailed analyses of glucose and lipid oxidation fluxes show that male SkM-Mfn1KO mice presented increased utilization of glucose especially during feeding conditions (during the night), and decreased utilization of lipids compared to their LoxP littermates (Figure 46A-B). These data are reflected in a significant increase in the mean respiratory exchange ratio (RER) (Figure 46C-D). Hence, these data indicate that male mice exhibit metabolic adaptations favoring glucose metabolism upon muscle Mfn1 depletion.

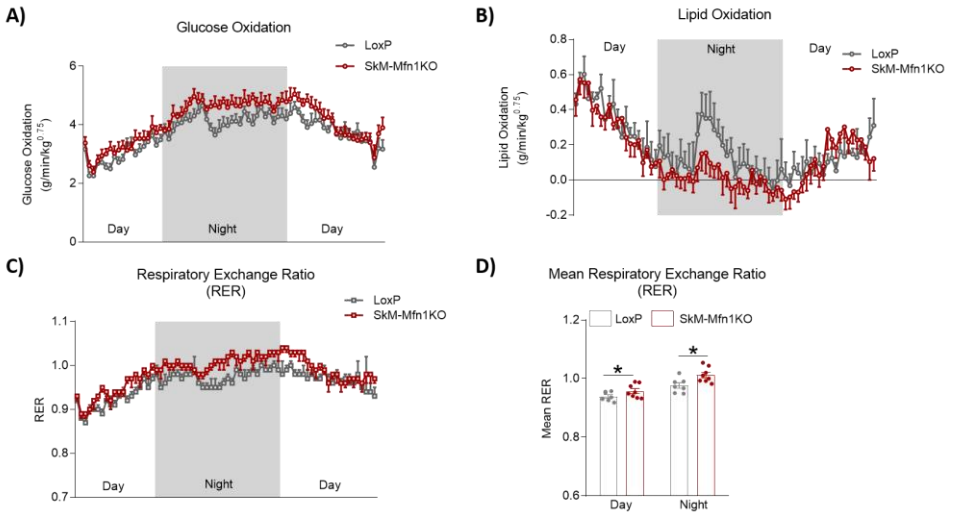

Figure 46: Substrate utilization in male mice. Oxidation of A) glucose and B) lipids. C) Respiratory exchange ratio and D) mean respiratory exchange ratio. Study performed 6 weeks after tamoxifen treatment. (n=8) Data represent mean ± SEM. *p<0.05 vs LoxP.

On the contrary to males, female SkM-Mfn1KO showed the opposite phenotype: we observed an increased utilization of lipids during both night and day, accompanied by a reduced glucose oxidation (Figure 47A-B). These results are also reflected as a decrease in the RER (Figure 47C-D). These data indicate that Mfn1 ablation in female mice favors lipid metabolism, while male mice show the opposite effect.

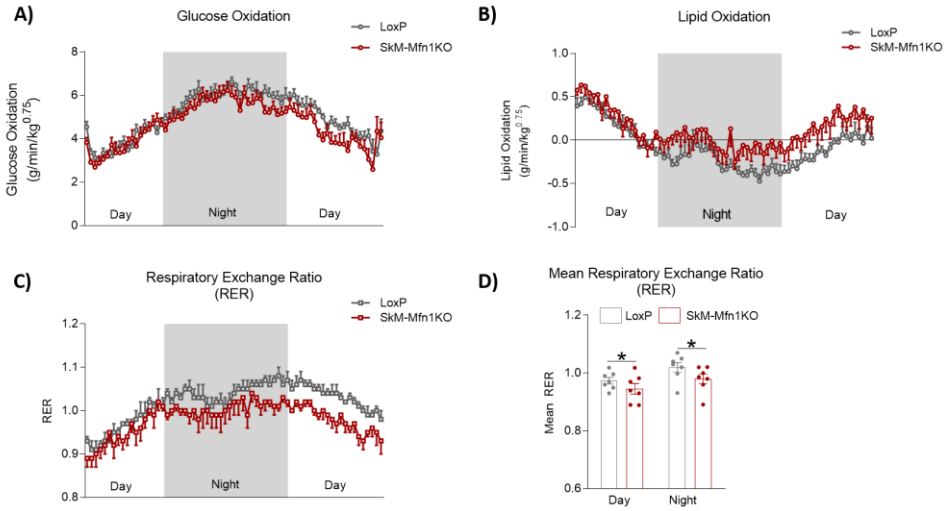

Figure 47: Substrate utilization in female mice. Oxidation of A) glucose and B) lipids. C) Respiratory exchange ratio and D) mean respiratory exchange ratio. Study performed 6 weeks after tamoxifen treatment. (n=7) Data represent mean ± SEM. *p<0.05 vs LoxP.

Taken together, our results show that substrate utilization is altered upon skeletal muscle Mfn1 ablation in a sex-dependent manner. With the aim of identifying whether these distinct metabolic adaptations to muscle Mfn1 depletion were due to altered mitochondrial respiration in muscle, we performed *ex vivo* high-resolution mitochondrial respirometry analyses in permeabilized muscle fibers from tibialis. These studies showed a trend to decreased mitochondrial respiration upon Mfn1 ablation in both sexes, although these effects were not statistically significant (Figure 48A-B). These data contradict the fact that Mfn1KD myoblast exhibit increased mitochondrial respiration, as well as isolated mitochondria from L-Mfn1KO mice[37] or POMC neuron-enriched samples from POMC-specific Mfn1KO mice[38].

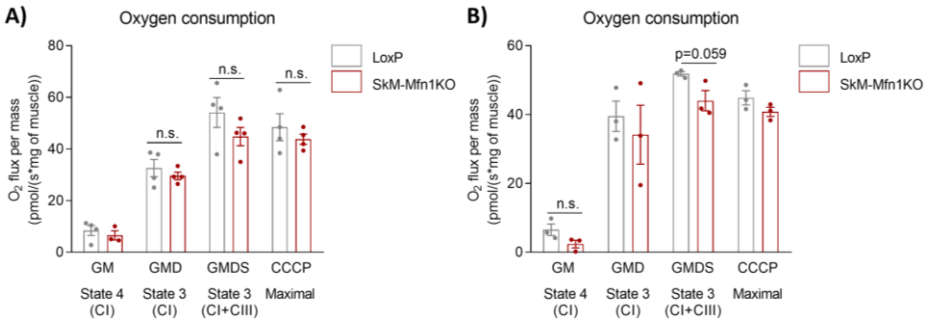

Figure 48: Mitochondrial respiration in permeabilized muscle fibers. Data of A) males and B) females. (GM = glutamate + malate; GMD = glutamate + malate + ADP; GMDS = glutamate + malate + ADP + succinate). Study performed 8 weeks after tamoxifen treatment. (n=3-4) Data represent mean ± SEM. *p<0.05 vs. LoxP.

Thus, our data indicate that sex-specific mechanisms, that are independent of primary alterations in muscle mitochondrial function, have an impact in the development of metabolic adaptations to the depletion of skeletal muscle Mfn1.

To characterize the impact of Mfn1 ablation in skeletal muscle health, several muscle parameters were assessed. First, fiber typing in gastrocnemius (mixed muscle) and soleus (red muscle) was performed. In fact, Mishra *et al*. 2015[201] described that low mitochondrial fusion rates are associated to more glycolytic or white fibers (types IIb and IIx), whereas high mitochondrial fusion rates link to more oxidative or red fibers (types I and IIa) (Figure 49).

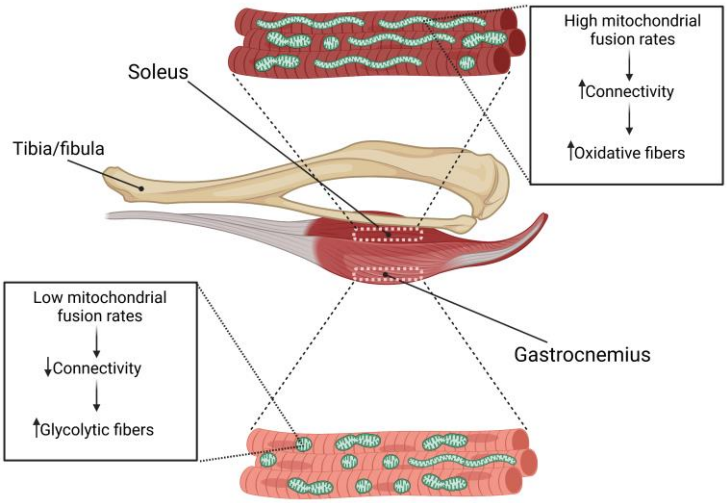

Figure 49: Schematic representation of the association between mitochondrial connectivity and fiber typing in skeletal muscles, adapted from Mishra *et al* 2015[201].

This distinction is also related to the fact that red fibers are considered slow-twitch fibers that support fatigue resistance, while white fibers are considered fast-twitch fibers that support power and force. Due to different expression levels of the isoforms of the myosin heavy chains in each fiber type, performing immunofluorescence assays in skeletal muscles allows fiber typing characterization. Our analyses suggest that, although a tendency to reduced number of red fibers and increased number of white fibers was observed in gastrocnemius of SkM-Mfn1KO mice compared to LoxP mice, a significant switch in the same direction was appreciated in soleus of SkM-Mfn1KO mice (Figure 50).

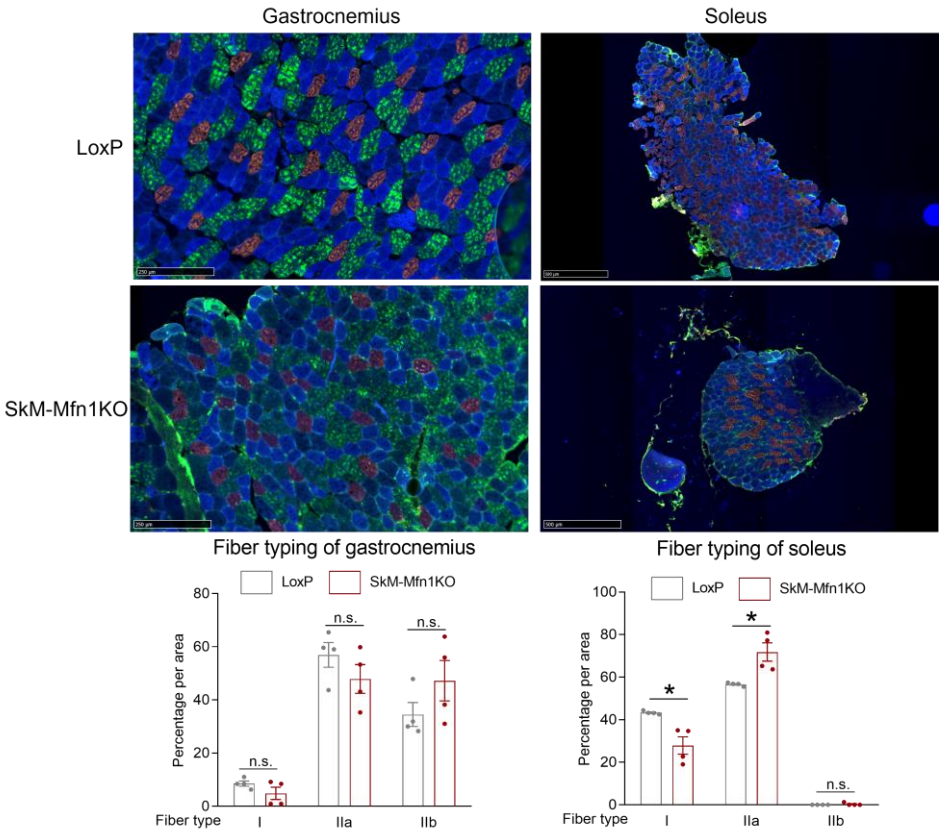

Figure 50: Fiber typing characterization. Gastrocnemius and soleus muscles sections of male LoxP and SkM-Mfn1KO mice 8 weeks after tamoxifen treatment. Fiber type I (red), fiber type IIa (blue), fiber type IIb (green). (n=4) Data represent mean ± SEM. *p<0.05 vs. LoxP.

These data corroborate the fact that decreased mitochondrial connectivity associates to increased contribution of white fibers especially in red muscles, as described by Mishra *et al*. 2015[201].

Next, we determined the development of muscle atrophy by different quantitative approaches, including muscle mass, cross-sectional area (CSA) of muscle fibers, plasma creatine kinase (CK) activity, atrophy-related gene (atrogene) expression and fibroblast growth factor 21 (FGF21) response.

Evaluation of the muscle mass revealed unchanged muscle weights in both male and female SkM-Mfn1KO mice compared to their LoxP littermates (Figure 51).

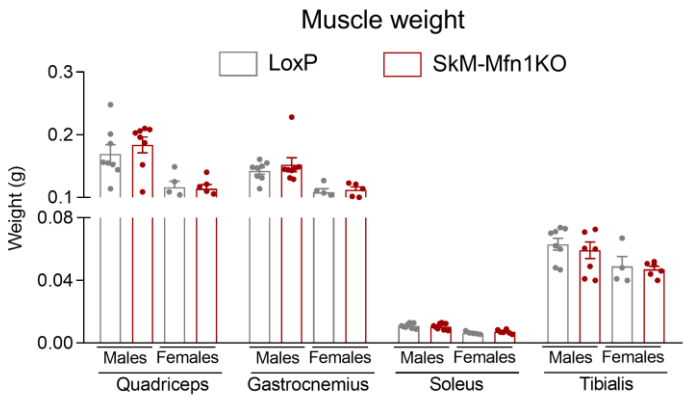

Figure 51: Muscle mass measurement. Study performed 6-8 weeks after tamoxifen treatment. (n=4-8) Data represent mean ± SEM.

However, histological analysis of the fiber size in gastrocnemius showed a 50% decrease in the CSA of male SkM-Mfn1KO and a 30% decrease in females compared to LoxP mice (Figure 52), suggesting muscle damage upon Mfn1 depletion.

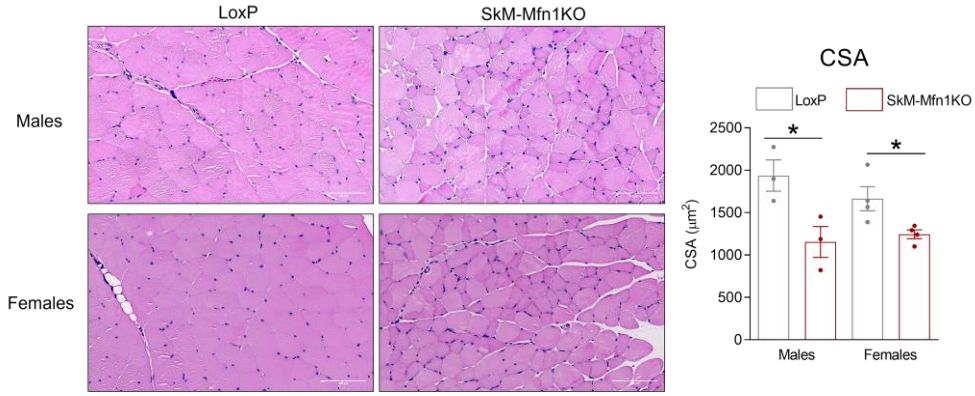

Figure 52: Quantification of the CSA. Characterization of the muscle fibers by hematoxylin-eosin staining in transversal sections of gastrocnemius muscles 8 weeks after tamoxifen treatment (n=3 mice per genotype, 300 fibers per mouse). Data represent mean ± SEM. *p<0.05 vs. LoxP.

The presence of muscle damage was corroborated by increased plasma CK activity in both male and female SkM-Mfn1KO mice (Figure 53). Nevertheless, expression levels of atrogenes in quadriceps of male mice remained unaltered within genotypes (Figure 54). Strikingly, muscle mRNA levels, as well as plasma levels, of the stress myokine FGF21 were increased in both male and female mice, although female SkM-Mfn1KO mice only showed statistical significance in muscle *Fgf21* expression (Figure 55A-B). In fact, the FGF21 response to Mfn1 ablation could be affecting not only the degree of the muscle atrophy, but also the metabolic alterations observed previously. Altogether, the evaluation of muscle atrophy-related parameters confirmed the development of muscle damage upon Mfn1 ablation.

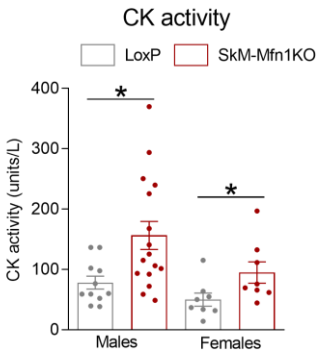

Figure 53: Measurement of plasma CK activity. Study performed 6 weeks after tamoxifen treatment. (n=6-16) Data represent mean ± SEM. *p<0.05 vs. LoxP.

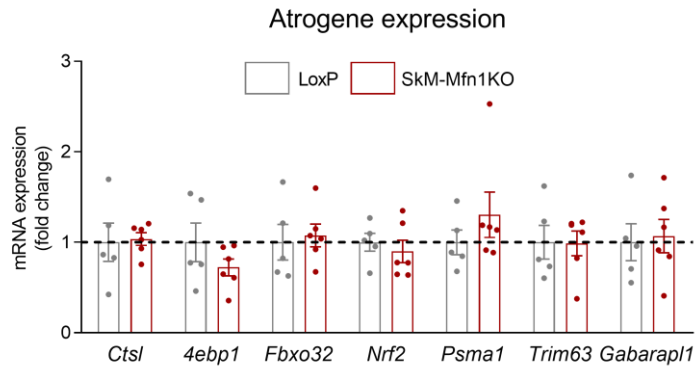

Figure 54: Atrogene expression. mRNA levels of atrogenes in quadriceps muscles of male mice 8 weeks after tamoxifen treatment**.** (n=5-6) Data represent mean ± SEM.

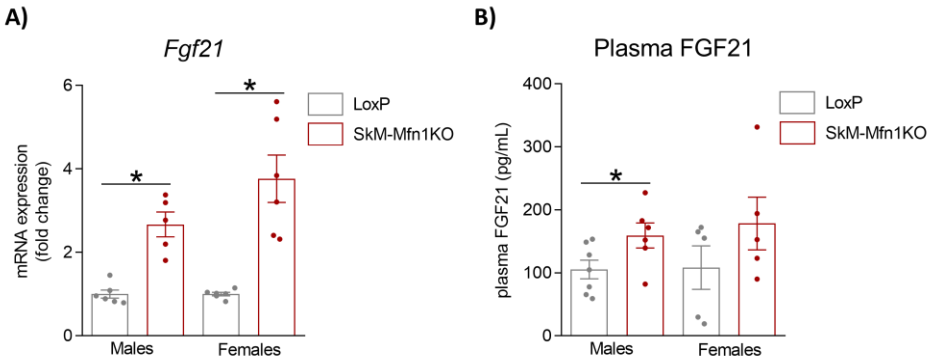

Figure 55: FGF21 response. A) mRNA expression levels of *Fgf21* in quadriceps muscles. B) Plasma FGF21 levels. Studies performed 6-8 weeks after tamoxifen treatment. (n=5-7) Data represent mean ± SEM. *p<0.05 vs. LoxP.

In conclusion, our data indicate that ablation of Mfn1 in the skeletal muscle of mice promotes changes in fiber typing in mixed and red muscles, as well as sex-dependent metabolic responses. Moreover, decreased CSA accompanied by increased CK activity and muscle FGF21 secretion are markers of muscle atrophy development, therefore suggesting that Mfn1 deficiency in the skeletal muscle triggers mechanisms leading to muscle atrophy.

4.3.2 Muscle inflammation and exercise performance of SkM-Mfn1KO mice

To further characterize the effects of Mfn1 depletion in skeletal muscles and to validate the results related to the trigger of inflammation upon Mfn1 deficiency in myoblasts, we evaluated the presence of muscle inflammation in SkM-Mfn1KO mice. For that, we first analyzed the expression levels of NFκB target genes (Figure 56A and C) and type I IFN response genes (Figure 56B and D) in quadriceps of both male and female mice. As observed in the *in vitro* model, Mfn1 deficiency triggers NFκB-driven inflammation in skeletal muscles, and not the type I IFN response.

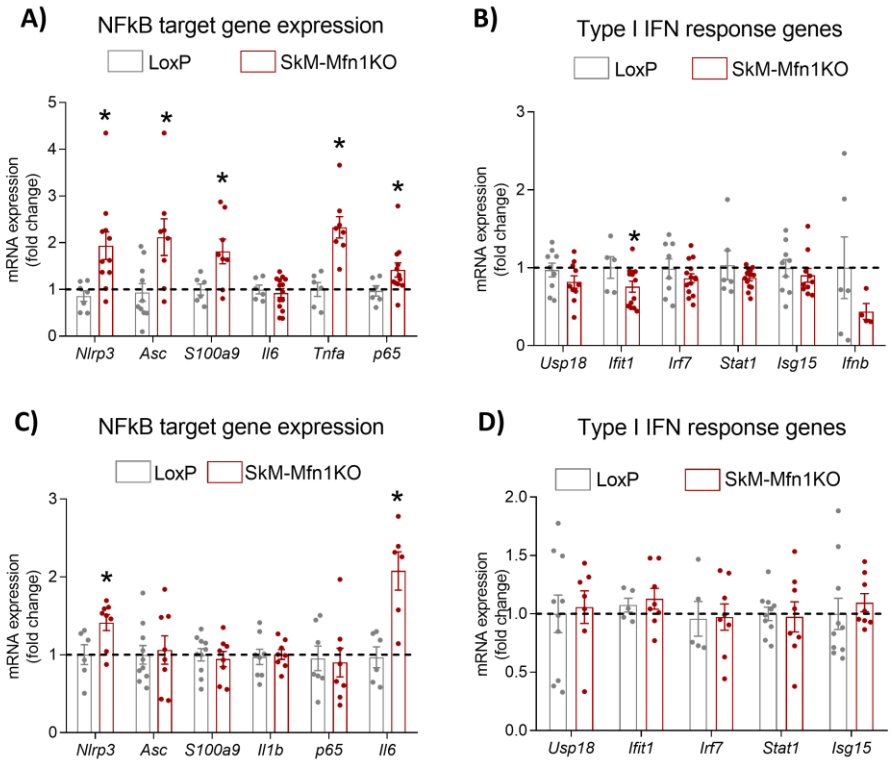

Figure 56: Assessment of inflammatory gene expression. A) NFκB target gene expression in males. B) Type I IFN response gene expression in males. C) NFκB target gene expression in females. D) Type I IFN response gene expression in females. Study performed 8 weeks after tamoxifen treatment. (n=6-10) Data represent mean ± SEM. *p<0.05 vs. LoxP.

Nonetheless, we observed that the profile of expression of NFκB target genes differs from male to female SkM-Mfn1KO mice, which could be explained by intrinsic sex-dependent mechanisms that modulate the extend of the inflammatory response. For this reason, we chose to use only male mice in the following experiments to further characterize the impact of Mfn1 ablation in the development of muscle inflammation.

To evaluate the extend of the muscle inflammatory response, we assessed the presence of systemic inflammation by three approaches: immunohistochemistry of IL1β and the macrophage marker F4/80 in gastrocnemius muscles, expression

levels of macrophage markers in quadriceps muscles, and plasma levels of the pro-inflammatory cytokines IL6 and TNFα. The immunohistochemistry assays did not show increased presence of IL1β or F4/80 staining in SkM-Mfn1KO compared to LoxP mice (Figure 57), which was corroborated by unaltered expression levels of macrophage markers in muscles (Figure 58), suggesting the absence of immune cell infiltration upon Mfn1 ablation in this tissue.

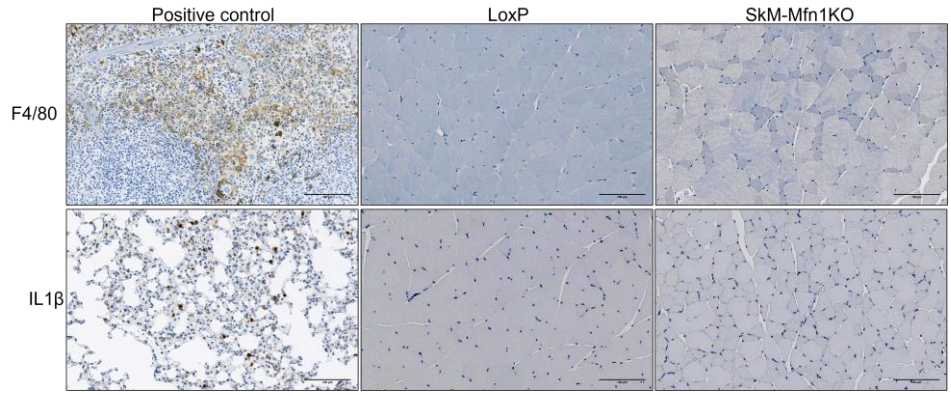

Figure 57: Macrophage infiltration assessment in muscles. Immunohistochemistry of gastrocnemius muscle sections from male LoxP and SkM-Mfn1KO mice against macrophage marker F4/80 (positive control is spleen) or IL1β (positive control is lung) 8 weeks after tamoxifen treatment. (n=4 per genotype)

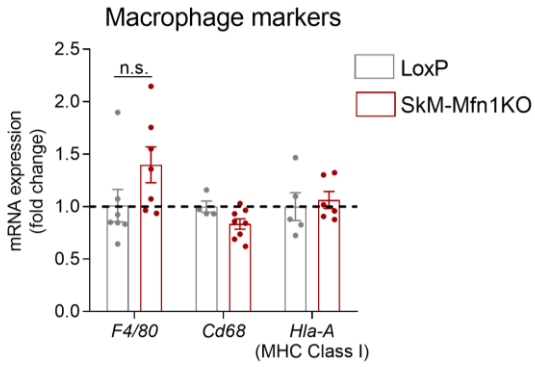

Figure 58: Gene expression of macrophage markers. mRNA levels of macrophage markers in quadriceps muscles of male mice 8 weeks after tamoxifen treatment. (n=5-6) Data represent mean ± SEM.

Furthermore, plasma levels of the pro-inflammatory cytokines IL6 and TNFα remained unchanged (Figure 59), indicating that the NFκB-driven inflammation

observed at muscle gene expression level remains local and does not trigger systemic inflammatory effects.

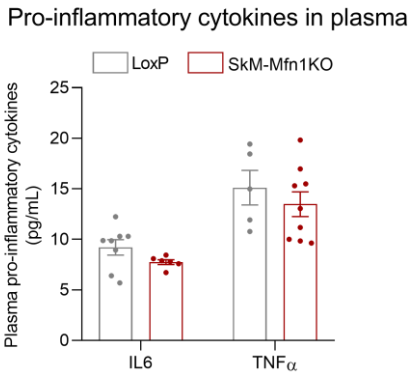

Figure 59: Plasma IL6 and TNFα levels. Studies performed in male mice 4 weeks after tamoxifen treatment. (n=5-9) Data represent mean ± SEM.

To assess the origin of the NFκB-mediated inflammation observed and to corroborate the data related to Mfn1KD in myoblasts, we treated mice with a single intraperitoneal injection (IP) of the antagonist of TLR9, ODN2088[190]. Forty-eight hours after IP injection, the expression levels of NFκB target genes were rescued in SkM-Mfn1KO mice compared to SkM-Mfn1KO injected with endotoxin-free water (Figure 60B). Thus, these results demonstrate that the NFκB-dependent inflammation triggered by Mfn1 deficiency in skeletal muscles is TLR9-mediated, which phenocopies the effects observed in Mfn1KD myoblasts.

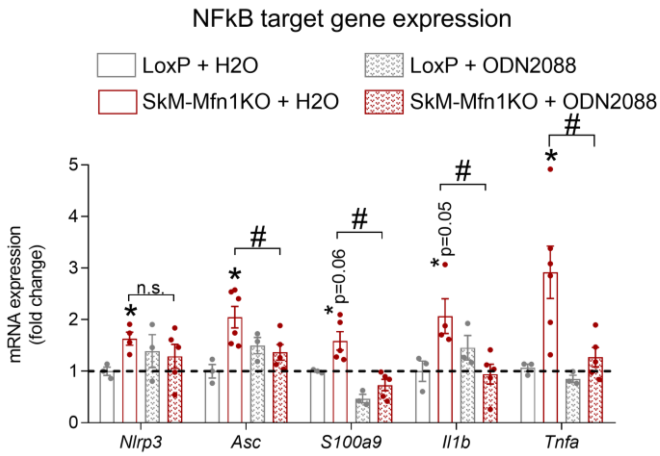

Figure 60: The involvement of TLR9 in the inflammatory response of SkM-Mfn1KO mice. NFκB target gene expression in quadriceps muscles of male mice upon acute ODN2088 administration 8 weeks after tamoxifen treatment. (n=3-6) Data represent mean ± SEM. *p<0.05 vs. LoxP+H2O; #p<0.05 vs. KO+H2O.

Considering the development of muscle atrophy and inflammation upon Mfn1 ablation and with the aim of assessing their potential physiological outcomes, we evaluated the physical performance of SkM-Mfn1KO mice, by subjecting them to two consecutive rounds of exercise on a treadmill until exhaustion (Figure 61).

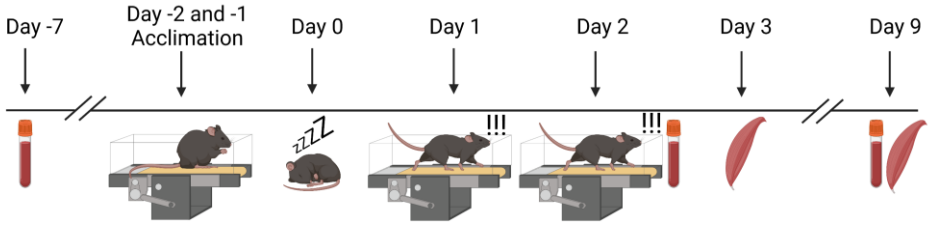

Figure 61: Treadmill test protocol. (See *section 7.2.1.8* for further details).

Despite SkM-Mfn1KO and their LoxP littermates did not present differences in their physical performance at day 1 of trial, interestingly, a decrease in the distance run at day 2 was observed in SkM-Mfn1KO compared to LoxP littermates (Figure 62A-B). These data may suggest that the tissue repair mechanisms triggered upon exercise-induced damage could be impaired in SkM-

Mfn1KO mice, which could prevent them from performing as their LoxP littermates at day 2.

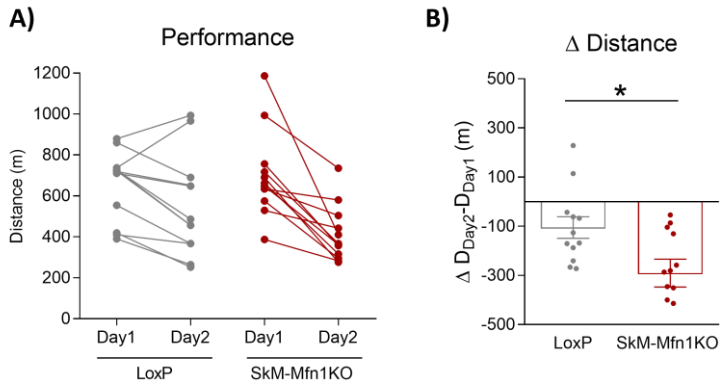

Figure 62: Physical performance assessment. Study performed 6 weeks after tamoxifen treatment. A) Distance run at day 1 and day 2 per mouse. B) Difference in the distance run from day 2 to day 1 per mouse. (n=11-12) Data represent mean ± SEM. *p<0.05 vs. LoxP.

To further characterize the effects of exercise, we focused on IL6, since this cytokine is physiologically secreted by the skeletal muscle upon exercise[202,203]. Hence, we assessed whether the inflammation present in muscles of SkM-Mfn1KO mice in resting conditions could exacerbate the IL6 response to exercise. Quantification of *Il6* mRNA levels in quadriceps and plasma levels of IL6 one day and seven days after the end of the trial showed that SkM-Mfn1KO mice indeed present increased muscle IL6 production and secretion upon exercise (Figure 63A-B). This could be a major driver of the impairment of tissue repair mechanisms and reduced physical performance in SkM-Mfn1KO mice.

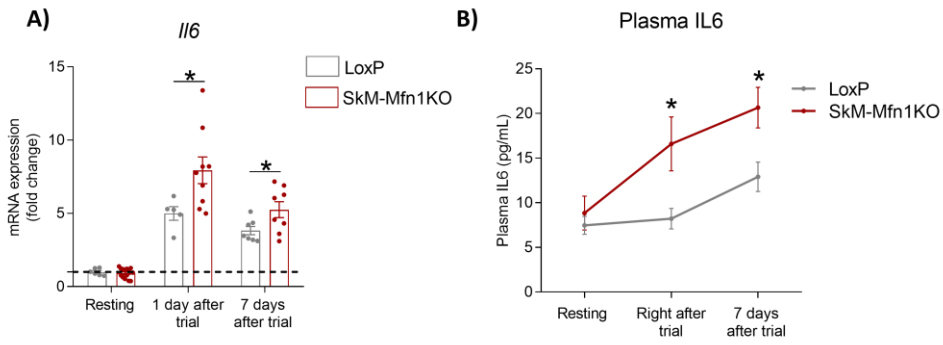

Figure 63: IL6 response to exercise. Study performed 6 weeks after tamoxifen treatment. A) mRNA levels in quadriceps muscles. B) Plasma IL6 levels. (n=5-10) Data represent mean ± SEM. *p<0.05 vs. LoxP.

Of note, we evaluated the expression levels of NFκB target genes, type I IFN response genes and macrophage markers in quadriceps of mice subjected to exercise. Strikingly, while NFκB target genes showed increased expression levels that could not be associated to genotypes or timepoints after the end of the treadmill test (Figure 64A), both type I IFN response genes and macrophage markers were highly expressed (Figure 64B-C). Indeed, regardless of the genotype, these genes were remarkably induced one day after the end of the test and completely restored their expression levels seven days after the end of the test, with the exception of *Irf7*.

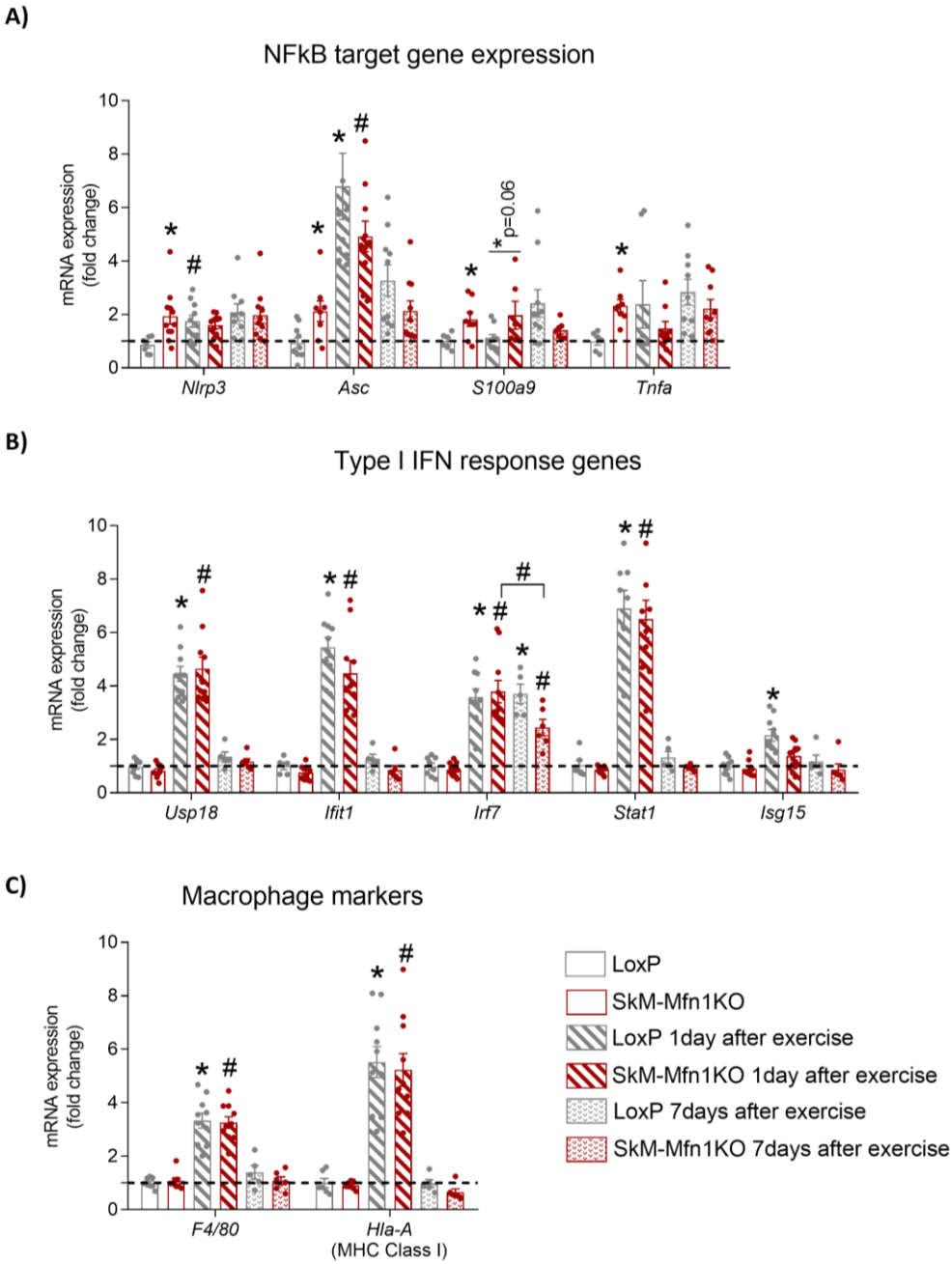

Figure 64: Inflammatory response to exercise in the muscle. mRNA levels in quadriceps muscles 6 weeks after tamoxifen treatment**.** A) NFκB target gene expression. B) Type I IFN response gene expression. C) Macrophage marker expression. (n=5-6) Data represent mean ± SEM. *p<0.05 vs. LoxP; #p<0.05 vs. KO.

Interestingly, induction of atrogene expression was observed seven days after the end of the test (Figure 65), once the interferon response and the immune infiltration was resolved. Based on these results, our data suggest two possibilities that are independent of the genotype: i) exercise induces a dramatic interferon-mediated response within the muscle that promotes acute immune infiltration; or ii) exercise-induced damage promotes muscle infiltration of immune cells that present induced interferon-stimulated gene (ISGs) expression. In any case, our data also suggest that induced expression of inflammatory genes precedes the upregulation of atrogenes upon exercise in the skeletal muscle.

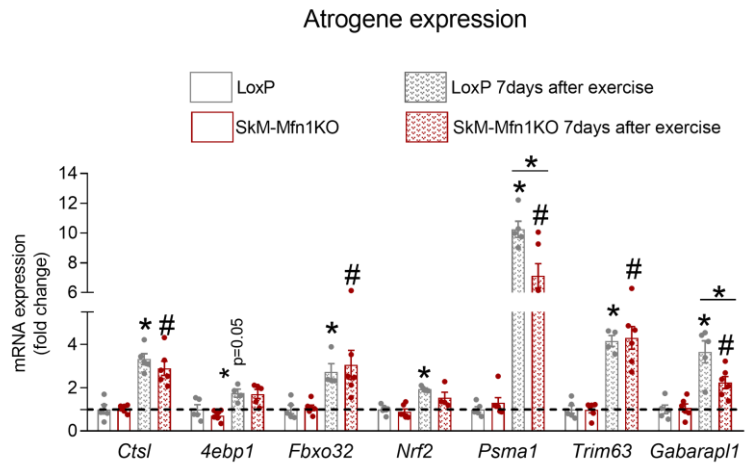

Figure 65: Atrogene expression in response to exercise. mRNA levels of atrogenes in quadriceps muscles 6 weeks after tamoxifen treatment. (n=5-6) Data represent mean ± SEM. *p<0.05 vs. LoxP; #p<0.05 vs. KO.

Taken together, our data indicate that Mfn1 deficiency in the skeletal muscle triggers local TLR9-mediated NFκB-dependent inflammation and muscle atrophy that compromises physical performance, exacerbates IL6 response to exercise, and possibly, impairs muscle repair mechanisms.

4.3.3 Impact of chronic anti-inflammatory treatment on inflammation, muscle atrophy and exercise performance in SkM-Mfn1KO mice

Finally, with the aim of identifying the contribution of TLR9-triggered NFκB-mediated inflammation upon Mfn1 ablation in skeletal muscles in the development of muscle atrophy and compromised physical performance, we treated mice for 28 days with sodium salicylate (200mg/kg per day), a well-known NFκB inhibitor[204]. Quantification of mRNA levels of the NFκB target genes in quadricep muscles showed that salicylate treatment normalized NFκB target gene expression in SkM-Mfn1KO mice (Figure 66), validating the anti-inflammatory effect of sodium salicylate.

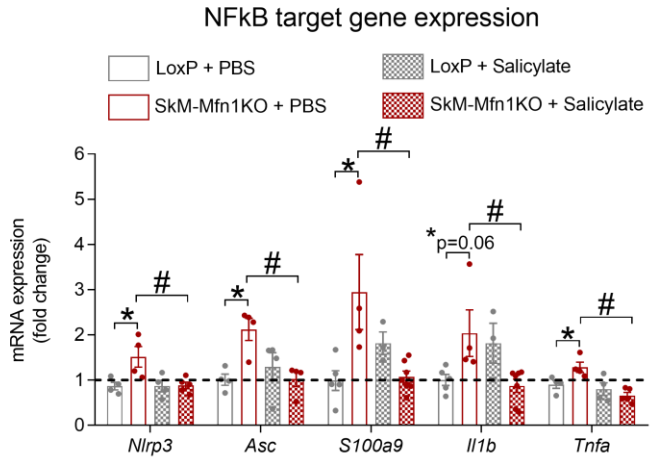

Figure 66: Inflammatory profile upon chronic sodium salicylate treatment. NFκB target gene expression in quadriceps muscles 10 weeks after tamoxifen treatment. (n=4-6) Data represent mean ± SEM. *p<0.05 vs. LoxP+PBS; #p<0.05 vs. KO+PBS.

Importantly, chronic anti-inflammatory treatment also normalized the reduced CSA (Figure 67), as well as the increased CK activity (Figure 68) in SkM-Mfn1KO mice. Besides, salicylate treatment also rescued the muscle mRNA and plasma levels of the myokine FGF21, although this rescue did not present statistical significance (Figure 69). These data indicate that upon Mfn1 ablation, TLR9-

induced NFκB activity plays a causative role in the development of muscle atrophy.

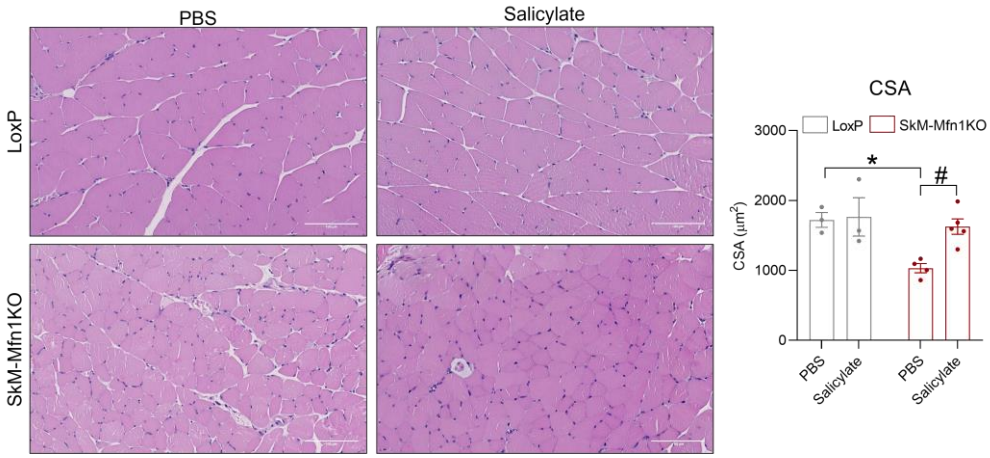

Figure 67: Quantification of the CSA upon chronic sodium salicylate treatment. Hematoxylin-eosin stainings in transversal sections of gastrocnemius muscles upon chronic sodium salicylate treatment 10 weeks after tamoxifen treatment. (n=3-4 mice per group, 300 fibers per mouse) Data represent mean ± SEM. *p<0.05 vs. LoxP+PBS; #p<0.05 vs. KO+PBS.

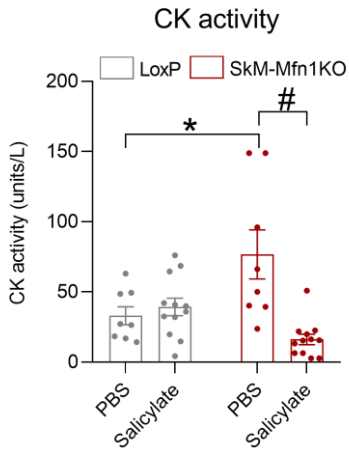

Figure 68: Plasma CK activity upon chronic sodium salicylate treatment. Study performed 10 weeks after tamoxifen treatment. (n=8-12) Data represent mean ± SEM. *p<0.05 vs. LoxP+PBS; #p<0.05 vs. KO+PBS.

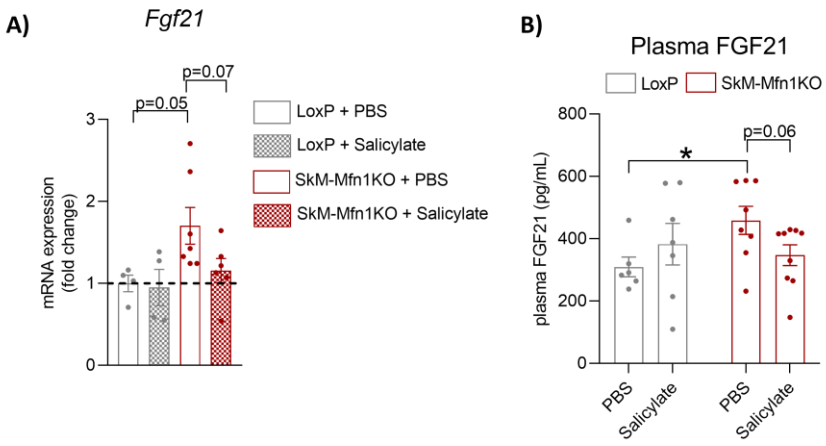

Figure 69: FGF21 response upon chronic sodium salicylate treatment. A) *Fgf21* mRNA levels in quadriceps muscles. B) Plasma levels of FGF21. Study performed in male mice 10 weeks after tamoxifen treatment. (n=4-9) Data represent mean ± SEM. *p<0.05 vs. LoxP+PBS; #p<0.05 vs. KO+PBS.

Assessment of the impact of the anti-inflammatory treatment on performance showed improved physical capacity of SkM-Mfn1KO (Figure 70), which suggests that by rescuing muscle atrophy induced by muscle inflammation, mice ameliorate their physical performance.

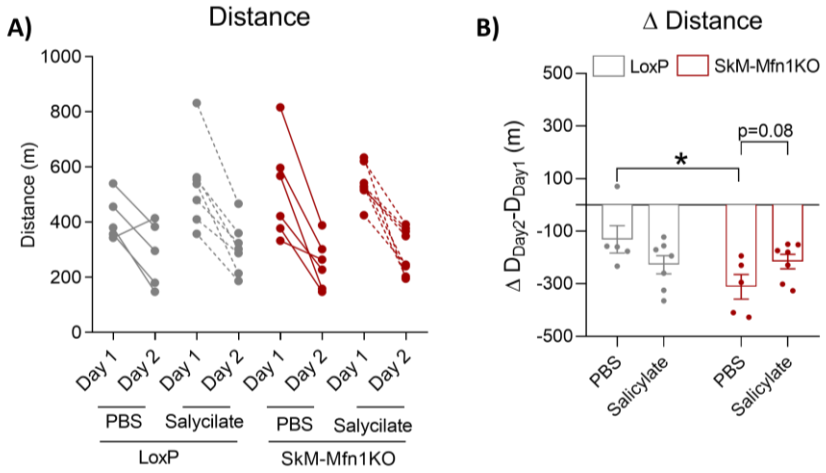

Figure 70: Physical performance assessment upon chronic sodium salicylate treatment. A) Distance run at day 1 and day 2 per mouse. B) Difference in the distance run from day 2 to day 1 per mouse. Study performed in male mice 10 weeks after tamoxifen treatment. (n=5-7) Data represent mean ± SEM. *p<0.05 vs. LoxP+PBS; #p<0.05 vs. KO+PBS.

To evaluate whether this improved performance could be explained by a restored IL6 response to exercise, we quantified plasma levels and muscle expression of IL6. Chronic anti-inflammatory treatment reduced the IL6 response to exercise in both LoxP and SkM-Mfn1KO animals (Figure 71A-B), although this reduced response was present at different timepoints. This is likely due to the activation of TLR9 present only in SkM-Mfn1KO, which might be contributing to an acute IL6 production in response to exercise in an NFκB-independent manner. Nevertheless, this response is rescued seven days after the end of the trial in SkM-Mfn1KO mice. Therefore, chronic anti-inflammatory treatment reduces the muscle IL6 response to exercise, however, its effects could be delayed in conditions characterized by a pre-existing muscle inflammation.

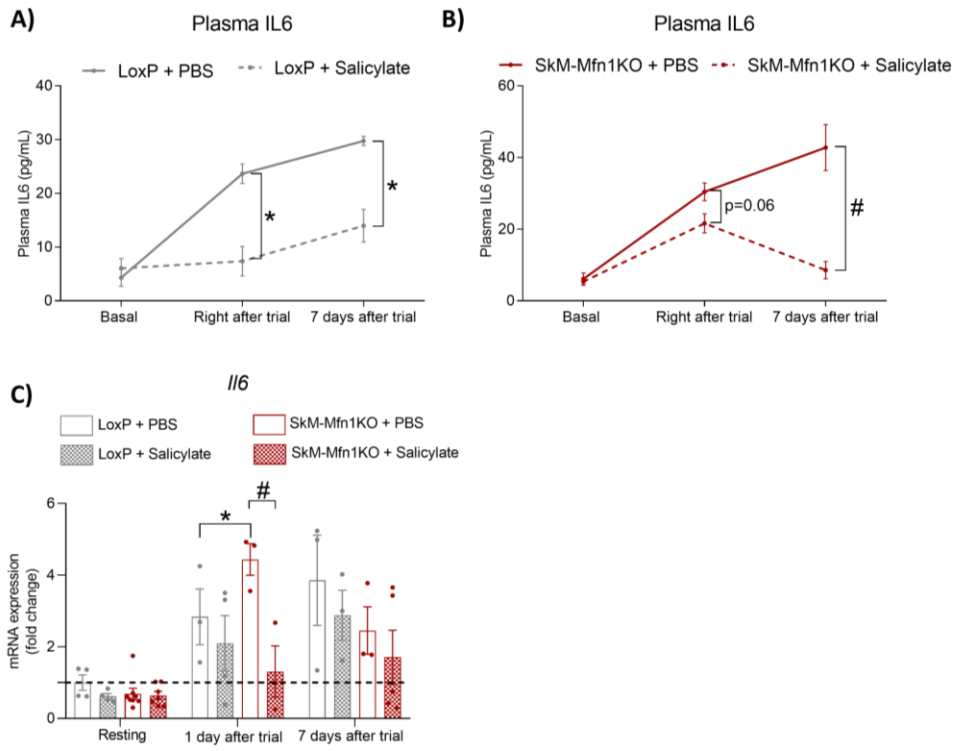

Figure 71: IL6 response to exercise upon chronic sodium salicylate treatment. Plasma IL6 levels in A) LoxP and in B) SkM-Mfn1KO mice. C) mRNA levels in quadriceps muscles. Study performed in male mice 10 weeks after tamoxifen treatment. (n=3-7) Data represent mean ± SEM. *p<0.05 vs. LoxP+PBS; #p<0.05 vs. KO+PBS.

Regarding the muscle *Il6* expression in response to exercise, our results are not conclusive, given the reduced statistical power (Figure 71C).

Taken together, our data suggest that a pre-existing muscle inflammation compromises not only the development of muscle atrophy and reduced physical performance, but also the IL6 response to exercise, and possibly, its role in muscle repair upon exercise-induced damage.

Muscle atrophy and muscle inflammation are widely considered hallmarks of impairment of muscle health[205], however, whether one precedes the other or they are independent mechanisms has remained unclear[206]. Our data has demonstrated that TLR9-induced NFκB-dependent inflammation triggered by mitochondrial fragmentation in the muscle is accompanied by the development of muscle atrophy. However, given that NFκB has also been reported to induce muscle atrophy pathways *per se*[207,208], it could also be discussed whether its action is mediated on inflammation and muscle atrophy in parallel. In any case, the combination of muscle inflammation and atrophy eventually compromises physical performance and the systemic response to exercise. In conclusion, these results provide insightful proof that inflammation-targeting treatments could be considered as feasible approaches in conditions where muscle atrophy and inflammation co-exist and compromise muscle homeostasis.

DISCUSSION

The results obtained in the present work can be summarized in the following concepts:

1. Imbalanced mitochondrial dynamics triggers DNA sensor-mediated inflammatory responses in muscle cells.
2. Mitochondrial fragmentation by Mfn1 deficiency promotes mtDNA and TLR9-driven NFκB inflammation due to early endosome and mitochondria close interactions.
3. Muscle inflammation and muscle atrophy compromise physical performance and IL6 response to exercise upon muscle mitochondrial fragmentation.

This chapter will be dedicated to the discussion of each of the concepts and to analyze the possible interpretations of the results.

Study I: Common mechanistic features linking imbalances in mitochondrial dynamics and sterile inflammation

Increasing evidence supports the link between mitochondrial stress and the induction of sterile inflammatory responses in non-immune cells. Furthermore, the involvement of mtDNA mislocation in the mechanisms implicated has been reported upon downregulation of mitochondrial proteins. Indeed, lack of proteins involved in the mitophagic process or mtDNA stability results in inflammation due to mtDNA leakage[55,120,121,160]. However, the molecular events taking place remain unaddressed. Also, the fact that deficiency of proteins involved in mitochondrial dynamics such Opa1 or its protease, Yme1L, triggers mtDNA-dependent inflammation suggests that maintenance of the balance between fusion and fission could be key in mitigating these responses. In the case of Opa1 downregulation in muscles, impaired mitophagy resolution leads to accumulation of defective mitochondria in late endosomes, which allows

mtDNA recognition by TLR9 and subsequent NFκB activation[51]. On the other hand, deficiency of the Opa1 protease Yme1L in MEFs promotes enhanced nucleotide import to mitochondria, which boosts mtDNA synthesis and results in leakage of mtDNA sequences to the cytosol, enabling their recognition by cGAS[55] (Figure 72). Indeed, our data on the inflammatory profiling of Yme1LKD muscle cells confirms the mtDNA exit to the cytosol and cGAS activation. However, whether imbalanced mitochondrial dynamics underlies as the key trigger of these events or it is the intrinsic properties and functions of Opa1 and Yme1L that play the main role in activating inflammation remains a unknown.

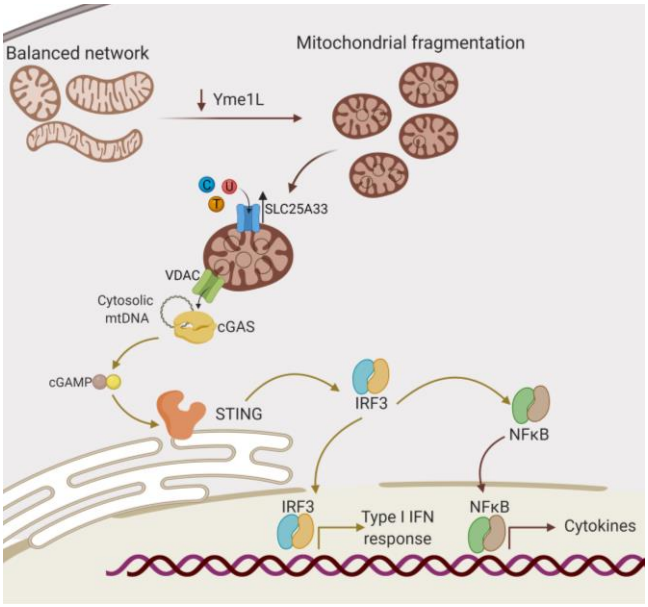

Figure 72: Molecular mechanism linking Yme1L deficiency to inflammation. According to Sprenger *et al*. 2021[55], Yme1L depletion promotes mitochondrial fragmentation and reduced SLC25A33 processing, which enables its accumulation. This promotes enhanced entry of pyrimidines into mitochondria, fuelling mtDNA synthesis and increasing its abundance. As an adaptive response to maintain mtDNA balance in mitochondria, mtDNA sequences are secreted to the cytosol through VDAC pores, where cGAS recognizes them, resulting in activation of NFκB-driven inflammation and the type I IFN response.

Interestingly, this hypothesis was tested by Sprenger *et al.* 2021 in their model of Yme1L deficiency in MEFs. Given that Yme1L ablation results in mitochondrial

fragmentation due to reduced Opa1 processing, the authors assessed whether downregulation of Drp1 in that context would restore the inflammatory profile, underpinning that imbalanced mitochondrial dynamics drives intracellular inflammation[55]. Nevertheless, double downregulation of Yme1L and Drp1 in MEFs, far from rescuing the inflammatory phenotype observed in Yme1L-deficient MEFs, it remarkably enhanced it, which permitted them to discard this hypothesis[55].

In this regard, we have demonstrated that, regardless of the cause of the imbalances in mitochondrial dynamics, this results in the activation of sterile intracellular responses. Indeed, we have observed that opposite mitochondrial morphologies induce different inflammatory profiles, which confirms our hypothesis that alterations in mitochondrial dynamics can be the primary cause of the initiation of sterile inflammation. Mechanistically, we have addressed the common molecular features operating upon ablation of mitochondrial dynamics proteins, and we report that mitochondrial fragmentation associates to TLR9-mediated inflammation, whereas mitochondrial elongation results in cGAS and TLR9 activation (Figure 73).

In the case of mitochondrial elongation, our data show that Fis1 or Drp1 deficiency in muscle cells induces both NFκB and type I IFN response, which is accompanied by mtDNA leakage to the cytosol. In these conditions, unravelling the molecular mechanisms coupling mitochondrial elongation mediated by Fis1 or Drp1 deficiency to mtDNA leakage was most challenging. Considering the process reported by Sprenger *et al.* 2021[55], which links Yme1L downregulation to reduced processing of the pyrimidine transporter SLC25A33, leading to an increased pyrimidine pool and resulting in mtDNA escape (Figure 72), evaluation of this pathway in Fis1 or Drp1KD muscle cells appeared to be relevant. Our data

show that, while the former could be associated to increased SLC25A33 levels, the latter drives an independent mechanism. Nevertheless, these data contradict the fact that Fis1KD muscle cells exhibit unaltered mtDNA abundance, while Drp1KD cells, similar to Yme1L deficiency, present increased mtDNA content. These results indicate that despite the fact that upon mitochondrial elongation the exit of mtDNA to the cytosol could be promoted by either altered nucleotide pool or mtDNA synthesis, the specific drivers involved in Fis1KD or Drp1KD cells are distinct.

Furthermore, dissecting the differences in the rescue effects on the inflammatory profile upon inhibition of cGAS or TLR9 in Fis1 or Drp1KD muscle cells was also a challenging aspect. Upon mitochondrial elongation, the implication of mtDNA leakage and subsequent cGAS activation was key in inducing the NFκB-mediated and the type I IFN responses. However, the contribution of mtDNA-mediated TLR9 activation remains unclear in this scenario. Although the increase in the co-distribution between mtDNA and TLR9 in such conditions might be caused by alterations in mitophagy, according to our data this mechanism can only be attributed to Fis1KD cells. This is due to the fact that we observed increased mitophagic flux in Fis1-deficient muscle cells, whereas Drp1KD cells present unaltered mitophagic flux. Interestingly, the impact of downregulation of mitochondrial fission proteins on mitophagy has been reported by others. On one hand, Zhang *et al.* 2019 described that Fis1 ablation in the skeletal muscle promotes increased co-distribution of mitochondria with autophagosomes[70]. In fact, Xian *et al.* 2019 characterized the molecular pathway linking Fis1 downregulation and increased mitophagy in HeLa cells. According to their data, Fis1 deficiency results in enhanced mitophagy due to the accumulation of Syntaxin 17 (STX17) onto mitochondria, which facilitates their inclusion into autophagosomes and subsequent fusion with $Rab7^{+}$

endolysosomes[209]. On the other hand, Favaro *et al.* 2019 and Dulac *et al*. 2020 showed that acute depletion of Drp1 in skeletal muscles causes autophagy and mitophagy impairment[65,66], resulting in muscle wasting. Given that our approach to measure the mitophagic flux in conditions that have been reported to impair mitophagy[19,65,66], *i.e.* Mfn2KD and Drp1KD, does not seem accurate, we could speculate that mtDNA-mediated activation of TLR9 upon mitochondrial elongation in muscle cells is promoted by altered mitophagic activity. In fact, increased mitophagy could promote enhanced co-distribution of mtDNA and TLR9 in Fis1KD cells, whereas the opposite effect on mitophagy could be promoting the encounter of mtDNA and TLR9 in Drp1KD cells.

Hence, our data demonstrate that mitochondrial elongation caused by deficiency of Drp1 or Fis1 results in the activation of the NFκB-driven pathway and the type I IFN response, which is mediated by mtDNA escape to the cytosol and subsequent cGAS activation (Figure 73). Despite the molecular events linking downregulation of Drp1 or Fis1 to such inflammatory responses differ, mtDNA leakage appears both as a common result and as a key driver of inflammation in the context of mitochondrial elongation.

In keeping with Opa1 downregulation[51], mitochondrial fragmentation induced by Mfn1 or Mfn2 deficiency in skeletal muscle cells associates to NFκB inflammation (Figure 73). However, the number of NFκB target genes upregulated in Mfn1 or Mfn2-deficient cells varies, which could be explained by the fact that these proteins, especially Mfn2, have other functions beyond mitochondrial fusion[188] that could impact the inflammatory outcome.

Although it has been reported that mitofusins are required to engage cognate immune responses upon immunogenic stimuli, such as lipopolysaccharide (LPS) treatment[42], TNFα treatment[210] or retroviral infections[211], as well as in cellular models of neuroinflammation[212], little has been described about deficiency of

mitofusins as a cause of sterile inflammation. Hernández-Álvarez *et al.* 2019 reported that liver Mfn2 ablation (L-Mfn2KO) recapitulated the progression of hepatocellular carcinoma, to which liver and systemic inflammation contribute considerably[33]. However, this was considered as a response to the loss of liver homeostasis rather than a direct consequence of Mfn2 deficiency. A similar conclusion was discussed in Kim *et al.* 2021, where they observed increased expression of pro-inflammatory cytokines in lungs whose microvascular endothelial cells lack of Mfn2 ($Mfn2^{EC-/-}$)[210]. In this case, the induced expression of cytokines in $Mfn2^{EC-/-}$ lungs was proposed as a result of increased lung vascular permeability, rather than Mfn2 deficiency itself. Therefore, our data on the trigger of sterile NFκB inflammation in muscle cells upon deficiency of mitofusins opens the question of whether in the contexts of L-Mfn2KO and in $Mfn2^{EC-/-}$, the observed phenotypes were indeed driven by the inflammation directly induced by Mfn2 deficiency.

Taken together, we have demonstrated that primary alterations in mitochondrial dynamics induce sterile inflammatory responses, which are different depending on the mitochondrial morphology. Whereas mitochondrial fragmentation associates to TLR9-mediated NFκB inflammation, mitochondrial elongation promotes the activation of both the NFκB-dependent pathway and the type I IFN response. However, some considerations have to be highlighted: in fact, within the same phenotype of mitochondrial morphology, differences in the inflammatory outcome can be observed. For instance, the number of inflammatory genes induced when comparing Mfn1 deficiency with Mfn2 deficiency vary, as well as the mechanisms responsible for mtDNA leakage or mtDNA-TLR9 co-distribution when comparing Fis1 deficiency with Drp1 deficiency. Thus, although the contribution of the intrinsic features of each mitochondrial dynamics protein cannot be underestimated, we strongly propose

that the inflammatory responses upon primary alterations in mitochondrial dynamics are direct consequences of such imbalances.

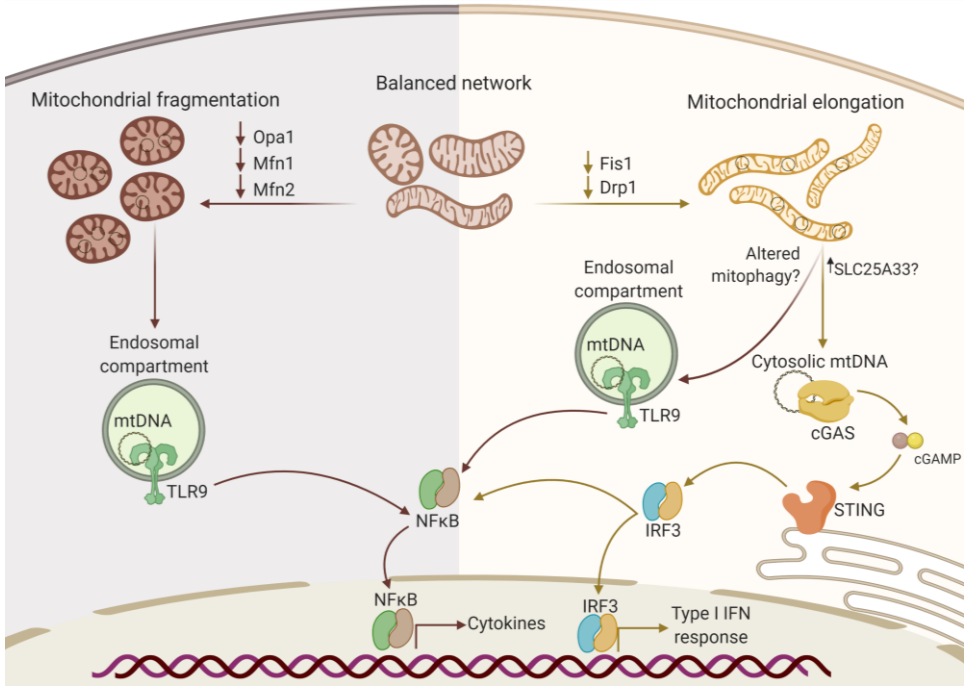

Figure 73: Working model of the biological processes linking imbalanced mitochondrial dynamics and sterile inflammation in muscle cells. Mitochondrial fragmentation induced by downregulation of Opa1, Mfn1 or Mfn2 induces TLR9-dependent NFκB-driven inflammation. Mitochondrial elongation induced by Fis1 or Drp1 deficiency promotes mtDNA leakage and cGAS activation, as well as increased mtDNA-TLR9 co-distribution, by different mechanisms. However, the activation of NFκB-mediated inflammation and type I IFN response is common in Fis1KD and Drp1KD cells.

Study II: Identification of the molecular pathways driving inflammation in Mfn1-deficient muscle cells

Based on our data, mitochondrial fragmentation induced by Mfn1 deficiency in muscle cells promotes TLR9-mediated NFκB-dependent inflammation. To elucidate the specific molecular events operating upon Mfn1 deficiency and driving NFκB activation, characterizing the accurate location of the encounter between mtDNA and TLR9 was essential. Our data show that early endosomal markers such as Rab5 and EEA1 exhibit an enhanced co-distribution with mtDNA and mitochondria, compared to that of other markers from the endosomal compartment. This suggests that it is in early endosomes where mtDNA is more likely to encounter TLR9 upon Mfn1 deficiency.

Nevertheless, it has been described that TLR9 can engage either the type I IFN response via TBK1 activation, or NFκB-mediated inflammation via TRAF6 activation, depending on the type of endosomes in which TLR9 is activated. Indeed, activation of TLR9 in late endosomes or MVBs is associated to NFκB inflammation[171], whereas early endosomal or lysosomal activation of TLR9 results in interferon-dependent responses[170], which contradicts our results regarding Mfn1 deficiency. However, it is worth to point out that these studies were performed in macrophages[171] and dendritic cells[170], respectively. This permits us to discuss that immune cells, whose main function is to provide orchestrated and cognate immune responses to immunogenic stimuli, exhibit broader molecular responses compared to non-immune cells, such as muscle cells. This could provide immune cells the capacity to cover a wide range of immune responses operating against the same immunogenic stimuli. Therefore, the fact that Mfn1 deficiency in muscle cells promotes an NFκB-mediated inflammation – and not type I IFN response - due to a preferable location of mtDNA and TLR9 encounter in early endosomes could be merely due to the non-

immunogenic nature of muscle cells, and their limited capacity to induce different inflammatory responses against the same stimuli.

Different processes are linked to the interaction between the endosomal compartment and mitochondria. For instance, “kiss and run” interactions between these two organelles have been reported to facilitate direct iron transfer in erythroid cells[192]. Close contacts between late endosomes and mitochondria have also been described in response to hypoxia in colon adenocarcinoma cell lines, as well as lysosome and mitochondria contacts in human tumors of lung adenocarcinoma[213]. Furthermore, late endosomal targeting of mitochondria is also a common feature during apoptosis signalling[214]. Also, several endosomal-dependent mitophagy pathways have been recently reported, including studies involving vesicles positive for Rab5[174], Rab7[196], Rab11A[215] or CARP2[216]. In this regard, the metabolic phenotyping of Mfn1-deficient cells suggested that an adaptive mitophagy pathway via mitochondrial engulfment by early endosomes could be involved, since Mfn1 deficiency promotes mitochondrial membrane depolarization, increased superoxide production and enhanced mitophagic flux.

However, our assays using immunogold and electron microscopy showed that Mfn1 deficiency favours the formation of close contacts between mitochondria and early endosomes. This implies the existence of a mitochondrial linker and its early endosomal partner in this context. Interestingly, Mfn2 has been reported to stablish contacts with different vesicular organelles to allow biological processes such as iron uptake and transfer to mitochondria[192], melanogenesis[195] or fusion of lysosomes to autophagosomes[196]. This permitted us to hypothesize that under conditions of Mfn1 deficiency, Mfn2 acts as the mitochondrial linker in mitochondria-early endosome contacts. Indeed, interactome studies performed by Isabel Gordaliza-Alaguero showed that Mfn2 interacts with the

early endosomal marker Rab5C, and induction of Mfn1 deficiency in muscle cells demonstrated that this interaction is enhanced in such conditions. Strikingly, Mfn2 interaction with Rab proteins has previously been described, as well as the modulation of this interaction in certain scenarios. Indeed, Zhao *et al.* 2012 reported that Mfn2 interacts with Rab7 in cardiomyocytes in basal conditions, and this interaction is enhanced upon starvation to enable the fusion of lysosomes to autophagosomes, and therefore, the progression of autophagy[196]. Hence, this study corroborates our data on the stimulation of the interaction between Mfn2 and Rab5C as a response to mitochondrial dysfunction. Although connections between mitochondria and other organelles have already been reported to be mediated by Mfn2[192,195,196], the relevance of these interactions in inducing or preventing stress responses remained unexplored. In this regard, our data not only describes a novel early endosomal partner for Mfn2, but it also highlights the importance of this interaction in promoting inflammatory responses upon mitochondrial fragmentation. In fact, functional assays to test the involvement of Mfn2-Rab5C interaction in inducing NFκB-dependent inflammation demonstrated that attenuation of this interaction restores the co-distribution of mtDNA with TLR9 and EEA1, as well as the resulting NFκB-driven inflammation.

Thus, our working model proposes that upon Mfn1 deficiency in muscle cells, Mfn2 and Rab5C interactions mediate the formation of close contacts between mitochondria and early endosomes, which facilitates the approximation of mtDNA to TLR9 and the resulting NFκB-mediated inflammation. This approximation could be driven by the shuttling of mtDNA sequences through pores. Interestingly, Das *et al.* 2016 characterized the duration and motility of the contacts between early endosomes and mitochondria in the events of iron transfer, and although they did not unravel the protein complexes responsible for the shuttling of iron transfer from early endosomes to mitochondria, they

proposed two candidates: the divalent metal transporter (DMT1) and VDAC pores[192]. Strikingly, Brahimi-Horn *et al.* 2015 described that under hypoxic conditions in colon carcinoma cells, VDAC pores locate at the juxtaposition of late endosome and mitochondria contacts, although the functional role of VDAC pores in those locations was not explored[213]. These antecedents suggest that VDAC pores could be promoting inter-organelle communication and transfer of molecules between the endosomal compartment and mitochondria. Furthermore, the implication of VDAC pores in the exit of mtDNA sequences from mitochondria to the cytosol has been demonstrated[55,167], therefore we hypothesized that in early endosome-mitochondria contacts of Mfn1-deficient cells, VDAC channels could be mediating the transport of mtDNA sequences to the lumen of early endosomes. However, our data are not conclusive in the involvement of VDAC pores in this process, which opens the question of whether other docking complexes could be mediating the shuttling of mtDNA from mitochondria to early endosomes. Although verifying the role of VDAC or unravelling the identity of such docking complexes is challenging, we propose that such proteins should gather the following features: ability to form pore-like complexes and location in the juxtaposition of inter-organelle contacts.

As explained above, mitochondria stablish contacts with several organelles to adequately adapt to environmental stimuli[9]. Indeed, the process by which Mfn2 stablishes enhanced interactions with Rab7 to enable fusion of lysosomes to autophagosomes in response to starvation appears as an adaptive response to promote survival. Thus, it could also be speculated that the formation of stronger bonds between mitochondria and early endosomes to promote mtDNA shuttling to the endosomal compartment in response to mitochondrial fragmentation acts as another adaptive response. However, it seems that in such scenario, mtDNA recognition by TLR9 precedes mtDNA degradation, and as a result, NFκB activates. Hence, this adaptive response to mitochondrial fragmentation could

be considered as a maladaptive mechanism that results in the induction of sterile inflammation.

In summary, the results in this study demonstrate the following upon mitochondrial fragmentation induced by Mfn1 deficiency in muscles cells: i) mitochondria and early endosomes form close contacts, ii) these contacts are mediated by Mfn2 and Rab5C interaction and iii) this interaction is essential in allowing mtDNA-TLR9 engagement to NFκB activation (Figure 74). Given that induction of NFκB target genes is also observed in Mfn2-deficient muscle cells and upon Opa1 downregulation in muscle cells[51], we propose that a similar biological process could be mediating the NFκB inflammation upon Mfn2 or Opa1 depletion. We speculate that either mitochondria-endosome contacts or engulfment of mitochondria in endosomes could be driving mtDNA and TLR9-dependent inflammation in these contexts. Indeed, it has been described that Opa1 or Mfn2 deficiency impair mitophagy[19,51], which allows the accumulation of mitochondria in mitophagosomes (autophagosomes that contain mitochondria) that eventually will fuse to endolysosomes. As a result, TLR9 is activated due to the recognition of mtDNA sequences, resulting in NFκB-mediated inflammation.

Based on the high identity between Mfn1 and Mfn2, we propose that upon downregulation of either Opa1, Mfn1 or Mfn2, mitofusins interact with endosomal markers such as Rab5C or Rab7[196], in order to either allow the formation of close contacts or to promote the engulfment of mitochondria to endosomes, which results in the encounter of mtDNA and TLR9, and subsequent NFκB activation (Figure 74). Although this hypothesis should be validated in Mfn2-deficient or Opa1-deficient muscle cells, this mechanism could be considered as common operating system in response to mitochondrial fragmentation leading to NFκB-dependent inflammation. Therefore, the tackling

of mitochondria-endosome contacts by targeting the interaction between mitofusins and their endosomal partners could be a feasible approach for the design of therapeutic strategies to treat inflammatory disorders characterized by altered mitochondrial dynamics.

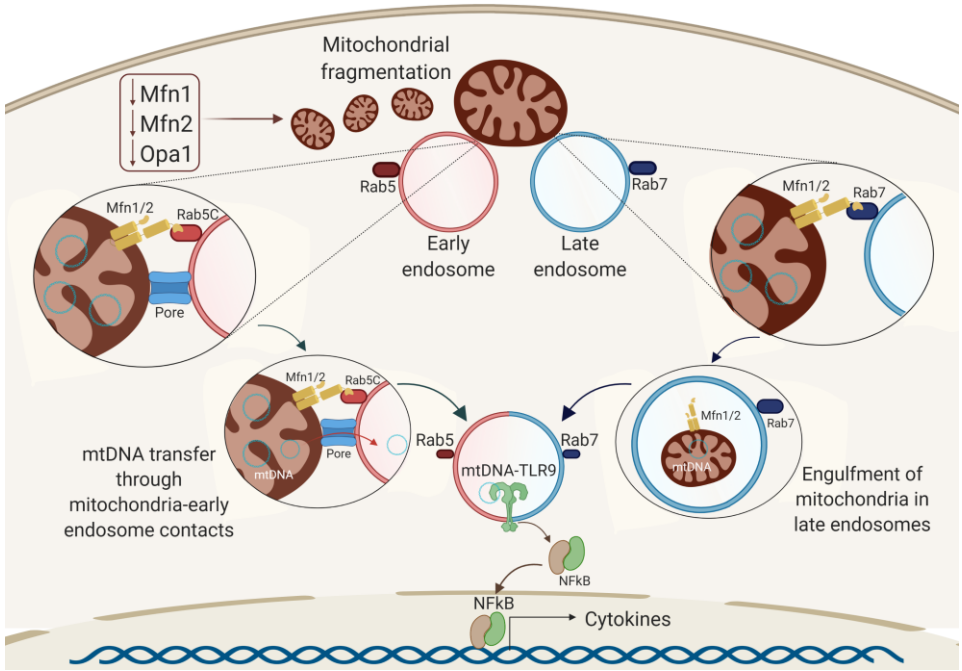

Figure 74: Proposed model for the common mechanisms linking mitochondrial fragmentation and TLR9-driven NFκB-dependent inflammation. Deficiency of Opa1, Mfn1 or Mfn2 promotes the approximation of endosomes to mitochondria. On one hand, physical interaction of mitofusins with Rab5C allows the formation of close contacts between mitochondria and early endosomes. This promotes the shuttling of mtDNA sequences to the lumen of early endosomes. On the other hand, physical interaction of mitofusins with Rab7 promotes the engulfment of mitochondria in late endosomes. In both scenarios, TLR9 recognizes mtDNA sequences resulting in NFκB-mediated inflammation.

Study III: Skeletal muscle health and performance upon Mfn1 ablation

The link between mitochondrial dysfunction induced by altered mitochondrial dynamics and the development of metabolic complications has been widely reported. The use of *in vivo* knockout models targeting Mfn2 in different highly metabolic tissues, *i.e.* white[41] and brown[29] adipose tissue, liver[33,217] or muscles[19], has provided extensive data on the need of maintaining mitochondrial dynamics to prevent alterations in glucose or lipid metabolism. For instance, loss-of-function of Mfn2 in skeletal muscles causes glucose intolerance[19], whereas liver Mfn2 depletion is also accompanied by impaired insulin signalling[33,217]. Mfn2 deficiency in brown adipose tissue impairs the respiratory capacity and the response to adrenergic stimuli[29], whereas its deficiency in white adipose tissue results in hyperphagia, increased adiposity and impaired glucose metabolism[41]. Regarding knockout models of Mfn1, interestingly, its deficiency in the liver promotes enhanced respiratory capacity and protects mice from HFD-induced insulin resistance[37].

In this regard, our data on the metabolic phenotyping of tamoxifen-inducible, SkM-Mfn1KO mice show unaltered body weight, food intake and body mass composition in both sexes. Despite the fact that female mice presented unchanged glucose and insulin tolerance, male SkM-Mfn1KO mice exhibited improved glucose tolerance with unaltered insulin levels. These differences to the ablation of Mfn1 within sexes suggest that distinct sex-dependent mechanisms govern the systemic responses to metabolic alterations. Besides, our data also show that, although total energy expenditure remained unchanged, male SkM-Mfn1KO mice preferably use carbohydrates as substrates compared to their LoxP littermates, whereas lipids are the preferable substrates in female SkM-Mfn1KO mice compared to LoxPs. This confirms the fact that sex is a determinant variable in the range of metabolic responses to primary

mitochondrial alterations in the skeletal muscle. Strikingly, these systemic alterations in males and females were independent of the mitochondrial respiration in muscle fibers, since this parameter exhibited a trend to be decreased in both sexes that was not statistically significant. Of note, among the studies mentioned above, only the one reported by Mancini *et al.* 2019, in which the white adipose tissue-specific Mfn2 knockout model was evaluated, used both males and females[41]. However, animals of both sexes were included in the same experimental groups, therefore the sex-dependent differences could not be noticed. On the other hand, Boutant *et al.* 2017 reported the use of brown adipose tissue-specific Mfn2 depleted male mice, with no reference on the use of females[29].

Given fundamental biological differences between sexes, many aspects of metabolism are controlled in a sexually dimorphic manner. However, how sex dimorphism affects energy metabolism is still considered highly complex. In this regard, sex hormones have been pointed as a key variable operating sex-dependent metabolic regulation. For instance, it has been reported that the action of estrogens – sex hormones present at significantly higher levels in females in reproductive age - in the central nervous system can modulate adiposity[218,219]. Besides, the hormone responsible for the development of male reproductive tissues, *i.e.* testosterone, has been proposed to play a protective role against obesity and insulin resistance[220]. Strikingly, preliminary data of transcriptomic analyses performed in quadriceps muscles of male LoxP and SkM-Mfn1KO showed increased muscle expression of *Esr1*, encoding for the estrogen receptor alpha. This data might be key in the metabolic adaptations observed in male mice and might explain the sex-dependent metabolic differences upon Mfn1 ablation. However, other possibilities should also be taken into consideration.

In fact, it has been described that FGF21 presents sex-dependent and tissue-specific responses in rodents and humans in certain metabolic conditions, such as fasting, refeeding or obesity[221,222]. Indeed, FGF21 is considered a systemic modulator of metabolic responses and an inductor of lipolysis[223]. Importantly, it also plays roles as a myokine, hepatokine and adipokine also in injury protection and diseases[224]. According to Bazhan *et al.* 2019, induction of *Fgf21* expression in the liver upon fasting or in local WAT and BAT upon refeeding is biased towards females. On the contrary, HFD-induced upregulation of hepatic and BAT *Fgf21* expression is biased towards males[221]. In this regard, our data indicate that muscle *Fgf21* expression and circulating levels of FGF21 are induced upon skeletal muscle Mfn1 ablation, regardless of the sex.

Considering these results, FGF21 could be discarded as the only modulator of the sex-dependent metabolic differences in our mouse model. Nonetheless, it can be speculated that the hormonal adaptations, such as muscle *Esr1* upregulation in male mice, in response to Mfn1 ablation could be playing a role upstream of FGF21. Therefore, this could be orchestrating the diverse effects of FGF21 in systemic metabolic responses in male and female mice. To test this hypothesis, circulating levels of sex hormones and the expression levels of their cognate receptors in target tissues of both male and female, LoxP and SkM-Mfn1KO mice could be evaluated. Also, the modulation of FGF21 in response to hormonal changes could be addressed, as well as the systemic metabolic effects this might implicate.

Taken together, our study on the metabolic phenotyping of SkM-Mfn1KO mice and the results obtained related to their sex-dependent differences sheds light to the need of performing all *in vivo* metabolic assays in both sexes. Regardless of that, our data also show that ablation of Mfn1 impacts on the utilization of substrates and confers with improved glucose tolerance only in male mice.

Mitochondrial dysfunction is considered a hallmark of muscle atrophy[205,225]. Indeed, as reviewed previously in this thesis, a wide range of myopathies are caused by mutations in mitochondrial proteins (Figure 4, Table 2). Also, few *in vivo* inducible models report that acute ablation of mitochondrial proteins in muscles results in muscle loss and degeneration[53,226]. These data directly link the need of maintaining mitochondrial fitness and homeostasis to prevent muscle disorders.

In keeping with previous findings of our group linking skeletal muscle Opa1[51] or Mfn2[19] deficiency with muscle atrophy, we have shown that both male and female SkM-Mfn1KO mice develop muscle atrophy. This is characterized by decreased CSA of the muscle fibers, increased plasma CK activity and, increased muscle FGF21 response and altered fiber typing. However, these alterations did not result in increased atrogene expression levels, and most strikingly, were independent of changes in muscle mass. Among the assessed atrogenes, *Fbxo32* and *Trim63* encode for E3 ubiquitin ligases (atrogin-1 and MuRF1, respectively) responsible for the selection of substrates targeted for ubiquitination and subsequent degradation by the 26S proteasome[227]. Indeed, enhanced protein degradation through the proteasome, along with other catabolic pathways such as autophagy, is crucial in the loss of muscle mass and the development of muscle atrophy[225,227]. Therefore, increased mRNA expression levels of *Fbxo32* and *Trim63* in skeletal muscles have been identified as markers for muscle atrophy.

Given that SkM-Mfn1KO mice do not present upregulated expression of atrogenes in resting conditions, it could be speculated that other molecular mechanisms, that are independent of proteasomal degradation and muscle mass regulation, lead to the modulation of the CSA of fibers and plasma CK activity. Hence, such mechanisms could also result in other types of muscle damage and

atrophy with unchanged muscle mass. In fact, Deguise MO *et al.* 2016 reported that two different *in vivo* models of spinal muscular atrophy were characterized by the activation of different pathways resulting in muscle atrophy[228]. In their study, activation of proteasomal pathways was observed in both models, whereas induced autophagy was only detected in one of the models. This work highlights the relevance of integrally assessing parameters associated to muscle health, as distinct molecular patterns of atrophy induction can govern the severity of the disease. Therefore, although muscle mass and atrogene expression remain unchanged, the presence of increased plasma CK activity, induced FGF21 response and reduced CSA of fibers confirm the development of muscle atrophy in the context of Mfn1 depletion in the skeletal muscle.

Muscle inflammation is widely linked to muscle damage or atrophy, both in physiological processes like aging[205], and in pathophysiological processes[118,175,205]. Indeed, characterization of the muscle health of SkM-Mfn1KO mice revealed that Mfn1 loss-of-function not only results in muscle atrophy, but also in the trigger of NFκB-mediated inflammation. In fact, ODN2088 treatment in these mice demonstrated that TLR9 activation drives increased NFκB target gene expression in Mfn1-deficient muscles, therefore phenocopying the observations made in Mfn1KD myoblasts. However, further characterization of the inflammatory phenotype in Mfn1-ablated muscles showed that the presence of immune cells in muscles and plasma levels of pro-inflammatory cytokines remained unchanged compared to LoxP littermates, suggesting that the induced inflammation is local and does not trigger systemic inflammatory responses.

According to studies reviewing the NFκB signalling pathways, besides its targeting on expression levels of pro-inflammatory genes, NFκB also induces the expression of genes involved in the ubiquitin-proteasome system[207,208]. In fact, Cai *et al.* 2004 and Mourkioti *et al.* 2006 described that the skeletal muscle

activation of NFκB impacts on the expression of MuRF1, resulting in muscle wasting. The former reported that transgenic expression of the enzyme responsible for NFκB processing, IKKβ, resulted in enhanced expression of MuRF1[207], whereas the latter described that depletion of IKKβ in the muscle prevented MuRF1 induced expression in response to muscle damage[208]. These studies establish a link between NFκB-driven muscle inflammation and MuRF1-mediated muscle atrophy. Nevertheless, given that SkM-Mfn1KO mice do not present enhanced *Trim63* expression, the mechanisms interplaying between muscle inflammation and muscle atrophy upon Mfn1 ablation remain unclear.

It is widely described that muscle damage triggers muscle regeneration or myogenesis[225,229]. This is the process by which multipotential mesodermal cells (satellite cells) give rise to proliferating myoblasts, which eventually exit the cell cycle and differentiate into muscle fibers[225,229]. Hence, the use of tamoxifen-inducible Cre recombinase systems under the control of the *HSA* promoter to generate knockout models in adult fibers can be counterproductive. In fact, the depletion of a certain protein in adult muscle fibers resulting in muscle damage would induce the myogenic process from satellite cells that do not express Cre recombinase[230,231]. Therefore, repetitive cycles of muscle damage and myogenesis would dilute the phenotype until the amount of adult muscle fibers expressing the Cre recombinase could be rejectable, unless tamoxifen treatment is continuously provided to induce Cre expression in the new adult muscle fibers. Considering that SkM-Mfn1KO mice present muscle damage and atrophy, assessing the maintenance of Mfn1 ablation over time appeared essential. Strikingly, Mfn1 protein levels in quadriceps of male and female mice remained downregulated 12 months after tamoxifen treatment. This suggests that despite Mfn1 deficiency causes muscle atrophy, the myogenic process in these muscles appears compromised, which results in an impairment to restore the muscle with new healthy muscle fibers. Importantly, a previous work performed in our group

by Dr. Eduard Noguera demonstrated that Mfn1-depleted myoblasts showed compromised myogenic differentiation, characterized by NFκB activation and decreased expression of genes involved in muscle differentiation, such as *MyoD* or *Myogenin*, among others. This resulted in a failed differentiation from cultured myoblasts to myotubes in conditions of Mfn1 deficiency.

Interestingly, accumulating literature reports the inhibitory role of NFκB on myogenesis. Lehtinen *et al.* 1996 were the first to describe that NFκB expression levels decrease during differentiation from myoblasts into myotubes and this decrease in NFκB expression precedes the induction of muscle-specific promoters and myoblasts fusion, which is the previous step to myotube formation[232]. They also observed that pharmacological inhibition of differentiation from myoblast into myotubes stimulated NFκB activation in myoblasts cultured in differentiation medium. More recently, Wang *et al.* 2007 reported that the inhibitory action of NFκB on myogenesis is mediated by its action on the expression levels of YingYang1 (YY1)[233]. YY1 is a negative regulator of myogenesis, as it directly represses the induction of genes involved in late-stage differentiation, including skeletal-α actin (*Acta1*) and muscle creatine kinase (*Ckm*)[233]. Thus, it could be speculated that NFκB activation triggered by Mfn1 loss-of-function in the muscle, on one hand, induces inflammatory pathways, and on the other hand, prevents the progression of myogenesis in damaged muscles. This combination results in a perpetuation of the muscle atrophy and strongly compromises the muscle health upon acute damage.

In summary, depletion of Mfn1 in skeletal muscles leads to muscle damage and atrophy, as well as TLR9-mediated NFκB muscle inflammation. Thus, evaluation of physiological parameters, such as tolerance to exercise, appeared to be relevant. Given that Sliter *et al.* 2018 subjected their total Pink1 or Parkin KO mice to three consecutive rounds of exercise until exhaustion on a treadmill and

assessed their inflammatory response[120], we chose a similar protocol to assess the physical performance of SkM-Mfn1KO mice. In our setting, LoxP and SkM-Mfn1KO male mice were subjected to two consecutive rounds of exercise until exhaustion (Figure 62). Our results show that despite there were no differences in the physical performance within genotypes at day 1 of the test, SkM-Mfn1KO mice exhibited reduced physical capacity at day 2 compared to their LoxP littermates. This suggests that muscle repair mechanisms could be potentially impaired in SkM-Mfn1KO mice, which would prevent them from performing as their LoxP littermates at day 2. Considering the inhibitory effect of NFκB on myogenesis and the impaired myogenic differentiation of Mfn1-deficient myoblasts described above, the presence of NFκB-mediated muscle inflammation in resting conditions caused by Mfn1 ablation could impede the activation of muscle repair mechanisms upon exercise-induced damage.

Of note, it is worth pointing out that a very clear pattern of expression of ISGs and macrophage markers was promoted in the muscle upon exercise. This pattern was independent of the genotype and consisted of an acute remarkable induction one day after the end of the test, and a complete restoration and resolution 7 days later. Regarding atrogene expression, their upregulation was sustained even when the expression of ISGs and macrophage markers normalized, therefore suggesting a possible role for inflammation in inducing atrophy-related responses to exercise.

Moreover, SkM-Mfn1KO mice exhibited enhanced IL6 expression and secretion in response to exercise, assessed by plasma IL6 levels and muscle *IL6* mRNA expression. Indeed, increased IL6 production is considered a physiological response to exercise[202], as it exerts many functions, which allows its recognition as a pleiotropic cytokine. It effects on the liver and adipose tissue contributing to the maintenance of glucose and lipid metabolism during exercise[203].

Furthermore, IL6 stimulates the expression of anti-oxidants in response to exercise-induced oxidative stress[234]. It has also been reported that IL6 promotes regeneration of muscle fibers upon exercise[235,236], potentially mediated by a mechanism involving STAT3[237]. Therefore, the exacerbated IL6 secretion upon exercise in SkM-Mfn1KO mice could be contributing to an adaptive response to exercise with the aim of restoring and repairing the pre-exiting muscle damage and inflammation.

It is clear that muscle damage and inflammation induced by Mfn1 depletion compromise the physical performance and its physiological outcomes. To unravel whether the action of NFκB was conditioning such complications, the NFκB inhibitor sodium salicylate was chronically provided to LoxP and SkM-Mfn1KO mice. One month after the initiation of the treatment, SkM-Mfn1KO mice restored the expression levels of NFκB target inflammatory genes, their plasma CK activity, the CSA of their fibers and the muscle FGF21 response, which suggested that NFκB acts on the development of muscle inflammation, as well as on muscle atrophy. This conclusion is supported by the studies mentioned above that link NFκB action with MuRF1-mediated muscle atrophy, however, at this point the molecular players promoting atrophy in the context of Mfn1-depletion remained unidentified. By improving the muscle health, SkM-Mfn1KO mice ameliorated their physical performance on the treadmill test, as well as their IL6 response to exercise. Interestingly, very similar observations were made by Mourkioti *et al.* 2006, who also demonstrated that specific deletion of IKKβ promotes skeletal muscle regeneration by limiting the inflammatory response and atrophy. As as a result, physical performance and the IL6 response to exercise ameliorated[208].

This study and our data strongly demonstrate the fact that NFκB activity plays a pivotal role in muscle health, by inducing local inflammation, promoting muscle

atrophy and potentially compromising muscle repair mechanisms, which negatively impact on physical performance and the IL6 response to exercise (Figure 75).

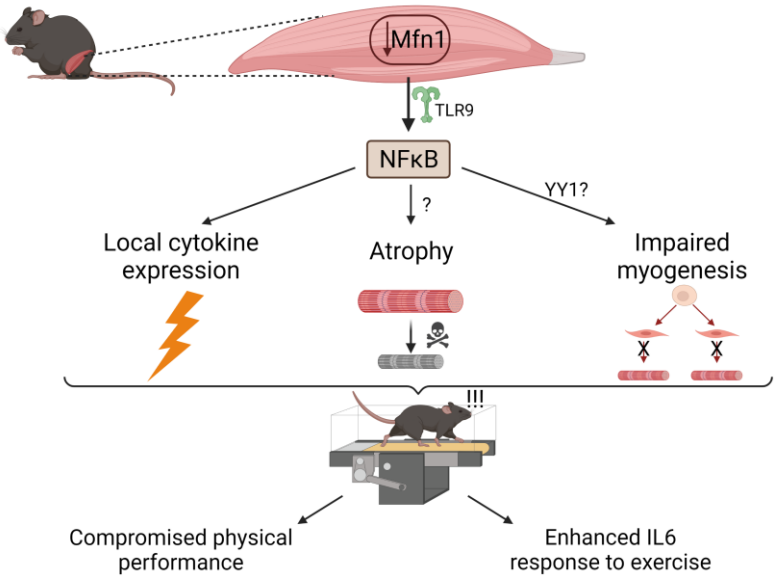

Figure 75: Working model of the effects observed in muscle health upon skeletal muscle Mfn1 depletion. Mfn1 downregulation promotes TLR9-dependent NFκB activation. This results in muscle cytokine production, muscle atrophy and possibly, impaired myogenesis. The molecular mediators connecting NFκB activation and muscle atrophy have not been deciphered in this work, although they are independent of MuRF1. Regarding the mediators impairing myogenesis, we propose that negative regulators of myogenesis, such as YY1, could be inhibiting this process upon Mfn1 deficiency-induced NFκB activation. As a result, the combination of muscle inflammation, atrophy and impaired regeneration compromises physical performance and promotes an enhanced IL6 response to exercise.

As discussed above, mitochondrial stress can induce sterile inflammation by inducing mtDNA mislocation and allowing its recognition by DNA sensors[51,55,120,121,160], mitochondrial dynamics are essential maintaining mitochondrial homeostasis[35] and muscle inflammation and atrophy are hallmarks of impaired muscle health[205,206]. However, the molecular connections between mitochondrial dynamics and mtDNA-dependent inflammation in the skeletal muscle, and their physiological implications, have not been reported yet.

In this regard, we have characterized the mechanisms linking imbalances in mitochondrial dynamics and sterile inflammation, with especial focus on the molecular events relating mitochondrial fragmentation and mtDNA and TLR9-dependent NFκB activation. Moreover, we extensively assessed their effects in skeletal muscle health, as well as the contribution of inflammation to muscle atrophy. Therefore, we propose mitochondrial dynamics maintenance as a key factor preventing the trigger of mtDNA-dependent inflammatory responses and we demonstrate that muscle inflammation and atrophy induced by mitochondrial fragmentation compromise physiological responses.

These findings open the way to new therapeutic strategies in inflammatory disorders characterized by altered mitochondrial dynamics. A number of chronic diseases - namely neurodegenerative disorders such as Parkinson's or Alzheimer's, cardiovascular diseases including atherosclerosis, obesity and type 2 diabetes mellitus – are thought to be caused by ROS-induced chronic inflammation[238]. In the particular case of muscle disorders, inflammatory myopathies or myositis are considered idiopathic[175]. Interestingly, a subtype known as sporadic inclusion body myositis is characterized by inflammation, mitochondrial dysfunction and accumulation of amyloidogenic proteins in the skeletal muscles[118,119]. Many of the disorders mentioned previously are also associated to mitochondrial dysfunction[238], hence, it could be speculated that imbalanced mitochondrial dynamics could also be contributing to the loss of mitochondrial homeostasis in such conditions[118,119,238].

The evaluation of mitochondrial dynamics and proper characterization of the mitochondrial health in those contexts could provide new therapeutic targets to treat these diseases. Given the findings obtained in this thesis, the strategies that we propose include: i) stimulation of balanced mitochondrial dynamics, ii) inhibition of interaction between mitofusins and endosomal markers, iii)

stimulation of mitophagy pathways independent of the endosomal compartment, iv) direct intracellular DNA sensor inhibition, and v) NFκB inhibition.

In conclusion, the work performed in this thesis has allowed the characterization of the molecular players linking imbalanced mitochondrial dynamics and the induction of sterile inflammation in muscle cells, as well as broadened the understanding of the physiological contribution of muscle NFκB-mediated inflammation to the loss of muscle health and physical performance. Future studies should be directed to the identification of the molecular pathways involved in triggering inflammation upon mitochondrial elongation and the exact events linking NFκB activity and muscle atrophy upon mitochondrial fragmentation.

CONCLUSIONS

The data compiled in this thesis allow us to conclude:

1. Imbalanced mitochondrial dynamics triggers sterile inflammation induced by DNA sensor-mediated recognition of mtDNA in muscle cells.

2. Mitochondrial elongation induced by Fis1 or Drp1 deficiency promotes mtDNA leakage to the cytosol and activation of both the NFκB and the type I IFN responses. In contrast, mitochondrial fragmentation induced by Mfn1 or Mfn2 deficiency triggers a TLR9-dependent NFκB-driven inflammation.

3. Mfn1 deficiency induces close contacts between early endosomes and mitochondria, which are mediated by Rab5C. This facilitates the recognition between mtDNA and TLR9, resulting in NFκB-dependent inflammation.

4. Mfn1 ablation in the skeletal muscle promotes TLR9-dependent NFκB activity resulting in muscle cytokine production and atrophy, leading to reduced physical performance and enhanced IL6 response to exercise.

5. We propose that mitochondrial dynamics controls sterile inflammation, which provides new insights on the design of therapeutic approaches to treat inflammatory disorders linked to mitochondrial dysfunction.

MATERIALS AND METHODS

7.1 Materials

7.1.1 Reagents

Name	*Working conditions*	*Application*	*Source*
Lipofectamine 2000	1:400, 24 h	siRNA transfection	Thermofisher Scientific
OptiMEM	1:8, 24 h	siRNA transfection	Thermofisher Scientific
MitoTracker deep red	50 nM, O/N	Mitochondrial mass quantification	Thermofisher Scientific
MitoTracker green	50 nM, 30 min	Mitochondrial mass quantification	Thermofisher Scientific
TMRM	50 nM, 30 min	ΔΨm quantification	Thermofisher Scientific
MitoSOX	2.5 nM, 30 min	Mitochondrial superoxide quantification	Thermofisher Scientific
Bafilomycin A1	200 nM, O/N	Autophagic flux inhibitor	Sigma-Aldrich
ODN2088	*In vitro*: 1 uM, 24 h *In vivo:* 100ug/mouse	TLR9 antagonist	Invivogen
Sodium salicylate	*In vivo:* 200mg/Kg	NFκB inhibitor	Sigma
Ru.521	1 uM, 24 h	cGAS inhibitor	Invivogen
VBIT-4	10 uM, 24 h	VDAC oligomerization inhibitor	Selleck Chemicals
Oligomycin	2 uM	Complex V inhibitor	Sigma-Aldrich
CCCP	Seahorse: 0.5 uM Oroboros: 1 uM 100 uM, 30 min	Uncoupler of oxidative phosphorilation ΔΨm depolarization	Sigma-Aldrich
Rotenone	Seahorse: 1 uM Oroboros: 0.5 uM	Complex I inhibitor	Sigma-Aldrich
Antimycin a	Seahorse: 1 uM Oroboros: 2.5 uM	Complex III inhibitor	Sigma-Aldrich
Glutamate	10 mM	Complex I substrate supply	Sigma-Aldrich
Malate	2 mM	Complex I substrate supply	Sigma-Aldrich
ADP	2.5 mM	Complex V substrate supply	Sigma-Aldrich
Succinate	10 mM	Complex II substrate supply	Sigma-Aldrich
Puromycin	1 ug/mL	Stable cell line selection	Sigma-Aldrich
Ampicilin	100 ug/mL	Bacterial selection	Sigma-Aldrich
FLAG-RAB5C vector	10 ug	FLAG-RAB5C overexpression	SinoBiological

			(HG15817-NF)
FLAG peptide	1:20	Elution of immunoprecipitation	Sigma-Aldrich (F3290)
Anti-FLAG magnetic beads	25 uL	Immunoprecipitation	Sigma-Aldrich (M8823)

7.1.2. MISSION siRNAs (Merck)

Gene	***Targeted exon***	***Reference***	***Sequence***
Opa1	Exon 3	SASI_Mm01_00113617	GGAUUGUGCCUGACUUUAU[dT][dT]
		SASI_Mm01_00113617_AS	AUAAAGUCAGGCACAAUCC[dT][dT]
Mfn1	Exon 2	SASI_Mm01_00037358	GUGUGAAGACUGUUAAUCA[dT][dT]
		SASI_Mm01_00037358_AS	UGAUUAACAGUCUUCACAC[dT][dT]
Mfn2	Exon 6	SASI_Mm01_00027321	GUGUCAAGACUGUGAACCA[dT][dT]
		SASI_Mm01_00027321_AS	UGGUUCACAGUCUUGACAC[dT][dT]
Oma1	Exon 3	SASI_Mm01_00170631	GACUGAACACAGUCAGUCA[dT][dT]
		SASI_Mm01_00170631_AS	UGACUGACUGUGUUCAGUC[dT][dT]
Yme1l	Exon 3	SASI_Mm01_00021570	GCAUGAAGCUCCCAGUAGU[dT][dT]
		SASI_Mm01_00021570_AS	ACUACUGGGAGCUUCAUGC[dT][dT]
Drp1	Exon 6	SASI_Mm01_00125378	GAGAACUUAUUCUUCGGUU[dT][dT]
		SASI_Mm01_00125378_AS	AACCGAAGAAUAAGUUCUC[dT][dT]
Mff	Exon 2	SASI_Mm01_00049362	CUUCUAAUCCUCAUCAUGA[dT][dT]
		SASI_Mm01_00049362_AS	UCAUGAUGAGGAUUAGAAG[dT][dT]
Fis1	Exon 1	SASI_Mm01_00022625	UGUAUUUGCUUCGAACCAG[dT][dT]
		SASI_Mm01_00022625_AS	CUGGUUCGAAGCAAAUACA[dT][dT]

Tlr9	Exon 2	SASI_Mm01_00126151	GGUGUAAGAACUUCAAGUU[dT][dT]
		SASI_Mm01_00126151_AS	AACUUGAAGUUCUUACACC[dT][dT]
Rab5C	Exon 1	SASI_Mm01_00105011	GAUACAUUUGCACGGGCUA[dT][dT]
		SASI_Mm01_00105011_AS	UAGCCCGUGCAAAUGUAUC[dT][dT]
Negative control		SIC001	

7.1.3. Packaging vectors

Name	*Vector*	*Bacterial selection*	*Function*
pMD2.G	Addgene: #12259	Ampicilin	VSV-G envelope expressing plasmid
psPAX2	Addgene: #12260	Ampicilin	2nd gen. lentiviral packaging plasmid

7.1.4. pLKO.1 shRNA-containing vectors

Target	*Oligo sequence*	*Bacterial Selection agent*	*Mammalian selection agent*
Dnml1 (Drp1)	CCGGCGGTGGTGCTAGGATTTGTTACTCG AGTAACAAATCCTAGCACCACCGTTTTT	Ampicilin	Puromycin
Mfn1	CCGGCCCAGTGTACTGAAAGTGTATCTCG AGATACACTTTCAGTACACTGGGTTTTTG	Ampicilin	Puromycin
Mfn2	CCGGGCTACAGCTCATCATCAGTTACTCGA GTAACTGATGATGAGCTGTAGCTTTTTG	Ampicilin	Puromycin
Fis1	CCGGCCTGATTGATAAGGCCATGAACTCG AGTTCATGGCCTTATCAATCAGGTTTTTG	Ampicilin	Puromycin
Yme1L	CCGGCGAGCCAAACATATCTTGAAACTCG AGTTTCAAGATATGTTTGGCTCGTTTTTG	Ampicilin	Puromycin
Scr	Empty Vector	Ampicilin	Puromycin

7.1.5. Real time PCR Sybr Green primers

Symbol	*Forward sequence*	*Reverse sequence*
4ebp1	CACGCTCTTCAGCACCAC	GGAGGCTCATCGCTGGTAG
Asc	GAAGCTGCTGACAGTGCAAC	GCCACAGCTCCAGACTCTTC

Atf4	CTCATGGGTTCTCCAGCGACAAG	GTCAAGAGCTCATCTGGCATGG
B Actin	GGTCATCACTATTGGCAACGA	GTCAGCAATGCCTGGGTACA
Cd68	TGTCTGATCTTGCTAGGACCG	GAGAGTAACGGCCTTTTTGTGA
Cgas	GGAAGTCCCCAGGATTGAGC	TGACTCAGCGGATTTCCTCG
Ctsl	GTGGACTGTTCTCACGCTCAAG	TCCGTCCTTCGCTTCATAGG
Drp1	AGCCAATCCATCTCAAGGTTTTCTC	ATCGCCTACAGGTACTTTGGTCATTC
F4/80	GACCGGGGAGAAGAAGGAGGACT	ATCTCTGCTTTGGCTGGATGTGCT
Fbxo32	GCAAACACTGCCACATTCTCTC	CTTGAGGGGAAAGTGAGACG
Fgf21	ATGGAATGGATGAGATCTAGAGTTGG	TCTTGGTGGTCATCTGTGTAGAGG
Fis1	TGTCCAAGAGCACGCAATTTG	CCTCGCACATACTTTAGAGCCTT
Gabarapl1	CATCGTGGAGAAGGCTCTA	ATACAGCTGGCCCATGGTAG
Gapdh	AGGCCGGTGCTGAGTATGTC	TGCCTGCTTCACCACCTTCT
Hmgb1	CGCGGAGGAAAATCAACTAA	TCATAACGAGCCTTGTCAGC
Ifit1	CTGAGATGTCACTTCACATGGAA	GTGCATCCCCAATGGGTTCT
Ifnb	CCCTATGGAGATGACGGAGA	CCCAGTGCTGGAGAAATTGT
Il1b	GCAACTGTTCCTGAACTCAACT	ATCTTTTGGGGTCCGTCAACT
IL6	TAGTCCTTCCTACCCCAATTTCC	TTGGTCCTTAGCCACTCCTTC
Irf7	CAATTCAGGGGATCCAGTTG	AGCATTGCTGAGGCTCACTT
Isg15	GGTGTCCGTGACTAACTCCAT	TGGAAAGGGTAAGACCGTCCT
Mfn1	CCTACTGCTCCTTCTAACCCA	AGGGACGCCAATCCTGTGA
Mfn2	AGAACTGGACCCGGTTACCA	CACTTCGCTGATACCCCTGA
Hla-A	TGGGGAGTCCTCAGTTTGCT	AACACACGTTAGAGTGAGCGT
Mt16s	CACTGCCTGCCCAGTGA	ATACCGCGGCCGTTAAA
MtCox2	CTACAAGACGCCACAT	GAGAGGGGAGAGCAAT
MtCytB	GCTTTCCACTTCATCTTACCATTTA	TGTTGGGTTGTTTGATCCTG
MtD-loop1	AATCTACCATCCTCCGTGAAACC	TCAGTTTAGCTACCCCCAAGTTTAA
MtD-loop3	TCCTCCGTGAAACCAACAA	AGCGAGAAGAGGGGCATT
MtNd4	AACGGATCCACAGCCGTA	AGTCCTCGGGCCATGATT
Myd88	TCATGTTCTCCATACCCTTGGT	AAACTGCGAGTGGGGTCAG
Nrf2	GCAACTCCAGAAGGAACAGG	AGGCATCTTGTTTGGGAATG
Opa1	CTGAGGCCCTTCTCTTGTTAGG	CTGACACCTTCCTGTAATGCTTG
Psma1	CATTGGAATCGTTGGTAAAGAC	GTTCATCGGCTTTTTCTGC
Rage	CCACTGGAATTGTCGATGAGG	CTCGGACTCGGTAGTTGGACT
S100a9	TGAGCAAGAAGGAATTCAG	TGTGTCCAGGTCCTCCATGA
SdhA	GGAACACTCCAAAAACAGACCT	CCACCACTGGGTATTGAGTAGAA
Stat1	CGCGCATGCAACTGGCATATAACT	ATGCTTCCGTTCCCACGTAGACTT
Tlr9	CTCCATCTCCCAACATGGTTCT	GCCAGCACTGCAGCCTGTA
Tnfa	CACAAGATGCTGGGACAGTGA	TCCTTGATGGTGGTGCATGA
Trim63	TGTCTGGAGGTCGTTTCCG	ATGCCGGTCCATGATCACTT

Usp18	AGAGTTAGCAAGCTCCGACAT	TGAGGTGAATGGTCAAGGTTTG
Yme1l	AAGGACACGACGTTTGCAGT	GGTCTTCTGTGTAAGAGCTTGAG

7.1.6. Genotyping PCR primers

Symbol	*Forward sequence*	*Reverse sequence*
Cre	CGGTCGATGCAACGAGTGATGAGG	CCAGAGACGGAAATCCATCGCTCG
Mfn1 floxed	GACAAGTAGTGGCAAGAGC	AGGAAGCAGTTGGTTGTG

7.1.7. Antibodies

7.1.7.1. Primary antibodies

Target	*Raised in*	*Working condition*	*Cat. number*	*Source*
Mfn1	Rabbit	WB: 1:1,000; O/N, 4 ºC	50330	Santa Cruz Biotechnology
Mfn2		WB: 1:1,000; O/N, 4 ºC	11925	Cell Signalling
Fis1	Rabbit	WB: 1:500; O/N, 4 ºC	GTX111010	GeneTech
YME1L	Rabbit	WB: 1:1,000; O/N, 4 ºC	11510-1-AP	Proteintech
Drp1	Mouse	WB: 1:500; O/N, 4 ºC	611112	BD transduction lab
SLC25A33	Rabbit	WB: 1:500; O/N, 4 ºC	TA309042	Origene
LAMP1	Rat	IF: 1:400; 30 min RT	Ab25630	Abcam
TOM20	Rabbit	IF: 1:400; 30 min RT	SC-17764	Santa Cruz Biotechnology
Sdha	Mouse	IG: 1:20	459200	Life Technologies
TLR9	Rabbit	IF: 1:400; 30 min RT	Ab134368	Abcam
cGAS	Rabbit	IF: 1:400; 30 min RT	79978	Werfen
dsDNA	Mouse	IF: 1:400; 30 min RT	Ab27156	Abcam
Rab5	Rabbit	IF: 1:400; 30 min RT IG: 1:4	1673547S	Cell Signalling
Rab5C	Rabbit	WB: 1:2000; O/N, 4 ºC	NBP1-80858	Novus
Rab7	Rabbit	IF: 1:400; 30 min RT	9367	Cell Signalling
IL1β	Rabbit	IHC in muscle sections 1:100, 60 min	Ab9722	Abcam

F4/80	Rat	IHC in muscle sections: 1:100, 60 min	14-4801-85	eBioscience
Myosin heavy chain isoform 1	Mouse	IF in muscle sections: 1:25; O/N, 4 ºC	BA-F8	DSHB
Myosin heavy chain isoform 2a	Mouse	IF in muscle sections: 1:20; O/N, 4 ºC	SC-71	DSHB
Myosin heavy chain isoform 2b	Mouse	IF in muscle sections: 1:10; O/N, 4 ºC	BF-F3	DSHB
Vinculin	Mouse	WB: 1:1,000; O/N, 4 ºC	Ab18058	Abcam
Tubulin	Mouse	WB: 1:1,000; O/N, 4 ºC	T5168	Sigma Aldrich
B Actin	Mouse	WB: 1:1,000; O/N, 4 ºC	A1978	Sigma Aldrich
HRS	Rabbit	IF: 1:400; 30 min RT	15087	Cell Signalling
EEA1	Rabbit	IF: 1:400; 30 min RT	3288S	Cell Signalling

7.1.7.2. Secondary antibodies

Target	*Conjugated*	*Working condition*	*Cat. number*	*Source*
Mouse	HRP	WB: 1:10,000; 1 h, RT	5127S	Jackson
	DyLight 800 PEG		SA535521	Invitrogen
	IRDye 680LT PEG		35518	Licor Biosciences
	Alexa Fluor-488	IF: 1:800; 30 min RT	A11029	Jackson
	Colloidal gold-12nm	IG: 1:30; 30 min	AB_2338734	Jackson
	Alexa Fluor 350 IgG1	IF in muscle sections: 1:500; 60 min	A-21120	Invitrogen
	Alexa Fluor 488 IgGM		A-21042	Invitrogen
	Alexa Fluor 568 IgG2b		A-21144	Invitrogen
Rabbit	HRP	WB: 1:10,000; 1 h RT	58802S	Jackson
	DyLight 800 PEG		SA5-35571	Life Technologies
	Alexa Fluor 680		A-21076	Life Technologies
	Alexa Fluor-568	IF: 1:800; 30 min RT	A11036	Invitrogen
	Colloidal Gold-18nm	IG: 1:30; 30 min	AB_2338017	Jackson

	BrightVision poly HRP-Anti-Rabbit IgG	IHC: 1:500; 45 min	DPVR-110HRP	ImmunoLogic
Rat	Alexa Fluor-647 OmniMap anti-Rat HRP	IF: 1:800; 30 min RT IHC: 1:500; 45 min	A21247 760-4457	Invitrogen Roche

7.2. Methods

7.2.1. Animal studies

7.2.1.1. Animal care

All animal experiments were done in compliance with the guidelines established by the Committee on Animal Care of the University of Barcelona. Mice were kept under a 12-h dark-light period and provided with a standard chow-diet and water *ad libitum.*

7.2.1.2. Generation of the animal model and genotyping

To generate the inducible skeletal muscle-specific deletion of *Mfn1*, the *Mfn1*$^{f/f}$ line was crossed with mice carrying Cre-ER under the control of the human skeletal actin tamoxifen-inducible promoter (HSA)[239]. Induction of expression of Cre was achieved by oral administration of a tamoxifen-enriched chow diet (Tam400/Cre ER Harlan), which was provided *ad libitum* for 2 weeks at the age of 12 weeks. Weight was monitored from the start of the induction. All the experiments were performed using male and female C57BL6/J mice aged between 4 and 6 months. Mice were kept in 12:12 h dark-light periods in a specific pathogen free (SPF) animal facility and provided with a standard chow diet and water *ad libitum*. At the indicated time, mice were anesthetized using isofluorane and euthanized by cervical dislocation.

. Animal genotype was assessed by PCR amplification of specific genomic fragments following the protocol detailed below:

- Mouse tail tips (1-2mm) are obtained at weaning and kept at -20 °C until processing. Tail tips are digested O/N at 55 °C and 450 rpm shaking in 500 µl of Lysis Buffer (5mM EDTA; 200 mM NaCl; 0.2 % SDS; 100 mM Tris-HCl (pH8.5)) + 10 µl of Proteinase K.
- Inactivate Proteinase K by warming samples up for 2 min at 80 °C and cool down on ice.
- Spin at 18,000 g for 15 min at room temperature (RT). Transfer supernatant to new eppendorf tubes containing 500 µl isopropanol and shake by inversion 10 times.
- Spin at 14,000 x g for 10 min at RT and discard supernatant.
- Wash pellet with 500 µl of EtOH 70 %.
- Spin at 14,000 x g for 5 min at RT and discard supernatant and let pellets dry capsized for 1 h.
- Before PCR, DNA is resuspended in 500 µL of water and heated for 2 min at 65 °C.
- PCR master mix is prepared for the total number of samples of the run. Primers used are detailed in *section 7.1.6.* For each sample the mix contains: 18.8 µl H2O, 2.5 µl 10xBuffer, 0.5 µl dNTPs (10 mM each), 0.5µl of each primer at 10 µM, 0.125 µl DNA Pol (Biotools 5U/ µl ref. 10043) and 1.5 µl DNA.
- The PCR program is: 4 min at 95 °C, 35 cycles of (30 s at 95 °C, 30 s at 60 °C and 3 min at 72 °C), 10 min at 72 °C and kept at 4 °C.
- Resolve PCR products in an agarose gel and document the resulted bands using a trans-illuminator. *Mfn1* $^{-/-}$ resulted in a band of 800 bp, *Mfn1*$^{f/f}$ resulted in a band of 1100bp. Regarding the Cre recombinase, the PCR assessed presence or absence of Cre: Cre negative 0 bp, and Cre positive 600 bp.

7.2.1.3. Mice treatments

Anti-inflammatory drugs were injected intra-peritoneally in two different settings:

- Acute treatment: one injection of the TLR9 antagonist ODN2088 (Invivogen)[190] was administered at a dose of 100ug/mice. For this, 1000 ug of ODN2088 were dissolved in 1 mL of endotoxin-free water and 100 uL of this solution were injected to each mouse. Forty-eight hours later, mice were euthanized and muscle samples were obtained. Negative controls were injected with 100 uL endotoxin-free water.
- Chronic treatment: daily sodium salicylate (Sigma)[204] injections were administered at a dose of 200mg/kg for 28 days. For this, sodium salicylate solutions at 40mg/mL in filtered PBS were prepared and mice were weighted weekly. Negative controls were injected with filtered PBS solutions.

7.2.1.4. Blood extraction and sample processing

Mice were immobilized and the tips of their tails were cut with the scalpel. Blood drops were collected in EDTA-containing capillary blood collection tubes (Microvette®, VWR) until the desired blood volume was obtained, allowing proper blood flow by massaging the tail. Then, blood samples were centrifuged at 2,500 rpm at 4 °C for 30 min, allowing separation of blood cells (pellet) and plasma (supernatant). The plasma was collected in Eppendorf tubes and stored at -20 °C.

7.2.1.5. Glucose tolerance test

The day of the experiment, 5g/mL Beta-D(+)-glucose (Sigma-Aldrich, catalog number: G8270) solution in saline (0.9 % NaCl) was prepared and blood glucose was measured at time 0 (basal levels) to fasted mice (16 h fasting) using an Accu-

Chek glucose monitor (Roche Diagnostics Corp.). Then, 1.5g/Kg of glucose solution was injected by intraperitoneal injection and blood glucose was monitored at 5 min, 15 min, 30 min, 60 min, 90 min and 120 min after injection. Blood samples were obtained in Microvettes® at 0 min, 5 min, 15 min 30 min and 60 min, and they were stored at 4 °C during the experiment. Plasmas were obtained as explained in section 7.2.1.4. for insulinemia analysis.

7.2.1.6. Insulin tolerance test

The day of the experiment, 0.06 U/mL in saline (0.9 % NaCl) was prepared and blood glucose was at time 0 (basal levels) to fasted mice (4 h fasting). Then, 0.6 U/Kg insulin was injected by intraperitoneal injection and blood glucose was monitored at 15 min, 30 min and 60 min.

7.2.1.7. Body mass composition assessment

The EchoMRI™ technology was used to acquire precise body composition measurements of fat, lean, free water and total water masses. Each measurement was made twice for each mouse.

7.2.1.8. Acute exercise on treadmill until exhaustion

Prior to the treadmill test, mice were acclimated over two consecutive days on the treadmill (BIOSEB) by 5 min of familiarization with no engagement of the treadmill belt and then 8 min of running at a speed of 14 cm/s and an incline of 0%. The mice rested on the following day. Next, they were subjected to two consecutive days of exercise until exhaustion. This protocol consisted of 8 min at a starting speed of 14 cm/s, which was increased by 2 cm every 2 min until reaching the maximal speed of 46 cm/s. Exhaustion was determined when mice

failed to re-engage the belt after falling onto the grid. The inclination was kept at 0% during the experiment and the intensity of the negative stimulus of the grid was set at the minimum, (0.2 mA). After each training, blood samples were obtained for plasma acquisition (see figure 62).

7.2.1.9. Respirometry

7.2.1.9.1. In vivo indirect calorimetry by Oxymax

Measurements of oxygen consumption (VO2) and CO2 production (VCO2) were performed using an indirect calorimetry system (Oxymax, Columbus Instruments). Mice were placed in the oxymax metabolic cages and provided with a standard chow-diet and water *ad libitum* for four days, during the first of which VO2 and VCO2 measurements were not taken and it accounted for acclimatization. Food intake and body weight was measured every day. At the end of the experiment, all the data was exported to Excel.

7.2.1.9.2. Ex vivo high-resolution respirometry by Oroboros

The respiration of permeabilized muscle was measured at 37 °C by high resolution respirometry with an Oxygraph-2k (Oroboros Instruments), as described[240]. Mice were euthanized and the tibialis muscle was removed and placed on a plastic Petri dish containing 1 mL of ice-cold isolation (BIOPS) solution. Individual fiber bundles were separated with two pairs of sharp forceps and then permeabilized for 30 min in 2 mL of ice-cold BIOPS solution containing 50 µg/mL saponin. After rinsing muscle bundles in respiration (MIRO5) medium. These solutions were composed by:

- BIOPS (isolation solution): 10 mM Ca-EGTA buffer (2.77 mM of CaK2EGTA + 7.23 mM of K2EGTA), 20 mM imidazole, 20 mM taurine, 50 mM K-MES, 3 mM K2HPO4, 6.5 mM MgCl2, 5.7 mM ATP, 15 mM phosphocreatine, and 0.5 mM DTT (pH 7.1).

- MIRO5 (respiration medium): 0.5 mM EGTA, 3 mM MgCl2·6H2O, 20 mM taurine, 10 mM KH2PO4 20 mM HEPES, 1 g/L BSA, 60 mM K-lactobionate, and 110 mM sucrose (pH 7.1).

Fibres were weighed and transferred (typically 2–4 mg wet weight) into the Oxygraph chamber containing 2 mL of air-saturated MIRO5 medium. All respiration measurements were made in duplicate and using the following protocol:

- Resting respiration (state 2, absence of adenylates) was assessed by the addition of 10 mM glutamate and 2 mM malate as the complex I substrate supply.
- State 3 respiration was assessed by the addition of 2.5 mM ADP.
- The addition of 10 mM succinate provided state 3 respiration with parallel electron input to complexes I and II.
- We examined ADP control of coupled respiration and uncoupling control through the addition of 1 uM of the uncoupler [(3-chlorophenyl) hydrazono] malononitrile (CCCP) (optimum concentration for maximal flux).
- The addition of 0.5 µM rotenone inhibited complex I, thereby allowing examination of O2 flux with the complex II substrate alone.
- 2.5 µM antimycin A was added to inhibit complex III in order to observe non-mitochondrial respiration.

The concentrations of substrates and inhibitors used were based on prior experiments conducted to optimize the titration protocols.

7.2.1.10. Histological analysis

For light microscopy, muscles were removed, fixed in PFA 4 % (Santa Cruz) and O/N at 4 °C. After being passed to sodium azide-containing PBS, which prevents

bacterial growth, the processing protocol was performed by the Histology Facility of the IRB and it was performed as follows: 10 µm cryosections of soleus, gastrocnemius and quadriceps muscles were generated and stained with:

a) Hematoxylin and eosin: following manufacturers standard protocol (CoverStainer, Dako – Agilent). Cross-Sectional Area (CSA) quantification was obtained using ImageJ.

b) Immunohistochemistry (IHC) against IL1β or F4/80: Ventana Discovery XT platform was used. Antigen retrieval was performed with proteinase K (S3020, Dako -Agilent) for 5 min at room temperature (RT) or with citrate buffer pH6 for 20 min at 97ºC with a pt link (Dako-Agilent), respectively. Blocking was done with Casein (ref: 760-219, Roche). Blocking was performed with Peroxidase-Blocking Solution at RT (S2023, Agilent) and 5 % of goat normal serum (16210064, Life technology) mixed with 2.5 % BSA diluted in wash buffer for 10 and 60 min at RT. Antigen–secondary antibody complexes were revealed with the 3-3'-diaminobenzidine (K346811, Agilent). Sections were counterstained with hematoxylin (CS700, Dako, Agilent) and mounted with Mounting Medium, Toluene-Free (CS705, Agilent) using a Dako CoverStainer. Specificity of staining was confirmed by staining with a rat IgG (ref: 6-001-F, R&D Systems, Biotechne) or a Rabbit IgG (ab27478, Abcam) isotype control.

c) Immunofluorescence for fiber typing: Previously starting the staining, samples were fixed with 10% of neutral buffer formalin, 10 min, at RT. Primary antibodies were incubated O/N at 4 ºC. Blocking was performed with 3% of fetal bovine serum for 120 min. Secondary antibodies were diluted at 1:500 for 60min and mounted with Fluorescence mounting medium (S3023 Dako). Specificity of staining was confirmed by staining with Mouse IgG2B Isotype Control (MAB0042, R&D Systems), mouse

IgG1, Kappa Monoclonal (NCG01) Isotype Control (ab81032, Abcam) or a mouse IgM (PFR-03) Isotype Control (A1-10438, Thermo).

Brightfield images were acquired with a NanoZoomer-2.0 HT C9600 digital scanner (Hamamatsu) equipped with a 20X objective. All images were visualized with a gamma correction set at 1.8 in the image control panel of the NDP.view 2 U12388-01 software (Hamamatsu, Photonics, France). Digital scanned fluorescent images were acquired using a NanoZoomer-2.0 HT C9600 scanner (Hamamatsu, Photonics, France) with the 20X objective and coupled to a mercury lamp unit L11600-05 and using NDP.scan3.3 software U10074-03 (Hamamatsu, Photonics, France). All images were visualized with a gamma correction set at 1.0 and the sharpen filter enabled in the image controls panel of the NDP.view 2 U12388-01 software (Hamamatsu, Photonics, France). Signal of all the samples has been acquired with the filter DAPI350 with an exposure time of 113ms and a gain of 6. Signal of all the samples has been acquired with the FITC filter with an exposure time of 57ms and a gain of 3. IV58B6 -Alexa 488 signal of all the samples has been acquired with the FITC filter with an exposure time of 113ms and a gain of 3. Signal of all the samples has been acquired with the TRITC filter with an exposure time of 28ms and a gain of 3.

7.2.1.11. Transmission electron microscopy in muscle tissues

Right after euthanasia, quadriceps muscles were dissected and cut into pieces of about 1 mm^3. Then the pieces of interest were transferred to glass vials filled with 2 % paraformaldehyde and 2.5 % glutaraldehyde in phosphate buffer. They were kept in the fixative for 24 h at 4 °C. The processing protocol was performed by the Electron Microscopy Facility of the IRB and it was performed as follows:

- Samples were then washed with the same buffer and post-fixed with 1 % osmium tetroxide in the same buffer containing 0.8 % potassium ferricyanide at 4 °C.
- The samples were then dehydrated in acetone, infiltrated with Epon resin for 2 days, embedded in the same resin orientated for longitudinal sectioning, and polymerized at 60 °C for 48 h.
- Semi-thin sections were made in order to corroborate that the orientation was satisfactory under the light microscope.
- Ultrathin sections were obtained using a Leica Ultracut UC6 ultramicrotome (Leica Microsystems, Vienna, Austria) and mounted on Formvar-coated copper grids.
- They were stained with 2 % uranyl acetate in water and lead citrate.

Sections were then observed undera JEM-1010 electron microscope (Jeol, Japan) equipped with a CCD camera SIS Megaview III and the AnalySIS software and the analysis was performed using ImageJ.

7.2.1.12. RNA extraction from muscle tissues

RNA from tissues was isolated by using the Trizol reagent followed by purification with PureLink RNA Mini Kit (Invitrogen) from approximately 20mg of tissue (further details in *section 7.2.3.5*). The concentration of total RNA extractions was quantified with the Nanodrop One (Thermo Fisher). Subsequent cDNA generation and qPCR are specified in section *section 7.2.3.5.*

.

7.2.2. Cell culture studies

7.2.2.1. Cell maintenance

The present work used C2C12 mouse skeletal muscle cells in myoblast differentiation state as a cellular model. Cells were obtained from ATCC CRL-

1772™. HEK293T were also used as lentiviral producing cells, these cells were provided by Dr Daniel Bach and Dr Didier Trono from EPH Lausana. C2C12 myoblasts were in DMEM (Invitrogen) with 10% FBS and 100 U/ml of penicillin/streptomycin (Invitrogen) (Growing medium) at 37 °C in a humidified atmosphere of 5 % CO2 and 95 % O2. Maintenance of C2C12 myoblasts required regular splitting. Three times a week cells were split: medium was aspirated from the 75 cm^2 flasks and one wash was performed by adding 5 mL of PBS. Then, 2 mL of trypsin were added and incubated for 2 min at RT. Trypsin was inactivated by the addition of 13 mL of compete media to the flask. Approximately 15 mL of cells in suspension was retrieved and the appropriate dilution was done (usually 1:5 to 1:10). Mycoplasma detection test was performed to ensure no contamination of the cells bi-monthly. When mycoplasma was detected the cells were either discarded or decontaminated with Plasmocin Treatment (Invivogen) for 2 weeks. To prevent contaminations, cells could be treated with Plasmocin Prophylactic (Invivogen).

Cellular stocks were kept at liquid nitrogen or -80°C. Cell freezing was performed by resuspension of approximately 2.5 million cells in 1.5 mL of freezing media (10% DMSO in FBS) in cryovials labelled appropriately. Cells were stored at -80 °C in boxes, and after 3-5 days those could be moved into liquid nitrogen tanks. C2C12 cells were always frozen at myoblast differentiation state. To thaw cell aliquots, cryovials were rapidly places at 37 °C water-bath to allow rapid thawing. Cells were then mixed in 10 mL of complete media and placed in the incubator.

7.2.2.2. Cell treatments and transfections

In order to perform the experiments related to the inflammatory phenotype rescue, cells were treated with inhibitors of the different pathways assessed. ODN2088 was used as an antagonist for TLR9[190], Ru.521 was used to inhibit the enzymatic activity of cGAS[191] and VBIT-4 was used to block VDAC pore

oligomerization[198]. The conditions optimized for each treatment are specified in *section 7.1.1*.

Transfections of short interference RNAs (siRNA) (*section 7.1.2)* or plasmids (FLAG-Rab5c) (*section 7.1.1)* were performed in myoblasts (myotubes present a very low transfection efficiency) at a 40-60 % confluency using Lipofectamine 2000 according to manufacturer's instructions. Briefly, two solutions were separately prepared: a Lipofectamine 2000 with OptiMEM solution and an siRNA with OptiMEM solution. After incubating the solutions for 5 min at RT, both solutions were combined and dispensed to the cells, which were placed at 37 °C for 24 h. The final concentrations used were 10 nM for siRNAs and 0.25 % for Lipofectamine 2000. In the case of overexpression vector transfection, 10ug were transfected in 15cm plates using 75uL of Lipofectamine 2000.

7.2.2.3. Generation of C2C12 stable knock-down cell line

Sequences encoding for shRNA were delivered to C2C12 myoblasts using lentiviral infection[241] in order to allow their stable expression. C2C12 stably expressing scramble shRNA (Scr) were used in parallel in all the experiments. Lentiviruses were produced by transfection of second-generation lentiviral packing plasmids and pLKO.1 (shRNA stable expression and antibiotic selection, Sigma) into a human embryonic kidney cell line (HEK 293T), using the following protocol:

- Day 0: Twenty-four hours before transfection, 3 million HEK293T cells are plated in a petri dish of 100 mm of diameter (p10), to achieve 70 % confluence at the moment of transfection.
- Day 1: Mix plasmids in 1560 µL of filtered 150 mM NaCl: 5 µg of pMD2.g + 5 µg of PAX2 + 10 µg of de specific pLKO.1 (*section 7.1.4*), and let the mixture equilibrate for 5 min.

- Add 78 µL of 40K-PEI (1mg/mL pH=7, filtered with 0.2mm filter) to the mixture.
- Incubate for 20 min at RT to allow the formation of DNA-PEI complexes.
- Add the transfection mixture gently to the media of HEK293T cells.
- After 6-8 h, change transfection media for fresh complete media.
- Place transfected cells in a 33 °C incubator to improve viral particle stability.

Lentiviral production was allowed for 48 h after transfection was performed. 24 h post-transfection (Day 3) C2C12 myoblasts were plated (target cells): 200,000 cells in p10 dishes, one p10 per shRNA, and one extra p10 was plated but not transduced, as a antibiotic selection control. Two subsequent transfections were performed, at day 4 and day 5, following the next protocol:

- Retrieve media containing the viral particles from HEK293T dishes.
- Filter media using a 0.45 µm filter.
- Add polybrene to a final concentration of 2.5 µg/mL to enhance viral infection.
- Add virus-containing and filtered media to the target cells, C2C12 myoblasts.
- Twenty-four to forty-eight hours after the second infection (Day 6-7), remove virus-containing media and add puromycin-supplemented fresh media to all C2C12 containing p10s, including the control p10. The puromycin concentration for antibiotic selection was of 2.5 µg/mL puromycin (Sigma).
- When all cells of the control p10 have died (around 48 h post-selection), reduce the puromycin concentration to 1 ug/mL.

All the work involving lentiviral viruses was performed in a cell culture room with a biosafety level of 2 and a hood with biosafety category IIA. When working with puromycin-resistant stable knock-down cell lines, the growing/differentiation

media was supplemented with 1 ug/mL of puromycin to prevent the growth of spontaneous mutants that may reduce the knock-down yield of the cell population.

7.2.2.4. In vitro respirometry: Seahorse

C2C12 cells were plated on Seahorse Bioscience XF24 plates. When working with myoblasts, cells were allowed to grow for 24 h after seeding and oxygen consumption was measured using a Seahorse Bioscience XF24 extracellular flux analyzer. In the case of myotubes, differentiation took place in the Seahorse Bioscience XF24 plates and once cells had undergone full differentiation to myotubes, oxygen consumption was measured. The instrument was calibrated the day before the experiment following the manufacturer's instructions. On the day of the experiment, the injection ports on the sensor cartridge were loaded with 1.25 µM oligomycin (complex V inhibitor) to distinguish the percentage of oxygen consumption devoted to ATP synthesis and the percentage required to overcome the natural proton leak across the inner mitochondrial membrane. We used 1 µM CCCP to calculate the maximal respiratory capacity of cells, which is defined as the quantitative difference between maximal uncontrolled OCR and the initial basal OCR, and 0.1 µM rotenone (complex I inhibitor) and 0.1 µM antimycin A (complex III inhibitor) to calculate the remaining respiration caused by oxidative side reactions. During the sensor calibration, cells were kept in a 37 °C incubator without CO2 in 700 µl of respiration buffer (DMEM, 5 mM glucose, 2 mM glutamine, 31.6 mM NaCl and Phenol Red). Plates were immediately placed in a calibrated Seahorse XF24 flux analyzer for mitochondrial bioenergetics analysis. Extracellular acidification rate of C2C12 cells (ECAR) was measured in parallel. After the experiment, the sensor plate was discarded and the plates cell plate was used to calculate the protein amount per well and use this value to obtain the OCR quantification per ug of protein.

7.2.2.5. Immunofluorescence and super-resolution confocal imaging

Cells were plated on 12 mm diameter coverslips in 24-well plates, 15,000 cells/well, to obtain a 50-70 % confluence upon fixation the next day. Cells were fixed in 4 % paraformaldehyde (PFA) in PBS for 20 min and washed with 50 mM NH4Cl. Immunofluorescence was performed as follows:

- In the cases when dsDNA is the target of the immunofluorescence cells were permeabilized in buffer A (0.1 % Triton X-100, 3 % FBS in PBS) for 30 min. Alternatively, when dsDNA is not immunolabeled, in order to avoid the extraction of membrane proteins from membranes as a result of Triton X-100 action, this step with buffer A was skipped.
- Incubate coverslips in plate for 10 min in approximately 200 µl of buffer B (0.05 % Saponin, 2 % FBS in PBS), which allow moderate permeabilization and blocking of the fixed cells.
- Dilute all primary antibodies in buffer B (dilutions specified in *section 7.1.7.1*) and distribute 35-40 µl drops on a flat parafilm piece.
- Place coverslips cell-face down on primary antibody drops and incubate in a dark wet chamber for 30 min.
- Return coverslips to plate and wash three times for 10 min with buffer B.
- Dilute all secondary antibodies in buffer B (dilutions specified in *section 7.1.7.2*) and distribute 35-40 µl drops on a flat parafilm piece.
- Place coverslips cell-face down on secondary antibody drops and incubate in a dark wet chamber for 30 min.
- Return coverslips to plate and wash three times for 10 min with buffer B.
- Wash coverslips in plate twice for 10 min with PBS.
- Dilute Hoechst 33342 1:10,000 in PBS and distribute 35-40 µl drops on a flat parafilm piece.

- Place coverslips cell-face down on Hoechst drops and incubate in a dark wet chamber for 10 min.
- Return coverslips to plate and washed twice with PBS.
- Mount coverslips onto microscope slides using Flouromount (Sigma).
- Let slides dry O/N at RT and then keep them in microscopy slides boxes at 4 °C.

Importantly, secondary antibodies must not recognize each other. In our lab, it had been detected that our anti-mouse antibody conjugated to alexa-568 (anti-mouse) was binding LAMP1 antibody raised in rat. To avoid cross-recognition, a different incubation condition was optimized in order to restrict the affinity of anti-mouse to rat IgG. First, the secondary antibodies were incubated in two steps: first anti-rat and anti-rabbit secondary antibodies and then anti-mouse secondary antibody, with the aim of covering the rat IgG. Besides, the concentration of anti-mouse antibody was reduced from 1:800 to 1:1,600 and the concentration of FBS in buffer B was increased from 2 % to 4 % as the blocking agent to reduce unspecific binding.

All immunofluorescences were imaged using the Airyscan detector from the Zeiss LSM 880 Super-resolution microscope with a x64 magnification oil objective lens with 1.40 NA. Image processing and quantification were performed using ImageJ software. All images of samples targeted for dsDNA were processed before quantification with a Macro designed by Dr. Nikolaos Nikiforos Giakoumakis from the Advanced Digital Microscopy Facility of the IRB Barcelona to remove the nuclei and allow a more accurate and faster quantification. Co-distribution studies were assessed with the plugin *"JACoP"*[242]. The quantification of the branch length of the mitochondrial network was performed with the plugin "*MiNA*". 3D image reconstructions were obtained from edited (nuclei removal) Z-stack images using IMARIS software.

7.2.2.6. Transmission electron microscopy and immunolabeling

Samples were prepared at the Electron Cryomicroscopy Unit from the CCiTUB, University of Barcelona by Yolanda Muela. Scr and Mfn1KD C2C12 myoblasts were washed twice with 0.1 M phosphate buffer (PB) at room temperature. For fixation, cells were fixed in 4 % paraformaldehyde 0.1 % glutaraldehyde in 0.1 M PB at room temperature for 60 min. Then, they were kept in 2 % paraformaldehyde in 0.1 M PB till at 4 ^{o}C an overnight. Samples were cryoimmobilized in 15 % dextran in 10 mM PBS as a cryoprotectant using a Leica HPM100 High-Pressure Freezer (Leica Microsystems, Vienna, Austria). Planchettes containing the frozen samples were transferred to cryotubes containing 0.5 % uranyl acetate (EMS, Hatfield, USA) in acetone under liquid nitrogen and were freeze substituted at -90 ^{o}C for 80 h in an EM AFS2 (Leica Microsystems, Vienna, Austria). Samples were warmed up to -40 ^{o}C at 5 ^{o}C/h slope and kept at -40 ^{o}C. They were rinsed with acetone and infiltrated in Lowicryl HM23 resin (EMS, Hatfield, USA) at -40 ^{o}C. Samples were polymerized under UV light: at – 40 ^{o}C for 24 h, during the warming up at 5 ^{o}C/h slope until 22 ^{o}C and at 22 ^{o}C for 48 h. Sections of 60 nm in thickness were obtained using a UC6 ultramicrotome (Leica Microsystems, Vienna, Austria). They were washed sequentially in 10 mM PBS, 10 mM glycine and 10 mM PBS. Then they were incubated on drops of 5 % bovine serum albumin (BSA) in 10 mM PBS for 20 min and they were changed to 1 % BSA in 10 mM PBS drops, followed by the incubation with SDHA antibody (1:20, ThermoFisherPro) and RAB5 antibody (1:4, Cell Signalling) in 10 mM PBS for 1 h. Then, they were washed in 0.25 % Tween 20 in 10 mM PBS and they were changed to 1 % BSA in 10 mM PBS, followed by the incubation in anti-mouse 12 nm 1:30 (Jackson) and anti-rabbit 18 nm 1:30 (Jackson) in 1 % BSA 10 mM PBS for 30 min. Samples were washed in 10 mM PBS, incubated in 1 % glutaraldehyde in PBS for 5 min and rinsed in milliQ water. As a negative control for non-specific binding of the colloidal gold-conjugated

antibody, the primary polyclonal antibody was omitted. Sections were stained with 2 % uranyl acetate and lead citrate and were observed in a Tecnai™ Spirit TWIN microscope (FEI, Eindoven, The Netherlands) equipped with a tungsten cathode from the Electron Cryomicroscopy Unit from the CCiTUB. Images were acquired at 120 kV with a CCD Megaview 1kx1k.

7.2.2.7. Flow cytometry analyses

Flow cytometry analyses allowed the assessment of different cellular parameters, including mitochondrial and lysosomal ones, incubating cells with different dyes (*section 7.1.1.*) and quantifying such parameters *in situ*. When using either myoblasts or myotubes, cells at 85 % or full confluency, respectively, were treated with different dyes for different times. Then, cells were washed with PBS, trypsinized, resuspended in 500 uL of growing or differentiation medium, according to the cell type used, and collected in 12 x 75 mm tubes. The Gallios Flow Cytometer (Beckman Coulter) was used to take the measurements and the settings were standardized according to the parameter to be assessed.

7.2.2.7.1. Assessment of mitochondrial parameters

The mitochondrial parameters assessed include mitochondrial mass (MitoTracker green), ΔΨm (TMRM) and mitochondrial superoxide (MitoSOX). Both TMRM and MitoSOX mean values were corrected by MitoTracker values, allowing quantification of either ΔΨm or mitochondrial superoxide per total mitochondrial mass per cell.

7.2.2.7.2. Mitophagy assessment

Mitophagy assessment through flow cytometry consists on the quantification of the total mitochondrial mass per cell in the presence or absence of a lysosomal

inhibitor. Therefore, the ratio +inhibitor/-inhibitor provides understanding on whether the mitophagic flux is promoted or inhibited in the case comparing to the control cells. The day before the experiment, cells were treated with 50 nM of MitoTracker DR for 30 min in order to stain all mitochondria of the cells. Then, the media was replaced with fresh media containing the lysosomal inhibitor (usually 200 nM of bafilomycin A1) or a control (DMSO). Cells were incubated for O/N, trypsinized, harvested and their mitochondrial mass was quantified the following day.

7.2.3. General molecular biology and biochemistry protocols

7.2.3.1. Cytosolic fraction obtention from C2C12 cells

To obtain cytosolic fractions, digitonin was used to slightly permeabilized the plasma membrane using the following protocol adapted from[121]:

- Trypsinize and count cells at least 10 million cells per condition are needed. Split the same number of cells into two 15mL falcon tubes: 5 million cells each.
- Spin cells at 500 x g and wash with 1mL of PBS and transfer to 1.5mL Eppendorf tubes named: “Total homogenate” and “Pellet”.
- Dived the “total homogenate” suspension into two tubes: for western blot and genomic DNA (gDNA) analysis, 2.5 million cells each.
- Spin all three tubes and aspirate PBS. Keep total homogenate tubes on ice or -20 °C for future processing.
- Resuspend the pellet in “Pellet” tube with 500 µL of digitonin buffer (150 mM NaCl, 50mM HEPES pH=7,4, 50 µg/mL Digitonin (Sigma)).
- Incubate end over end for 10min 4 °C to allow selective plasma membrane permeabilization.
- Spin at 980 x g for 4 min at 4 °C. Transfer the supernatant to a new tube and save the first pellet as “Pellet”.

- Spin at 980 x g for 4 min at 4 °C and transfer the supernatant to a new tube. Spin at 17,000 x g for 10 min at 4 °C to pellet any remaining cellular debris, yielding cytosolic preparations free of nuclear, mitochondrial and endoplasmic reticulum contamination. Transfer the supernatant to a new tube named “cytosol” and save it as the cytosolic fraction.
- Divide the three fractions (Total homogenate, pellet and cytosol) into two tubes, each for subsequent genomic DNA (gDNA) or western bolt analysis.

7.2.3.2. Protein extraction, concentration quantification and western blotting

Total cellular protein extracts for western blot analysis were performed as follows: cells were rinsed in ice-cold PBS and scraped from culture plates in lysis buffer (50 mM Tris pH 8, 150 mM NaCl, 1% NP-40, 0.1% SDS, 1 mM EDTA, 50 mM NaF, 5 mM sodium pyrophosphate and protease inhibitors cocktail tablet). Cellular primary homogenates from plate were further homogenized by passing them through a 25G syringe avoiding the generation of bubble or foam. Homogenates were centrifuged at 13,000 rpm for 30 min at 4 °C and supernatants protein extracts were transferred to new tubes and kept at -20 °C. Tissue samples were homogenized in 10 volumes of lysis buffer using polytron. Homogenates were rotated for 1h at 4 °C and centrifuged at 13,000 rpm for 15 min at 4 °C.

Protein quantification was performed using the Pierce BCA Protein assay kit (Thermo Fisher Scientific). Briefly, a standard curve is generated between 1 mg/mL to 10 mg/mL BSA. After sample distribution in a 96 well-plate, 200 µL of reaction mixture (A+B solutions at 50:1 ratio) was added to each well using a multichannel pipette to avoid differential time of incubation throughout the plate. The plate was incubated for 30 min at 37 °C and absorbance at 562 nm was measured. Sample protein concentration was calculated by interpolation

from the standard curve. All protein extracts, obtained either from cells or tissues, were stored at -20 °C.

To quantify protein abundance, western blotting was performed. For that, samples were prepared by the addition of the specific volume of sample (to add from 10-50 µg of protein, depending on the protein to be assessed) and Loading Sample Buffer with 100 mM DTT to ensure denaturing of protein secondary structures and disulfide bridges. Samples were boiled at 95 °C for 5 min and loaded into SDS-PAGE gels, which allowed protein resolving by size by electrophoresis. The resolving gel had different concentrations of acrylamide depending on the size of proteins to be resolved (usually 7.5 %, 10 % 12.5% or 15 %). Samples were run besides a molecular weight marker Spectra™ Multicolor Broad Range Protein Ladder (Thermo Fisher Scientific). Voltage was maintained at 30mA per gel until the blue color front given by the Loading Sample buffer escaped from the bottom part of the gel. Then, proteins resolved in the electrophoresis gel were transferred to Immobilon PVDF membranes (Millipore) for 3 h at 250 mA in the presence of iced-gel blocks or by O/N at 97mAmp at RT. Membranes were blocked in 5 % milk in PBS-Tween (PBS-T: 0,1 % Tween in PBS 1X buffer) for 30 min-1 h at RT. Membranes were incubated in primary antibody diluted as specified in *section 7.1.7.1.*, in PBS-T O/N at 4 °C. Membranes were washed three times for 5 min with PBS-T and then incubated for 1 h at RT with diluted secondary antibodies (as specified in *section 7.1.7.2*), and then, membranes were washed three times with PBS-T for 5 min. Two developing techniques were performed:

- Chemi-luminiscence: Horseradish peroxidase (HRP)-conjugated secondary antibodies diluted in PBS-T were used. After the appropriate washes, membranes were exposed to developing agents' mixture 1:1 for 1 min (Ge Healthcare), and immediately after, placed into developing

cassettes. In the dark room, films were expose to membranes with chemiluminescent bands and developed using a HyperProcessorR Model AM4 (Amersham Pharmacia Biotech).

- Fluorescence: fluorochrome-conjugated secondary antibodies diluted in PBS-T were used. After the appropriate washes, membranes were scanned by the Odyssay (Li-COR) membrane scanning system.

In the case that membranes were reused with other antibodies, they were stripped incubating the membranes twice for 5 min with boiling water, or 15 min with the Restore™ Western Blot Stripping Buffer (ThermoFisher Scientific). At this state, membranes had to be blocked again with 5 % milk in PBS-T. Bands were quantified using QuantityOne (Bio-Rad).

7.2.3.3. Immunoprecipitation

Myoblasts were grown in 6 15 cm plates and transfected with 10 ug of FLAG-RAB5C (HG15817-NF, SinoBiological) per plate. Forty-eight hours after transfection, cells were collected and solubilized in lysis buffer (Tris HCl 50 mM, NaCl 150 mM, EDTA 5 mM, 1 % digitonin)* for 20 min in ice to allow homogenization. Samples were centrifuged at 21,000 g for 10 min at 4 ºC and supernatants were kept. A fraction of the lysate of each sample was kept as an input control. 20-30 uL of magnetic anti-FLAG magnetic beads (Sigma Aldrich) were incubated with 2.5-5 mg of protein from lysates O/N at 4 ºC. Unbound supernatant was separated from the beads using a magnetic rack (Applied Biosystems Dynal MPC-S Dynabeads). A fraction of each supernatant was kept as an unbound or flowthrough control and the rest was discarded. Beads were washed 3 times in wash buffer (Tris HCl 50 mM, NaCl 150 mM, EDTA 5 mM, 0.1% digitonin)*. Elution was achieved by incubating the beads with 20uL of 1:50 FLAG peptide (Sigma Aldrich) for 15 min in ice. All input, unbound (flowthrough, FT)

and immunoprecipitated fractions were mixed with 4X LSB+DTT and loaded in a western blot.

*Lysis and wash buffer preparation: 0.05 g of digitonin were loaded in 1 mL of solution A, containing Tris HCl 50 mM, NaCl 150 mM and EDTA 5 mM. Tube was warmed up at 95 ºC for 15 min at a 450 rpm shaking speed. Once dissolved, it was diluted in 4 mL of solution A in order to obtain the lysis buffer. Wash buffer was obtained diluting the lysis buffer 1:10 in solution A. Both lysis and wash buffers were stored at -20 ºC.

7.2.3.4. DNA extraction and concentration quantification

Total genomic DNA was extracted from cells from using DNeasyR Blood & Tissue Kit columns (Qiagen) following the manufacturer's instructions:

- Resuspend in pellet fractions or cells in 200 µL of PBS and add 20 µL of proteinase K.
- Add 200 µL of Buffer AL. Mix thoroughly by vortexing.
- Incubate the samples at 56 °C for 10 min. Add 200 µL ethanol (96-100%). Mix thoroughly by vortexing.
- Pipet the mixture into a DNeasy Mini spin column placed in a 2 mL collection tube. Centrifuge at 6000 x g for 1 min. Discard the flow-through and add 500 µL of Buffer AW1.
- Centrifuge for 1 min at 6000 x g. Discard the flow-through and add 500 µL of Buffer AW2
- Centrifuge for 3 min at 20000 x g. Transfer the spin column to a new 1.5 mL Eppendorf tube.
- Elute DNA from cell suspensions/pellet fractions with 100 µL of Buffer AE, and cytosolic fraction with 50 µL of Buffer AE.

Incubate for 1 min at RT and centrifuge for 1 min at 6000 x g. DNA was quantified using Nanodrop™ 2000/2000c spectrometer (Thermo Fisher Scientific) and the

ND1000 software (Thermo Fisher Scientific). DNA purity was determined by the A260/A280 and A260/A230 absorbance ratio. A A260/A280 ratio of 1.8 is accepted as pure DNA. Samples were stored at -20 °C.

7.2.3.5. RNA extraction and quantification, retro-transcription reaction and qPCR

RNA extraction from tissues was performed using RNAeasyR minikit columns (Qiagen), following the manufacturer's instructions. Briefly, cellular lysis was performed using Lysis buffer from the kit containing 2 % DTT and 25G syringe homogenization. Then, RNA purification followed the next protocol:

- Add one volume 70 % ethanol in RNase-free water to each volume of cell or tissue homogenate.
- Transfer up to 700 µL of the sample to the spin cartridge with a collection tube.
- Centrifuge at 12,000 x g for 30 s at RT. Discard the flow-through and add 700 µL Wash Buffer I to the spin cartridge.
- Centrifuge at 12000 x g for 30 s at RT. Discard the flow-through and add 500 µL Wash Buffer II to the spin cartridge.
- Centrifuge at 12,000 x g for 30 s at RT. Discard the flow-through.
- Repeat step wash step with Wash Buffer II. Centrifuge the spin cartridge at 12,000 x g for 1-2 min to dry the membrane with bound RNA.
- Add 30 µL RNase-free water and incubate at RT for 1 minute.
- Elute by centrifugation at 12,000 x g for 2 min at RT.

RNA samples were quantified using the Nanodrop™ 2000/2000c spectrometer (Thermo Fisher Scientific) and the ND1000 software (Thermo Fisher Scientific). RNA purity was determined by the A260/A280 and A260/A230 absorbance ratio. A A260/A280 ratio of 2.0 is accepted as pure RNA. RNA samples were stored at -80 °C.

Reverse transcription reaction was performed mixing the RNA samples with 4 uL of qScript cDNA SuperMix (QuantaBio) and using a 2720™ Thermal Cycler (Applied Biosystems). Briefly, 500 ng of RNA and RNase-free water were added to PCR tubes to a final volume of 16 µL. Then, 4 uL of qScript cDNA SuperMix was added to the samples. The reverse transcription reaction cycle was as follows:

- DNA polymerization: at 42 °C for 53 min.
- Reaction stop: at 70 °C for 15 min
- Sample preservation: at 4 °C until sample storage.

Generated cDNAs were diluted to 10 ng/ µL with Milli-Q H2O and stored at 4 °C or -20 °C. To quantify mRNA expression levels, real time quantitative PCR was performed (qPCR). For that, two solutions were separately prepared, with the following volumes per well:

- SYBR-primer mix: 3.8 µL of SYBR Green PCR Master Mix (Applied Biosystems) were combined with 0.6 µL of 10 µM primer mix (forward and reverse). Primers used in the present work are detailed in *section 7.1.5.*
- cDNA: 10 ng/µL cDNA were diluted to 1ng/uL in Milli-Q H2O and 4.8uL of that dilution were used.

Three-hundred and eighty-four-well plates were loaded with 5.2 µL of SYBR-primer mix, and next, 4.8 µL of 1 ng/µL cDNAn sample was loaded, yielding a final reaction volume of 10 uL. RT-PCR negative controls were loaded to identify cross-contamination and 2 technical replicates were analyzed per sample. Quantitative real-time PCR was performed using the QuantStudio 6 and 7 Flex Real-Time PCR System (Applied Biosystems) and the setting of the cycles used was the one suggested by default for comparative Ct studies. All measurements were normalized to housekeeping mRNAs, which include *β-actin*, *Arp*, *Gapdh* or *18s*.

7.2.3.6. Mitochondrial DNA abundance quantification

Quantitative PCR was performed to quantify mtDNA abundance relative to nDNA. For this, after genomic DNA extraction, mtDNA and nDNA sequences were amplified, including *MtD-Loop1/2/3*, *MtCyb*, *MtNd4* and *MtCox2* for the former (*section 7.1.5.)*. 5 ng of gDNA were used and measurements were normalized to *SdhA* or *β-actin* as nuclear genes.

7.2.3.7. Cytokine and creatine kinase activity quantification in plasma

Plasma concentrations of IL6 and TNFα (Abnova), FGF21 (Millipore) and Insulin (Crystal Chem) were measured by ELISA assay following the manufacturer's instructions in either plasma samples or cell culture mediums. Briefly, a standard curve at known concentration of each factor was assayed in parallel to the samples. Samples were loaded to wells containing immobilized antibody, then, biotinylated antibody was added to the bound samples and Avidin-Biotin-Peroxidase Complex (ABC) was added and developed with TMB. The reaction was stopped using acidic stop solution. The absorbance at 450 nm was measured and sample concentration was interpolated with the standard curve.

Creatine kinase (CK) activity (Sigma Aldrich) was measured in plasmas following manufacturers protocol. In brief, 10 uL of plasmas per duplicate were dispensed to a 96-well plate. Two wells contained 110 uL of water (blank) and two wells contained 10 uL of the Calibrator. 100 uL of Reconstituted reagent (100 uL of assay buffer, 10 uL of substrate solution and 1 uL of enzyme) were added to each well and the plate was incubated for 20 min at either RT or 37 °C. Then, the initial absorbance read at 340 nm was obtained since creatine kinase is fully activated within 20 minutes due to the glutathione present in the substrate solution. The plate was again incubated for 20 min at either RT or 37 °C and a final absorbance

read at 340 nm was obtained. The following formula was applied in order to obtain the creatine kinase activity (units/L) per well:

$$CK\ activity\ (units/L) = \frac{(A_{340})_{final} - (A_{340})_{initial}}{\bar{x}_{(A_{340})_{Calibrator}} - \bar{x}_{(A_{340})_{Blank}}} x150$$

where: 150 is the equivalent activity (units/L) of the calibrator when the initial read is taken at 20 min and at 40 min. All absorbance reads were performed using the TECAN plate reader (Life Sciences TECAN).

7.2.4. Graphics

The graphics shown in figures 1, 2, 3, 4, 5, 9, 27, 38, 48, 62, 72, 73, 74 and 75 were made in ©BioRender - biorender.com (Toronto, Canada).

7.2.5. Statistics

The data presented here were analyzed using the Student *t*-test or analysis of variance (ANOVA) with an appropriate post-hoc test. Data are presented as mean ± SEM unless stated otherwise. Significance was established at $p<0.05$. Statistical analysis was only applied to data from $n \geq 3$ independent experiments.

RESUMEN EN CASTELLANO

8.1. Introducción

8.1.1. Mitocondrias: función, dinámica y degradación.

Las mitocondrias son orgánulos celulares que desarrollan un papel fundamental en diversos procesos biológicos, como la producción de energía en forma de ATP, almacenamiento y gestión del calcio intracelular, señalización de vías de muerte celular como apoptosis, metabolismo y homeostasis del hierro, síntesis de macromoléculas, producción de especies reactivas de oxígeno (ROS) y detección y modulación de respuestas inmunitarias[3,6]. Es por esto que una correcta función mitocondrial es esencial para preservar diversos procesos biológicos y la homeostasis celular.

Debido a su naturaleza dinámica, las mitocondrias interaccionan entre sí mediante eventos de fusión y fisión, los cuales están estrechamente regulados y permiten el correcto funcionamiento de la red mitocondrial. Por ello, el proceso que gobierna la transición de mitocondrias fusionadas a fragmentadas, y viceversa, se denomina dinámica mitocondrial y se lleva a cabo por la acción de grandes GTPasas que conforman su maquinaria central[243]. Por un lado, la fusión mitocondrial es un proceso de dos pasos en el cual dos mitocondrias se fusionan en una. El primer paso depende de la acción de las proteínas mitofusina 1 y 2 (Mfn1/2), que llevan a cabo la fusión de la membrana mitocondrial externa. El siguiente paso es la fusión de la membrana mitocondrial interna, la cual se lleva a cabo por la acción de la proteína Opa1. Las proteasas Yme1L y OMA1 son las responsables del procesamiento de las diferentes isoformas de Opa1, por lo que también se podrían considerar proteínas con efectos en dinámica mitocondrial. Por otro lado, la fisión mitocondrial se lleva a cabo mediante la constricción de las membranas mitocondriales interna y externa de una mitocondria, que desencadena su separación en dos mitocondrias independientes. La proteína

que desarrolla dicha la función de constricción es Drp1, mediante proteínas efectoras como Mff, Fis1, MID49 y MID50.

A la vez que la propia homeostasis mitocondrial es esencial para su función, la degradación controlada de mitocondrias dañadas también es necesaria en la correcta salud mitocondrial. La degradación selectiva de mitocondrias dañadas puede darse por diferentes procesos, incluyendo la autofagia mitocondrial o mitofagia. La mitofagia depende de proteínas que pueden desarrollar diversas funciones mitofágicas, incluyendo etiquetar las mitocondrias dañadas que deben ser degradadas o mediar su incorporación en autofagosomas. Entre dichas proteínas se encuentran Pink1, Parkin, BNIP3 o FUNDC1, entre otras[244]. Además, la dinámica mitocondrial y la mitofagia son dos procesos que están íntimamente interconectados. Varios estudios han demostrado que alteraciones en dinámica mitocondrial disrumpen la mitofagia, y a su vez, está ampliamente aceptado que la mitofagia puede modular la dinámica mitocondrial para poder promover una correcta respuesta a estímulos ambientales[245]. La dinámica mitocondrial, la mitofagia, y su inter-regulación conforman el sistema de control de calidad mitocondrial, el cual es esencial en el desarrollo de diversas enfermedades.

8.1.2 Disfunción mitocondrial en distrofias musculares.

Alteraciones en el sistema de control de calidad mitocondrial han sido asociadas a enfermedades del músculo estriado esquelético, también conocidas como miopatías o distrofias musculares. Dichas enfermedades se caracterizan por la pérdida de masa muscular (sarcopenia), dolor muscular, pérdida de su función y atrofia. A pesar de que la causa de muchas de estas enfermedades es la presencia de mutaciones en genes que codifican para proteínas no mitocondriales, como es el caso de la distrofia muscular de Duchenne (DMD), muchas de ellas están

asociadas a disfunción mitocondrial y alteraciones en auto/mitofagia. Estos casos se conocen como miopatías mitocondriales.

Otros tipos de miopatía con causa desconocida o miopatías idiopáticas son las miopatías inflamatorias o miositis, las cuales se caracterizan por inflamación del tejido muscular y de los tejidos adyacentes, lo cual produce dolor y debilidad muscular, y eventualmente atrofia. Se considera que la inflamación muscular produce disfunción mitocondrial y autofágica; sin embargo, estudios recientes apuntan a que la propia disfunción mitocondrial y/o alteraciones en autofagia pueden desencadenar procesos inflamatorios[51,54,55,70,120,121,160], lo cual cuestiona el hecho de que la inflamación muscular sea un efecto primario o secundario en el desarrollo de la enfermedad. Por lo tanto, esta controversia requiere de una mayor investigación, ya que la correcta identificación de la causa primaria de estas enfermedades promueve el diseño de terapias dirigidas a la base de la enfermedad.

8.1.3. Mitocondrias e inflamación.

Entre las funciones mitocondriales se incluyen la detección y modulación de respuestas inmunitarias[6]. Por un lado, las mitocondrias sirven como plataforma para el reclutamiento y ensamblaje de complejos que conducen respuestas inmunitarias frente a infecciones víricas o bacterianas. Por otro lado, también se consideran fuentes de patrones moleculares asociados a peligro (PAMPs) o a daño (DAMPs), entre los cuales se incluye el ADN mitocondrial (mtDNA)[138]. Numerosas evidencias han descrito que frente a estímulos que disrumpen la homeostasis mitocondrial, el mtDNA escapa del interior de las mitocondrias y, al localizarse en el medio intracelular o extracelular, es reconocido por diversos sensores que activan vías inflamatorias.

En lo que a ello respecta, se han descrito tres sensores de mtDNA con localización intracelular: el receptor tipo *Toll* 9 (TLR9), la sintetasa de GMP-AMP cíclico (cGAS) y los inflamasomas. Por un lado, la localización de mtDNA en el compartimiento endosomal promueve su reconocimiento por TLR9, lo cual activa la secreción de citoquinas dependiente del factor nuclear κB (NF-κB). Por otro lado, cuando el mtDNA o fragmentos del mismo se encuentran libres en el citoplasma, pueden ser reconocidos por cGAS o por los inflamasomas. En este caso, se desencadena tanto la secreción de citoquinas dependiente de NFκB como la respuesta del interferón tipo 1. Por último, la interacción entre inflamasomas y mtDNA promueve la secreción de interleucinas 1β y 18 (IL1β y IL18) mediante la acción de caspasas pro-inflamatorias.

8.1.4. Conectando disfunción mitocondrial, inflamación y distrofias musculares.

Recientes estudios en modelos animales describen los mecanismos moleculares por los cuales alteraciones primarias en la función mitocondrial o en la autofagia resultan en inflamación muscular o sistémica. Por un lado, niveles reducidos de Opa1 en el músculo esquelético promueven la activación de la vía inflamatoria dependiente de NFκB mediante la interacción de mtDNA y TLR9[51]. Además, tanto niveles reducidos de Pink1 o Parkin a nivel global, como de Fis1 específicamente en el músculo esquelético, alteran el proceso de mitofagia, promoviendo la acumulación de mitocondrias dañadas, de las cuales el mtDNA escapa e interacciona con cGAS en el citoplasma dando lugar a inflamación muscular y sistémica[70,120]. Otros estudios con el hígado, el sistema nervioso central o los riñones como tejidos diana, demuestran que niveles reducidos de FUNDC1, Yme1L o TFAM, respectivamente, desencadenan la activación de vías inflamatorias mediante el reconocimiento extra-mitocondrial del

mtDNA[54,55,121,160]. Estas evidencias sugieren que la conexión entre alteraciones primarias en el sistema de control de calidad mitocondrial y la consecuente activación de vías inflamatorias es un mecanismo global que, aplicado al músculo esquelético, puede dar respuestas a los mecanismos moleculares responsables de miopatías inflamatorias, lo cual aportaría un mayor conocimiento en el desarrollo de terapias eficaces diseñadas para tratar la raíz de la enfermedad.

8.2. Objetivos

Dados estos antecedentes, el objetivo principal del trabajo realizado en esta tesis es el de describir los mecanismos moleculares por los que alteraciones en la dinámica mitocondrial desencadenan inflamación en el músculo, así como el impacto fisiológico que esto puede causar. Este objetivo principal se divide en tres partes:

1. Descripción de las alteraciones en la dinámica mitocondrial que inducen inflamación y evaluación de las características moleculares comunes involucradas.
2. Caracterización de los mecanismos moleculares que relacionan la fragmentación mitocondrial inducida por la deficiencia de Mfn1 con la inflamación intracelular.
3. Evaluación del impacto de la depleción de Mfn1 en el desarrollo de la inflamación muscular y atrofia, así como la evaluación de la capacidad física.

8.3. Resultados y discusión

Estudio 1: Características mecanísticas comunes que relacionan desequilibrios en la dinámica mitocondrial con inflamación estéril.

Estudios previos realizados en nuestro grupo de investigación identificaron que la depleción de Opa1 en el músculo esquelético desencadena vías inflamatorias intracelulares dependientes de NFκB y mediadas por el reconocimiento de mtDNA por TLR9[51]. Estos resultados motivaron el estudio del impacto del resto de proteínas de dinámica mitocondrial en la activación de respuestas inflamatorias en células musculares. Para ello, se generaron líneas celulares de músculo esquelético de ratón (mioblastos C2C12) con deficiencia estable de las proteínas Mfn1, Mfn2, Yme1L, Fis1 o Drp1 (Mfn1KD, Mfn2KD, Yme1LKD, Fis1KD y Drp1KD, respectivamente). En paralelo, se generaron líneas celulares control (Scr), las cuales se han utilizado como control negativo en todos los experimentos. Para validar el efecto de la deficiencia de estas proteínas, se evaluó la morfología mitocondrial mediante inmunofluorescencia de la proteína de membrana mitocondrial externa TOM20. Por un lado, la ausencia de Mfn1, Mfn2 o Yme1L dio lugar a fragmentación mitocondrial debido a una disminución en la fusión mitocondrial. El efecto de la deficiencia de Yme1L en la fragmentación de la red mitocondrial se debe a que la ausencia de esta proteína provoca un defecto en el procesamiento de Opa1, dando lugar a menor fusión mitocondrial. Por el otro, la ausencia de Fis1 o Drp1 resulta en el efecto contrario, dando lugar a elongación mitocondrial (Figura 1).

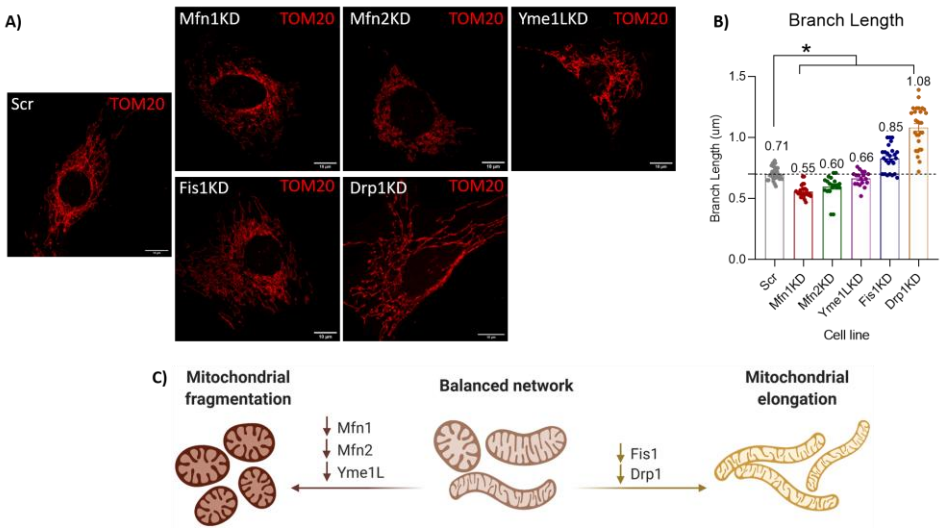

Figura 1: Evaluación de la morfología mitocondrial en las diversas líneas celulares. A) Imagen representativa de inmunofluorescencia contra TOM20 (n=20). B) Cuantificación de la longitud de la rama en la red mitocondrial (n=20). C) Representación esquemática de los efectos de la deficiencia de proteínas de dinámica mitocondrial en la morfología mitocondrial. Los datos representan la media ± SEM. *p<0.05 vs Scr.

Para realizar la caracterización del perfil inflamatorio en cada línea celular, se cuantificó la expresión de genes inflamatorios. Esto demostró que las líneas celulares que presentan fragmentación mitocondrial por ausencia de Mfn1 o Mfn2 presentan una activación exclusiva de genes dependientes de NFκB, mientras que la ausencia de Yme1L induce la activación tanto de la vía mediada por NFκB como la respuesta a interferón de tipo 1 (Figura 2). En el caso de las líneas celulares que presentan elongación mitocondrial, *i.e.* Fis1 o Drp1KD, también se observó la inducción de ambas vías (Figura 3).

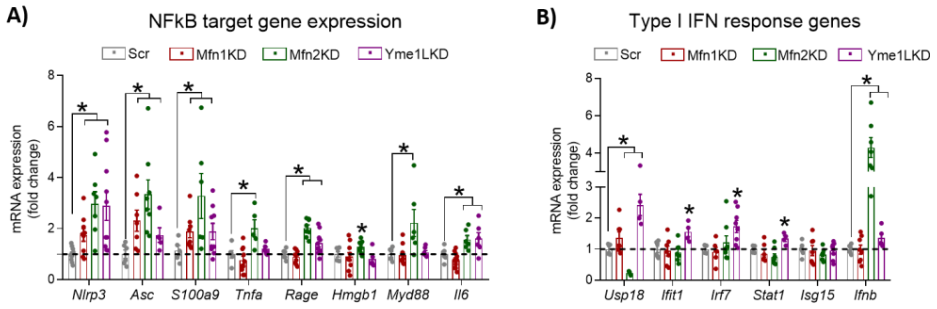

Figura 2: Perfil inflamatorio de mioblastos Mfn1KD, Mfn2KD y Yme1LKD. A) Expresión de genes diana de NFκB. B) Expresión de genes de la respuesta a interferón de tipo 1. (n=7) Los datos representan la media ± SEM. *p<0.05 vs Scr.

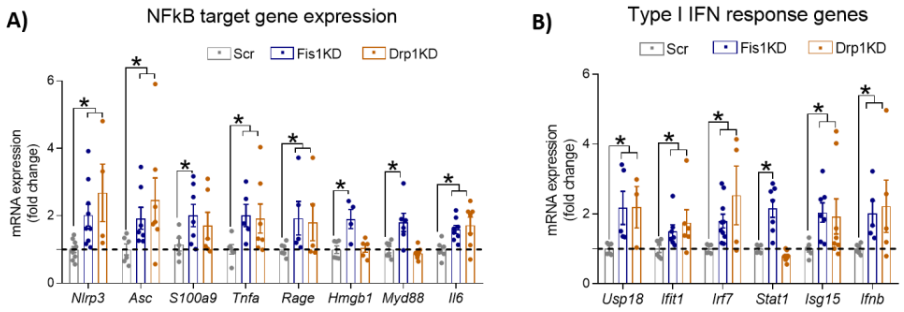

Figura 3: Perfil inflamatorio de mioblastos Fis1KD o Drp1KD. A) Expresión de genes diana de NFκB. B) Expresión de genes de la respuesta a interferón de tipo 1. (n=7) Los datos representan la media ± SEM. *p<0.05 vs Scr.

Estos datos indican que morfologías mitocondriales opuestas inducen diferentes perfiles inflamatorios, lo cual sugiere la presencia de mecanismos moleculares comunes que conectan fragmentación o elongación mitocondrial con inflamación. Aunque la deficiencia de Yme1L no siguiera la misma línea que Mfn1 o Mfn2KD, esto podría deberse a su amplia cantidad de sustratos diana, entre los que se encuentra Opa1, pudiendo contribuir a mecanismos diferentes que resulten en inflamación.

Dadas descripciones anteriores en las que la inflamación mediada por la ausencia de Opa1 en el músculo se debe al reconocimiento de mtDNA por TLR9, decidimos

evaluar la co-distribución entre mtDNA y los sensores de DNA intracelulares TLR9 y cGAS. Los resultados correlacionan con el hecho de que las células Mfn1KD y Mfn2KD presentan una co-distribución aumentada entre mtDNA y el sensor de DNA endosomal TLR9 y no el citosólico cGAS, lo cual se asemeja al caso de la deficiencia de Opa1. En el caso de mioblastos Yme1LKD, esta co-distribución sólo se ve aumentada entre mtDNA y cGAS, lo cual también corrobora el hecho de que estas células presentan activación de la vía mediada por NFκB y la respuesta de interferón de tipo 1. En el caso de los mioblastos Fis1 y Drp1KD se presentan co-distribuciones aumentadas de mtDNA tanto con TLR9 como con cGAS (Figura 5).

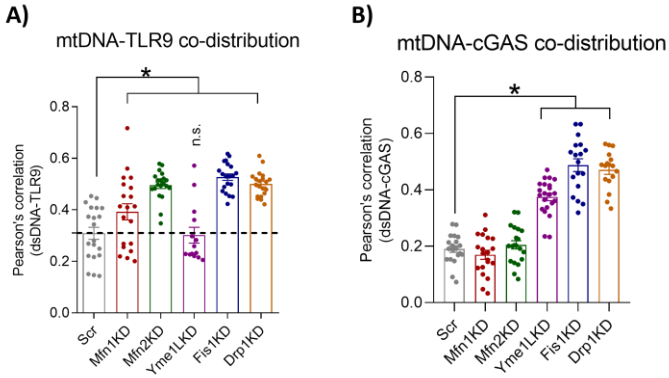

Figura 4: Cuantificación de la co-distribución entre mtDNA y sensores intracelulares de DNA. A) Correlación de Pearson entre mtDNA y TLR9 o B) mtDNA y cGAS (n=20). Los datos representan la media ± SE. *p vs scr <0.05.

Para validar estos resultados, tratamos estas células con el antagonista de TLR9, ODN2088, o el inhibidor de cGAS, Ru.521. Dado que las células Mfn1KD y Mfn2KD presentan una aumentada co-distribución entre mtDNA y TLR9, estas células fueron tratadas solamente con ODN2088. Nuestros resultados indican que el bloqueo de TLR9 normaliza los niveles de expresión de genes diana de NFκB en células Mfn1KD y Mfn2KD, lo cual confirma que la activación de NFκB en estas células es mediada por TLR9 (Figura 5).

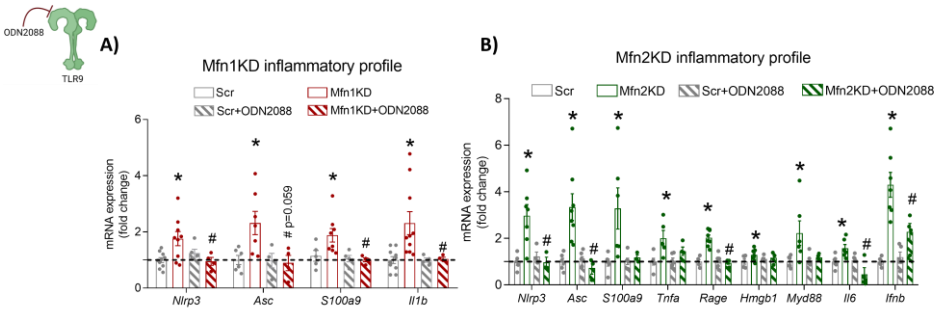

Figura 5: Perfil inflamatorio de mioblastos Mfn1KD y Mfn2KD tratados con ODN2088. A) Rescate del perfil inflamatorio en células Mfn1KD. B) Rescate del perfil inflamatorio en células Mfn1KD. (n=6-8) Los datos representan la media ± SEM. *p<0.05 vs Scr.

Dado que los mioblastos Yme1LKD presentan una aumentada co-distribución de mtDNA con cGAS, estas células fueron tratadas únicamente con Ru.521. Asimismo, la inhibición de cGAS en las células Yme1LKD normaliza tanto los genes diana de NFκB como los genes de la respuesta a interferón de tipo 1 (Figura 6), lo cual sugiere que la inflamación inducida por la deficiencia de Yme1L es promovida por cGAS y su interacción con mtDNA.

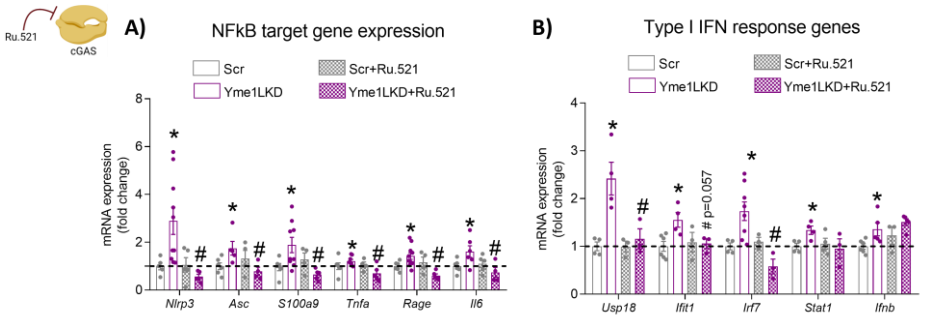

Figura 6: Perfil inflamatorio de mioblastos Yme1LKD tratados con Ru.521. A) Expresión de genes diana de NF-κB. B) Expresión de genes de la respuesta a interferón de tipo 1. (n=4-8) Los datos representan la media ± SEM. *p<0.05 vs Scr.

Por último, las células Fis1KD y Drp1KD fueron tratadas tanto con ODN2088 y Ru.521, y los resultados muestran que ambos sensores de DNA contribuyen al perfil inflamatorio en diferentes medidas en ambas líneas (Figura 7-8).

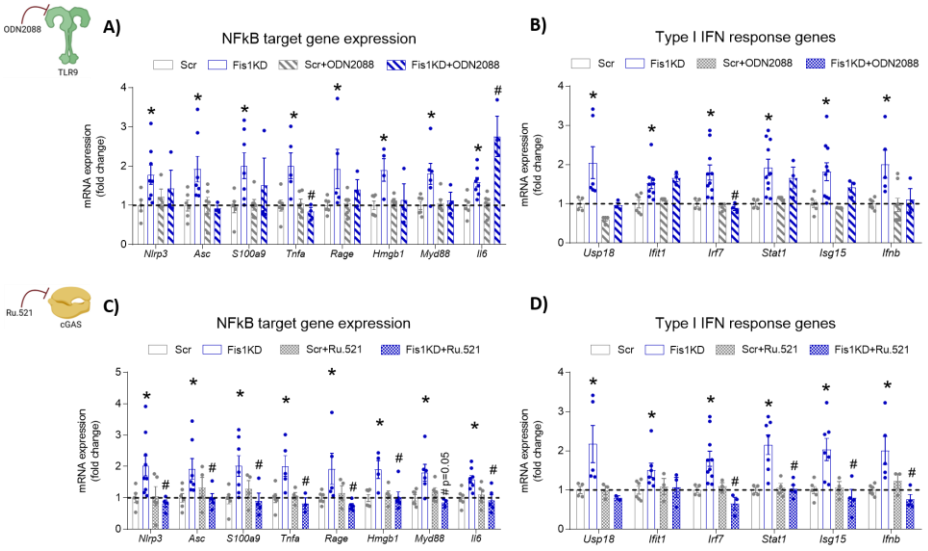

Figura 7: Perfil inflamatorio de mioblastos Fis1KD tratados con ODN2088 o Ru.521. A) Efecto en la Expresión de genes diana de NFκB al tratamiento de ODN2088. B) Efecto en la expresión de genes de la respuesta a interferón de tipo 1 al tratamiento de ODN2008. C) Efecto en la Expresión de genes diana de NFκB al tratamiento de Ru.521. D) Efecto en la expresión de genes de la respuesta a interferón de tipo 1 al tratamiento de Ru.521. (n=4-9) Los datos representan la media ± SEM. *p<0.05 vs Scr.

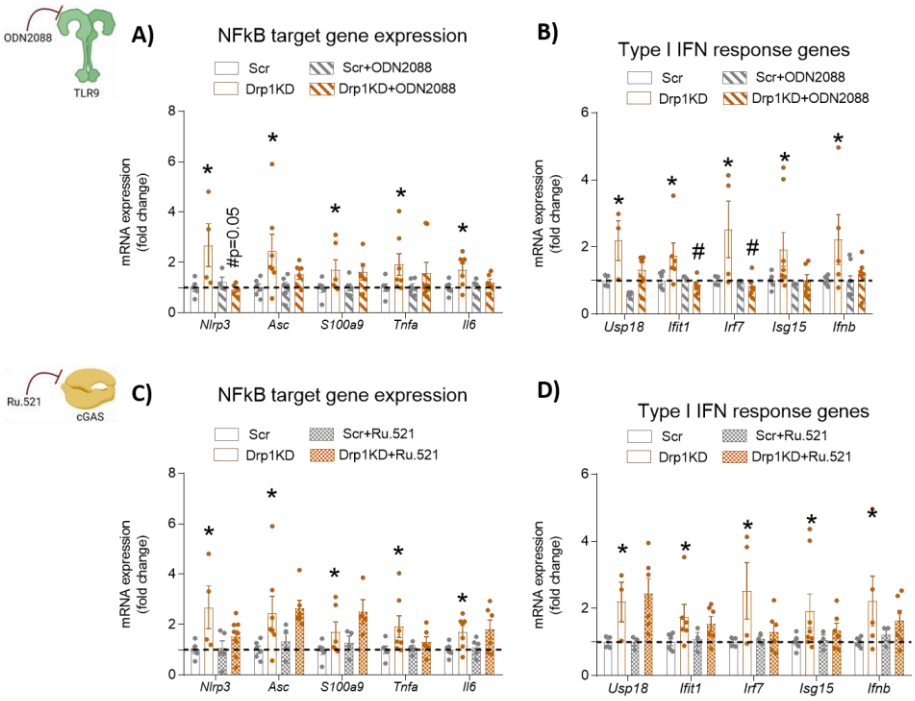

Figura 8: Perfil inflamatorio de mioblastos Drp1KD tratados con ODN2088 o Ru.521. A) Efecto en la Expresión de genes diana de NFκB al tratamiento de ODN2088. B) Efecto en la expresión de genes de la respuesta a interferón de tipo 1 al tratamiento de ODN2008. C) Efecto en la Expresión de genes diana de NFκB al tratamiento de Ru.521. D) Efecto en la expresión de genes de la respuesta a interferón de tipo 1 al tratamiento de Ru.521. (n=4-5) Los datos representan la media ± SEM. *p<0.05 vs Scr.

Estos resultados indican que desequilibrios en la dinámica mitocondrial generan respuestas inflamatorias diferentes. Sin embargo, los mecanismos que desencadenan inflamación tanto en respuesta a fragmentación como a elongación mitocondrial dependen de la localización extra-mitocondrial del mtDNA y de su reconocimiento por sensores de DNA intracelulares, como TLR9 o cGAS.

Estudio 2: Identificación de las vías moleculares que desencadenan inflamación en células deficientes de Mfn1.

Dados los resultados iniciales y observándose que la deficiencia de Mfn1 o Mfn2 provoca una respuesta inflamatoria caracterizada por única activación de la vía dependiente de NFκB mediada por TLR9, nos centramos en describir los mecanismos moleculares involucrados en esos contextos. Debido a que Mfn2 ejerce diversas funciones más allá de la fusión mitocondrial[188], decidimos explorar los mecanismos responsables en los mioblastos Mfn1KD.

El sensor de DNA TLR9 se localiza en el compartimento endosomal, por lo que identificar el tipo de endosoma donde el mtDNA tiene más probabilidades de ser identificado por TLR9 fue prioritario. Para ello, realizamos una batería de inmunofluorescencias entre mtDNA y diversos marcadores del compartimento endosomal, en los que se incluyen: Rab5 y EEA1 para endosomas tempranos, Rab7 para endosomas tardíos y lisosomas, HRS para especies intermedias y LAMP1 para endosomas tardíos, lisosomas y autolisosomas. Sorprendentemente, la cuantificación de la co-distribución entre mtDNA y dichos marcadores demuestra que el mtDNA presenta una mayor interacción con marcadores de endosomas tempranos como Rab5 y EEA1 (Figura 9).

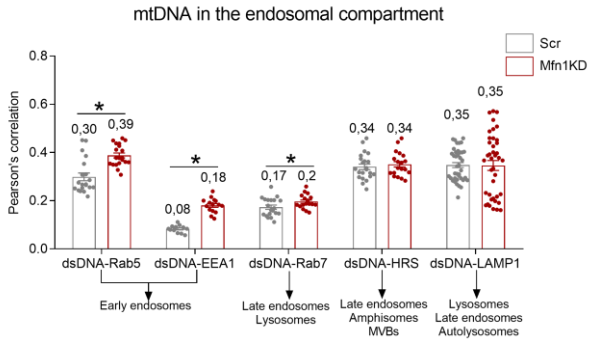

Figura 9: Evaluación de la localización del mtDNA en el compartimento endosomal en ausencia de Mfn1. Cuantificación de la correlación de Pearson en la co-distribución entre mtDNA y cada marcador endosomal en mioblastos control y Mfn1KD (n=20). Los datos representan la media ± SEM. *p<0.05 vs Scr.

Para poder descartar algunos de los mecanismos por los que, en ausencia de Mfn1, el mtDNA se localiza en endosomas tempranos, realizamos ensayos de co-distribución entre mitocondrias, Rab5 y TLR9. Para ello, se realizaron ensayos de inmunofluorescencias entre dichos marcadores y *Mitotracker Deep Red (MTDR)*, una sonda que penetra en las mitocondrias y permite su visualización después de fijar las células. La cuantificación de la correlación de Pearson entre MTDR y Rab5 o TLR9 mostró una mayor interacción entre mitocondrias y dichos marcadores en células deficientes de Mfn1 (Figura 10), lo cual sugiere que los mecanismos por los que el mtDNA llega a endosomas tempranos depende de la implicación de la red mitocondrial.

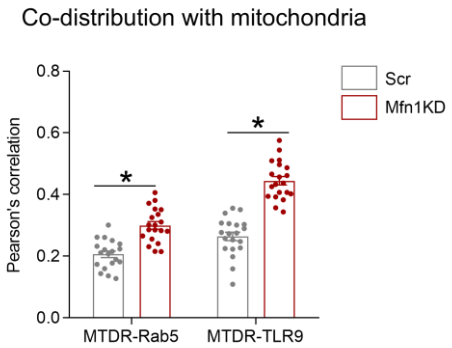

Figura 10: Co-distribución entre mitocondrias (MTDR) y Rab5 o TLR9 en mioblastos Mfn1KD. Cuantificación de la correlación de Pearson entre mtDNA y cada marcador en mioblastos control y Mfn1KD (n=20). Los datos representan la media ± SEM. *p<0.05 vs Scr.

De hecho, ensayos de microscopía electrónica con inmunomarcaje con anticuerpos secundarios conjugados con oro coloidal contra Rab5 (18nm) y SdhA (12nm), los cuales marcan endosomas tempranos (EE) y mitocondrias (M) respectivamente, nos permitieron visualizar que en células Mfn1KD hay una propensión a establecer contactos directos entre las membranas de ambos organelos (Figura 11A). Estos resultados fueron validados cuantificando la distancia media entre los organelos marcados y el porcentaje de contactos <30nm por ensayo en cada línea celular (Figura 11B).

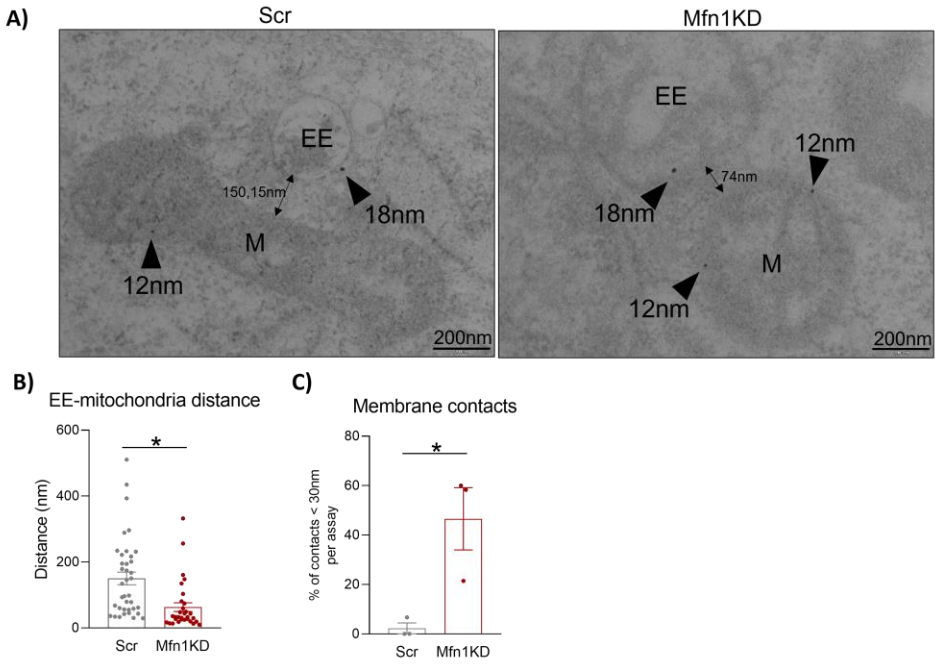

Figura 11: Distribución espacial de endosomas tempranos y mitocondrias en mioblastos Mfn1KD. A) Imágenes representativas de inmunomarcaje seguido de microscopía electrónica. B) Cuantificación de la distancia entre orgánulos marcados. C) Porcentaje de contactos <30nm por ensayo. Los datos representan la media ± SEM. *p<0.05 vs Scr.

Estos datos indican que en ausencia de Mfn1, las mitocondrias fragmentadas establecen contactos estrechos con endosomas tempranos, a través de los cuales podría realizarse una transferencia de mtDNA. Esto permitiría la identificación de mtDNA por TLR9 en el lumen de los endosomas, lo que finalmente desencadena la inflamación mediada por NF-κB.

Estudio 3: Caracterización de la salud y capacidad muscular en ausencia de Mfn1.

Para evaluar la implicación fisiológica que tiene el impacto en la activación de la inflamación en ausencia de Mfn1, generamos un modelo in vivo con deleción

inducible de *Mfn1* únicamente en el músculo esquelético. Para ello, cruzamos animales transgénicos que expresan la recombinasa Cre inducible por tamoxifeno bajo el control del promotor específico de músculo esquelético HSA (del inglés, *human skeletal actin*) con animales que contienen secuencias flanqueantes en el exón 4 del gen *Mfn1*. De la descendencia, los animales Cre positivos son animales *knockout* de *Mfn1* (SkM-Mfn1KO) mientras que los Cre negativos son los controles (LoxP). Para inducir la expresión de la recombinasa Cre, a las 12 semanas de edad los animales fueron alimentados *ab libitum* con dieta enriquecida en tamoxifeno durante 2 semanas. Este protocolo permitió validar la depleción de Mfn1 únicamente en los músculos esqueléticos de ratones SkM-Mfn1KO (Figura 12).

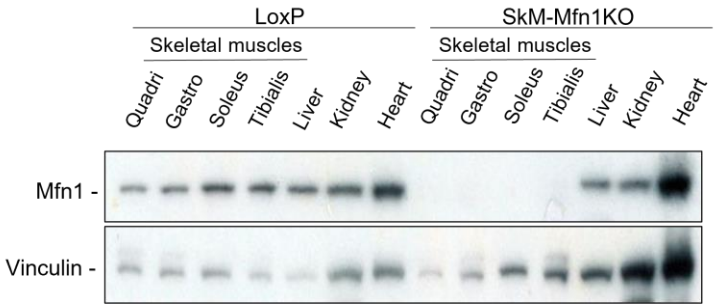

Figura 12: Validación de los niveles proteicos de Mfn1 en el modelo animal de estudio. Inmunoblot representativo de Mfn1 y vinculina (n=3).

Para analizar el impacto de la depleción de Mfn1 en el músculo esquelético, realizamos tinciones de hematoxilina y eosina en gastrocnemios de ratones LoxP y SkM-Mfn1. La cuantificación del área cros-seccional de las fibras musculares (CSA) determinó que los animales SkM-Mfn1KO presentan atrofia muscular, ya que muestran una reducción del 50% en su CSA (Figura 13).

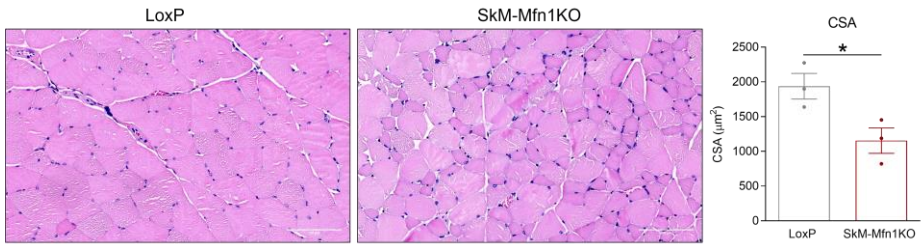

Figura 13: Evaluación del CSA de las fibras musculares. Tinción de hematoxilina y eosina de cortes transversales de gastrocnemios y cuantificación del CSA (n=3 animales por genotipo, 300 fibras por animal). Los datos representan la media ± SEM. *p<0.05 vs LoxP.

Además, estos resultados fueron validados por el análisis de la actividad en plasma de la enzima creatina quinasa (CK), ya que los animales SkM-Mfn1ko presentan una elevada actividad de CK, lo cual es indicativo de daño muscular.

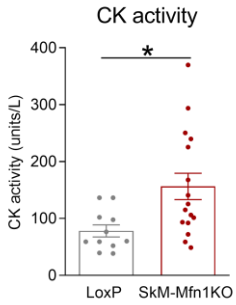

Figura 14: Cuantificación de la actividad en plasma de CK. (n=10-16). Los datos representan la media ± SEM. *p<0.05 vs LoxP.

Para validar los datos que relacionan la ausencia de Mfn1 con la activación de inflamación mediada por NFκB en el modelo celular, evaluamos la expresión génica de genes diana de NFκB en ratones LoxP y SkM-Mfn1KO. Además, los sometimos a tratamiento agudo del antagonista de TLR9 para valorar la implicación de este sensor de DNA en la activación de la inflamación muscular. Este ensayo indicó que los ratones SkM-Mfn1KO presentan activación de la vía NFκB en el músculo esquelético, la cual es dependiente de TLR9, lo cual fenocopia los resultados obtenidos en las células Mfn1KD (Figura 15A). Sin embargo, observamos que no hay cambios en niveles de citocinas pro-

inflamatorias como IL6 y TNFα en plasma, lo cual descarta el hecho de que estos animales presenten inflamación sistémica.

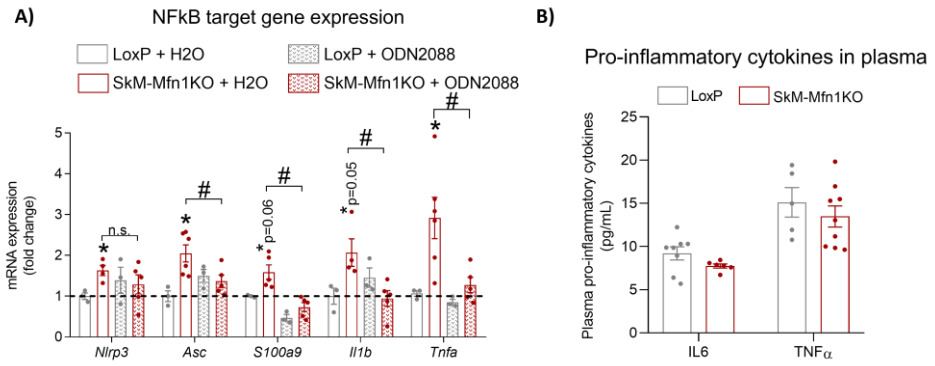

Figura 15: Evaluación del perfil inflamatorio de los ratones SkM-Mfn1KO. A) Cuantificación de la expresión génica de genes diana de NFκB en respuesta a tratamiento de ODN2088. (n=3-6) B) Niveles en plasma de citocinas pro-inflamatorias. (n=5-9). Los datos representan la media ± SEM. *p<0.05 vs LoxP.

Dado que la depleción de Mfn1 en el músculo esquelético genera atrofia e inflamación muscular, decidimos evaluar la capacidad física de los ratones SkM-Mfn1KO. Para ello, los ratones fueron sometidos a dos rondas consecutivas de ejercicio sobre cinta hasta el agotamiento. Los resultados indican que, a pesar de que no se observaron diferencias en la distancia corrida entre genotipos a día 1 de ensayo, los ratones SkM-Mfn1KO presentan una reducida capacidad física a día 2 de ensayo en comparación a los ratones LoxP (Figura 16).

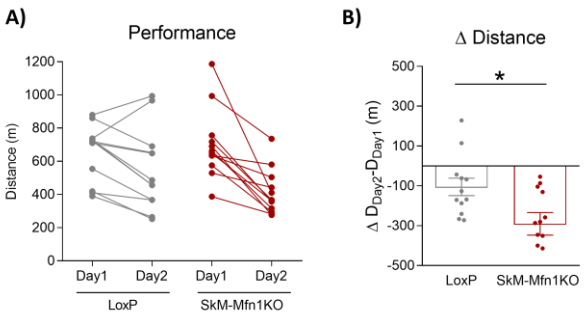

Figura 16: Evaluación de la capacidad física. A) Distancia corrida a día 1 y día por ratón. B) Diferencia en la distancia corrida de día 2 a día 1 por ratón (n=11-12). Los datos representan la media ± SEM. *p<0.05 vs LoxP.

Estos datos sugieren que la ausencia de Mfn1 provoca alteraciones en los mecanismos de reparación del músculo esquelético en respuesta a ejercicio agudo.

Para evaluar la contribución de la inflamación muscular al desarrollo de atrofia muscular y la reducción en la capacidad física, sometimos a los ratones a un tratamiento crónico de salicilato de sodio, un conocido inhibidor de NFκB (ref). Sorprendentemente, la inhibición de NFκB provocó una normalización de los marcadores de atrofia, los cuales incluyen el CSA (Figura 17) y la actividad en plasma de CK (Figura 18).

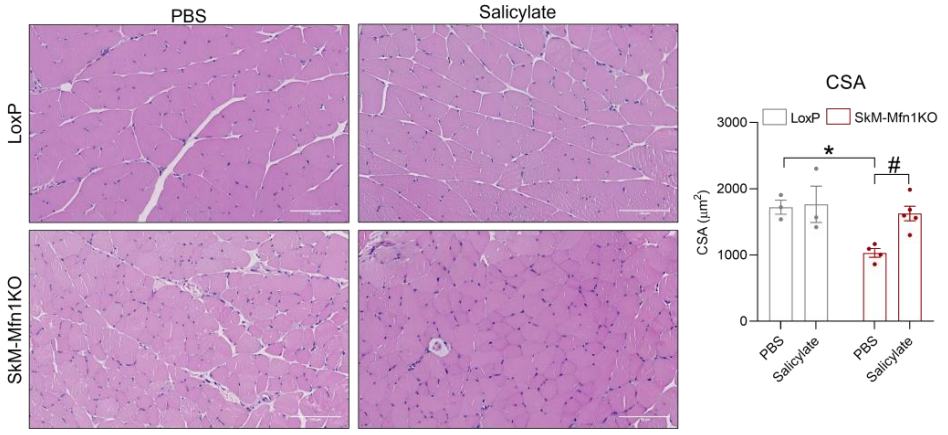

Figura 17: Evaluación del CSA de las fibras musculares en respuesta a tratamiento con salicilato. Tinción de hematoxilina y eosina de cortes transversales de gastrocnemios y cuantificación del CSA (n=3-4 animales por genotipo, 300 fibras por animal). Los datos representan la media ± SEM. *p<0.05 vs LoxP+PBS; #p<0.05 vs. SkM-Mfn1KO+PBS.

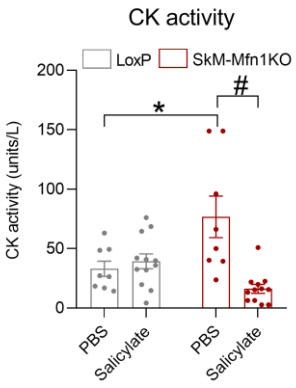

Figura 18: Cuantificación de la actividad en plasma de CK en respuesta a tratamiento con salicilato. (n=8-12). Los datos representan la media ± SEM. *p<0.05 vs LoxP+PBS; #p<0.05 vs. SkM-Mfn1KO+PBS.

Por último, la inhibición de la inflamación muscular mediada por NFκB mediante el tratamiento crónico de salicilato, además de restaurar la salud muscular, promovió una mejora en la capacidad física de los animales tratados (Figura 19).

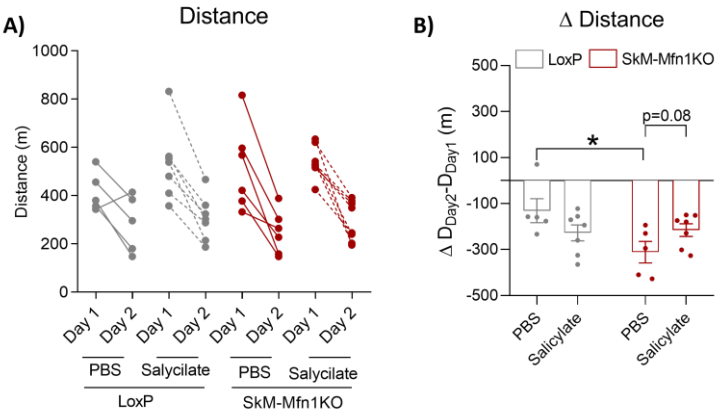

Figura 19: Evaluación de la capacidad física en respuesta a tratamiento con salicilato. A) Distancia corrida a día 1 y día por ratón. B) Diferencia en la distancia corrida de día 2 a día 1 por ratón (n=5-7). *p<0.05 vs LoxP+PBS; #p<0.05 vs. SkM-Mfn1KO+PBS.

Estos datos indican que la activación de la inflamación dependiente de NFκB inducida por la depleción de Mfn1 puede jugar un rol causativo en el desarrollo de la atrofia muscular y en la capacidad física. Sin embargo, dado que se ha documentado que la propia acción de NFκB actúa promoviendo vías relacionadas con la atrofia muscular[207,208], podría ser que, en nuestro modelo, NFκB actúe

promoviendo inflamación y atrofia en paralelo. En cualquier caso, proponemos que el diseño de estrategias terapéuticas con el objetivo de mejorar la dinámica mitocondrial puede proporcionar un enfoque efectivo en el tratamiento de enfermedades inflamatorias musculares, así como de otro tipo de enfermedades inflamatorias.

8.4. Conclusiones

Los datos recopilados en esta tesis permiten establecer las siguientes conclusiones:

1. Alteraciones primarias en dinámica mitocondrial inducen la activación de vías inflamatorias estériles.

2. La fragmentación mitocondrial está asociada a la activación de NFκB mediada por TLR9. La elongación mitocondrial promueve la activación tanto de la inflamación mediada por NFκB como la respuesta a interferón de tipo 1, mediante la acción de cGAS y TLR9.

3. La activación de NFκB en ausencia de Mfn1 se debe a un acercamiento de endosomas tempranos y mitocondrias mediado por Rab5C. Esto permite el reconocimiento de mtDNA por parte de TLR9.

4. La ausencia de Mfn1 induce la acción de NFκB causando inflamación y atrofia muscular, lo que compromete la capacidad física y la respuesta sistémica al ejercicio.

5. Proponemos que el desarrollo de terapias que mejoren la dinámica mitocondrial pueden ser efectivas en el tratamiento de alteraciones inflamatorias.

REFERENCES

1. Wallin I. On the nature of mitochondria. IX. Demonstration of the bacterial nature of mitochondria. *Am J Anat*. 1922;36:131-149. doi:10.1002/aja.1000360106

2. Sagan L. The origin of mitosing cells. *J NIH Res*. 1993;5:65-72.

3. Nunnari J, Suomalainen A. Mitochondria: In sickness and in health. *Cell*. 2012;148(6):1145-1159. doi:10.1016/j.cell.2012.02.035

4. Hockenbery D, Nuñez G, Milliman C, Schreiber RD, Korsmeyer SJ. Bcl-2 is an inner mitochondrial membrane protein that blocks programmed cell death. *Nature*. 1990;348(6299):334-336. doi:10.1038/348334a0

5. Gunter TE, Buntinas L, Sparagna GC, Gunter KK. The Ca2+ transport mechanisms of mitochondria and Ca2+ uptake from physiological-type Ca2+ transients. *Biochim Biophys Acta - Bioenerg*. 1998;1366(1-2):5-15. doi:10.1016/S0005-2728(98)00117-0

6. Cloonan SM, Choi AMK. Mitochondria: Sensors and mediators of innate immune receptor signaling. *Curr Opin Microbiol*. 2013;16(3):327-338. doi:10.1016/j.mib.2013.05.005

7. Zhang Q, Raoof M, Chen Y, et al. Circulating mitochondrial DAMPs cause inflammatory responses to injury. *Nature*. 2010;464(7285):104-107. doi:10.1038/nature08780

8. Blachly-Dyson E, Forte M. VDAC channels. *IUBMB Life*. 2001;52(3-5):113-118. doi:10.1080/15216540152845902

9. Gordaliza-Alaguero I, Cantó C, Zorzano A. Metabolic implications of organelle–mitochondria communication. *EMBO Rep*. 2019;20(9):1-27. doi:10.15252/embr.201947928

10. Lübeck J, Heins L, Soll J. Protein import into mitochondria. *Physiol Plant*. 1997;100(1):53-64. doi:10.1034/j.1399-3054.1997.1000105.x

11. Zick M, Rabl R, Reichert AS. Cristae formation-linking ultrastructure and function of mitochondria. *Biochim Biophys Acta - Mol Cell Res*. 2009;1793(1):5-19. doi:10.1016/j.bbamcr.2008.06.013

12. Vogel F, Bornhövd C, Neupert W, Reichert AS. Dynamic subcompartmentalization of the mitochondrial inner membrane. *J Cell Biol*. 2006;175(2):237-247. doi:10.1083/jcb.200605138

13. Jayashankar V, Mueller IA, Rafelski SM. Shaping the multi-scale architecture of mitochondria. *Curr Opin Cell Biol*. 2016;38:45-51. doi:10.1016/j.ceb.2016.02.006

14. Jornayvaz FR. and SGI. Regulation of mitochondrial biogenesis. *Essays Biochem*. 2014;47:1-15. doi:10.1042/bse0470069.Regulation

15. Johri A, Chandra A, Beal MF. PGC-1α, mitochondrial dysfunction, and Huntington's disease. *Free Radic Biol Med*. 2013;62:37-46. doi:10.1016/j.freeradbiomed.2013.04.016

16. Eisner V, Picard M, Hajnóczky G. Mitochondrial dynamics in adaptive and maladaptive cellular stress responses. *Nat Cell Biol*. 2018;20(7):755-765. doi:10.1038/s41556-018-0133-0

17. Tilokani L, Nagashima S, Paupe V, Prudent J. Mitochondrial dynamics: Overview of molecular mechanisms. *Essays Biochem*. 2018;62(3):341-360. doi:10.1042/EBC20170104

18. Koshiba T, Detmer SA, Kaiser JT, Chen H, McCaffery JM, Chan DC. Structural basis of mitochondrial tethering by mitofusin complexes. *Science (80-)*. 2004;305(5685):858-862. doi:10.1126/science.1099793

19. Sebastián D, Sorianello E, Segalés J, et al. Mfn2 deficiency links age-related sarcopenia and impaired autophagy to activation of an adaptive mitophagy pathway. *EMBO J*. 2016;35(15):1677-1693. doi:10.15252/embj.201593084

20. Rambold AS, Cohen S, Lippincott-Schwartz J. Fatty acid trafficking in starved cells: Regulation by lipid droplet lipolysis, autophagy, and mitochondrial fusion dynamics. *Dev Cell*. 2015;32(6):678-692. doi:10.1016/j.devcel.2015.01.029

21. Xue R, Yang J, Jia L, et al. Mitofusin2, as a protective target in the liver, controls the balance of apoptosis and autophagy in acute-on-chronic liver failure. *Front Pharmacol*. 2019;10(MAY):1-10. doi:10.3389/fphar.2019.00601

22. Pyakurel A, Savoia C, Hess D, Scorrano L. Extracellular Regulated Kinase Phosphorylates Mitofusin 1 to Control Mitochondrial Morphology and Apoptosis. *Mol Cell*. 2015;58(2):244-254. doi:10.1016/j.molcel.2015.02.021

23. Park YY, Cho H. Mitofusin 1 is degraded at G2/M phase through ubiquitylation by MARCH5. *Cell Div*. 2012;7(1):1. doi:10.1186/1747-1028-7-25

24. Chen KH, Dasgupta A, Ding J, Indig FE, Ghosh P, L. Longo D. Role of mitofusin 2 (Mfn2) in controlling cellular proliferation. *FASEB J*. 2014;28(1):382-394. doi:10.1096/fj.13-230037

25. Li X, Hong Y, He H, et al. FGF21 mediates mesenchymal stem cell senescence via regulation of mitochondrial dynamics. *Oxid Med Cell Longev*. 2019;2019. doi:10.1155/2019/4915149

26. Park YY, Lee S, Karbowski M, Neutzner A, Youle RJ, Cho H. Loss of MARCH5 mitochondrial E3 ubiquitin ligase induces cellular senescence through dynamin-related protein 1 and mitofusin 1. *J Cell Sci*. 2010;123(4):619-626. doi:10.1242/jcs.061481

27. Yasukawa K, Oshiumi H, Takeda M, et al. Mitofusin 2 inhibits mitochondrial antiviral signaling. *Sci Signal*. 2009;2(84):1-12. doi:10.1126/scisignal.2000287

28. Onoguchi K, Onomoto K, Takamatsu S, et al. Virus-infection or 5'ppp-RNA activates antiviral signal through redistribution of IPS-1 mediated by MFN1. *PLoS Pathog*. 2010;6(7):1-17. doi:10.1371/journal.ppat.1001012

29. Boutant M, Kulkarni SS, Joffraud M, et al. Mfn2 is critical for brown adipose tissue thermogenic function. *EMBO J*. 2017;36(11):1543-1558. doi:10.15252/embj.201694914

30. Naon D, Zaninello M, Giacomello M, et al. Critical reappraisal confirms that Mitofusin 2 is an endoplasmic reticulum-mitochondria tether. *Proc Natl Acad Sci U S A*. 2016;113(40):11249-11254. doi:10.1073/pnas.1606786113

31. Schneeberger M, Dietrich MO, Sebastián D, et al. Mitofusin 2 in POMC neurons connects ER stress with leptin resistance and energy imbalance. *Cell*. 2013;155(1):172-187. doi:10.1016/j.cell.2013.09.003

32. Muñoz JP, Zorzano A. Mfn2 modulates the unfolded protein response. *Cell Cycle*. 2014;13(4):491-492. doi:10.4161/cc.27782

33. Hernández-Alvarez MI, Sebastián D, Vives S, et al. Deficient Endoplasmic Reticulum-Mitochondrial Phosphatidylserine Transfer Causes Liver Disease. *Cell*. 2019;177(4):881-895.e17. doi:10.1016/j.cell.2019.04.010

34. Chen W, Sun Y, Sun Q, et al. MFN2 Plays a Distinct Role from MFN1 in Regulating Spermatogonial Differentiation. *Stem Cell Reports*. 2020;14(5):803-817. doi:10.1016/j.stemcr.2020.03.024

35. Liesa M, Palacín M, Zorzano A. Mitochondrial dynamics in mammalian health and disease. *Physiol Rev*. 2009;89(3):799-845. doi:10.1152/physrev.00030.2008

36. Chen H, Detmer SA, Ewald AJ, Griffin EE, Fraser SE, Chan DC. Mitofusins

Mfn1 and Mfn2 coordinately regulate mitochondrial fusion and are essential for embryonic development. *J Cell Biol*. 2003;160(2):189-200. doi:10.1083/jcb.200211046

37. Maria IHA, Kulkarni SS, Joffraud M, et al. Mfn1 deficiency in the liver protects against diet-induced insulin resistance and enhances the hypoglycemic effect of metformin. *Diabetes*. 2016;65(12):3552-3560. doi:10.2337/db15-1725

38. Ramírez S, Gómez-Valadés AG, Schneeberger M, et al. Mitochondrial Dynamics Mediated by Mitofusin 1 Is Required for POMC Neuron Glucose-Sensing and Insulin Release Control. *Cell Metab*. 2017;25(6):1390-1399.e6. doi:10.1016/j.cmet.2017.05.010

39. Papanicolaou KN, Ngoh GA, Dabkowski ER, et al. Cardiomyocyte deletion of mitofusin-1 leads to mitochondrial fragmentation and improves tolerance to ROS-induced mitochondrial dysfunction and cell death. *Am J Physiol - Hear Circ Physiol*. 2012;302(1):167-179. doi:10.1152/ajpheart.00833.2011

40. Sebastián D, Hernández-Alvarez MI, Segalés J, et al. Mitofusin 2 (Mfn2) links mitochondrial and endoplasmic reticulum function with insulin signaling and is essential for normal glucose homeostasis. *Proc Natl Acad Sci U S A*. 2012;109(14):5523-5528. doi:10.1073/pnas.1108220109

41. Mancini G, Pirruccio K, Yang X, Blücher M, Rodeheffer M, Horvath TL. Mitofusin 2 in Mature Adipocytes Controls Adiposity and Body Weight. *Cell Rep*. 2019;26(11):2849-2858.e4. doi:10.1016/j.celrep.2019.02.039

42. Tur J, Pereira-Lopes S, Vico T, et al. Mitofusin 2 in Macrophages Links Mitochondrial ROS Production, Cytokine Release, Phagocytosis, Autophagy, and Bactericidal Activity. *Cell Rep*. 2020;32(8). doi:10.1016/j.celrep.2020.108079

43. Züchnery S. Charcot-Marie-Tooth Neuropathy Type 2A Summary Genetic counseling Clinical Diagnosis. Published online 2020:1-12.

44. Akepati VR, Müller EC, Otto A, Strauss HM, Portwich M, Alexander C. Characterization of OPA1 isoforms isolated from mouse tissues. *J Neurochem*. 2008;106(1):372-383. doi:10.1111/j.1471-4159.2008.05401.x

45. Olichon A, ElAchouri G, Baricault L, Delettre C, Belenguer P, Lenaers G. OPA1 alternate splicing uncouples an evolutionary conserved function in mitochondrial fusion from a vertebrate restricted function in apoptosis.

Cell Death Differ. 2007;14(4):682-692. doi:10.1038/sj.cdd.4402048

46. Ishihara N, Fujita Y, Oka T, Mihara K. Regulation of mitochondrial morphology through proteolytic cleavage of OPA1. *EMBO J*. 2006;25(13):2966-2977. doi:10.1038/sj.emboj.7601184

47. Anand R, Wai T, Baker MJ, et al. The i-AAA protease YME1L and OMA1 cleave OPA1 to balance mitochondrial fusion and fission. *J Cell Biol*. 2014;204(6):919-929. doi:10.1083/jcb.201308006

48. Ban T, Ishihara T, Kohno H, et al. Molecular basis of selective mitochondrial fusion by heterotypic action between OPA1 and cardiolipin. *Nat Cell Biol*. 2017;19(7):856-863. doi:10.1038/ncb3560

49. Del Dotto V, Mishra P, Vidoni S, et al. OPA1 Isoforms in the Hierarchical Organization of Mitochondrial Functions. *Cell Rep*. 2017;19(12):2557-2571. doi:10.1016/j.celrep.2017.05.073

50. Belenguer P, Pellegrini L. The dynamin GTPase OPA1: More than mitochondria? *Biochim Biophys Acta - Mol Cell Res*. 2013;1833(1):176-183. doi:10.1016/j.bbamcr.2012.08.004

51. Rodríguez-Nuevo A, Díaz-Ramos A, Noguera E, et al. Mitochondrial DNA and TLR9 drive muscle inflammation upon Opa1 deficiency. *EMBO J*. 2018;37(10):1-18. doi:10.15252/embj.201796553

52. Pereira RO, Tadinada SM, Zasadny FM, et al. OPA 1 deficiency promotes secretion of FGF 21 from muscle that prevents obesity and insulin resistance . *EMBO J*. 2017;36(14):2126-2145. doi:10.15252/embj.201696179

53. Tezze C, Romanello V, Desbats MA, et al. Age-Associated Loss of OPA1 in Muscle Impacts Muscle Mass, Metabolic Homeostasis, Systemic Inflammation, and Epithelial Senescence. *Cell Metab*. 2017;25(6):1374-1389.e6. doi:10.1016/j.cmet.2017.04.021

54. Sprenger H, Wani G, Hesseling A, et al. Loss of the mitochondrial i - AAA protease YME 1L leads to ocular dysfunction and spinal axonopathy . *EMBO Mol Med*. 2019;11(1):1-20. doi:10.15252/emmm.201809288

55. Sprenger H, Macvicar T, Bahat A, et al. Cellular pirymidin imbalance triggers mitochondrial DNA – dependent innate immunity. *Nat Metab*. Published online 2021. doi:10.1038/s42255-021-00385-9

56. Delettre C, Lenaers G, Griffoin JM, et al. Nuclear gene OPA1, encoding a mitochondrial dynamin-related protein, is mutated in dominant optic

atrophy. *Nat Genet*. 2000;26(2):207-210. doi:10.1038/79936

57. Alexander C, Votruba M, Pesch UEA, et al. OPA1, encoding a dynamin-related GTPase, is mutated in autosomal dominant optic atrophy linked to chromosome 3q28. *Nat Genet*. 2000;26(2):211-215. doi:10.1038/79944

58. Friedman JR, Lackner LL, West M, DiBenedetto JR, Nunnari J, Voeltz GK. ER tubules mark sites of mitochondrial division. *Science (80-)*. 2011;334(6054):358-362. doi:10.1126/science.1207385

59. Dikov D, Reichert AS. How to split up: Lessons from mitochondria. *EMBO J*. 2011;30(14):2751-2753. doi:10.1038/emboj.2011.219

60. Otera H, Ishihara N, Mihara K. New insights into the function and regulation of mitochondrial fission. *Biochim Biophys Acta - Mol Cell Res*. 2013;1833(5):1256-1268. doi:10.1016/j.bbamcr.2013.02.002

61. Waterham HR, Koster J, Van Roermund CWT, Mooyer PAW, Wanders RJA, Leonard J V. A lethal defect of mitochondrial and peroxisomal fission. *N Engl J Med*. 2007;356(17):1736-1741. doi:10.1056/NEJMoa064436

62. Bartsakoulia M, Pyle A, Troncoso-Chandía D, et al. A novel mechanism causing imbalance of mitochondrial fusion and fission in human myopathies. *Hum Mol Genet*. 2018;27(7):1186-1195. doi:10.1093/hmg/ddy033

63. Shamseldin HE, Alshammari M, Al-Sheddi T, et al. Genomic analysis of mitochondrial diseases in a consanguineous population reveals novel candidate disease genes. *J Med Genet*. 2012;49(4):234-241. doi:10.1136/jmedgenet-2012-100836

64. Ikeda Y, Shirakabe A, Maejima Y, et al. Endogenous Drp1 mediates mitochondrial autophagy and protects the heart against energy stress. *Circ Res*. 2015;116(2):264-278. doi:10.1161/CIRCRESAHA.116.303356

65. Favaro G, Romanello V, Varanita T, et al. DRP1-mediated mitochondrial shape controls calcium homeostasis and muscle mass. *Nat Commun*. 2019;10(1). doi:10.1038/s41467-019-10226-9

66. Dulac M, Leduc-Gaudet JP, Reynaud O, et al. Drp1 knockdown induces severe muscle atrophy and remodelling, mitochondrial dysfunction, autophagy impairment and denervation. *J Physiol*. 2020;598(17):3691-3710. doi:10.1113/JP279802

67. Lewis TL, Kwon SK, Lee A, Shaw R, Polleux F. MFF-dependent

mitochondrial fission regulates presynaptic release and axon branching by limiting axonal mitochondria size. *Nat Commun*. 2018;9(1):1-15. doi:10.1038/s41467-018-07416-2

68. Zhang Z, Sliter DA, Bleck CKE, Ding S. Fis1 deficiencies differentially affect mitochondrial quality in skeletal muscle. *Mitochondrion*. 2019;49(September):217-226. doi:10.1016/j.mito.2019.09.005

69. Kim D, Song J, Kang Y, et al. Fis1 depletion in osteoarthritis impairs chondrocyte survival and peroxisomal and lysosomal function. *J Mol Med*. 2016;94(12):1373-1384. doi:10.1007/s00109-016-1445-9

70. Yu R, Jin S, Lendahl U, Nistér M, Zhao J. Human Fis1 regulates mitochondrial dynamics through inhibition of the fusion machinery. *EMBO J*. 2019;38(8):1-21. doi:10.15252/embj.201899748

71. Otera H, Miyata N, Kuge O, Mihara K. Drp1-dependent mitochondrial fission via MiD49/51 is essential for apoptotic cristae remodeling. *J Cell Biol*. 2016;212(5):531-544. doi:10.1083/jcb.201508099

72. Xian H, Liou Y-C. Loss of MIEF1/MiD51 confers susceptibility to BAX-mediated cell death and PINK1-PRKN-dependent mitophagy. *Autophagy*. 2019;15(12):2107-2125. doi:10.1080/15548627.2019.1596494

73. Mizushima N, Komatsu M. Autophagy: Renovation of cells and tissues. *Cell*. 2011;147(4):728-741. doi:10.1016/j.cell.2011.10.026

74. Ding WX, Yin XM. Mitophagy: Mechanisms, pathophysiological roles, and analysis. *Biol Chem*. 2012;393(7):547-564. doi:10.1515/hsz-2012-0119

75. Lazarou M, Jin SM, Kane LA, Youle RJ. Role of PINK1 Binding to the TOM Complex and Alternate Intracellular Membranes in Recruitment and Activation of the E3 Ligase Parkin. *Dev Cell*. 2012;22(2):320-333. doi:10.1016/j.devcel.2011.12.014

76. Geisler S, Holmström KM, Skujat D, et al. PINK1/Parkin-mediated mitophagy is dependent on VDAC1 and p62/SQSTM1. *Nat Cell Biol*. 2010;12(2):119-131. doi:10.1038/ncb2012

77. Gegg ME, Cooper JM, Chau KY, Rojo M, Schapira AHV, Taanman JW. Corrigendum to Mitofusin 1 and mitofusin 2 are ubiquitinated in a pink1/parkin-dependent manner upon induction of mitophagy [Human Molecular Genetics, 19:24 (2010) 4861-4870] doi:10.1093/hmg/ddq419]. *Hum Mol Genet*. 2013;22(8):1697. doi:10.1093/hmg/ddt046

78. Johansen T, Lamark T. Selective autophagy mediated by autophagic

adapter proteins. *Autophagy*. 2011;7(3):279-296. doi:10.4161/auto.7.3.14487

79. Chan NC, Salazar AM, Pham AH, et al. Broad activation of the ubiquitin-proteasome system by Parkin is critical for mitophagy. *Hum Mol Genet*. 2011;20(9):1726-1737. doi:10.1093/hmg/ddr048

80. Xiao Y, Zhou Y, Lu Y, Zhou K, Cai W. PHB2 interacts with LC3 and SQSTM1 is required for bile acids-induced mitophagy in cholestatic liver. *Cell Death Dis*. 2018;9(2). doi:10.1038/s41419-017-0228-8

81. Chu CT, Ji J, Dagda RK, et al. Cardiolipin externalization to the outer mitochondrial membrane acts as an elimination signal for mitophagy in neuronal cells. *Nat Cell Biol*. 2013;15(10):1197-1205. doi:10.1038/ncb2837

82. Orvedahl A, Sumpter R, Xiao G, et al. Image-based genome-wide siRNA screen identifies selective autophagy factors. *Nature*. 2011;480(7375):113-117. doi:10.1038/nature10546

83. Fu M, St-Pierre P, Shankar J, Wang PTC, Joshi B, Nabi IR. Regulation of mitophagy by the Gp78 E3 ubiquitin ligase. *Mol Biol Cell*. 2013;24(8):1153-1162. doi:10.1091/mbc.E12-08-0607

84. Liu L, Feng D, Chen G, et al. Mitochondrial outer-membrane protein FUNDC1 mediates hypoxia-induced mitophagy in mammalian cells. *Nat Cell Biol*. 2012;14(2):177-185. doi:10.1038/ncb2422

85. Schwarten M, Mohrlüder J, Ma P, et al. Nix directly binds to GABARAP: A possible crosstalk between apoptosis and autophagy. *Autophagy*. 2009;5(5):690-698. doi:10.4161/auto.5.5.8494

86. Rikka S, Quinsay MN, Thomas RL, et al. Bnip3 impairs mitochondrial bioenergetics and stimulates mitochondrial turnover. *Cell Death Differ*. 2011;18(4):721-731. doi:10.1038/cdd.2010.146

87. Schweers RL, Zhang J, Randall MS, et al. NIX is required for programmed mitochondrial clearance during reticulocyte maturation. *Proc Natl Acad Sci U S A*. 2007;104(49):19500-19505. doi:10.1073/pnas.0708818104

88. Bhujabal Z, Birgisdottir ÅB, Sjøttem E, et al. FKBP8 recruits LC3A to mediate Parkin-independent mitophagy. *EMBO Rep*. 2017;18(6):947-961. doi:10.15252/embr.201643147

89. Saita S, Shirane M, Nakayama KI. Selective escape of proteins from the mitochondria during mitophagy. *Nat Commun*. 2013;4:1-14.

doi:10.1038/ncomms2400

90. Murakawa T, Yamaguchi O, Hashimoto A, et al. Bcl-2-like protein 13 is a mammalian Atg32 homologue that mediates mitophagy and mitochondrial fragmentation. *Nat Commun*. 2015;6(May). doi:10.1038/ncomms8527

91. Twig G, Elorza A, Molina AJA, et al. Fission and selective fusion govern mitochondrial segregation and elimination by autophagy. *EMBO J*. 2008;27(2):433-446. doi:10.1038/sj.emboj.7601963

92. Ni HM, Williams JA, Ding WX. Mitochondrial dynamics and mitochondrial quality control. *Redox Biol*. 2015;4:6-13. doi:10.1016/j.redox.2014.11.006

93. Gomes LC, Benedetto G Di, Scorrano L. During autophagy mitochondria elongate, are spared from degradation and sustain cell viability. *Nat Cell Biol*. 2011;13(5):589-598. doi:10.1038/ncb2220

94. Heeman B, Van den Haute C, Aelvoet SA, et al. Depletion of PINK1 affects mitochondrial metabolism, calcium homeostasis and energy maintenance. *J Cell Sci*. 2011;124(7):1115-1125. doi:10.1242/jcs.078303

95. Ju L, Chen S, Alimujiang M, et al. A novel role for Bcl2l13 in promoting beige adipocyte biogenesis. *Biochem Biophys Res Commun*. 2018;506(3):485-491. doi:10.1016/j.bbrc.2018.10.034

96. Landes T, Emorine LJ, Courilleau D, Rojo M, Belenguer P, Arnauné-Pelloquin L. The BH3-only Bnip3 binds to the dynamin Opa1 to promote mitochondrial fragmentation and apoptosis by distinct mechanisms. *EMBO Rep*. 2010;11(6):459-465. doi:10.1038/embor.2010.50

97. Ross MH, Pawlina W. *Histology: A Text and Atlas : With Correlated Cell and Molecular Biology*. Wolters Kluwer/Lippincott Williams & Wilkins Health; 2011. https://books.google.es/books?id=SVjtwAEACAAJ

98. Hanson J, Huxley HE. Structural Basis of the Cross-Striations in Muscle. *Nature*. 1953;172(4377):530-532. doi:10.1038/172530b0

99. Sweeney HL, Hammers DW. Muscle Contraction. *J Physiol*. 1995;487:151-165. doi:10.1113/jphysiol.1995.sp020931

100. Lieberman 1950 M. *Marks' Basic Medical Biochemistry : A Clinical Approach*. Fourth edition. Philadelphia : Wolters Kluwer Health/Lippincott Williams & Wilkins, [2013] https://search.library.wisc.edu/catalog/9910207808902121

101. Boyer O, Nevo F, Plaisier E, et al. INF2 mutations in Charcot-Marie-Tooth

disease with glomerulopathy. *N Engl J Med*. 2011;365(25):2377-2388. doi:10.1056/NEJMoa1109122

102. Cuesta A, Pedrola L, Sevilla T, et al. The gene encoding ganglioside-induced differentiation-associated protein 1 is mutated in axonal Charcot-Marie-Tooth type 4A disease. *Nat Genet*. 2002;30(1):22-25. doi:10.1038/ng798

103. Züchner S, Noureddine M, Kennerson M, et al. Mutations in the pleckstrin homology domain of dynamin 2 cause dominant intermediate Charcot-Marie-Tooth disease. *Nat Genet*. 2005;37(3):289-294. doi:10.1038/ng1514

104. Bitoun M, Maugenre S, Jeannet PY, et al. Mutations in dynamin 2 cause dominant centronuclear myopathy. *Nat Genet*. 2005;37(11):1207-1209. doi:10.1038/ng1657

105. Nasca A, Scotton C, Zaharieva I, et al. Recessive mutations in MSTO1 cause mitochondrial dynamics impairment, leading to myopathy and ataxia. *Hum Mutat*. 2017;38(8):970-977. doi:10.1002/humu.23262

106. Carrascoso I, Sánchez-Jiménez C, Silion E, Alcalde J, Izquierdo JM. A Heterologous Cell Model for Studying the Role of T-Cell Intracellular Antigen 1 in Welander Distal Myopathy. *Mol Cell Biol*. 2018;39(1):1-17. doi:10.1128/mcb.00299-18

107. El-Hattab AW, Craigen WJ, Scaglia F. Mitochondrial DNA maintenance defects. *Biochim Biophys Acta - Mol Basis Dis*. 2017;1863(6):1539-1555. doi:10.1016/j.bbadis.2017.02.017

108. Ahmed ST, Craven L, Russell OM, Turnbull DM, Vincent AE. Diagnosis and Treatment of Mitochondrial Myopathies. *Neurotherapeutics*. 2018;15(4):943-953. doi:10.1007/s13311-018-00674-4

109. Andreu AL, Hanna MG, Reichmann H, et al. EXERCISE INTOLERANCE DUE TO MUTATIONS IN THE CYTOCHROME b GENE OF MITOCHONDRIAL DNA. *N Engl J Med*. Published online 1999:1037-1044.

110. Santorelli FM, Tanji K, Kulikova R, et al. Identification of a novel mutation in the mtDNA ND5 gene associated with MELAS. *Biochem Biophys Res Commun*. 1997;238(2):326-328. doi:10.1006/bbrc.1997.7167

111. Emna Mkaouar-Reba, B RF, B MT, et al. Mitochondrial DNA triplication and punctual mutations in patients with mitochondrial neuromuscular disorders. Published online 2016.

112. Pitceathly RDS, Murphy SM, Cottenie E, et al. Genetic dysfunction of MT-ATP6 causes axonal charcot-Marie-Tooth disease. *Neurology*. 2012;79(11):1145-1154. doi:10.1212/WNL.0b013e3182698d8d

113. Taylor RW, Turnbull DM. MITOCHONDRIAL DNA MUTATIONS IN HUMAN DISEASE. *Nat Rev Genet*. 2007;6(5):389-402. doi:10.1038/nrg1606.MITOCHONDRIAL

114. Mkaouar-Rebai E, Ben Mahmoud A, Chamkha I, et al. A novel MT-CO2 m.8249G > A pathogenic variation and the MT-TW m.5521G > A mutation in patients with mitochondrial myopathy. *Mitochondrial DNA*. 2014;25(5):394-399. doi:10.3109/19401736.2013.803086

115. Nemazanyy I, Blaauw B, Paolini C, et al. Defects of Vps15 in skeletal muscles lead to autophagic vacuolar myopathy and lysosomal disease. *EMBO Mol Med*. 2013;5(6):870-890. doi:10.1002/emmm.201202057

116. Sebori R, Kuno A, Hosoda R, Hayashi T, Horio Y. Resveratrol decreases oxidative stress by restoring mitophagy and improves the pathophysiology of dystrophin-deficient MDX mice. *Oxid Med Cell Longev*. 2018;2018. doi:10.1155/2018/9179270

117. Ryu D, Mouchiroud L, Andreux PA, et al. Urolithin A induces mitophagy and prolongs lifespan in C. elegans and increases muscle function in rodents. *Nat Med*. 2016;22(8):879-888. doi:10.1038/nm.4132

118. de Paepe B. Sporadic inclusion body myositis: An acquired mitochondrial disease with extras. *Biomolecules*. 2019;9(1). doi:10.3390/biom9010015

119. Catalán-García M, Garrabou G, Morén C, et al. Mitochondrial DNA disturbances and deregulated expression of oxidative phosphorylation and mitochondrial fusion proteins in sporadic inclusion body myositis. *Clin Sci*. 2016;130(19):1741-1751. doi:10.1042/CS20160080

120. Sliter DA, Martinez J, Hao L, et al. Parkin and PINK1 mitigate STING-induced inflammation. *Nature*. 2018;561(7722):258-262. doi:10.1038/s41586-018-0448-9

121. West AP, Khoury-Hanold W, Staron M, et al. Mitochondrial DNA stress primes the antiviral innate immune response. *Nature*. 2015;520(7548):553-557. doi:10.1038/nature14156

122. Stuart E. Turvey DHB. Innate Immunity. *J Allergy Clin Immunol*. 2010;125(2 Suppl 2):1-4. doi:10.1016/j.jaci.2009.07.016.Chapter

123. Kim J. Regulation of immune cell functions by metabolic reprogramming.

J Immunol Res. 2018;2018. doi:10.1155/2018/8605471

124. Tredget EE, Yu YM, Zhong S, et al. Role of interleukin 1 and tumor necrosis factor on energy metabolism in rabbits. *Am J Physiol - Endocrinol Metab*. 1988;255(6). doi:10.1152/ajpendo.1988.255.6.e760

125. Vary TC, Siegel JH. Effect of sepsis on activity of pyruvate dehydrogenase complex in skeletal muscle and liver. *Am J Physiol*. 1989;256(3 Pt 1):634-640.

126. Zell R, Geck P, Werdan K, Boekstegers P. TNF-α and IL-1α inhibit both pyruvate dehydrogenase activity and mitochondrial function in cardiomyocytes: Evidence for primary impairment of mitochondrial function. *Mol Cell Biochem*. 1997;177(1-2):61-67. doi:10.1023/A:1006896832582

127. Samavati L, Lee I, Mathes I, Lottspeich F, Hüttemann M. Tumor necrosis factor α inhibits oxidative phosphorylation through tyrosine phosphorylation at subunit I of cytochrome c oxidase. *J Biol Chem*. 2008;283(30):21134-21144. doi:10.1074/jbc.M801954200

128. Motori E, Puyal J, Toni N, et al. Inflammation-induced alteration of astrocyte mitochondrial dynamics requires autophagy for mitochondrial network maintenance. *Cell Metab*. 2013;18(6):844-859. doi:10.1016/j.cmet.2013.11.005

129. Hahn WS, Kuzmicic J, Burrill JS, et al. Proinflammatory cytokines differentially regulate adipocyte mitochondrial metabolism, oxidative stress, and dynamics. *Am J Physiol - Endocrinol Metab*. 2014;306(9):1033-1045. doi:10.1152/ajpendo.00422.2013

130. Anusree SS, Nisha VM, Priyanka A, Raghu KG. Insulin resistance by TNF-α is associated with mitochondrial dysfunction in 3T3-L1 adipocytes and is ameliorated by punicic acid, a PPARγ agonist. *Mol Cell Endocrinol*. 2015;413:120-128. doi:10.1016/j.mce.2015.06.018

131. White JP, Puppa MJ, Sato S, et al. IL-6 regulation on skeletal muscle mitochondrial remodeling during cancer cachexia in the ApcMin/+ mouse. *Skelet Muscle*. 2012;2(1):1-16. doi:10.1186/2044-5040-2-14

132. Seth RB, Sun L, Ea CK, Chen ZJ. Identification and characterization of MAVS, a mitochondrial antiviral signaling protein that activates NF-κB and IRF3. *Cell*. 2005;122(5):669-682. doi:10.1016/j.cell.2005.08.012

133. Misawa T, Takahama M, Saitoh T. Mitochondria–Endoplasmic Reticulum Contact Sites Mediate Innate Immune Responses BT - Organelle Contact

Sites: From Molecular Mechanism to Disease. In: Tagaya M, Simmen T, eds. Springer Singapore; 2017:187-197. doi:10.1007/978-981-10-4567-7_14

134. Lamkanfi M, Dixit VM. Inflammasomes and Their Roles in Health and Disease. *Annu Rev Cell Dev Biol*. 2012;28(1):137-161. doi:10.1146/annurev-cellbio-101011-155745

135. Zhou R, Yazdi AS, Menu P, Tschopp J. A role for mitochondria in NLRP3 inflammasome activation. *Nature*. 2011;469(7329):221-226. doi:10.1038/nature09663

136. Park S, Juliana C, Hong S, et al. The Mitochondrial Antiviral Protein MAVS Associates with NLRP3 and Regulates Its Inflammasome Activity. *J Immunol*. 2013;191(8):4358-4366. doi:10.4049/jimmunol.1301170

137. ShankarS I, Q H, JR J, et al. Mitochondrial cardiolipin is required for Nlrp3 inflammasome activation. *Immunity*. 2013;23(1):1-7. doi:10.1038/jid.2014.371

138. Rodríguez-Nuevo A, Zorzano A. The sensing of mitochondrial DAMPs by non-immune cells. *Cell Stress*. 2019;3(6):195-207. doi:10.15698/cst2019.06.190

139. Bours MJL, Swennen ELR, Di Virgilio F, Cronstein BN, Dagnelie PC. Adenosine 5′-triphosphate and adenosine as endogenous signaling molecules in immunity and inflammation. *Pharmacol Ther*. 2006;112(2):358-404. doi:10.1016/j.pharmthera.2005.04.013

140. Julian MW, Shao G, Bao S, et al. Mitochondrial Transcription Factor A Serves as a Danger Signal by Augmenting Plasmacytoid Dendritic Cell Responses to DNA. *J Immunol*. 2012;189(1):433-443. doi:10.4049/jimmunol.1101375

141. Tannahill GM, Curtis AM, Adamik J, et al. Succinate is an inflammatory signal that induces IL-1β through HIF-1α. *Nature*. 2013;496(7444):238-242. doi:10.1038/nature11986

142. Carp BH. MITOCHONDRIAL N-FORMYLMETHIONYL PROTEINS AS CHEMOATTRACTANTS FOR NEUTROPHILS. *J Exp Med*. 1982;155(January):264-275.

143. Dieudé M, Striegl H, Tyznik AJ, et al. Cardiolipin Binds to CD1d and Stimulates CD1d-Restricted γδ T Cells in the Normal Murine Repertoire. *J Immunol*. 2011;186(8):4771-4781. doi:10.4049/jimmunol.1000921

144. Bonawitz ND, Clayton DA, Shadel GS. Initiation and Beyond: Multiple Functions of the Human Mitochondrial Transcription Machinery. *Mol Cell*. 2006;24(6):813-825. doi:10.1016/j.molcel.2006.11.024

145. Legros F, Malka F, Frachon P, Lombès A, Rojo M. Organization and dynamics of human mitochondrial DNA. *J Cell Sci*. 2004;117(13):2653-2662. doi:10.1242/jcs.01134

146. Kukat C, Wurm CA, Spåhr H, Falkenberg M, Larsson NG, Jakobs S. Super-resolution microscopy reveals that mammalian mitochondrial nucleoids have a uniform size and frequently contain a single copy of mtDNA. *Proc Natl Acad Sci U S A*. 2011;108(33):13534-13539. doi:10.1073/pnas.1109263108

147. West AP, Shadel GS. Mitochondrial DNA in innate immune responses and inflammatory pathology. *Nat Rev Immunol*. 2017;17(6):363-375. doi:10.1038/nri.2017.21

148. Li Y, Berke IC, Modis Y. DNA binding to proteolytically activated TLR9 is sequence-independent and enhanced by DNA curvature. *EMBO J*. 2012;31(4):919-931. doi:10.1038/emboj.2011.441

149. Pazmandi K, Agod Z, Kumar B V., et al. Oxidative modification enhances the immunostimulatory effects of extracellular mitochondrial DNA on plasmacytoid dendritic cells. *Free Radic Biol Med*. 2014;77:281-290. doi:10.1016/j.freeradbiomed.2014.09.028

150. Andreeva L, Hiller B, Kostrewa D, et al. CGAS senses long and HMGB/TFAM-bound U-turn DNA by forming protein-DNA ladders. *Nature*. 2017;549(7672):394-398. doi:10.1038/nature23890

151. Lood C, Blanco LP, Purmalek MM, et al. Neutrophil extracellular traps enriched in oxidized mitochondrial DNA are interferogenic and contribute to lupus-like disease. *Nat Med*. 2016;22(2):146-153. doi:10.1038/nm.4027

152. Mankan AK, Schmidt T, Chauhan D, et al. Cytosolic RNA:DNA hybrids activate the cGAS –STING axis . *EMBO J*. 2014;33(24):2937-2946. doi:10.15252/embj.201488726

153. Shimada K, Crother TR, Karlin J, et al. Oxidized Mitochondrial DNA Activates the NLRP3 Inflammasome during Apoptosis. *Immunity*. 2012;36(3):401-414. doi:10.1016/j.immuni.2012.01.009

154. Jabir MS, Hopkins L, Ritchie ND, et al. Mitochondrial damage contributes to pseudomonas aeruginosa activation of the inflammasome and is

downregulated by autophagy. *Autophagy*. 2015;11(1):166-182. doi:10.4161/15548627.2014.981915

155. Bae JH, Jo SI, Kim SJ, et al. Circulating Cell-Free mtDNA Contributes to AIM2 Inflammasome-Mediated Chronic Inflammation in Patients with Type 2 Diabetes. *Cells*. 2019;8(4):328. doi:10.3390/cells8040328

156. Pérez-Treviño P, Velásqueza M, García N. Mechanisms of mitochondrial DNA escape and its relationship with different metabolic diseases. Published online 2020.

157. Giorgio V, Guo L, Bassot C, Petronilli V, Bernardi P. Calcium and regulation of the mitochondrial permeability transition. *Cell Calcium*. 2018;70:56-63. doi:10.1016/j.ceca.2017.05.004

158. García N, Chávez E. Mitochondrial DNA fragments released through the permeability transition pore correspond to specific gene size. *Life Sci*. 2007;81(14):1160-1166. doi:10.1016/j.lfs.2007.08.019

159. Nakahira K, Haspel JA, Rathinam VAK, et al. Autophagy proteins regulate innate immune responses by inhibiting the release of mitochondrial DNA mediated by the NALP3 inflammasome. *Nat Immunol*. 2011;12(3):222-230. doi:10.1038/ni.1980

160. Li W, Li Y, Siraj S, et al. FUN14 Domain-Containing 1–Mediated Mitophagy Suppresses Hepatocarcinogenesis by Inhibition of Inflammasome Activation in Mice. *Hepatology*. 2019;69(2):604-621. doi:10.1002/hep.30191

161. Oka T, Hikoso S, Yamaguchi O, et al. Mitochondrial DNA that escapes from autophagy causes inflammation and heart failure. *Nature*. 2012;485(7397):251-255. doi:10.1038/nature10992

162. Galluzzi L, Vitale I, Aaronson SA, et al. Molecular mechanisms of cell death: Recommendations of the Nomenclature Committee on Cell Death 2018. *Cell Death Differ*. 2018;25(3):486-541. doi:10.1038/s41418-017-0012-4

163. Saito Y, Hikita H, Nozaki Y, et al. DNase II activated by the mitochondrial apoptotic pathway regulates RIP1-dependent non-apoptotic hepatocyte death via the TLR9/IFN-β signaling pathway. *Cell Death Differ*. 2019;26(3):470-486. doi:10.1038/s41418-018-0131-6

164. Rongvaux A, Jackson R, Harman CCD, et al. Apoptotic caspases prevent the induction of type i interferons by mitochondrial DNA. *Cell*. 2014;159(7):1563-1577. doi:10.1016/j.cell.2014.11.037

165. White MJ, McArthur K, Metcalf D, et al. Apoptotic caspases suppress mtDNA-induced STING-mediated type i IFN production. *Cell*. 2014;159(7):1549-1562. doi:10.1016/j.cell.2014.11.036

166. Bao D, Zhao J, Zhou X, et al. Mitochondrial fission-induced mtDNA stress promotes tumor-associated macrophage infiltration and HCC progression. *Oncogene*. 2019;38(25):5007-5020. doi:10.1038/s41388-019-0772-z

167. Kim J, Gupta R, Blanco LP, et al. VDAC oligomers form mitochondrial pores to release mtDNA fragments and promote lupus-like disease. *Science (80-)*. 2019;366(6472):1531-1536. doi:10.1126/science.aav4011

168. Chung KW, Dhillon P, Huang S, et al. Mitochondrial Damage and Activation of the STING Pathway Lead to Renal Inflammation and Fibrosis. *Cell Metab*. 2019;30(4):784-799.e5. doi:10.1016/j.cmet.2019.08.003

169. Marongiu L, Gornati L, Artuso I, Zanoni I, Granucci F. Below the surface: The inner lives of TLR4 and TLR9. *J Leukoc Biol*. 2019;106(1):147-160. doi:10.1002/JLB.3MIR1218-483RR

170. Honda K, Ohba Y, Yanai H, et al. Spatiotemporal regulation of MyD88-IRF-7 signalling for robust type-I interferon induction. *Nature*. 2005;434(7036):1035-1040. doi:10.1038/nature03547

171. Duhamel M, Rodet F, Murgoci AN, et al. The proprotein convertase PC1/3 regulates TLR9 trafficking and the associated signaling pathways. *Sci Rep*. 2016;6(January):1-13. doi:10.1038/srep19360

172. Todkar K, Chikhi L, Germain M. Mitochondrial interaction with the endosomal compartment in endocytosis and mitochondrial transfer. *Mitochondrion*. 2019;49(March):284-288. doi:10.1016/j.mito.2019.05.003

173. Sugiura A, McLelland G, Fon EA, McBride HM. A new pathway for mitochondrial quality control: mitochondrial-derived vesicles. *EMBO J*. 2014;33(19):2142-2156. doi:10.15252/embj.201488104

174. Hammerling BC, Shires SE, Leon LJ, Cortez MQ, Gustafsson ÅB. Isolation of Rab5-positive endosomes reveals a new mitochondrial degradation pathway utilized by BNIP3 and Parkin. *Small GTPases*. 2020;11(1):69-76. doi:10.1080/21541248.2017.1342749

175. Rayavarapu S, Coley W, Kinder TB, Nagaraju K. Idiopathic inflammatory myopathies: Pathogenic mechanisms of muscle weakness. *Skelet Muscle*. 2013;3(1):1. doi:10.1186/2044-5040-3-13

176. Luecke S, Holleufer A, Christensen MH, et al. cGAS is activated by DNA in a length-dependent manner . *EMBO Rep*. 2017;18(10):1707-1715. doi:10.15252/embr.201744017

177. Cai X, Chiu YH, Chen ZJ. The cGAS-cGAMP-STING pathway of cytosolic DNA sensing and signaling. *Mol Cell*. 2014;54(2):289-296. doi:10.1016/j.molcel.2014.03.040

178. Dunphy G, Flannery SM, Almine JF, et al. Non-canonical Activation of the DNA Sensing Adaptor STING by ATM and IFI16 Mediates NF-κB Signaling after Nuclear DNA Damage. *Mol Cell*. 2018;71(5):745-760.e5. doi:10.1016/j.molcel.2018.07.034

179. Zevini A, Olagnier D, Hiscott J. Cross-Talk between the Cytoplasmic RIG-I and STING Sensing Pathways. *Trends Immunol*. 2015;176(1):139-148. doi:10.1016/j.physbeh.2017.03.040

180. Zhou R, Xie X, Li X, et al. The triggers of the cGAS-STING pathway and the connection with inflammatory and autoimmune diseases. *Infect Genet Evol*. 2020;77(November 2019):104094. doi:10.1016/j.meegid.2019.104094

181. Abdul-Sater AA, Saïd-Sadier N, Ojcius DM, Yilmaz Ö, Kelly KA. Inflammasomes bridge signaling between pathogen identification and the immune response. *Drugs of Today*. 2009;45(SUPPL. B):105-112.

182. Lammert CR, Frost EL, Bellinger CE, et al. AIM2 inflammasome surveillance of DNA damage shapes neurodevelopment. *Nature*. 2020;(May 2018). doi:10.1038/s41586-020-2174-3

183. Zhong Z, Liang S, Sanchez-Lopez E, et al. New mitochondrial DNA synthesis enables NLRP3 inflammasome activation. *Nature*. 2018;560(7717):198-203. doi:10.1038/s41586-018-0372-z

184. Mittmann N, Stout NK, Lee P, et al. NF-κB Restricts inflammasome activation via elimination of damaged mitochondria. *Cell*. 2015;26(12):16-25. doi:10.1002/nbm.3369.Three

185. Gaidt MM, Ebert TS, Chauhan D, et al. The DNA Inflammasome in Human Myeloid Cells Is Initiated by a STING-Cell Death Program Upstream of NLRP3. *Cell*. 2017;171(5):1110-1124.e18. doi:10.1016/j.cell.2017.09.039

186. Masanori K, Masafumi T, Takeki H, et al. Inflammasome Activation of Cardiac Fibroblasts Is Essential for Myocardial Ischemia/Reperfusion Injury. *Circulation*. 2011;123(6):594-604. doi:10.1161/CIRCULATIONAHA.110.982777

187. Mangan MSJ, Olhava EJ, Roush WR, Seidel HM, Glick GD, Latz E. Targeting the NLRP3 inflammasome in inflammatory diseases. *Nat Rev Drug Discov*. 2018;17(8):588-606. doi:10.1038/nrd.2018.97

188. Filadi R, Pendin Di, Pizzo P. Mitofusin 2: From functions to disease. *Cell Death Dis*. 2018;9(3). doi:10.1038/s41419-017-0023-6

189. Ryu MJ, Kim SJ, Kim YK, et al. Crif1 Deficiency Reduces Adipose OXPHOS Capacity and Triggers Inflammation and Insulin Resistance in Mice. *PLoS Genet*. 2013;9(3). doi:10.1371/journal.pgen.1003356

190. Stunz LL, Lenert P, Peckham D, et al. Inhibitory oligonucleotides specifically block effects of stimulatory CpG oligonucleotides in B cells. *Eur J Immunol*. 2002;32(5):1212-1222. doi:10.1002/1521-4141(200205)32:5<1212::AID-IMMU1212>3.0.CO;2-D

191. Vincent J, Adura C, Gao P, et al. Small molecule inhibition of cGAS reduces interferon expression in primary macrophages from autoimmune mice. *Nat Commun*. 2017;8(1):1-12. doi:10.1038/s41467-017-00833-9

192. Das A, Nag S, Mason AB, Barroso MM. Endosome-mitochondria interactions are modulated by iron release from transferrin. *J Cell Biol*. 2016;214(7):831-845. doi:10.1083/jcb.201602069

193. Hsu F, Spannl S, Ferguson C, Hyman T, Parton R, Zerial M. Rab5 and Alsin regulate stress-activated cytoprotective signaling on mitochondria. *bioRxiv*. Published online 2017:200428. doi:10.1101/200428

194. Giacomello M, Pellegrini L. The coming of age of the mitochondria-ER contact: A matter of thickness. *Cell Death Differ*. 2016;23(9):1417-1427. doi:10.1038/cdd.2016.52

195. Daniele T, Hurbain I, Vago R, et al. Mitochondria and melanosomes establish physical contacts modulated by Mfn2 and involved in organelle biogenesis. *Curr Biol*. 2014;24(4):393-403. doi:10.1016/j.cub.2014.01.007

196. Zhao T, Huang X, Han L, et al. Central role of mitofusin 2 in autophagosome-lysosome fusion in cardiomyocytes. *J Biol Chem*. 2012;287(28):23615-23625. doi:10.1074/jbc.M112.379164

197. Merithew E, Stone C, Eathiraj S, Lambright DG. Determinants of Rab5 interaction with the N terminus of early endosome antigen 1. *J Biol Chem*. 2003;278(10):8494-8500. doi:10.1074/jbc.M211514200

198. Ben-Hail D, Begas-Shvartz R, Shalev M, et al. Novel compounds targeting the mitochondrial protein VDAC1 inhibit apoptosis and protect against

mitochondrial dysfunction. *J Biol Chem*. 2016;291(48):24986-25003. doi:10.1074/jbc.M116.744284

199. Bell MB, Bush Z, McGinnis GR, Rowe GC. Adult skeletal muscle deletion of Mitofusin 1 and 2 impedes exercise performance and training capacity. *J Appl Physiol*. 2019;126(2):341-353. doi:10.1152/japplphysiol.00719.2018

200. Sebastián D, Zorzano A. Mitochondrial dynamics and metabolic homeostasis. *Curr Opin Physiol*. 2018;3:34-40. doi:10.1016/j.cophys.2018.02.006

201. Mishra P, Varuzhanyan G, Pham AH, Chan DC. Mitochondrial Dynamics Is a Distinguishing Feature of Skeletal Muscle Fiber Types and Regulates Organellar Compartmentalization. *Cell Metab*. 2015;22(6):1033-1044. doi:10.1016/j.cmet.2015.09.027

202. Ostrowski K, Rohde T, Zacho M, Asp S, Pedersen BK. Evidence that interleukin-6 is produced in human skeletal muscle during prolonged running. *J Physiol*. 1998;508(3):949-953. doi:10.1111/j.1469-7793.1998.949bp.x

203. Pedersen BK, Steensberg A, Schjerling P. Muscle-derived interleukin-6: Possible biological effects. *J Physiol*. 2001;536(2):329-337. doi:10.1111/j.1469-7793.2001.0329c.xd

204. Kopp E, Ghosh S. Inhibition of NF-κB by sodium salicylate and aspirin. *Science (80-)*. 1994;265(5174):956-959. doi:10.1126/science.8052854

205. Ligibel JA, Schmitz KH, Berger NA. Sarcopenia in aging, obesity, and cancer. *Transl Cancer Res*. 2020;9(9):5760-5771. doi:10.21037/tcr-2019-eaoc-05

206. Wang J, Leung KS, Chow SKH, Cheung WH. Inflammation and age-associated skeletal muscle deterioration (sarcopaenia). *J Orthop Transl*. 2017;10:94-101. doi:10.1016/j.jot.2017.05.006

207. Cai D, Frantz JD, Tawa NE, et al. IKKβ/NF-κB activation causes severe muscle wasting in mice. *Cell*. 2004;119(2):285-298. doi:10.1016/j.cell.2004.09.027

208. Mourkioti F, Kratsios P, Luedde T, et al. Targeted ablation of IKK2 improves skeletal muscle strength, maintains mass, and promotes regeneration. *J Clin Invest*. 2006;116(11):2945-2954. doi:10.1172/JCI28721

209. Xian H, Yang Q, Xiao L, Shen HM, Liou YC. STX17 dynamically regulated by

Fis1 induces mitophagy via hierarchical macroautophagic mechanism. *Nat Commun*. 2019;10(1). doi:10.1038/s41467-019-10096-1

210. Kim YM, Krantz S, Jambusaria A, et al. Mitofusin-2 stabilizes adherens junctions and suppresses endothelial inflammation via modulation of β-catenin signaling. *Nat Commun*. 2021;12(1):1-17. doi:10.1038/s41467-021-23047-6

211. Koshiba T, Yasukawa K, Yanagi Y, Kawabata SI. Mitochondrial membrane potential is required for MAVS-mediated antiviral signaling. *Sci Signal*. 2011;4(158):1-8. doi:10.1126/scisignal.2001147

212. Hou S, Wang L, Zhang G. Mitofusin-2 regulates inflammation-mediated mouse neuroblastoma N2a cells dysfunction and endoplasmic reticulum stress via the Yap-Hippo pathway. *J Physiol Sci*. 2019;69(5):697-709. doi:10.1007/s12576-019-00685-6

213. Brahimi-Horn MC, Lacas-Gervais S, Adaixo R, et al. Local Mitochondrial-Endolysosomal Microfusion Cleaves Voltage-Dependent Anion Channel 1 To Promote Survival in Hypoxia. *Mol Cell Biol*. 2015;35(9):1491-1505. doi:10.1128/mcb.01402-14

214. Wang T Sen, Coppens I, Saorin A, Brady NR, Hamacher-Brady A. Endolysosomal Targeting of Mitochondria Is Integral to BAX-Mediated Mitochondrial Permeabilization during Apoptosis Signaling. *Dev Cell*. 2020;53(6):627-645.e7. doi:10.1016/j.devcel.2020.05.014

215. Puri C, Vicinanza M, Ashkenazi A, et al. The RAB11A-Positive Compartment Is a Primary Platform for Autophagosome Assembly Mediated by WIPI2 Recognition of PI3P-RAB11A. *Dev Cell*. 2018;45(1):114-131.e8. doi:10.1016/j.devcel.2018.03.008

216. Ravindran R, Velikkakath AK, Narendradev N, Chandrasekharan A, Santhoshkumar TR, Srinivasula S. Endosomes facilitate mitochondrial clearance by enhancing Mfn2 degradation and subsequent Parkin recruitment. Published online 2020. doi:10.1101/2020.02.19.955880

217. Sebastián D, Hernández-Alvarez MI, Segalés J, et al. Mitofusin 2 (Mfn2) links mitochondrial and endoplasmic reticulum function with insulin signaling and is essential for normal glucose homeostasis. *Proc Natl Acad Sci U S A*. 2012;109(14):5523-5528. doi:10.1073/pnas.1108220109

218. Liang Y-Q, Akishita M, Kim S, et al. Estrogen receptor beta is involved in the anorectic action of estrogen. *Int J Obes Relat Metab Disord J Int Assoc Study Obes*. 2002;26(8):1103-1109. doi:10.1038/sj.ijo.0802054

219. Jones MEE, Thorburn AW, Britt KL, et al. Aromatase-deficient (ArKO) mice have a phenotype of increased adiposity. *Proc Natl Acad Sci U S A*. 2000;97(23):12735-12740. doi:10.1073/pnas.97.23.12735

220. Mårin P, Holmäng S, Jönsson L, et al. The effects of testosterone treatment on body composition and metabolism in middle-aged obese men. *Int J Obes Relat Metab Disord J Int Assoc Study Obes*. 1992;16(12):991-997.

221. Bazhan N, Jakovleva T, Feofanova N, et al. Sex Differences in Liver, Adipose Tissue, and Muscle Transcriptional Response to Fasting and Refeeding in Mice. *Cells*. 2019;8(12):1-18. doi:10.3390/cells8121529

222. Bazhan N, Jakovleva T, Balyibina N, et al. Sex dimorphism in the Fgf21 gene expression in liver and adipose tissues is dependent on the metabolic condition. *Online J Biol Sci*. 2019;19(1):28-36. doi:10.3844/ojbsci.2019.28.36

223. Tezze C, Romanello V, Sandri M. FGF21 as modulator of metabolism in health and disease. *Front Physiol*. 2019;10(MAR):1-9. doi:10.3389/fphys.2019.00419

224. Itoh N. FGF21 as a hepatokine, adipokine, and myokine in metabolism and diseases. *Front Endocrinol (Lausanne)*. 2014;5(JUL):4-7. doi:10.3389/fendo.2014.00107

225. McKinnell IW, Rudnicki MA. Molecular mechanisms of muscle atrophy. *Cell*. 2004;119(7):907-910. doi:10.1016/j.cell.2004.12.007

226. Shin J, Lee SH, Kwon MC, et al. Cardiomyocyte Specific Deletion of Crif1 Causes Mitochondrial Cardiomyopathy in Mice. *PLoS One*. 2013;8(1). doi:10.1371/journal.pone.0053577

227. Bodine SC, Baehr LM. Skeletal muscle atrophy and the E3 ubiquitin ligases MuRF1 and MAFbx/atrogin-1. *Am J Physiol Endocrinol Metab*. 2014;307(6):E469-E484. doi:10.1152/ajpendo.00204.2014

228. Deguise MO, Boyer JG, McFall ER, Yazdani A, De Repentigny Y, Kothary R. Differential induction of muscle atrophy pathways in two mouse models of spinal muscular atrophy. *Sci Rep*. 2016;6(April):1-13. doi:10.1038/srep28846

229. Chargé SBP, Rudnicki MA. Cellular and Molecular Regulation of Muscle Regeneration. *Physiol Rev*. 2004;84(1):209-238. doi:10.1152/physrev.00019.2003

230. Lahoute C, Sotiropoulos A, Favier M, et al. Premature aging in skeletal muscle lacking serum response factor. *PLoS One*. 2008;3(12). doi:10.1371/journal.pone.0003910

231. Nicole S, Desforges B, Millet G, et al. Intact satellite cells lead to remarkable protection against Smn gene defect in differentiated skeletal muscle. *J Cell Biol*. 2003;161(3):571-582. doi:10.1083/jcb.200210117

232. Lehtinen SK, Rahkila P, Helenius M, Korhonen P, Salminen A. and NF- k B Precedes Myocyte Differentiation. *Biochem Biophys Res Commun*. 1996;43:36-43.

233. Wang H, Hertlein E, Bakkar N, et al. NF-κB Regulation of YY1 Inhibits Skeletal Myogenesis through Transcriptional Silencing of Myofibrillar Genes. *Mol Cell Biol*. 2007;27(12):4374-4387. doi:10.1128/mcb.02020-06

234. Sacheck JM, Cannon JG, Hamada K, Vannier E, Blumberg JB, Roubenoff R. Age-related loss of associations between acute exercise-induced IL-6 and oxidative stress. *Am J Physiol - Endocrinol Metab*. 2006;291(2):340-349. doi:10.1152/ajpendo.00052.2005

235. Cantini M, Massimino ML, Rapizzi E, et al. Human Satellite Cell-Proliferation in Vitro Is Regulated by Autocrine Secretion of IL-6 Stimulated by a Soluble Factor(s) Released by Activated Monocytes. *Biochem Biophys Res Commun*. 1995;216(1):49-53. doi:10.1006/bbrc.1995.2590

236. Steensberg A, Febbraio MA, Osada T, et al. Interleukin-6 production in contracting human skeletal muscle is influenced by pre-exercise muscle glycogen content. *J Physiol*. 2001;537(2):633-639. doi:10.1111/j.1469-7793.2001.00633.x

237. Serrano AL, Baeza-Raja B, Perdiguero E, Jardí M, Muñoz-Cánoves P. Interleukin-6 Is an Essential Regulator of Satellite Cell-Mediated Skeletal Muscle Hypertrophy. *Cell Metab*. 2008;7(1):33-44. doi:10.1016/j.cmet.2007.11.011

238. Geto Z, Molla MD, Challa F, Belay Y, Getahun T. Mitochondrial dynamic dysfunction as a main triggering factor for inflammation associated chronic non-communicable diseases. *J Inflamm Res*. 2020;13:97-107. doi:10.2147/JIR.S232009

239. Schuler M, Ali F, Metzger E, Chambon P, Metzger D. Temporally controlled targeted somatic mutagenesis in skeletal muscles of the mouse. *Genesis*. 2005;41(4):165-170. doi:10.1002/gene.20107

240. Kuznetsov A V., Veksler V, Gellerich FN, Saks V, Margreiter R, Kunz WS. Analysis of mitochondrial function in situ in permeabilized muscle fibers, tissues and cells. *Nat Protoc*. 2008;3(6):965-976. doi:10.1038/nprot.2008.61

241. Muñoz JP, Zorzano A. Analysis of Mitochondrial Morphology and Function Under Conditions of Mitofusin 2 Deficiency. In: Weissig V, Edeas M, eds. Springer New York; 2015:307-320. doi:10.1007/978-1-4939-2288-8_21

242. Bolte S, Cordelières FP. A guided tour into subcellular colocalization analysis in light microscopy. *J Microsc*. 2006;224(3):213-232. doi:10.1111/j.1365-2818.2006.01706.x

243. Liesa M, Palacín M, Zorzano A. Mitochondrial dynamics in mammalian health and disease. *Physiol Rev*. 2009;89(3):799-845. doi:10.1152/physrev.00030.2008

244. Fivenson EM, Lautrup S, Sun N, et al. Mitophagy in neurodegeneration and aging. *Neurochem Int*. 2017;109(December):202-209. doi:10.1016/j.neuint.2017.02.007

245. Sebastián D, Palacín M, Zorzano A. Mitochondrial Dynamics: Coupling Mitochondrial Fitness with Healthy Aging. *Trends Mol Med*. 2017;23(3):201-215. doi:10.1016/j.molmed.2017.01.003

Watercolor illustration made by Ana García Cerdeño.